

Eivind Rørvik Solum

# Distributed Fiber Optic Sensing for monitoring stabilized clay

An experimental study

Master's thesis in Civil and Environmental Engineering

Supervisor: Priscilla Paniagua (NTNU/NGI)

Co-supervisor: Stefan Ritter, Henrik Meland and Sølve Hov (NGI)

June 2023



Eivind Rørvik Solum

# **Distributed Fiber Optic Sensing for monitoring stabilized clay**

An experimental study

Master's thesis in Civil and Environmental Engineering  
Supervisor: Priscilla Paniagua (NTNU/NGI)  
Co-supervisor: Stefan Ritter, Henrik Meland and Sølve Hov (NGI)  
June 2023

Norwegian University of Science and Technology  
Faculty of Engineering  
Department of Civil and Environmental Engineering





# Preface

This M.Sc. Thesis was conducted as a culmination of the Master's degree in Civil and Environmental Engineering at NTNU Gløshaugen in Trondheim. The thesis was completed in the spring of 2023, building upon a literature review conducted on the same topic as part of the Project Thesis in the fall of 2022. This thesis has been written in collaboration with NGI and as part of a larger research project called GOAL.

I would like to express my gratitude to several individuals who have contributed to this thesis and deserve recognition. First and foremost, I would like to extend a big thank you to my external main supervisor, Stefan Ritter from NGI, for closely guiding me throughout the entire process of both the Project Thesis and this M.Sc. Thesis and for providing me with this exciting research topic. He has always been available, provided valuable input, and assisted me whenever needed. A special thank you goes to my co-supervisor, Henrik Meland at NGI, who has facilitated my visits to Oslo and supported me with all the laboratory work. He has also greatly contributed to my deeper understanding of DFOS. I would also like to thank my main supervisor at NTNU, Priscilla Paniagua, for engaging in fruitful discussions and providing valuable insights throughout these two semesters. I must also acknowledge the tremendous support of PhD candidate Sølve Hov during this spring. He has provided assistance with laboratory work, offered valuable insights continuously, and displayed great enthusiasm. He has always been available and has made significant contributions to the development and progress of the thesis.

Finally, I would like to thank all the skilled personnel at the laboratories of both NGI and NTNU for providing me with all the necessary equipment and assisting me whenever I had questions. In addition, I want to thank my family and friends for supporting me throughout this work. Also, *Geohjørnet 2023* has played a crucial role in making this semester enjoyable.

Trondheim, June 2023

A handwritten signature in black ink that reads "Eivind Rørvik Solum". The signature is written in a cursive style and is underlined with a horizontal line.

Eivind Rørvik Solum



# Abstract

Dry Deep Soil Mixing (DDSM) is an often-used method for improving the engineering properties of soft soil. Different chemically composed materials are used as binders to enhance the performance of exposed soil. The binders, such as lime and cement, are injected in dry form into remoulded soil by the use of a rotating mixing tool. There are a lot of uncertainties related to the production of lime/cement-stabilized soil columns. For instance, the estimation of strength and stiffness are based on approximate methods such as unconfined compression tests in the laboratory.

The design properties of the stabilized soil are today usually based on results from laboratory tests of the soil that is to be stabilized. However, this laboratory procedure of estimating the strength and stiffness of the stabilized soil has been shown to greatly underestimate the obtained properties. A laboratory test cannot determine the integrity of in situ stabilized soil, as lab samples are created in a more idealized setting than what exists in the field. The integrity of soil refers here to its homogeneity, strength and stiffness, indicating its ability to withstand external forces and maintain its structural integrity.

Methods of estimating the obtained mechanical properties based on the in situ stabilized soil also exist, nevertheless, neither these methods are satisfactory. This is because the methods investigating the in situ stabilized clay are resource-intensive, considering factors such as economics, human labor and large-scale machinery, in addition to being destructive. A system for detecting possible imperfections along the height of stabilized soil columns is also lacking.

One of the most promising of the emerging monitoring methods is Distributed Fiber Optic Sensing (DFOS). DFOS enables continuous measurements, both spatially and temporally, over large spans. DFOS consists of several methods for measuring different parameters, such as Distributed Strain Sensing (DSS), Distributed Temperature Sensing (DTS) and Distributed Acoustic Sensing (DAS). These methods have been used for several different applications, also within the field of geotechnical engineering. However, little research has been conducted on the use of DFOS for detecting irregularities within stabilized soil columns and examining the strain transfer mechanism between fiber cable and the stabilized soil.

This M.Sc. Thesis is an experimental study on the use of DFOS for monitoring the achieved quality of stabilized soil. More precisely, the curing process of a layered sample with one lime-stabilized half and the strain development of a fully LC-stabilized sample during unconfined compressive testing was monitored at laboratory scale. DTS has been used to investigate the

possibility of detecting weakness zones within the stabilized soil. A loose tube fiber optic setup was used to observe the heat transfer in a layered soil sample. The results indicate that a layer of unstabilized soil with a thickness of less than 5 cm can be detected with the method.

DSS has been applied to try to identify the strain development in stabilized soil exposed to compressive loading. Results indicate that DSS can map the strain regime of stabilized soil. The strain values were not accurately reproduced, but the temporal development pattern closely resembled that measured by the reference measurement. This research shows that DFOS can be used to monitor the integrity development and the performance of stabilized soil columns during loading. More economic design without compromising the safety can likely be carried out in the future. Additionally, it will likely be a better understanding of the quality of the produced columns.

---



# Sammendrag

Grunnforsterkning ved innblanding av tørt bindemiddel i jorda er en mye brukt metode for å øke styrke og stivhet av bløt jord. Forskjellig kjemisk sammensatte materialer brukes som bindemidler for å øke ytelsen av utsatt jord. Bindemidlene, som for eksempel kalk og sement, sprøytes inn i omrørt jord ved hjelp av et roterende mikseapparat. Det er mye usikkerhet knyttet til grunnforsterkning med kalksementpeler. For eksempel, estimeres styrke og stivhet basert på omtrentlige metoder slik som for eksempel enaksielle trykkforsøk i laboratoriet.

Dimensjoneringsverdiene av stabilisert jord blir i dag vanligvis basert på resultater fra laboratorieforsøk av jorda som skal stabiliseres. Men, denne metoden for å fastsette styrke og stivhet av stabilisert jord er funnet til å kraftig underestimere de faktiske egenskapene. En laboratorietest kan ikke bestemme integriteten av in situ stabilisert jord i og med at prøver fra laboratoriet er laget under mer ideelle forhold enn det som er tilfelle i felt. Med integriteten av jord så menes det her dens homogenitet, styrke og stivhet, altså er det en indikasjon på jordas evne til å motstå ytre belastning og beholde sin strukturelle integritet.

Det finnes også metoder for å estimere oppnådde mekaniske egenskaper, men heller ingen av disse metodene er tilfredsstillende. Dette er fordi metodene som undersøker jord som har blitt stabilisert in situ er resurskrevende når det kommer til økonomi, arbeidskraft og bruken av store maskiner, i tillegg til å være destruktive. Et system for å avdekke mulige defekter langs en pel av stabilisert jord mangler også.

En av de mest lovende fremadstormende overvåkingssystemene er Distributed Fiber Optic Sensing (DFOS). DFOS gjør det mulig med kontinuerlige målinger, både i rom og tid, over store lengder. DFOS består av flere metoder for å måle forskjellige parametere, som for eksempel Distributed Strain Sensing (DSS), Distributed Temperature Sensing (DTS) og Distributed Acoustic Sensing (DAS). Disse metodene har allerede blitt brukt for mange forskjellige formål, også innen geoteknikk. Men, lite forskning er gjort på bruken av DFOS for å detektere svakheter i peler av stabilisert jord og for å undersøke tøyningsoverføring mellom stabilisert jord og fiberkabel.

Denne masteroppgaven er en eksperimentell studie av bruken av DFOS for å overvåke oppnådd kvalitet av stabilisert jord. Både herdeprosessen av en lagdelt jordprøve, hvor det ene laget har vært stabilisert med kalk, og tøyningutviklingen i en fullt stabilisert kalk/sement-prøve under enaksielt trykk har blitt overvåket i laboratoriet. DTS har blitt benyttet for å undersøke muligheten for å detektere svakhetssoner i kalksementpeler. Et oppsett med en fiberkjerne løst

inni et tynt plastrør ble brukt for å observere varmeoverføring i en lagdelt jordprøve. Resultatene indikerer at et lag av ustabilisert jord med tykkelse mindre enn 5 cm kan bli oppdaget ved bruk av denne metoden.

DSS har blitt benyttet for å prøve å identifisere tøyingsutviklingen i stabilisert jord utsatt for trykkbelastning. Resultatene indikerer at DSS kan gjengi trenden i tøyingsutvikling med tid for stabilisert jord. Tøyingsverdiene ble ikke nøyaktig gjengitt, men formen av tøyingsutviklingen med tid samstemte svært godt med referansemålingen. Forskningen i denne oppgaven viser at DFOS kan brukes for å overvåke utviklingen av integriteten og kvaliteten av stabiliserte jordpeler under belastning. I fremtiden kan det sannsynligvis utføres mer økonomisk dimensjonering uten å kompromittere sikkerheten. I tillegg vil det antageligvis være bedre forståelse for den oppnådde kvaliteten av installerte peler av stabilisert jord.

---

# Contents

<b>Preface</b> . . . . .	<b>iii</b>
<b>Abstract</b> . . . . .	<b>v</b>
<b>Sammendrag</b> . . . . .	<b>vii</b>
<b>Contents</b> . . . . .	<b>ix</b>
<b>Figures</b> . . . . .	<b>xvii</b>
<b>Tables</b> . . . . .	<b>xxi</b>
<b>List of Symbols</b> . . . . .	<b>xxiv</b>
<b>Acronyms</b> . . . . .	<b>xxvii</b>
<b>1 Introduction</b> . . . . .	<b>1</b>
1.1 Background . . . . .	1
1.2 Research objectives . . . . .	2
1.3 Report structure . . . . .	3
<b>Part 1 - Theory</b> . . . . .	<b>5</b>
<b>2 Ground improvement</b> . . . . .	<b>7</b>

2.1	Existing methods . . . . .	7
2.2	Procedure in Norway . . . . .	8
2.3	Climate footprint of LC-stabilization . . . . .	10
2.4	Different types of binders . . . . .	11
2.5	Lime . . . . .	11
2.5.1	Production of lime . . . . .	11
2.5.2	Heat development due to lime . . . . .	12
2.5.3	Strength contribution from lime . . . . .	13
2.6	Cement . . . . .	14
2.6.1	Production of cement . . . . .	14
2.6.2	Heat development due to cement . . . . .	15
2.6.3	Strength contribution from cement . . . . .	16
2.7	Lime and cement . . . . .	17
2.7.1	Heat-development of LC-clay . . . . .	17
2.7.2	Strength-development of LC-clay . . . . .	19
2.8	The maturity concept . . . . .	22
2.9	Monitoring of field performance . . . . .	23
2.10	Types of binders used in this M.Sc. Thesis . . . . .	23
<b>3</b>	<b>Distributed Fiber Optic Sensing . . . . .</b>	<b>25</b>
3.1	Optical fibers . . . . .	25

---

3.2	Light scattering . . . . .	26
3.3	The concept of DFOS . . . . .	27
3.4	Different techniques of DFOS . . . . .	28
3.5	Applications of DFOS . . . . .	29
3.6	Previous geotechnical projects using DFOS . . . . .	31
3.7	Choice of fiber optic cables for this M.Sc. Thesis . . . . .	32
<b>4</b>	<b>Material . . . . .</b>	<b>33</b>
4.1	Clay . . . . .	33
4.1.1	Definition of clay . . . . .	33
4.1.2	Quick clay . . . . .	34
4.2	Tiller-Flotten . . . . .	35
4.2.1	Quaternary geology . . . . .	36
4.3	Characteristics of Tiller-Flotten clay . . . . .	37
4.3.1	General description of the clay . . . . .	38
4.3.2	Clay used in this M.Sc. Thesis . . . . .	40
	<b>Part 2 - Methodology . . . . .</b>	<b>43</b>
<b>5</b>	<b>Temperature tests of layered sample . . . . .</b>	<b>45</b>
5.1	Purpose . . . . .	45
5.2	Equipment . . . . .	45
5.3	Test setup . . . . .	47

---

5.4	Procedure . . . . .	51
5.4.1	Preparations . . . . .	51
5.4.2	Mixing of quick clay . . . . .	52
5.4.3	Tamping of stabilized clay and filling of remoulded clay . . . . .	54
5.4.4	Reference measurement for DFOS . . . . .	55
5.4.5	Measurements . . . . .	56
<b>6</b>	<b>Cross-sectional temperature test . . . . .</b>	<b>57</b>
6.1	Purpose . . . . .	57
6.2	Equipment . . . . .	58
6.3	Test setup . . . . .	58
6.4	Procedure . . . . .	61
6.4.1	Preparations . . . . .	61
6.4.2	Mixing of quick clay . . . . .	61
6.4.3	Tamping of stabilized clay . . . . .	61
6.4.4	Reference measurement . . . . .	62
6.4.5	Measurements . . . . .	62
<b>7</b>	<b>Strain tests . . . . .</b>	<b>63</b>
7.1	Purpose . . . . .	63
7.2	Equipment . . . . .	63
7.3	Test setup . . . . .	66

---

7.4	Procedure . . . . .	68
7.4.1	Preparations . . . . .	68
7.4.2	Mixing of quick clay . . . . .	68
7.4.3	Tamping of strain samples . . . . .	68
7.4.4	Reference measurement . . . . .	70
7.4.5	Measurements . . . . .	70
<b>Part 3 - Results and discussions . . . . .</b>		<b>73</b>
<b>8</b>	<b>Temperature tests - results . . . . .</b>	<b>75</b>
8.1	DFOS-scans along entire sample height . . . . .	75
8.1.1	All DFOS-scans in the first 8.5 hours . . . . .	75
8.1.2	One DFOS-scan per hour the first 8 hours . . . . .	78
8.1.3	All DFOS-scans in the first hour . . . . .	80
8.2	Temperature change with time for 2. test . . . . .	82
8.3	Comparison between thermocouples and DFOS for 2. test . . . . .	83
8.4	Comparison between thermocouples and the reference sample for 2. test . . . . .	85
8.5	Cross-sectional temperature test - Results . . . . .	87
8.5.1	Thermo element (PT100) measurements . . . . .	88
8.5.2	Comparison of measurement methods . . . . .	89
8.5.3	DFOS measurements . . . . .	90
<b>9</b>	<b>Strain tests - Results . . . . .</b>	<b>91</b>

---

9.1	Mechanical properties of the samples . . . . .	91
9.2	Failure pattern of the samples . . . . .	94
9.3	Strain change along sample height before cable slippage . . . . .	96
9.4	Strain magnitude . . . . .	99
9.4.1	Strain magnitude of Sample 1 . . . . .	99
9.4.2	Strain magnitude of Sample 2 . . . . .	100
9.4.3	Strain magnitude of Sample 3 . . . . .	101
9.5	Shape of the strain profiles . . . . .	102
9.5.1	Shape of strain profiles for Sample 1 . . . . .	103
9.5.2	Shape of strain profiles for Sample 2 . . . . .	104
9.5.3	Shape of strain profiles for Sample 3 . . . . .	105
9.6	The effect of relaxation for the two last tests . . . . .	106
9.6.1	The effect of relaxation for Sample 2 . . . . .	106
9.6.2	The effect of relaxation for Sample 3 . . . . .	107
<b>10</b>	<b>Discussion . . . . .</b>	<b>109</b>
10.1	Discussion of the temperature tests . . . . .	109
10.1.1	DFOS to measure temperature during curing . . . . .	109
10.1.2	DFOS to detect weakness zones . . . . .	110
10.1.3	Uncertainties related to the temperature tests . . . . .	111
10.2	Discussion of the strain tests . . . . .	112

---



10.2.1 Strain profiles . . . . . 112

10.2.2 Strain magnitude . . . . . 113

10.2.3 The role of interface bonding . . . . . 113

10.2.4 Bond loss at cable slippage . . . . . 118

10.2.5 Limitations . . . . . 119

**Part 4 - Conclusion . . . . . 125**

**11 Conclusion . . . . . 127**

11.1 Conclusions . . . . . 127

11.2 Limitations . . . . . 128

11.3 Further work . . . . . 128

11.3.1 Temperature tests - Further work . . . . . 129

11.3.2 Strain tests - Further work . . . . . 129

**Bibliography . . . . . 131**

**A Sketches of the isolation box used for temperature tests . . . . . 135**

**B Sketches of the uniaxial device and plastic blocks used for strain tests . . . . . 139**

**C Results from the temperature tests . . . . . 143**

**D Results from the strain tests . . . . . 153**

**E Calculations of required bond length for Sample 3 . . . . . 163**

**F Table of cable comparison . . . . . 169**

---



# Figures

2.1	Principle of LC-stabilization . . . . .	9
2.2	LC-columns as a bracing system for construction pits . . . . .	10
2.3	Hydration of lime - temperature development . . . . .	12
2.4	Ion exchange and flocculation . . . . .	13
2.5	Hydration of cement - Heat development . . . . .	16
2.6	CSH-gel . . . . .	17
2.7	Temperature development in lab - Wiersholm (2018) . . . . .	18
2.8	Strength development of laboratory-stabilized clay samples . . . . .	21
3.1	Optical fiber . . . . .	26
3.2	Schematic of DFOS . . . . .	28
3.3	Different DFOS systems . . . . .	29
3.4	The two fiber optic cables used in this M.Sc. Thesis . . . . .	32
4.1	Grain structures of clays . . . . .	34
4.2	Formation of quick clay . . . . .	35
4.3	Quarternary geology at Tiller-Flotten . . . . .	36
4.4	Terrain elevation at Tiller-Flotten . . . . .	37
4.5	Index parameters of Tiller-Flotten clay . . . . .	39
5.1	Positioning of integrated thermocouples . . . . .	47
5.2	Schematic sketch of temperature tests . . . . .	48

5.3	Bare fiber used for temperature tests . . . . .	49
5.4	Temperature test - Setup . . . . .	50
5.5	Setup of reference measurements during temperature tests . . . . .	51
5.6	Mixing of remoulded quick clay and lime . . . . .	53
5.7	Tamping and filling of temperature sample . . . . .	54
5.8	Layered soil sample for temperature testing . . . . .	55
6.1	Cross-sectional temperature test - Setup . . . . .	59
6.2	Cross-sectional temperature test - Position of sensors . . . . .	60
7.1	Schematic setup of strain testing . . . . .	65
7.2	Strain testing - Setup . . . . .	66
7.3	Tamping of a strain sample . . . . .	69
7.4	Strain testing - Measurement setup . . . . .	71
8.1	Temperature results from first 8.5 hours . . . . .	76
8.2	Temperature results from first 8.5 hours - Scatter plots . . . . .	77
8.3	1. Temperature test - One scan per hour . . . . .	78
8.4	2. Temperature test - One scan per hour . . . . .	79
8.5	1. Temperature test - All scans the first hour . . . . .	80
8.6	2. Temperature test - All scans the first hour . . . . .	81
8.7	2. Temperature test - Temperature change with time . . . . .	82
8.8	Temperature change during temperature test 2 - Comparison between DFOS and thermocouples . . . . .	83
8.9	2. Temperature test - Normalized comparison between measurement types . . .	84
8.10	2. Temperature test - Comparison with reference sample . . . . .	86
8.11	2. Temperature test - Comparison between thermocouple, PT100 and DFOS . . .	87
8.12	Cross-sectional temperature test - Comparison between PT100s and theromcouple	88
9.1	Strain tests - Plots of mechanical properties . . . . .	92

---

9.2	Strain tests - Comparison with previous experience . . . . .	93
9.3	Strain Sample 1 - Failure pattern . . . . .	95
9.4	Strain Sample 2 - Failure pattern . . . . .	95
9.5	Strain Sample 3 - Failure pattern . . . . .	96
9.6	Strain tests - Strain change for all samples . . . . .	97
9.7	Strain tests - Comparison between DFOS and uniaxial results for Sample 1 . . .	100
9.8	Strain tests - Comparison between DFOS and uniaxial results for Sample 2 . . .	101
9.9	Strain tests - Comparison between DFOS and uniaxial results for Sample 3 . . .	102
9.10	Strain tests - Comparison between shapes of DFOS and uniaxial graphs for Sample 1 . . . . .	103
9.11	Strain tests - Comparison between shapes of DFOS and uniaxial graphs for Sample 2 . . . . .	104
9.12	Strain tests - Comparison between shapes of DFOS and uniaxial graphs for Sample 3 . . . . .	105
9.13	Strain tests - Effect of relaxation for Sample 2 . . . . .	106
9.14	Strain tests - Effect of relaxation for Sample 3 . . . . .	108
10.1	Temperature signature in the transition between different soil layers . . . . .	110
10.2	Theoretical strain profile . . . . .	114
10.3	Imperfect topbond of Sample 2 . . . . .	117
10.4	Strain tests - Measurements after cable slippage . . . . .	119
10.5	Visual inspection of imperfections of Sample 2 . . . . .	120
10.6	Strain tests - Positions of fiber optic cable . . . . .	121
C.1	Cross-sectional temperature test - DFOS measurements . . . . .	152
D.1	Strain tests - Strain change for Sample 1 . . . . .	160
D.2	Strain tests - Strain change for Sample 2 . . . . .	160
D.3	Strain tests - Strain change for Sample 3 . . . . .	161
D.4	Strain tests - Mean and maximum strain from DFOS for Sample 1 . . . . .	161

---

D.5 Strain tests - Mean and maximum strain from DFOS for Sample 2 . . . . . 162

D.6 Strain tests - Mean and maximum strain from DFOS for Sample 3 . . . . . 162

E.1 Elasticity ratio between fiber cable and strain samples . . . . . 163



# Tables

2.1	Hydration properties . . . . .	18
4.1	Index parameters of Tiller-Flotten quick clay . . . . .	38
9.1	Mechanical properties of the strain samples . . . . .	91







# List of Symbols

Symbol	Description	Unit
$M_T$	Maturity number	[-]
$T$	Curing temperature	[°C]
$K$	Maturity factor related to soil type, binder and curing temperature	[-]
$t$	Curing time	[days]
$T_n$	Curing temperature number n	[°C]
$t_{n+1}$	Curing time number n+1	[days]
$t_n$	Curing time number n	[days]
$\Lambda$	Grating length for FBG-sensors	[nm]
$\lambda$	Design wavelength of incident light	[nm]
$w_P$	Plastic limit	[%]
$w_L$	Liquid limit	[%]
$I_P$	Plasticity index	[-]
$c_u$	Undrained shear strength	[kPa]
$c_{u,r}$	Remoulded shear strength	[kPa]
$S_t$	Sensitivity	[-]
$I_L$	Liquidity index	[-]
$\gamma_s$	Grain density	[g/cm <sup>3</sup> ]
$\gamma_t$	Bulk density	[kN/m <sup>3</sup> ]
$w_n$	Natural water content	[%]
$\varepsilon$	Strain	[-]
$\varepsilon^{tot}$	Total strain of fiber core	[-]
$\varepsilon^M$	Mechanical strain of fiber core	[-]
$\varepsilon^T$	Thermal strain of fiber core	[-]
$S_w$	Water saturation	[%]
$A_0$	Original cross-sectional area	[mm <sup>2</sup> ]
$A$	Corrected cross-sectional area	[mm <sup>2</sup> ]
$\varepsilon_A$	Axial strain	[-]
$\sigma$	Stress	[kPa]
$\sigma_1$	Largest principal stress	[kPa]
$\sigma_3$	Smallest principal stress	[kPa]
$\Delta L$	Change in length	[mm]
$\tau_f$	Maximum shear stress	[kPa]
$q_u$	Ultimate compressive strength	[kPa]

Symbol	Description	Unit
$F$	Force applied from uniaxial device	[kN]
$E$	Young's modulus	[kPa]
$E_{50}$	Young's modulus of soil	[kPa]
$E_{FC}$	Stiffness (Young's modulus) of fiber cable	[kPa]
$E_{LC}$	Stiffness (Young's modulus) of lime/cement-stabilized soil sample	[kPa]
$F_{FC}$	Force in fiber cable	[kN]
$F_{LC}$	Force in lime/cement-stabilized soil sample	[kN]
$\varepsilon_{FC}$	Strain in fiber cable	[-]
$\varepsilon_{LC}$	Strain in lime/cement-stabilized soil sample	[-]
$\sigma_{FC}$	Stress in fiber cable	[kPa]
$\sigma_{LC}$	Stress in lime/cement-stabilized soil sample	[kPa]
$\varphi_{FC}$	Diameter of fiber cable	[mm]
$\varphi_{LC}$	Diameter of lime/cement-stabilized soil sample	[mm]
$f_{bd}$	Design bond strength	[kPa]
$\eta_1$	Factor related to bond conditions and positioning of reinforcement bar	[-]
$\eta_2$	Factor related to diameter of reinforcement bar	[-]
$f_{ctd}$	Design tensile strength	[kPa]
$L_{b,rqd}$	Required bond length	[mm]
$\sigma_{FC,real}$	Theoretically real stress in fiber cable	[kPa]
$\varepsilon_{FC,real}$	Theoretically real strain in fiber cable	[-]



# Acronyms

**C-A-H** Calcium Aluminate Hydrate. 14

**C-S-H** Calcium Silicate Hydrate. 14–16

**CKD** Cement Kiln Dust. 11

**CPT** Cone Penetration Test. 2

**DAS** Distributed Acoustic Sensing. v, vii, 30

**DDSM** Dry Deep Soil Mixing. v, 8, 9

**DFOS** Distributed Fiber Optic Sensing. iii, v–viii, 2, 3, 25, 27–32, 46, 48, 52, 55, 56, 62, 63, 66, 67, 70, 75, 78, 81–87, 89–91, 96–107, 109–113, 116–119, 121, 127, 128, 143

**DSM** Deep Soil Mixing. 7, 8

**DSS** Distributed Strain Sensing. v–viii, 30, 32, 70, 71

**DTS** Distributed Temperature Sensing. v, vii, 30, 31, 56, 62, 71

**FBG** Fiber Bragg Grating. 30

**FEM** Finite Element Method. 31

**GOAL** Green sOil stAbiLisation. iii, 67

**GWL** Groundwater Level. 39

**IBP** Industrial By-Products. 11

**LC** Lime and Cement (stabilized). 1, 19, 127, 129

**NGI** Norwegian Geotechnical Institute. iii, 32, 67, 68

**NGTS** Norwegian Geo-Test Sites. 35, 36

**NGU** Geological Survey of Norway. 36

**NTNU** Norwegian University of Science and Technology. iii

**OFDR** Optical Frequency Domain Reflectometry. 56, 71

**OPC** Ordinary Portland Cement. 11, 14

**WDSM** Wet Deep Soil Mixing. 8



# Chapter 1

## Introduction

### 1.1 Background

Lime and cement have been used for the stabilization of soft soil in Norway since the mid-1970s (Wiersholm 2018). Stabilization can be necessary for soils that are too weak, too soft/-compressible, too erodible and too sensitive to changes in the groundwater table. In general, stabilization can be used to increase the durability of the soil and to ensure the longevity of structures built upon the soil.

With the ongoing growth in construction activities, the utilization of lime/cement-stabilization is also steadily increasing. Despite the fact that there exist other binders, in addition to the emergence of new environmentally friendly binders, lime and cement are still heavily used, and are likely to be used in the foreseeable future as well. Lime/cement-stabilization of soil is a well-functioning method, however, there are significant emissions associated with the production of the binders. As much as 7% of the global  $CO_2$ -emissions come from cement production (Wu et al. 2021).

In addition to emitting considerable amounts of  $CO_2$  during the production of these binders, the design principles are typically conservative because reliable measurements of the in situ performance of LC-columns are still lacking. Due to insufficient and resource-intensive in situ methods, the design strength and stiffness of LC-columns are most often based on laboratory tests of the soil. However, research on the stabilization of sensitive Norwegian clays has shown that the strength estimated in the laboratory often greatly underestimates the strength of the in situ stabilized soil columns (Bache et al. 2022). Laboratory-prepared samples of soil can not be directly compared to the field as the in situ curing conditions differ significantly from the conditions in the laboratory. The surrounding temperature and the confining stress condition affect both the peak strength and the development of strength with time (Bache et al. 2022).

Several different methods for testing the strength of installed LC-columns already exist. Examples of the methods that are used in Norway today are pre-installed pile probes (i.e. FOPS

and FKPS), Cone Penetration Test (CPT) and laboratory tests of drilled core samples (NGF 2012). In addition, some research has been done on installing standard temperature sensors at some depths to measure the temperature in piles. However, there is room for improvement in the monitoring methods.

An important feature related to the curing of soil stabilized with lime and cement is the fact that a lot of heat is generated, especially due to the lime. The more binder that is reacting with the natural water content of the soil, the more heat is generated. One possible way of detecting zones of weakness in a stabilized soil column is by monitoring its heat development. Temperature sensors enable the possibility of following the temperature development due to the chemical reactions during the curing process of the columns. However, as these are only point sensors, they will not give sufficient data to provide reliable temperature plots throughout the whole height of the columns. Such a monitoring system will hence not be able to detect any possible weak zones based on its temperature development.

Also the overall strength and stiffness of stabilized soil can be calculated based on the temperature measurements of the curing process. By using a concept called "Maturity", with some corresponding laboratory investigations on the soil that is to be stabilized, it is possible to develop formulas for the strength and stiffness of the LC-column as a function of its curing age and temperature development. The maturity concept is generally a concept that combines the curing age and curing temperature of a material into one parameter, and the concept is discussed in multiple research papers, like for example by Zhang et al. (2014).

The in situ stiffness of stabilized soil columns can be estimated based on load tests if the resulting strain is known. By measuring the strain along the entire height of the installed piles, very accurate estimates of the stiffness can be made. In addition, such strain monitoring of the entire height would also make it possible to detect weakness zones of the column. These zones would be evident by being significantly more compressed than other parts of the column.

Monitoring systems providing continuous measurements in both space and time of temperature and strain in stabilized soil have, so far, not been established. The development of such a system would be interesting for several reasons:

- Strength and stiffness of LC-columns can be calculated more reliably.
- Weakness zones of LC-columns can be detected.
- The real field performance of stabilized soil columns can be quantified and thus the onset of failures can be better estimated.
- Future design can likely be optimized in terms of material savings and cost-effectiveness when getting further insight into the field performance of the stabilized soil.

## 1.2 Research objectives

The aim of this M.Sc. Thesis is to study the use of Distributed Fiber Optic Sensing (DFOS) for monitoring the strength, stiffness and homogeneity of stabilized soft soil. The possibility

---



of using this method as a non-destructive and reliable way of monitoring the integrity of LC-columns has been examined. The research are threefold.

- Is DFOS able to measure the temperature development in stabilized soil?
- Can DFOS be used to reliably detect zones of unstabilized quick clay within a stabilized soil column?
- Can DFOS reproduce the strain development of stabilized soil subjected to loading?

### 1.3 Report structure

This M.Sc. Thesis is divided into four parts, which are theory, methodology, results and discussion, and lastly conclusion.

**Part 1 - Theory** build upon the Project thesis written by the author in the fall of 2022. Firstly, a chapter discussing the procedure of ground improvement in Norway comes. Secondly, the two most widely used binders are discussed. Thirdly, an overview of Distributed Fiber Optic Sensing and its current applications is presented. All of these mentioned chapters are inspired by the Project thesis. In addition, one section describing on which basis the fiber optic cables used for this thesis were chosen is added. As parts of the theory come from the Project thesis, and this thesis is not published anywhere, it is uploaded as an attachment for this M.Sc. Thesis. The material that is tested in this thesis is also thoroughly described in the theory part.

**Part 2 - Methodology** gives a thorough description of the three different laboratory tests that were conducted.

**Part 3 - Results and discussion** presents the temperature results followed by the strain results. Furthermore, the different results are discussed.

**Part 4 - Conclusion** summarizes the main findings of the research. In addition, potential further work is outlined.

---



# Part 1 - Theory



## Chapter 2

# Ground improvement

This chapter discusses ground improvement, both in general and in more detail about how ground improvement is carried out in Norway. The most used method, more precisely dry deep mixing, is described with regard to procedure and areas of usage. Further are the two most commonly used binders, lime and cement, presented. Their characteristics related to production, exothermic heat development and strength contribution are discussed. Also, the basics of a methodology for estimating the development of strength and stiffness based on the curing conditions are presented. In addition, limitations of existing monitoring systems for measuring temperature development and estimating the strength and stiffness of in situ stabilized soil are highlighted.

### 2.1 Existing methods

A range of different ground improvement methods exist. In general, all methods can be divided into two groups, mechanical improvement of the soil and chemical improvement of the soil (Patel 2019). In mechanical improvement, the soil can be mixed with other soil types in order to change its grading, and then also its characteristics. It can also be mechanically treated, for example by compaction, to make the soil body denser and also improve its strength and stiffness. In chemical improvement, the soil is mixed with some chemical aggregate which results in modified properties of the soil due to chemical reactions.

Chemical improvement of soil can be divided into several different sub-methods. It consists for instance of mass stabilization, Deep Soil Mixing (DSM) and salt stabilization, and DSM can for example be further divided into mechanical mixing and jet mixing (Larsson 2005). Also the form of the binder that is mixed with the soil plays a role in the classification of the methods. A thorough classification of deep mixing methods can be found in the work of Larsson (2005).

Mass stabilization is used for stabilizing a whole soil body, in other words, there is a 100% ratio of replacement for the given volume. It is relevant in situations with large volumes of soft soil

or when there is a need for securing contaminated sediments (NGF 2012). Deep mixing is used for stabilizing only some specific volume parts of a soil body, in the form of circular columns. Columns can be made at very close distance to each other, resulting in a similar replacement ratio as mass stabilization. An important difference between these two main methods is that while DSM can give columns of approximately 30 m depth, mass stabilization in comparison is limited to about 5-7 m depth (NGF 2012).

In Deep Soil Mixing (DSM), the soil is mixed with the binder in situ. It is done by a mixing tool that remolds the soil while it is being pushed down and then further injects the binder into the soil body on its way up. Deep Soil Mixing (DSM) can be divided into Wet Deep Soil Mixing (WDSM) and Dry Deep Soil Mixing (DDSM), depending on the form of the binder that is applied.

The binder is injected into the soil as a slurry, in other words, a mixture of binder and water, in WDSM (Topolnicki 2016). The reason for the binder being mixed with water to create a slurry is that there has to be enough water for all the chemical reactions to take place. In DDSM, the binder is in powder form (Topolnicki 2016). This method is used in soils with a high natural water content, in other words, in soils that do not need additional water to initiate the chemical reactions. It is not preferable to have too much water, hence the binder should be added dry in these types of soils.

Both wet mixing and dry mixing are used in the soil stabilization industry today. However, in Scandinavia, DDSM is the standard method for the stabilization of sensitive clays. Due to the relatively high groundwater table in the Scandinavian countries, the clays often have sufficiently high water content. It is the DDSM that will be focused on in this project.

## 2.2 Procedure in Norway

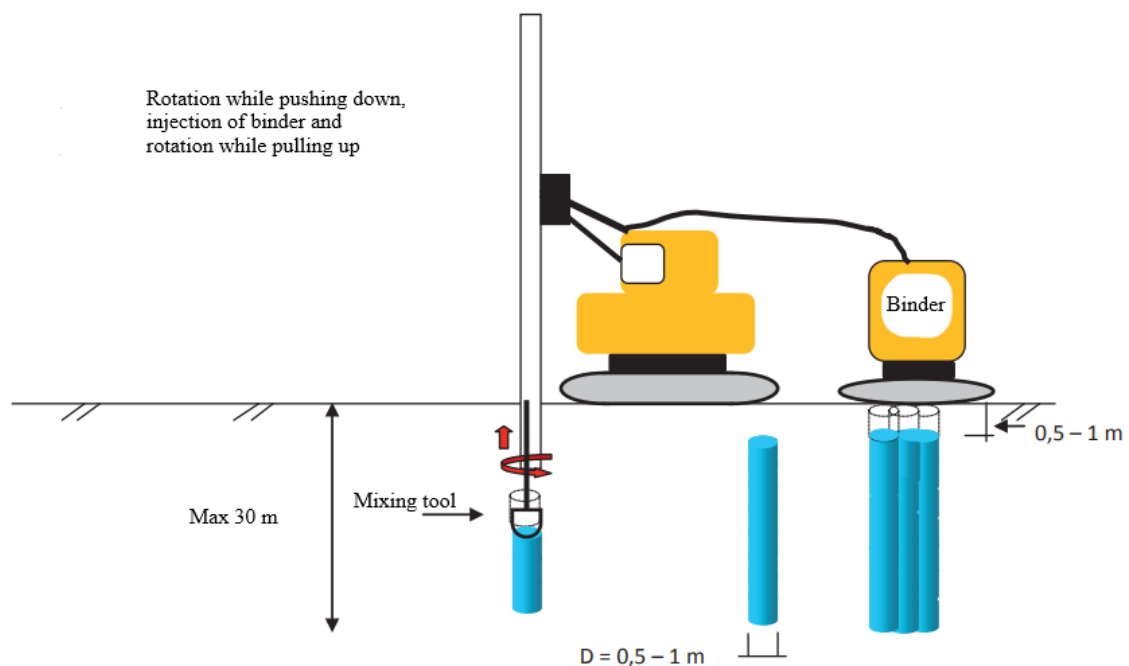
Dry Deep Soil Mixing (DDSM) is the prevailing technique employed in Norway, as well as in the wider Scandinavian region. This method involves the mechanical manipulation of soil, followed by in-situ blending with cementitious binders (Paniagua et al. 2019). The blending process is facilitated by a specialized rig connected to one or more material tanks containing binders, such as lime and cement, as depicted in Figure 2.1. Soil remoulding is achieved by the rotational and axial movement of a mixing tool attached to the drill rod, allowing it to reach the desired depth. Subsequently, compressed air is employed to introduce the binder into the soil while continuously rotating and extracting the mixing tool (Timoney et al. 2012). The chemical reactions initiated by the interaction between the natural water content and the dry binder result in enhanced strength and stiffness of the soil. In Norway, LC-columns typically possess diameters ranging from 0.5 to 1.0 meters, with a maximum depth of 30 meters (NGF 2012). The injection of binders should cease no later than 0.5 meters below ground level.

As mentioned earlier, deep dry mixing is a process involving the blending of dry binders into the soil to promote reactions between the binders, soil particles and pore water. These chemical reactions lead to stronger bonds within the soil matrix, resulting in a denser and more compact

---

structure. In Norway, this method is mainly employed in exposed areas with sensitive clay with shear strength ranging from 5 to 30 kPa (NGF 2012). Dry Deep Soil Mixing (DDSM) facilitates rapid strength enhancement, and experience shows that Norwegian clays treated with this technique can gain an undrained shear strength in the range of 100-1000 kPa (NGF 2012). Lime and cement are commonly used as the dry binders for this method, and both normal clay and quick clay can obtain a strength increase of 10-50 times their original strength when mixed with these binders (Christensen et al. 1998).

The fact that both the remoulding of the material (soil) and the injection of binder is done in situ introduce uncertainties related to the quality of the stabilized soil columns. The dimension of the mixing tool will determine the dimension of the remoulded soil columns. However, as the binder is distributed to the remoulded soil by utilizing compressed air, and the stabilized columns are not made by a slurry material mixed in controlled conditions similar to concrete columns, there will be uncertainties related to the binder distribution in produced soil columns. There can even be small weakness zones along the height of the columns, where the binder has not been distributed to the same extent as in the remaining volume. However, it has still not been possible to examine the homogeneity of stabilized soil columns due to the lack of sufficient methods for monitoring the achieved integrity.

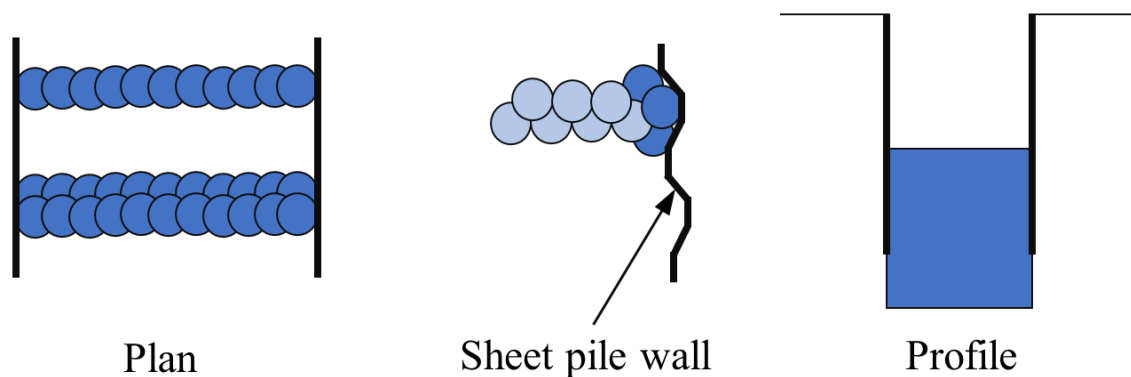


**Figure 2.1:** Principle of LC-stabilization. Figure modified from (NGF 2012).

Deep dry mixing has been applied for a variety of different purposes in Norway. The most common areas of usage according to the Norwegian Geotechnical Association are discussed in the guidelines given in NGF (2012). The method is utilized in situations where there can be challenges related to the stability of the ground, this yields for example cuttings, embankments

and natural slopes. Columns of lime/cement-stabilized soil are also used for bracing systems, either as the bracing system itself or as a part of the system. LC-columns as bracing systems have been applied to ensure adequate safety in several construction projects, such as construction pits, trenches and bridge foundations (NGF 2012). The use of LC-columns as a bracing system for a construction pit with sheet pile walls is visualized in Figure 2.2. In addition to assisting with the bracing of the construction pit, the installation of LC-columns also improves the accessibility in the pit and enhances the safety against uplift.

The introduction of lime/cement-stabilization can also help enhance several aspects related to the serviceability limit state. Columns of stabilized soil have been applied in order to solve challenges related to settlements and vibrations. Settlements develop more rapidly, and not to the same extent as before when the use of LC-columns is applied, compared to a situation where such measures are not taken (NGF 2012). When it comes to the reduction of vibration problems by the use of soil stabilization, the stabilized soil columns can either be installed below the source of vibration to reduce it or as a "shield" to protect adjacent structures (NGF 2012).



**Figure 2.2:** Principle of LC-columns as a bracing system for construction pits. Figure inspired by (NGF 2012).

### 2.3 Climate footprint of LC-stabilization

Wu et al. (2021) has described the production of cement as a "non-sustainably production technology with significantly negative environmental impacts, including over-consumption of non-renewable resources, high energy input and high CO<sub>2</sub>-emissions". As approximately 7% of the global CO<sub>2</sub>-emissions comes from the production of cement, measures need to be taken to reduce the consumption of this environmentally hazardous binder (Wu et al. 2021). If there is to be an improvement to the development of the climate changes that the world is now facing, the entire society needs to contribute, and the field of soil stabilization is no exception. The soil stabilization industry, using binders responsible for significant emissions, needs to do an effort to reduce its burden on the climate.

---



As also discussed earlier, the real strength of Norwegian stabilized soft sensitive clays is often greatly underestimated based on laboratory tests of the same soil (Bache et al. 2022). As there is lacking sufficient methods to quantify the obtained quality of soil stabilized in the field there is a possibility that LC-columns that are produced in different projects are over-dimensioned. This would clearly be an unfavorable situation. It may be the case that the industry today uses more energy, emits more CO<sub>2</sub> and consumes more non-renewable resources than what is actually necessary. In other words, there is a great potential for innovation within the soil stabilization industry, in order to gain better control over the result of the stabilization and reduce the climate impact of the process. An important step on the way will be to implement new methods for monitoring the piles.

## 2.4 Different types of binders

Several binders and binder additives that can be used for the stabilization of clay and other sensitive soils exists. Both fly ash, steel slag, gypsum, and biochar have been used for stabilization purposes (Wu et al. 2021) (Jafarbiglookarami 2021). It is also an increasing market for more sustainable binders both in the soil stabilization and concrete industries, with different recycled materials and bio-based binders being tested. Various studies, including the research of (Wu et al. 2021), have been exploring the use of Industrial By-Products (IBP).

Another binder, which is way more often used for standard soil stabilization, is Cement Kiln Dust (CKD) (NGF 2012). It is a by-product from the production of cement and contains significantly more lime than Ordinary Portland Cement (OPC), but less than burnt lime (NGF 2012). According to NGF (2012) CKD has in later years replaced quicklime in binder compositions with OPC in many projects.

However, despite many different options, lime and cement are still the by far most used binders for the stabilization of Scandinavian clays as well as other sensitive soils. Hence, these two binders and their properties are discussed in detail in the following.

## 2.5 Lime

### 2.5.1 Production of lime

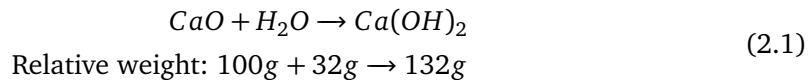
The production procedure for lime is briefly explained in NGF (2012), and is in the following described based on that explanation. Quicklime is produced by burning limestone (CaCO<sub>3</sub>) under significant heat in a shaft furnace. The temperature in the oven is about 1100-1200°C, and the burning procedure emits CO<sub>2</sub>. The end product is CaO of very fine grading, more precisely in the form of powder, which can be used as a binder for soil stabilization.

---

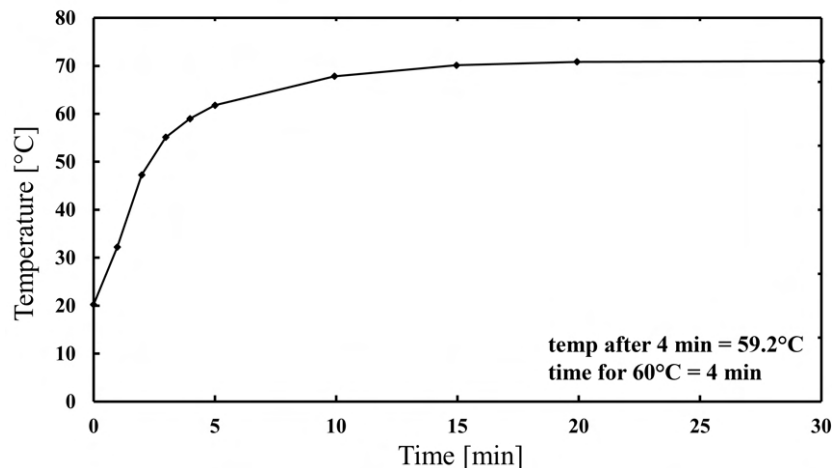
## 2.5.2 Heat development due to lime

Significant heat production is an effect of soil stabilization, in other words, is the mixing of soil with dry binders an exothermic reaction. As the binders are in control of both the heat and strength development during LC-stabilization, it is essential to discuss their properties (Wiersholm 2018). The exothermic reaction that causes heat generation and further reactions to take place is called hydration, and this is the reaction between the dry binders and the natural porewater in the soil.

The lime that is utilized for soil stabilization is, as described in Section 2.5.1, a result of limestone ( $\text{CaCO}_3$ ) being burnt under high temperatures, leading to calcium oxide ( $\text{CaO}$ ) being produced (NGF 2012). During the reaction between burnt lime and water, a significant amount of heat is generated, and slaked lime ( $\text{Ca(OH)}_2$ ) is produced. This reaction also contributes to the drying of the soil body. The presence of large amounts of calcium hydroxide in the water solution causes the pH to increase to 12.5 (Åhnberg, Johansson et al. 1995). This highly alkaline environment facilitates the interaction between clay particles and calcium ions, leading to the formation of cementitious compounds such as calcium silicates and aluminates, which bind the soil particles together (Barnes 2022). The hydration reaction of burnt lime in addition to the relative weight of the involved molecules is shown in Equation (2.1) (Åhnberg, Johansson et al. 1995).



The exact rate of the hydration of burnt lime is influenced by factors such as the burning procedure and particle size. Figure 2.3 is showing the slaking curve for quick lime used for soil stabilization, and is visualizing the temperature development of pure lime hydration.



**Figure 2.3:** Slaking curve for the temperature development of quick lime used for soil stabilization, starting at 20°C. Figure inspired by (Åhnberg, Johansson et al. 1995).

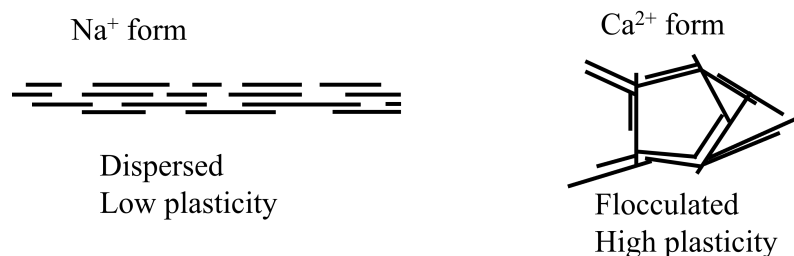
The reaction initiates immediately, and maximum heat generation is almost reached after 5 minutes (Åhnberg, Johansson et al. 1995). The total amount of heat generated during the hydration process of burnt lime is 1163 kJ/kg (Boynton 1980). Lime hydration leads to a significant increase in temperature within the surrounding soil. In situ measurements have indicated temperature rises of around 40-50°C in the soil body (Christensen et al. 1998). Locally, the soil temperature has exceeded 100°C in some instances (Christensen et al. 1998).

### 2.5.3 Strength contribution from lime

The five main strength-contributing mechanisms due to the reaction between lime and clay are hydration, flocculation/agglomeration, ion (cation) exchange, carbonation and pozzolanic reactions (Hov et al. 2022). These five different stabilizing effects will in the following paragraphs be described mainly based on the work of Hov et al. (2022).

Both ion exchange and flocculation/agglomeration occur immediately upon mixing and are typically completed within the initial minutes or hours. There is a close relation between these two effects. The ion exchange mechanism promotes the binding of clay particles, resulting in the formation of a denser structure. This phenomenon, where multiple particles aggregate to form larger-sized particles, is commonly referred to as flocculation or agglomeration. The process of ion exchange between dispersed clay particles and calcium ions, leading to a flocculated clay, is illustrated in Figure 2.4. Despite the strength-enhancing effects of ion exchange and flocculation, their contribution to overall strength generation is relatively limited.

The hydration process itself does not have a significant impact on the strength development of lime-stabilized clay (Hov et al. 2022). However, the hydration of lime initiates significant heat development in the clay, and this heating of the soil skeleton has a drying effect that enhances the strength (NGF 2012). However, this limited strength enhancement that is a consequence of the drying of the soil skeleton may be reversed. This happens if the soil is wetted, hence hydration does generally not have any long-term contribution to the strength of lime-stabilized clay (Janz and Johansson 2002). Purely lime-stabilized clays normally reach their original strength within 1 to 2 hours (Hov et al. 2022). This is an indication of the fact that the strength enhancement due to hydration, ion exchange and flocculation/agglomeration, which all are effects that introduce most of their strength-contributions within the first 2 hours, is limited.



**Figure 2.4:** The concept of ion exchange and flocculation. Figure inspired by (Janz and Johansson 2002).

Pozzolanic reactions play a crucial role in the strength development of lime-stabilized clay. These reactions occur between the hydration product, more precisely  $Ca(OH)_2$ , and the clay particles (Janz and Johansson 2002). The resulting products of the pozzolanic reactions are cementitious compounds, such as calcium silicate hydrate (C-S-H) and/or calcium aluminate hydrate (C-A-H), and it is these compounds that increase the strength of lime-stabilized clay (Hov et al. 2022). The composition of C-A-H is similar to C-S-H, but with aluminate replacing silicate. In other words, it is simply calcium aluminate hydrate of unspecified composition.

Extensive research, including the work by Hov et al. (2022), has highlighted a rapid and substantial increase in strength immediately after the mixing of lime-stabilized clay. Considering that hydration, ion exchange and flocculation/agglomeration have minimal influence on strength generation, this implies that the effects from pozzolanic reactions are indeed significant and contribute to the observed strength improvement.

Also carbonation contributes to some degree of strength development in lime-stabilized clay. Carbonation is a process in which  $CO_2$  reacts with slaked lime, causing the lime to revert back to its original state as limestone and regain some of its strength (NGF 2012). However, it should be noted that carbonation primarily occurs on the surface of the stabilized soil, where there is sufficient access to  $CO_2$ .

Overall, the stabilization of clay using lime tends to yield a more ductile behavior of the clay (NGF 2012). Enhancement of strength due to stabilization with lime takes a long time. The pozzolanic reactions, in other words, the most important strength-contributing reactions of lime-stabilization, depend heavily on the surrounding temperature, and the strength generation flattens out when the stabilized material reaches the original ground temperature (Janz and Johansson 2002). The strength generation of soil due to stabilization by the use of lime can take several months (Janz and Johansson 2002).

## 2.6 Cement

### 2.6.1 Production of cement

Different types of cement, with different constituents and different properties exist. Jacobsen et al. (2021) describes how an Ordinary Portland Cement is made in Norway, which will be briefly summarized in the following.

The main constituent in OPC is limestone, which accounts for more than 90% of the cement clinker. The limestone is mixed with minor constituents such as bauxite, quartz and gypsum. These minor constituents are mixed with the limestone to provide the correct composition of oxides. Cement is very dependent on the oxide composition of the raw material mix with regard to its quality. Gypsum also has an important role in controlling the setting time of the cement. The mix of raw materials is finely ground into a so-called raw meal in a rotating mill. The main source of calcium in the raw meal is limestone, whilst the minor constituents provide an additional supply of aluminum, iron, alkalis and other elements in small quantities.

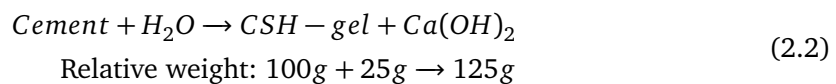
---

The heating process of the raw meal consists of several important steps, but it is ultimately heated to a temperature of about 1450°C. This is done in a rotary kiln. The process is called calcination, and it causes the raw meal to undergo many important chemical reactions that result in the formation of a cement clinker. Lastly, after both the heating and cooling of the clinker are finished, it is mixed with a few percent of gypsum or some other calcium sulfate, and ground finely to the powder known as cement.

### 2.6.2 Heat development due to cement

As for soil stabilized with lime, the hydration process is what is causing heat generation from cement-stabilization of soil.

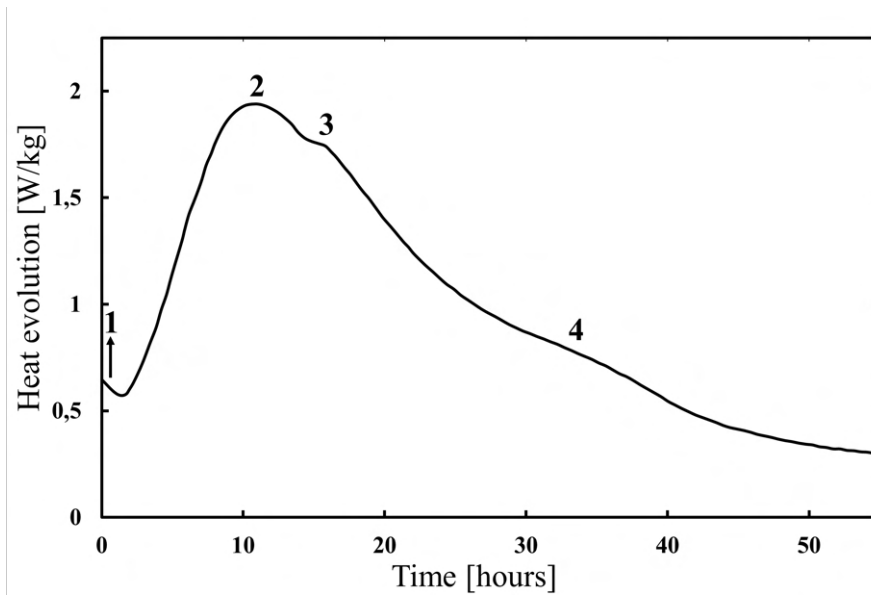
Upon contact with water, the hydration of cement initiates immediately, followed by the release of heat as soluble salts are dissolved (Christensen et al. 1998). This process leads to the formation of a hard cement gel (C-S-H), which plays a crucial role in the strength and stiffness of the stabilized soil. Additionally, calcium hydroxide ( $\text{Ca}(\text{OH})_2$ ) is produced during the hydration of cement (NGF 2012). The presence of reactive alkali sulfates, along with the production of  $\text{Ca}(\text{OH})_2$ , significantly increases the alkalinity of the material, resulting in a pH level of approximately 13 (Åhnberg, Johansson et al. 1995). The reaction equation for the hydration of cement, in addition to the relative weights of the reaction, is presented in Equation (2.2) (Åhnberg, Johansson et al. 1995).



Where C-S-H is a calcium silicate hydrate of unspecified composition, which is often referred to as a gel due to its poorly crystalline structure (Taylor 1990). The (isotherm) heat generation at 20°C from the hydration of ordinary Portland Cement is shown in Figure 2.5. The figure provides a clear representation of the heat evolution during the reaction between cement and water. Point 1, the initial peak, corresponds to the immediate exothermic wetting and the early-stage reactions (Taylor 1990). This initial heat development is relatively low.

Following the initial peak, there is a declining trend in the heat evolution before the onset of the main chemical reactions, mainly involving the aluminate and silicate reactions, where calcium silicate hydrate (C-S-H) and carbon-hydrogen bond (CH) are the products (Janz and Johansson 2002). These reactions begin to take place after a few hours, leading to a rapid increase in heat evolution, as demonstrated by the steep slope in the graph. The peak, denoted as point 2, is typically reached around 10 hours into the hydration process (Åhnberg, Johansson et al. 1995). Subsequently, the heat evolution gradually diminishes until the completion of the hydration process.

---



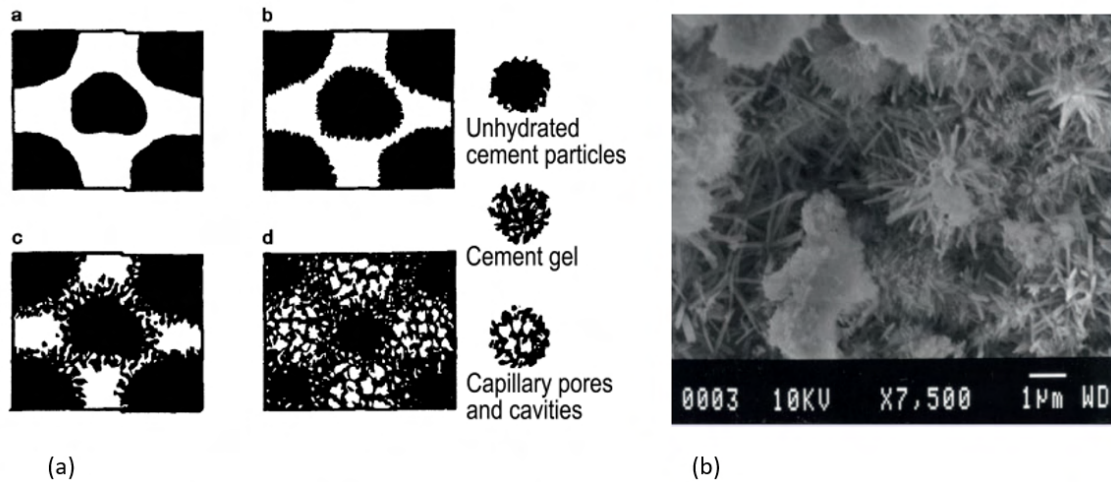
**Figure 2.5:** Isotherm heat development at 20°C for hydration of cement. Figure inspired by (Taylor 1990).

The total generated heat from the hydration of ordinary Portland cement is approximately 450 kJ/kg (Boynton 1980). Ambient soil can experience a temperature increase of about 5-10°C as a result of the heat generation due to the hydration of cement when soil is stabilized with this binder (Åhnberg, Johansson et al. 1995). Compared to soil stabilization with lime, the temperature rise of the soil body due to the hydration of cement is minimal.

### 2.6.3 Strength contribution from cement

It is the CSH-gel that gives the strength and stiffness of cement-stabilized clay (NGF 2012). C-S-H is formed through the hydration of cement, as described in Section 2.6.2. The chemical reactions responsible for the development of CSH-gel occur on the surface of the cement grains, leading to the formation of needle-like crystals (NGF 2012). These C-S-H-crystals continue to grow, and binding of the CSH-gel is obtained when the crystals have grown together with the crystals from other cement grains, and hence filled the pores. The formation process of CSH-gel is illustrated in Figure 2.6, and the figure is highlighting the function of the CSH-gel in strengthening the cement-stabilized clay.

The formation of CSH-gel, which connects the clay particles together and makes a denser structure, is a rapid process. The majority of the strength in clay stabilized by cement is obtained within days (Janz and Johansson 2002). Figure 2.6 (b) shows an X-ray of a real CSH-gel from the hydration of cement. The fact that oblong, needle-like, crystals are formed on the surface of the cement grains and make a more compact/dense structure can be clearly seen from the figure.



**Figure 2.6:** (a) Principle of formation of CSH-gel (Janz and Johansson 2002). (b) An X-ray showing CSH-gel from cement hydration (NGF 2012).

In addition to the formation of CSH-gel, cement stabilization can also involve some pozzolanic reactions (Janz and Johansson 2002). Along with CSH-gel, calcium hydroxide ( $\text{Ca}(\text{OH})_2$ ) is also a byproduct of cement hydration, as shown in Equation 2.2. If the clay being stabilized contains some pozzolans, there is a possibility of some pozzolanic reactions occurring between the pozzolanic material and ( $\text{Ca}(\text{OH})_2$ ) also during cement stabilization. While some additional strength may be gained through pozzolanic reactions, the primary source of strength in cement-stabilized clay is attributed to the formation of CSH-gel resulting from cement hydration.

## 2.7 Lime and cement

### 2.7.1 Heat-development of LC-clay

As discussed previously, lime consumes slightly more water than cement during hydration, however, it also produces more than 2.5 times as much heat compared to cement. Lime also has a significantly more rapid temperature development due to hydration than cement. The generated heat caused by the lime-hydration accelerates the chemical reactions in the cement (Christensen et al. 1998). Some relevant hydration properties of lime and cement based on what has been discussed in the previous sections are summarized in Table 2.1.

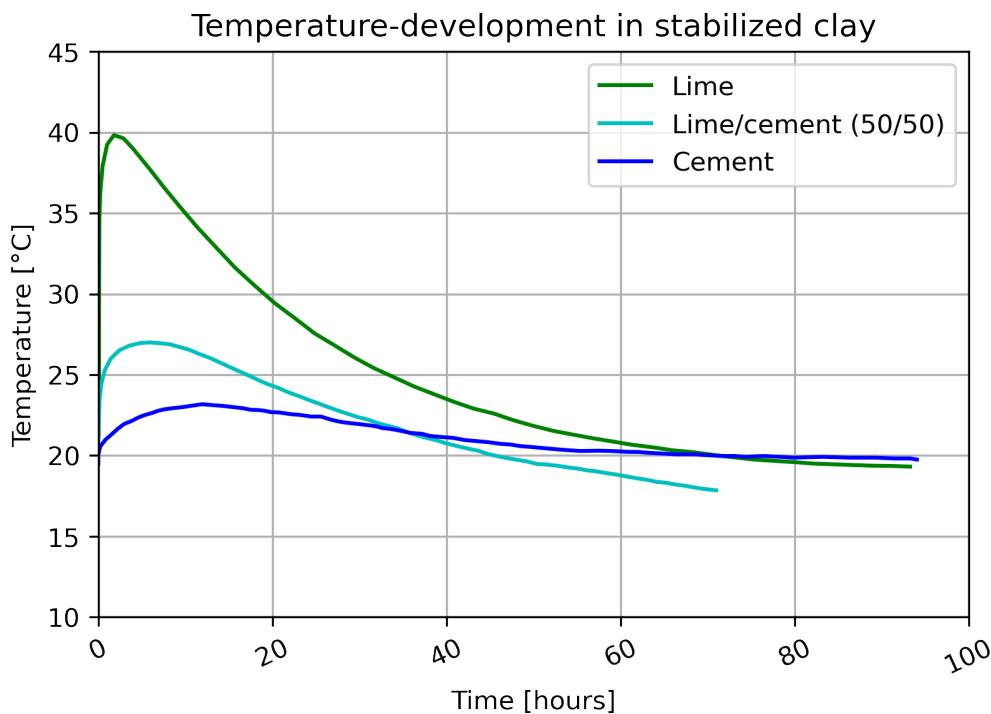
Soil stabilization has complex strength-enhancing mechanisms. Both hydration and pozzolanic reactions, which are the most important chemical reactions with regard to strength, have a close relation to the curing temperature. A higher density of both reactions and their strength contributions will take place as a result of higher temperatures, thus also the strength will improve with higher curing temperature (Zhang et al. 2014). In other words, the temperature

	Total heat	Time for peak heat	Temperature rise	Water pr. 100g binder
Lime	1163 kJ/kg	20-30 min	40-50°C	32 g
Cement	450 kJ/kg	10 hours	5-10°C	25 g

**Table 2.1:** Properties related to hydration of lime and cement based on the research of Boynton (1980), Åhnberg, Johansson et al. (1995) and (Wiersholm 2018).

of curing has a noticeable effect on the chemical reactions and ultimate properties of stabilized soil. Thus, for LC-stabilized soil heating from lime-hydration will, naturally, influence the chemical reactions linked with the cement.

The two presented binders ensure two different developments with time when it comes to temperature changes. To exemplify the heat development of the two binders separately, and together as a binder composition, a closer look will be taken at the research conducted by Wiersholm (2018). The Figure 2.7 presents the temperature development with time for Norwegian clays stabilized in the laboratory with three different binder compositions of the two binders. The tested material was quick clay from Klett (Trondheim) in the vicinity of Tiller-Flotten, and a binder content of  $80 \text{ kg/m}^3$  was applied for these specific samples. Several of the discussed aspects related to the chemistry of the two binders can be seen from the laboratory work performed by Wiersholm (2018).



**Figure 2.7:** Temperature development in Norwegian clay stabilized in the laboratory. Data from (Wiersholm 2018).



From Figure 2.7 it can be observed that purely lime-stabilized clay had a far greater temperature increase than purely cement-stabilized clay. Additionally, the maximum temperature was obtained significantly more rapidly for the lime-stabilized clay compared to the clay stabilized with cement. These findings fit well with Table 2.1

The clay that was stabilized with a 50/50-combination of lime and cement, behaved somewhat as a linear combination of the two different binders. The temperature rise of the LC-clay was between the corresponding values of the two samples stabilized with solely one binder, and the same yields for the time required to reach the maximum temperature. The fact that the LC-clay was some sort of a linear combination between the two samples stabilized with solely one binder can also be seen from the shape of the curve. The shape illustrates the temperature change with time.

The exothermic temperature development in LC-stabilized soil is a phenomenon that can be utilized to detect potential weakness zones. Substantial research, including the works that have been presented in this section, has been conducted on temperature development in stabilized soil due to the hydration of the binders. By analyzing the temperature development in stabilized soil columns it can be possible to detect irregularities related to the distribution of the binders along the height of the columns. This can be done by utilizing the fact that zones with not satisfactory mixing of the binders will emit less heat than the rest of the soil column.

However, it does not exist any accepted and satisfactory method for monitoring the temperature profile in an entire LC-column. Standard point temperature sensors have been applied in some research, for instance in the work of Wiersholm (2018), to monitor the temperature of in situ stabilized clay. However, as point sensors are restricted to monitoring only a few selected points along the height, they can not be utilized to reliably detect weakness zones. These potential irregularities of the stabilized soil columns can occur anywhere along the height. Hence, in order to utilize the exothermic heat development from hydration to detect weakness zones of stabilized soil columns, a system that is able to produce measurements continuously along the whole height is required. Such a system is lacking today.

### 2.7.2 Strength-development of LC-clay

Lime and cement contribute differently to the strength development in stabilized clay. Cement acts as a hydraulic binder and enhances the strength and stiffness of the clay by densifying it with CSH-gel formed during hydration (NGF 2012). On the other hand, lime acts as a pozzolanic binder. There is an initial hydraulic reaction when lime is used for stabilization of clay, where  $\text{Ca}(\text{OH})_2$  is the product and is further used in a secondary reaction (Janz and Johansson 2002). However, it is the secondary pozzolanic reaction that generates the strength increase in the clay due to the lime portion of the binder (Janz and Johansson 2002).

While the strength-generation from the hydration of cement is a relatively rapid reaction, the pozzolanic reactions are a much more time-consuming process (NGF 2012). Both of these two mentioned strength-enhancing mechanisms are dependent on the curing temperature, as the temperature conditions can affect the rate and extent of the chemical reactions.

---

Zhang et al. (2014) has studied the effect of curing temperature on stabilized soil. In summary, it was found that an increase in curing temperature accelerates cement hydration, leading to higher early-age strength. Moreover, it facilitates a greater quantity of products from cement hydration, particularly  $\text{Ca(OH)}_2$ , which promotes a higher number of pozzolanic reactions compared to lower curing temperatures. Thus, higher curing temperatures contribute to both higher short-term and long-term strength enhancement in lime/cement-stabilized clay.

To examine the strength development due to the two different binders solely, in addition to a binder composition of both, a closer look will be taken on some laboratory research performed by Åhnberg, Johansson et al. (1995). In their study, Åhnberg, Johansson et al. (1995) investigated the strength development of lime, cement and lime/cement (25%/75%) stabilized Swedish clay. Uniaxial tests were conducted on clay samples with a binder weight ratio of 10%. The samples stabilized with cement and lime/cement were stored at a temperature of 8°C, which represents the typical ground temperature in Sweden. On the other hand, the lime-stabilized samples were cured at a temperature of 20°C.

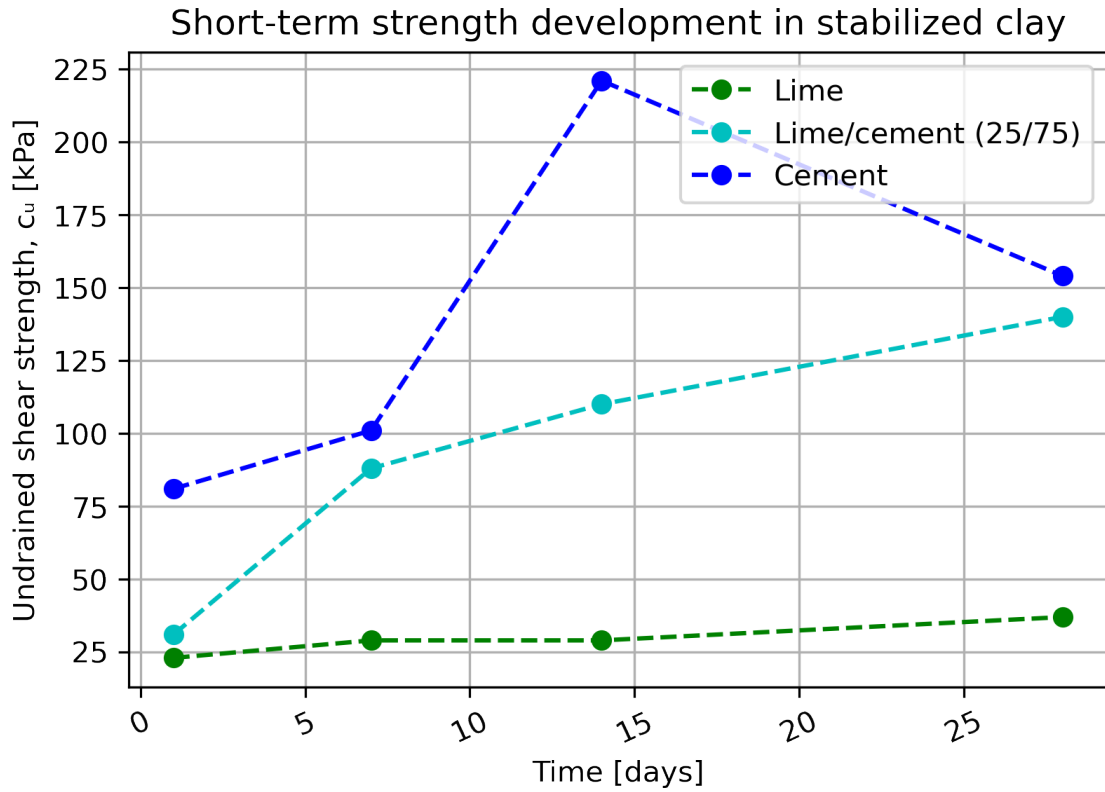
The laboratory tests conducted by Åhnberg, Johansson et al. (1995) revealed several noteworthy findings that align with the theoretical understanding of the strength-contributions of the different binders, as discussed previously. The study examined both short-term and long-term strength generation. The results of the laboratory testing are presented in Figure 2.8.

The short-term strength of stabilized clay is primarily influenced by the binder composition. Cement-stabilized clay exhibits the highest short-term strength due to the chemical reactions involved, as discussed earlier. This observation is supported by the findings presented in Figure 2.8a. In the tests conducted over the first 28 days, the cement binder consistently provided the highest shear strength among all samples. In contrast, the lime-stabilized samples showed a limited increase in short-term strength.

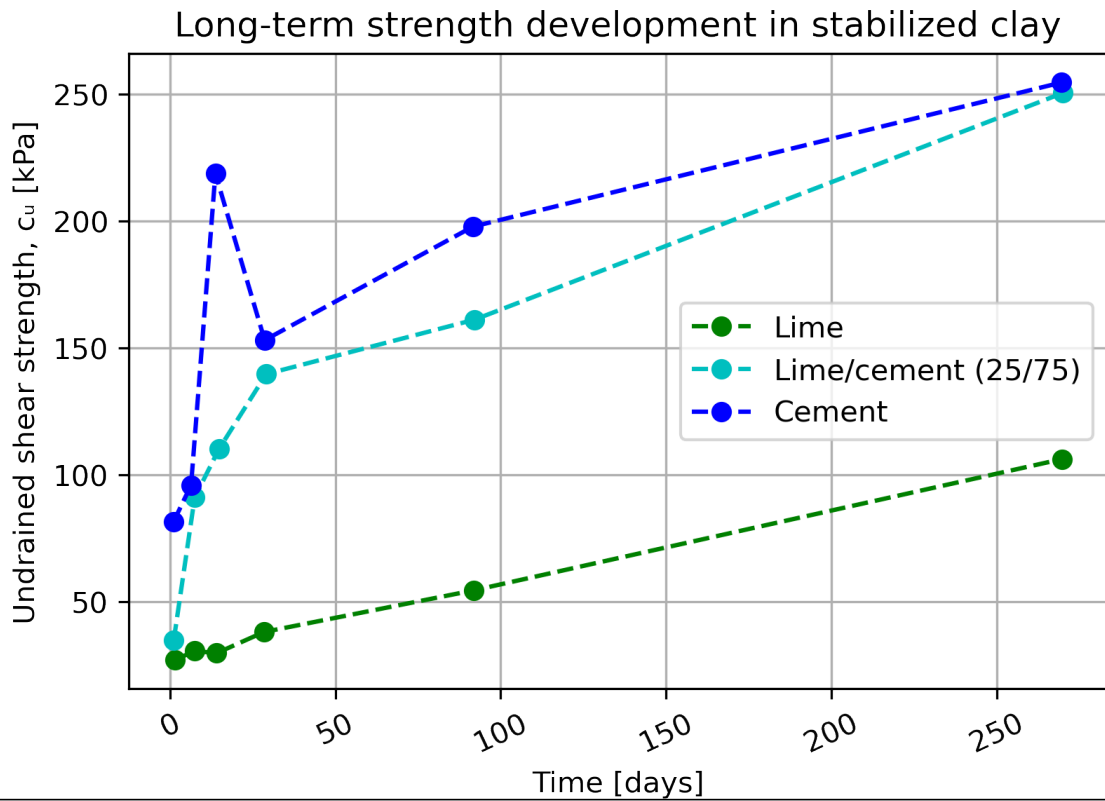
While the clay samples stabilized with cement and lime/cement showed relatively rapid strength developments in the first 28 days, these stabilized into an approximately linearly increasing trend following the initial strength enhancement. Figure 2.8b shows this finding, where the two binder compositions are observed to give a stable increase at a high strength level. Also the strength enhancement of the clay stabilized with lime was stable, and nearly parallel to the two other evolutions, but at a lower strength level.

A noteworthy observation from Figure 2.8b is the gradual convergence of the strength development between the lime/cement-samples and the cement-samples over time. This can be attributed to the time-dependent nature of the strength-contribution from the lime portion of the binder composition. For the samples stabilized with cement and lime/cement, more than 50% of the total strength development was achieved within the first 28 days. In contrast, only about 17% of the total strength development for the lime-stabilized samples was achieved within the same period. This reinforces the notion that lime's strength contribution requires a longer time to fully manifest itself. Lime has the potential to provide a comparable level of strength to the soil as cement, but it takes a considerable amount of time for this contribution to become evident (Åhnberg, Johansson et al. 1995).

---



(a) Short-term development



(b) Long-term development

**Figure 2.8:** Strength development of laboratory-stabilized clay samples. Data from (Åhnberg, Johansson et al. 1995).

## 2.8 The maturity concept

Maturity is a concept where the curing effect of both temperature and time is combined into one parameter (Bache et al. 2022). A general expression for the maturity number for stabilized soil was proposed by Åhnberg and Holm (1987) and is shown in Equation 2.3.

$$M_T = [20 + (T - 20) \cdot K]^2 \cdot \sqrt{t} \quad (2.3)$$

where T is the curing temperature [°C], t is the curing time [days] and K is a factor dependent on the soil type, binder and curing temperature (Åhnberg and Holm 1987). Åhnberg and Holm (1987) found that  $K = 0.5$  provided good results for Scandinavian clay stabilized with lime and cement. For stabilized soil cured under varying temperatures, Bache et al. (2022) suggest that Equation 2.4 can be applied.

$$M_T = \sum_n^i [20 + (T_n - 20) \cdot K]^2 \cdot [\sqrt{t_{n+1}} - \sqrt{t_n}] \quad (2.4)$$

This parameter, namely the maturity number, enables the possibility to estimate the strength and stiffness of stabilized soil columns based on their curing condition. By creating exponential regression curves of the correlation between the undrained shear strength ( $c_u$ ) and the maturity number ( $M_T$ ), it is possible to estimate the obtained strength (Bache et al. 2022). Similar procedure can be carried out to estimate the stiffness of the stabilized soil based on the maturity number (Bache et al. 2022).

The relationship between the maturity and obtained strength and stiffness is not universal, hence the relationship has to be derived for all different combinations of soil and binder, both amount and type, that is to be evaluated based on the maturity concept (Bache et al. 2022). These relationships are derived by testing the strength and stiffness of the specific materials under different temperatures and/or curing ages, in other words for different maturities (Bache et al. 2022).

Helle et al. (2022) has developed a work methodology for a more reliable estimation of obtained strength over the entire height of columns of stabilized soil compared to the existing methods for determining the mechanical properties. This methodology is based on performing temperature measurements of the curing process over the entire column height to enable the use of the maturity concept to estimate the strength. Due to limitations with the existing methods for determining obtained strength, the measurements normally have to be performed within the first week after mixing (Helle et al. 2022). However, there are still considerable developments in strength and stiffness after the first week. The methodology proposed by Helle et al. (2022) enables the estimation of the obtained strength of the stabilized soil column independent of the strength at the time of testing. This can facilitate more accurate strength estimation, and hence allow reduction of either binder amount or amount of soil to be stabilized (Helle et al. 2022).

---

In order to be able to estimate the strength of an entire column of stabilized soil accurately, as many temperature measurements as possible along the height of the column should be performed. Helle et al. (2022) propose that temperature sensors should be installed evenly from 0.5 m above the bottom of the column, with a minimum of 4 temperature sensors per 10 m of the stabilized soil column. The introduction of a system able to monitor temperature development continuously over the entire length of the columns would allow even more exact estimates of the entire column's strength.

Currently, there is no accepted method that enables measuring the temperature during curing at a high spatial resolution to obtain information about the quality of the mixing, in addition, to translating the temperature measurements to more reliable estimates of obtained strength and stiffness. The existing methods are destructive and can only be used once. The methods also have limitations, leading to the measurements being performed long before the curing is completed. In other words, today's methods do not either give any information on the strength and stiffness at later stages of the curing process.

## 2.9 Monitoring of field performance

Equally as for the development of curing temperature, no method has been developed to monitor the strain along the whole height of stabilized soil columns. Currently, it does not exist any reliable monitoring methods which provide information about the response of stabilized soil columns during different loading stages. Overall displacements can be measured, but information about how the stresses and strains are distributed along the height of the stabilized soil column is missing in the existing methods. Such information could provide vital information into the field performance of the LC-columns. In order to obtain this information, a system able to provide reliable strain measurements with a high resolution, both spatially and temporally, is needed.

## 2.10 Types of binders used in this M.Sc. Thesis

The binders that have been utilized for the laboratory tests in this M.Sc. Thesis are quicklime (QL) and Portland cement CEM I. For the performed temperature tests, purely QL was used as the binder, whilst for the strain test a binder composition of 50% QL and 50% CEM I was used. The quicklime is, as described in Section 2.5.1, produced by burning limestone ( $CaCO_3$ ), and the end product is CaO of very fine grading. The Portland cement CEM I is made of 90.2% cement clinker, 5.5% gypsum and 4.3% limestone filler (Norcem 2022). The production process of the cement follows what was described in Section 2.6.1.

---



## Chapter 3

# Distributed Fiber Optic Sensing

This chapter will cover the fundamental aspects related to the Distributed Fiber Optic Sensing (DFOS) technology. This includes the physical phenomena that form the basis for the technology and also the general setup of how a monitoring system based on DFOS is built up. Also, the necessary materials and equipment are mentioned. The different measuring techniques that are applied based on DFOS and some of their current applications are described. Lastly, some applications more specifically related to geotechnical engineering are discussed.

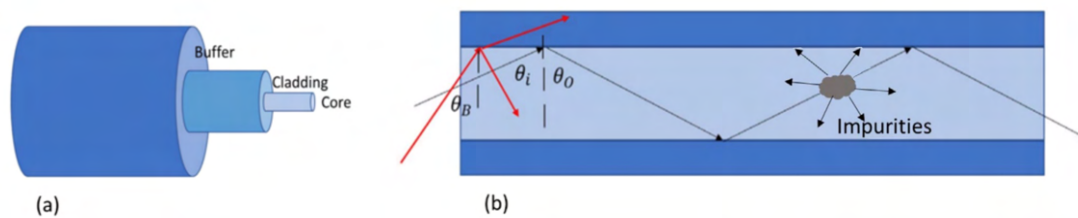
### 3.1 Optical fibers

Distributed Fiber Optic Sensing (DFOS) is a sensing technology that utilizes optical fibers and light scattering to measure physical quantities such as strain and temperature for instance. Soga and Luo (2018) provide a comprehensive overview of DFOS, and the following sections are based on the most important aspects of their article. Optical fibers serve as circular waveguides capable of carrying light (energy) within the infrared or visible parts of the electromagnetic spectrum (Soga and Luo 2018). The structure of an optical fiber cable consists generally of three parts, namely a core surrounded by a cladding and a buffer protecting the two already mentioned parts from environmental damage. Figure 3.1(a) illustrates the general structure of an optical fiber.

The optical fiber core is typically composed of either glass or silica and possesses a specific refractive index (Soga and Luo 2018). Surrounding the core is the cladding, which has a lower refractive index compared to the core. The refractive index difference between the core and the cladding causes light waves to undergo refraction at the interface between the two materials (Soga and Luo 2018). When the angle of the incident light falls within an acceptable range, the light will continue to propagate along the fiber's length through multiple reflections. However, if the launching angle exceeds a certain limit, some of the light will escape through the cladding and be lost from the fiber. This phenomenon is depicted in 3.1(b), where the continuous propagation of light is represented by black arrows, while the loss of light energy

is indicated by red arrows.

In terms of dimensions, the cladding of an optical fiber typically has a diameter of approximately  $125\ \mu\text{m}$  (Soga and Luo 2018). The core, on the other hand, can have different diameters depending on whether it is a single-mode or multimode fiber. For single-mode fibers, the core diameter is typically around  $10\ \mu\text{m}$ , whereas, for multimode fibers, the core diameter is typically around  $62.5\ \mu\text{m}$  (Soga and Luo 2018). The distinction between single-mode and multimode fibers lies in the number of possible modes of light propagation. In a multimode fiber, the larger core diameter allows for multiple modes of light propagation, while in a single-mode fiber, there is only one possible mode due to the smaller core diameter, which restricts the transmission angle of the incident light (Soga and Luo 2018).



**Figure 3.1:** Principle of an optical fiber using light scattering (Soga and Luo 2018).

## 3.2 Light scattering

Also this section is based on the work from Soga and Luo (2018). Light traveling through an optical fiber will lose some power. Power loss in optical fibers can occur through various mechanisms, including bending loss, material absorption and scattering. Scattering is the physical phenomenon where light waves are forced to deviate from their original path when they encounter non-uniformities or irregularities in the fiber material (Soga and Luo 2018). When light undergoes scattering, some of the scattered light beams continue to propagate forward in a homogeneous material, while a small fraction of the scattered light will move in the opposite direction in a non-homogeneous material.

Every material has impurities, they are in other words non-homogeneous, hence light transmitted in a fiber optic cable will always have corresponding backscattered waves (Soga and Luo 2018). As shown in Figure 3.1(b), scattering occurs when incident light encounters impurities or irregularities in the fiber material, leading to a redirection of light waves in various directions. When an optical fiber is subjected to external factors such as mechanical strain or temperature changes, it can result in density fluctuations along the fiber length (Soga and Luo 2018). These fluctuations influence the characteristics of the backscattered light beams.

By analyzing the changes in the properties of the backscattered light, it becomes possible to detect and quantify the effects of for instance mechanical strain or temperature that is experienced by the fiber cable. To analyze these changes, a frequency profile or spectrum is plotted



based on the backscattered light (Soga and Luo 2018). This spectrum, along with its frequency shift, provides valuable information about the characteristics and magnitude of the strain, temperature or vibration at different points along the fiber. The flight time of the backscattered light is utilized to determine the exposed position.

In the context of optical fiber sensing, there are two types of physical scattering: elastic scattering and inelastic scattering (Soga and Luo 2018). Elastic scattering is a linear collision process where the energy of the photons remains unchanged. It is commonly referred to as Rayleigh scattering. In contrast, inelastic scattering is a non-linear collision process where the energy of the photons is altered. This inelastic scattering is either Raman scattering or Brillouin scattering.

In the case of inelastic scattering, there is an energy exchange between the incident light photon and phonons of the material (Soga and Luo 2018). In Brillouin scattering the incident photon interacts with acoustic phonons of the material, whilst the Raman technology involves optic phonons of the material (Soga and Luo 2018). The mentioned exchange can result in the generation of a Stokes wave if the photon loses energy or an anti-Stokes wave if the photon gains energy (Soga and Luo 2018). The ratio between the anti-Stokes and Stokes waves can provide valuable information about changes along the cable. By analyzing the change in this ratio obtained from the frequency spectra of the backscattered light, it is possible to determine the temperature change profile of the monitored structure (Soga and Luo 2018). Raman-based systems primarily focus on temperature measurement. Systems based on Rayleigh or Brillouin scattering have the capability to measure both strain and temperature changes (Soga and Luo 2018).

### 3.3 The concept of DFOS

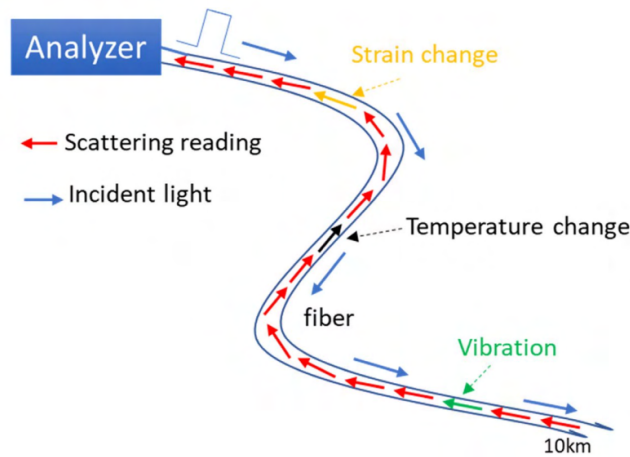
Soga and Luo (2018) is the main inspiration also for this section, any additional references are stated clearly in the text. Distributed Fiber Optic Sensing (DFOS) offers a promising alternative to traditional strain gauges and thermo elements by leveraging optical fibers and light scattering phenomena. It overcomes uncertainties associated with point sensors and provides the capability to capture localized effects, in addition to giving high-resolution measurements throughout the entire length of the fiber cable.

This technology has the potential to become the preferred choice for sensing in various civil engineering projects due to its clear advantages over standard point sensors. DFOS offers continuous measurements and has already been widely applied for monitoring structures such as tunnels, thermal piles, diaphragm walls and preliminary testing of piles (Rui et al. 2017). Figure 3.2 provides a schematic representation of a distributed fiber optic sensor system.

In summary, a distributed fiber optic sensing system includes an interrogator that emits a light pulse into the optical fiber cable and analyzes the reflected light. The interrogator scans and analyzes the backscattered light signal, allowing for the detection and quantification of the changes in the relevant quantity at each location along the cable.

---

As mentioned earlier, there will always be backscattered light from an incident light traveling through an optical fiber, and this is visualized by the red arrows in Figure 3.2. However, it is the transformed backscattered signals due to external impact which are of interest. They are represented by the green arrow for vibration, the black arrow for temperature change and the yellow arrow for strain change in Figure 3.2.



**Figure 3.2:** A schematic showing the principle of a distributed fiber optic sensing system (Soga and Luo 2018).

An important consideration regarding DFOS-systems is that they can only measure relative values, meaning they calculate the changes in the physical quantities. To obtain absolute values, for example of the temperature, an initial measurement using additional measurement equipment, such as traditional thermo elements, is required. This initial measurement provides the baseline values that serve as a reference for the subsequent relative measurements performed by the DFOS-system. Therefore, a well-functioning monitoring system based on DFOS incorporates both the DFOS-technology for continuous monitoring of changes and complementary measurement apparatus for obtaining the absolute values.

### 3.4 Different techniques of DFOS

In the following, the broad spectrum of different techniques of DFOS is discussed according to Soga and Luo (2018). The DFOS-technology consists of various systems that are characterized by the type of cable, the domain for analysis and the scattering technique employed. Figure 3.3 provides a schematic representation of the different DFOS-systems. Firstly, the system can be classified as either a single-end access sensor or a both-end access sensor. In a single-end access sensor, only one end of the fiber optic cable is connected to the interrogator, while the remaining portion is embedded within the structure being monitored (Soga and Luo 2018). On the other hand, a both-end access sensor system involves connecting the cable in a loop to the structure, with both ends free and connected to the interrogator (Soga and Luo 2018).

The OTDR-method (Optical Time Domain Reflectometry) is using a pulse light that is being pumped into the fiber cable, while for the OFDR-method (Optical Frequency Domain Reflectometry) measurements of the optical frequency of this pump light are utilized (Soga and Luo 2018). When it comes to the resolution spatially, it depends on the width of the pulse for OTDR, while for OFDR it is a function of the frequency change rate (Soga and Luo 2018). OADR (Optical Correlation Domain Reflectometry) is another method, which is pumping correlation codes of varying complexity and uses these to analyze the exposed areas along the fiber cable (Soga and Luo 2018).

Lastly, BOTDA (Brillouin Optical Time Domain Analysis) is a method involving sending pump and probe lights from both ends of the fiber cable and analyzing the power difference that occurs (Soga and Luo 2018). ROTDA is another analysis method based on OTDR, but which is using Raman scattering (Soga and Luo 2018). The different DFOS systems are ultimately dependent on the scattering technique being utilized. These techniques are often the already mentioned ones, in other words, Rayleigh, Raman and Brillouin.

Due to the fact that so many factors can be adjusted, it exists many different DFOS-systems that can be constructed and utilized for sensing purposes. The extensive number of systems that can be created is visualized by the "system-tree" in Figure 3.3. The wide range of DFOS-systems opens up numerous areas of application for the technology.

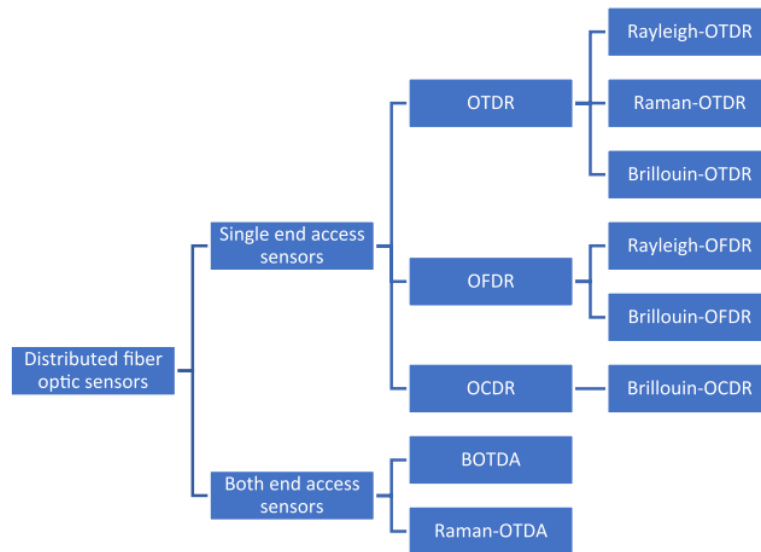


Figure 3.3: A schematic showing different DFOS systems (Soga and Luo 2018).

### 3.5 Applications of DFOS

Distributed Fiber Optic Sensing (DFOS) has found practical applications in various fields. Hjelstuen (2020) from the Department of Smart Sensor Systems at SINTEF Digital held an inform-

ative webinar on the topic under the auspices of Tekna, and this webinar forms the basis for the following paragraphs. Two specific applications of DFOS, Distributed Temperature Sensing (DTS) and Distributed Strain Sensing (DSS), have already been mentioned. In addition, Distributed Acoustic Sensing (DAS) will be presented. The few examples which, based on the webinar of Hjelstuen (2020), are following are presented to visualize the possibilities of the promising monitoring system which DFOS is. The different methods are very relevant for use in geotechnical engineering, and the following exemplifies the performance of the methods.

DTS has proven to be valuable in different scenarios, including fire detection in tunnels, power cable monitoring, ecological monitoring and leakage detection at dikes and dams. The method can achieve a spatial resolution of up to 0.12 m for fiber optic cables that span lengths of 100 km.

DSS has been utilized for landslide early-warning systems in addition to offering a wide range of applications in structural health monitoring. It is commonly used for monitoring pipelines, bridges and piles, among other structures. The use of Distributed Strain Sensing (DSS) can provide high-quality measurements. To exemplify, Soga and Luo (2018) found in their work that DSS can have a measurement resolution of a very high degree for 10 km cables with a spatial resolution of 2 m.

Another notable application of DFOS is Distributed Acoustic Sensing (DAS). In DAS, laser pulses are employed to detect disturbances along the fiber optic cable. All human activities which may harm our structure make some sort of sound waves, leading to acoustic disturbances on the cable. These disturbances result in microscopic elongations or compressions of the cable.

DAS has found applications in monitoring pipelines and oil wells, as well as sensing seismic activity. It provides valuable insights into the condition and integrity of these structures and helps detect potential issues. It can work as a crucial tool for maintenance planning. The spatial resolution of DAS can reach as low as 1 m for cable lengths of up to 50 km.

Fiber Bragg Grating (FBG) sensors are another application of fiber optic technology, providing a middle ground between standard point sensors and the continuous sensing system of DFOS (Soga and Luo 2018). FBG sensors operate as point sensors based on fiber optic technology (Soga and Luo 2018). The system is based on making several fictitious point sensors equally spaced by introducing a different refractive index at each of these points.

The distance between the gratings, denoted as  $\Lambda$ , is determined by the design wavelength of the incident light, given by  $\lambda = 2n\Lambda$  (Soga and Luo 2018). When an FBG point on the fiber optic cable is subjected to temperature or strain, the length of the grating ( $\Lambda$ ) changes proportionally to the temperature or strain (Soga and Luo 2018). This change affects the characteristics of the backscattered light, and by analyzing the alterations in these light beams, the corresponding temperature or strain change at that specific point can be determined (Soga and Luo 2018).

Multiple FBG points can be implemented on a single fiber cable by utilizing different wavelength ranges for each point. However, due to the limited bandwidth of light that can propagate through the cable, the number of points is typically limited to around 10-20 per channel (Soga and Luo 2018). While FBG sensors can provide accurate measurements at specific points, their

---

spatial resolution is not comparable to that of DFOS due to the limitations on the number of points that can be installed.

### 3.6 Previous geotechnical projects using DFOS

DFOS is already used for several different geotechnical projects. To mention some examples, both monitoring of slope stability, ground deformations due to tunneling work and monitoring of pile foundations have been performed with the help of DFOS (Shi et al. 2021). For slope monitoring, real-time deformations can be provided continuously, to enable the possibility of observing all movements of the slope. In addition, DFOS can provide an early warning for landslides (Hjelstuen 2020).

With regards to ground deformations induced by the construction of tunnels, DFOS can provide high-resolution measurements of the movements of the surrounding soil, making it easier to predict the behavior of the ground. Both the tunnel structure, the support structure and the surrounding soil can be monitored (Shi et al. 2021). This can enable an advanced sensor system that is able to assess the quality and safety of the tunneling work by the use of DFOS.

DFOS has also been used to monitor piles. Shi et al. (2021) describes the use of the technology to monitor pile foundations, and some of the aspects will be presented in the following. Distributed monitoring can be performed of both strain and temperature, and this data can give several relevant insights into the performance of the pile foundation through post-processing. For instance, strain along the whole height can be measured during loading. This enables the possibility of determining the force behavior of the pile (Shi et al. 2021). This includes axial force, side friction resistance and compression of the pile (Shi et al. 2021). In addition, estimates of the stiffness of the soil and the bearing capacity of the pile foundation can be made based on the force distribution (Shi et al. 2021). Also the pile driving process can be monitored by DFOS (Shi et al. 2021).

Continuous temperature measurements by the use of DTS are also valuable for pile monitoring. Rui et al. (2017) examined the use of DFOS to evaluate the integrity of cast-in-place foundation piles. There are major concerns related to the integrity and quality of cast-in-place piles in the geotechnical industry due to the lack of sufficient methods for controlling these parameters (Rui et al. 2017). Rui et al. (2017) used DFOS to measure the exothermic heat development due to hydration during the curing of a large cast-in-place pile and utilized this data to create a FEM-model to estimate the dimensions of the installed pile. The measurements and calculations provided a better understanding of the obtained integrity of the pile.

In short, Distributed Fiber Optic Sensing (DFOS) is a promising technology that, in addition to being applied in other construction projects, has been used widely for geotechnical monitoring. The area of usage within the field of geotechnics is wide, and ever-increasing. More and more projects are using DFOS, and the results are often very satisfactory.

---

### 3.7 Choice of fiber optic cables for this M.Sc. Thesis

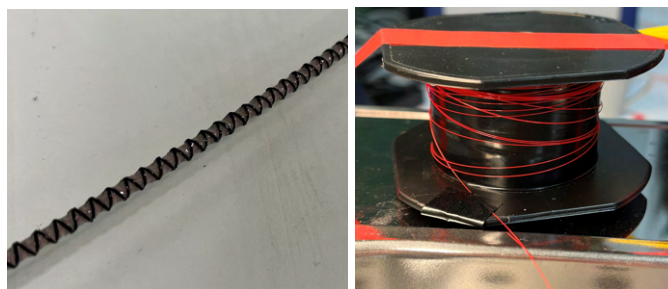
There is an extensive variety of fiber optic cables available, each with different specifications, advantages and disadvantages. There are numerous manufacturers and suppliers, and the possibilities are vast. Hence, a thorough and detailed evaluation of which cable types to test in this M.Sc. Thesis has been carried out. Some of the most important aspects that have been investigated are:

- Cable diameter
- Jacket material
- Measurement type
- Sensitivity
- Bending radius
- Stiffness

A large amount of data was collected and compiled in an elaborate table. The mentioned table is added in Appendix F. This table made the basis for the final choice of cables. The decision on cables was made in consultation with experts from NGI. The manufacturer was a key point for the choice that was taken. What was important with regard to the manufacturer was:

- Production of cables fulfilling our request
- Previous experience
- Helpfulness
- Opportunity for research collaboration

*NERVE-SENSORS*, which is a Polish company that both produces cables and performs a lot of research on DFOS, was chosen as the manufacturer. For the temperature tests, a bare fiber was provided from *NERVE-SENSORS* to help perform the measurements. This bare fiber is an extremely thin and fragile thread. For the strain tests, the standard EpsilonSensor DSS cable was utilized. EpsilonSensor is designed to ensure good adhesion to the soil. The chosen cables are depicted in Figure 3.4.



(a) EpsilonSensor.

(b) Bare fiber core.

**Figure 3.4:** The two fiber optic cables that have been used in this M.Sc. Thesis.

---

# Chapter 4

## Material

This chapter covers the basics of clay definition in addition to a brief description of the formation and characteristics of quick clay. Further on, the test site which is the origin of the tested material is presented in terms of both quaternary geology, prehistoric geological activity and topography. Lastly, the most important index parameters of the clay tested in this M.Sc. Thesis are presented.

### 4.1 Clay

#### 4.1.1 Definition of clay

Clay is the name of both a particle size and a soil type. All particles with a diameter of less than  $2\mu\text{m}$  are described as clay particles (Barnes 2022). Clay, as the term for soil type, is by definition soil where more than 30% of the mass is of clay particles, in other words, grains with a diameter smaller than  $2\mu\text{m}$  (NGF 2011). This is determined by producing a grain size distribution graph for the material, and this is essential to do as the grain size distribution is one of the most important physical characteristics of the soil (Standard Norge 2017).

Several different characteristics exist for clay. For instance, the clay particles have a distinct and unique shape. They have a flake shape, i.e. the clay particles look like tiny plates, and they are flat and oblong (NTNU 2020). The particles are made up of sheet-like clay minerals (Barnes 2022). Apart from the shape of its particles, clay is known for being a soil type with high plasticity, low permeability and low stiffness compared to the other types. Also, it is known for its cohesiveness, high capillary effect and significant suction forces in the unsaturated zone.

### 4.1.2 Quick clay

The strength of clay is referring to the undrained shear strength ( $c_u$ ) of the material. Undrained shear strength ( $c_u$ ) is a measure of the shear strength of fine-graded soil under undrained conditions, in other words, situations where the pore water is restricted from dissipating (NGF 2011). This parameter can be expressed based on the principal stresses as shown in Equation 4.1.

$$c_u = \frac{\sigma_1 - \sigma_3}{2} \quad (4.1)$$

When failure occurs in clay, large deformations often happen, hence a parameter providing a measure of the strength of disturbed clay is an important characterization for clay (NGF 2011). This parameter is referred to as remoulded shear strength ( $c_{u,r}$ ).

Quick clay is defined as clay with a remoulded shear strength of  $c_{u,r} \leq 0.33$  kPa (NVE 2020). This unique type of clay is known for its very high sensitivity ( $S_t$ ), in other words the ratio between the intact shear strength and remoulded shear strength ( $S_t = \frac{c_u}{c_{u,r}}$ ) is significant. In other words, quick clay can often take significantly high loads, but immediately when it is overloaded, it loses more or less all its strength and can not carry the load anymore. The consistency of the clay goes from stiff, hard and intact clay to a totally remoulded, soup-like consistency with no load-bearing capacity.

The formation of quick clay is a lengthy and complex process, and will in the following be described according to NTNU (2020). Quick clay can only occur in clay deposits below the marine limit, which is the highest level that the sea has previously had. Under the marine limit, clay has been deposited in a saline environment. This clay is called marine clay and is known for its edge-to-face grain structure, similar to a cardhouse's structure. This is because clays deposited in saline environments bind water so that the active volume of the particles increases and the structure appears open.

Figure 4.1a visualizes the structure of marine clay. The figure clearly shows the absorbed water film surrounding the clay particles. This cardhouse-like grain structure is distinctive for marine clays and distinguishes it from other clays. Unlike the porous soil skeleton of marine clays, the clays deposited in freshwater are relatively densely packed. Figure 4.1b shows the difference in structure for these two types of clay.

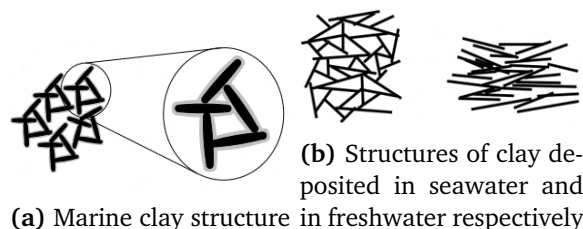


Figure 4.1: Grain structures of clays (NTNU 2020)



In marine clay, the salt binds the particles together chemically and helps stabilize the cardhouse-like structure. However, due to the land uplift after the last ice age, these marine clays have been exposed to washing out of salt pore water from groundwater flow. Such a leaching process, where most of the salt is washed out of the clay, is a long-term process. Thus, the particles have created mechanical bonds in the contact points, enabling the clay to take high loads despite its unstable structure. But as soon as the clay is overloaded, it collapses completely and the clay floats in its own pore water. Figure 4.2 is visualizing the process of land uplift which moves the marine limit, relatively, upwards and leaching of the marine clay, which makes the clay quick after some time.

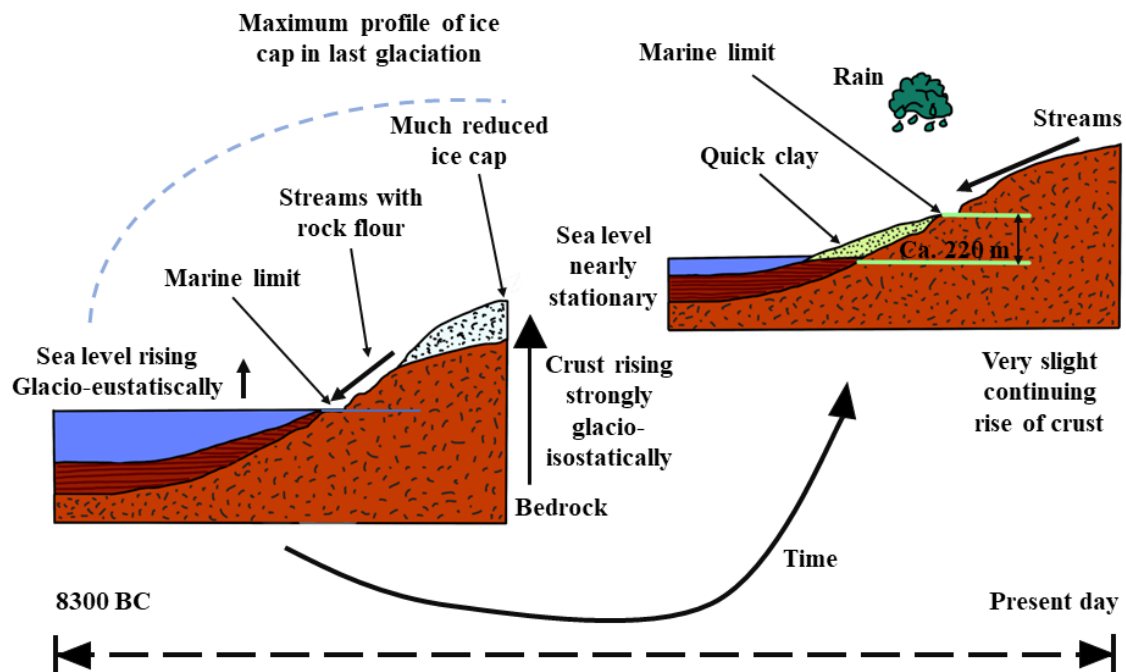


Figure 4.2: A schematic drawing of the formation process of quick clay inspired by (Giles 2023).

## 4.2 Tiller-Flotten

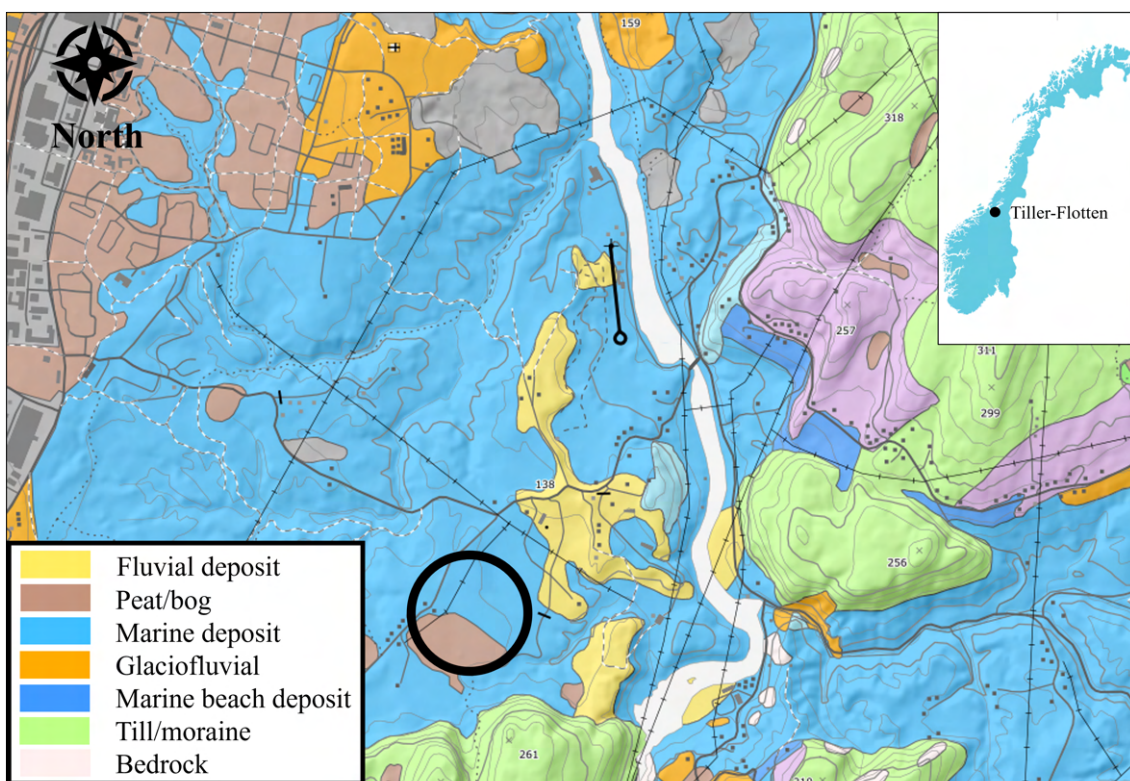
Tiller-Flotten is located about 10 km south of the city of Trondheim, in the middle of Norway (L'Heureux et al. 2019). The area consists mainly of clay, much of which is quick clay. This thick deposit of very sensitive clay is part of a national research program in Norway, Norwegian Geo-Test Sites (NGTS), which is supported by The Research Council of Norway as part of its infrastructure program (NGI 2023). The aim of the project is to increase the knowledge of the most common soil types of future Norwegian infrastructure projects. For more information about NGTS a closer look should be taken at NGI (2023).

As a result of the research project, the material from Tiller-Flotten is heavily investigated, and

as the area has shown to be homogeneous, the soil characteristics from the site are known. In the following section, the site from which the tested soil originates will be described in more detail, and the most important properties of the clay will be discussed.

#### 4.2.1 Quarternary geology

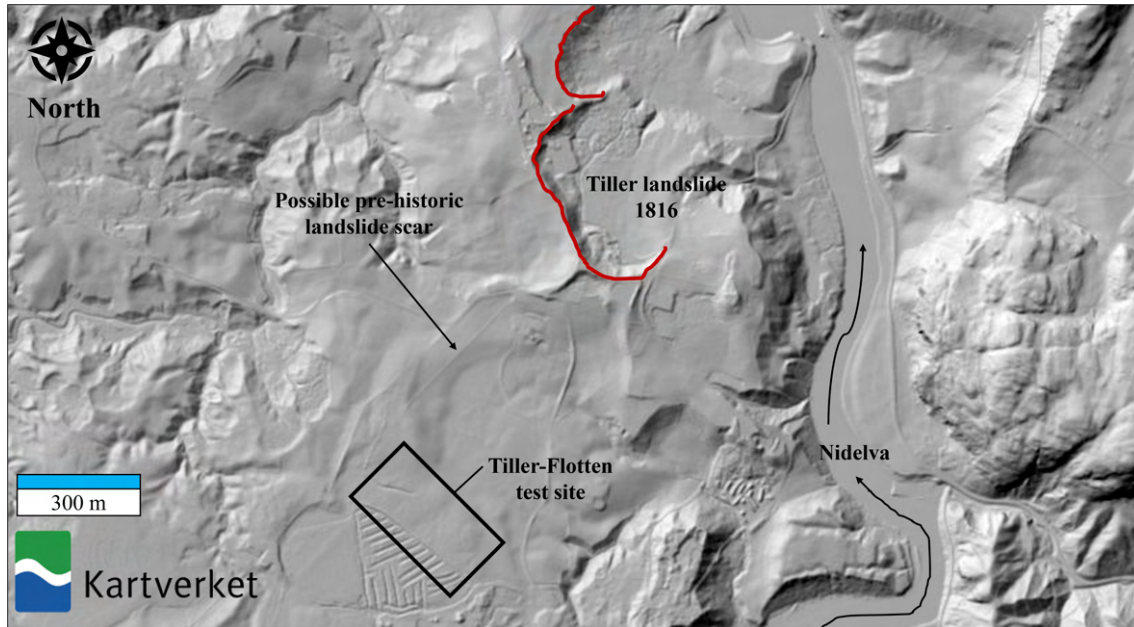
The quarternary geology at the Tiller-Flotten site will in the following section be described according to L'Heureux et al. (2019). Figure 4.3 illustrates the quarternary geology of Tiller-Flotten and the surrounding area.



**Figure 4.3:** A quarternary geology map of the site at Tiller-Flotten, Trondheim. The map is taken from (NGU 2023).

Most of the land at the site is used for agricultural purposes. However, an area of approximately 150 m by 300 m is designated for the NGTS-project. In situ soundings have revealed that the thickness of the deposits is more than 50 m (L'Heureux et al. 2019). As can be seen from Figure 4.3, most of the area consists of marine deposits and peat. The elevation of the site is 125 m.a.s.l., and the marine limit in the area is 176 m.a.s.l. according to geological maps from Geological Survey of Norway (NGU). Hence, the site is below the marine limit and the material has been deposited in a saline environment. The clay is thus defined as marine clay, and a large

proportion of the clay is quick (L'Heureux et al. 2019). The surroundings are characterized by prehistoric geological activity. The elevation of the terrain in the area is shown in Figure 4.4.



**Figure 4.4:** LIDAR data showing the elevation of the terrain at Tiller-Flotten (Kartverket 2023). The figure is inspired by (L'Heureux et al. 2019).

The geotechnical test site at Tiller-Flotten is located in a flat area. However, it can be seen from Figure 4.4 that the surrounding terrain is hilly. In addition to the hills south and east of the site, and the slope down to Nidelava river, it is obvious that there are a lot of smaller and bigger ravines, which are often typical marks after landslides. There was a catastrophic landslide in 1816 that caused 15 deaths (Reite et al. 1999). There are also traces of pre-historic landslide activity in the form of scars. Both the Tiller landslide and a pre-historic landslide scar are shown in Figure 4.4. The mentioned areas are only a few hundred meters from the Tiller-Flotten test site, but at a slightly longer distance, there are also several other known landslides that have occurred (L'Heureux et al. 2019).

### 4.3 Characteristics of Tiller-Flotten clay

The work from (L'Heureux et al. 2019) has a thorough evaluation and description of the soil conditions at Tiller-Flotten. This work forms the basis for the following section.

The quick clay deposit at Tiller-Flotten is found at 7.5 m depth, and is at least 12.5 m thick. It shows low to medium plasticity and a liquidity index ( $I_L$ ) above 1.6 throughout its thickness (L'Heureux et al. 2019). Also, the quick clay is lightly overconsolidated, which is a result of the site's glacial history. The strength of the very sensitive clay ( $c_u$ ), with corresponding anisotropy,

and stiffness fits well with the broad experience of other sensitive clays in Norway (L'Heureux et al. 2019).

### 4.3.1 General description of the clay

L'Heureux et al. (2019) divided the soil profile into three different units: Unit I, Unit IIA and Unit IIB. The upper part of the soil profile, Unit I, is a 2 m dry crust of stiff, desiccated and weathered clay (L'Heureux et al. 2019).

The lower part of the soil profile, more precisely from 2 m to 20 m depth, is divided into two sub-units, namely Unit IIA and Unit IIB. Both sub-units exhibit similar characteristics in terms of clay content and structure, as they consist of marine clay. However, there is a distinct difference in sensitivity between the sub-units. The upper sub-unit (Unit IIA) consists of low to medium sensitive clay, whereas the lower sub-unit (Unit IIB) displays extreme sensitivity (often exceeding 100), indicating that the clay in the lower sub-unit is quick clay.

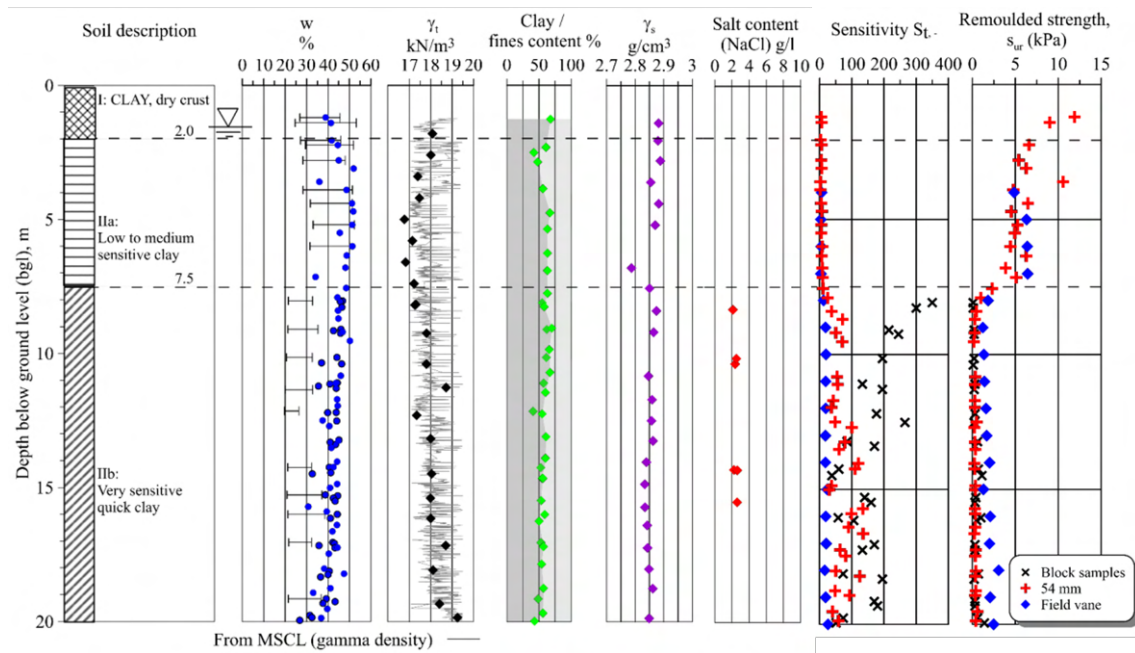
For this M.Sc. Thesis, it is the quick clay from Unit IIB that has been used for all laboratory testing. Some of the geotechnical index parameters of the quick clay (Unit IIB) from Tiller-Flotten are summarized in Table 4.1.

Index parameter	Range of values	Unit
Clay content	45 - 70	[%]
Salt content	0.21 - 0.26	[%]
Grain density, $\gamma_s$	2.835 - 2.875	[ $g/cm^3$ ]
Bulk density, $\gamma_t$	17.5 - 19	[ $kN/m^3$ ]
Natural water content	30 - 50	[%]
Plastic limit, $w_p$	20	[%]
Liquid limit, $w_L$	27 - 38	[%]
Plasticity index, $I_p$	7 - 17	[-]
Liquidity index, $I_L$	1.6 - 9.3	[-]
Sensitivity, $S_t$	50 - 350	[-]
OCR	1.5 - 3	[-]
Undrained shear strength, $c_u$	60 - 125	[kPa]

**Table 4.1:** A summary of some of the most important index parameters of the quick clay (Unit IIB) at Tiller-Flotten (L'Heureux et al. 2019).

A plot of some of the basic index parameters in the first 20 meters of the clay deposit is shown in Figure 4.5.

The clay content varies from 45-70%. Out of 35 data points, only 3 are below 50%, and as the lowest clay content is 45%, all of the soil in the soil profile is characterized as clay. The clay content is decreasing slightly from 70% at 7.5 m depth to about 50% at the bottom of the soil profile.



**Figure 4.5:** A plot showing some of the most common index parameters of clay. Plot is modified after L'Heureux et al. (2019).

With a Groundwater Level (GWL) located between 1 and 2 m depth, closer to 2 m depth, the clay deposit at Tiller-Flotten is expected to be of 100% saturation below the dry crust, in other words from 2 m depth and downwards. The natural water content,  $w_n$ , of the clay is above 40% for almost all measurements along the height of the soil profile.  $w_n$  varies from about 40% close to the surface to a value of approximately 50% at 5 m depth, before it decreases to a range between 30-35% at 20 m depth.

From Figure 4.5 it can be seen that the remoulded shear strength ( $c_{u,r}$ ) drops from around 5 kPa in Unit IIA to just above 0 kPa in the entire Unit IIB. It is this low remoulded shear strength that defines Unit IIB as a quick clay deposit, as  $c_{u,r} \leq 0.33 \text{ kPa}$  throughout the entire height of the unit. In addition, L'Heureux et al. (2019) present several aspects of the measured index parameters which support the definition of Unit IIB as a quick clay deposit. These parameters are listed in the following paragraph, but for a more detailed description, the article from L'Heureux et al. (2019) should be reviewed.

The natural water content ( $w_n$ ) of the clay in Unit IIB is above the liquid limit ( $w_L$ ), in addition, the salt content is less than 0.5% which is much less than the 3.5% which yields for seawater. The clay in Unit IIB also shows a very high liquidity index, more precisely in the range of 1.6 - 9.3 as shown in Table 4.1. Also the sensitivity ( $S_t$ ) is seen to increase drastically from Unit IIA to Unit IIB. A range of 50 - 350 yields for the sensitivity. As the entire Unit IIB has  $S_t > 30$ , the clay is defined as "very sensitive" (NGF 2011). This significant sensitivity is a result of the clay's depositional history and post-depositional processes that have led to a flocculated, open and unstable material structure (L'Heureux et al. 2019).

### **4.3.2 Clay used in this M.Sc. Thesis**

In this work, all tests have been performed on quick clay from Unit IIB at Tiller-Flotten. The cylinders were taken from two different boreholes, at the following depths:

- 15-16 m
- 16-17 m
- 17-18 m

As all tests conducted in this M.Sc. Thesis have involved testing of stabilized clay, sampling has been carried out with the help of a standard tube sampler. There was no need for more advanced sampling techniques such as the use of a mini-block sampler for instance. The clay was in all cases remoulded, hence the intact sample quality was of no importance for the tests conducted in this thesis.

---







## **Part 2 - Methodology**



## Chapter 5

# Temperature tests of layered sample

For this M.Sc. Thesis, three temperature experiments have been carried out. Two of the experiments aimed at testing whether it is possible to detect impurities within columns of stabilized soil. One additional temperature experiment examined how the temperature developed along the cross-section of a stabilized soil sample. All of the tests were carried out during the spring of 2023. In the following chapter, the methodology of the two equal temperature experiments will be described thoroughly, whilst the cross-sectional test will be described in Chapter 6.

### 5.1 Purpose

The aim of using fiber optic technology for stabilized soil is to monitor the achieved integrity of the columns. An important part of being able to determine the obtained integrity of LC-columns, is to detect any possible weakness zones along the height of the columns.

With today's methods of monitoring LC-columns, it is not possible to be sure whether the binders are distributed perfectly throughout the whole height. There might be some small layers that have been remoulded by the mixing rig on the way down, without the binders being satisfactorily mixed with the clay on the way upwards. In other words, there can be some thin layers of remoulded, unstabilized clay within constructed LC-columns. Hence, tests of the heat transfer between layers of stabilized and unstabilized quick clay have been conducted to examine whether it is possible to detect such weakness zones of unstabilized, remoulded quick clay by the use of a fiber optic cable. The idea was to detect the unstabilized layers by monitoring the heat transfer between the clay layers with a bare fiber core.

### 5.2 Equipment

For the temperature tests, the following equipment has been used:

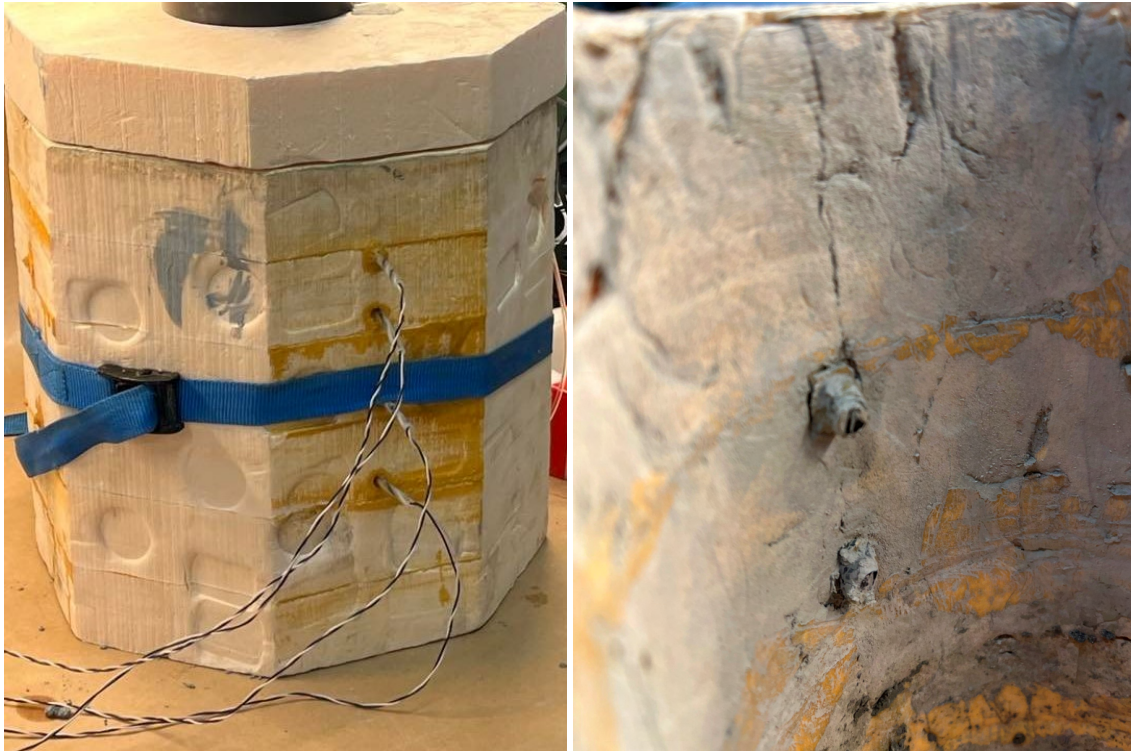
- Plastic bucket
- Kenwood stand mixer
- Laboratory weights
- Spatula
- Tamping stick made of metal
- Isolation box with integrated thermocouples
- Bare fiber produced by Nerve-Sensors
- Hydraulic oil
- Thin plastic tube
- PT100 thermo elements
- Luna OBR interrogator
- Laboratory computer for fiber optic measurements
- Laboratory computer for thermocouple measurements
- Laboratory computer for PT100 measurements

Some standard laboratory equipment was utilized to handle the material of the test. A plastic bucket was used for remolding and storage of the quick clay. Both the necessary clay and lime were measured by the use of a standard laboratory weight and a more sensitive laboratory weight, respectively. The spatula and the Kenwood stand mixer were used for mixing lime with the quick clay. A metal stick was used to tamp the stabilized clay into the box.

The isolation box was used to create an ideal curing condition, where minimal heat was lost to the surroundings. It was made up of 7 XPS-plates, which were glued together. Sketches illustrating the structure of the isolation box are added in Appendix A. The box had two functional thermocouples integrated. The design of the integrated temperature sensors is shown in Figure 5.1. Well-describing pictures of the box made up of XPS-plates can be seen, in addition to Figure 5.1, also in Figures 5.3 and 5.4.

A bare fiber was used to perform the DFOS-measurements, and it was protected inside an oil-filled plastic tube. In addition to the bare fiber, an interrogator was necessary to be able to perform the DFOS-measurements. Both the DFOS-measurements system and the thermocouples were connected to separate laboratory computers. Standard PT100 thermo elements were also utilized during the temperature testing. Both room temperature and the temperature of a reference sample of lime-stabilized quick clay were recorded. The PT100 elements were also connected to a laboratory computer.

---



(a) Position on the outside of the box

(b) Thermocouples inside the box

**Figure 5.1:** Position and appearance of the integrated thermocouples.

### 5.3 Test setup

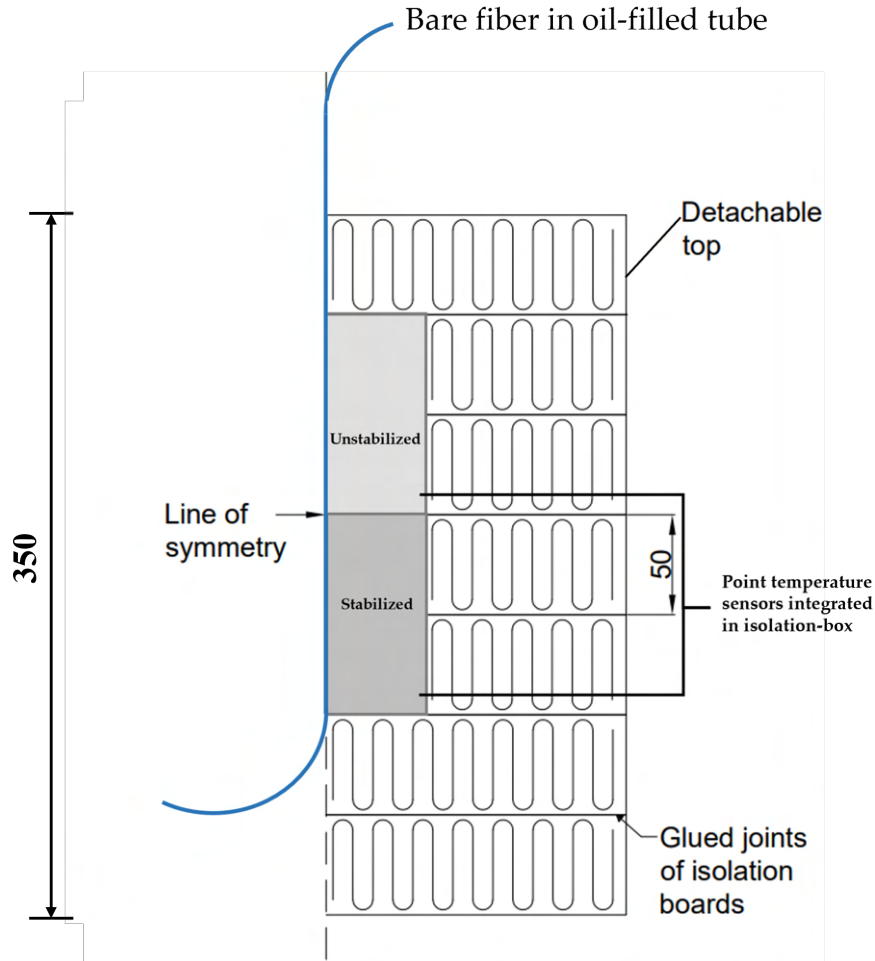
A schematic drawing of the laboratory setup is shown in Figure 5.2. Note the location of the two functioning integrated thermocouples.

The soil samples were of cylindrical shape, with a diameter of  $D = 100$  mm and a height of  $H = 200$  mm. In order to reproduce a possible situation of thin layers of imperfections along the height of an LC-column, the soil samples of these tests were also layered. The bottom halves of the samples were made of quick clay stabilized by  $50 \text{ kg/m}^3$  lime, whilst the upper half consisted of remoulded, unstabilized quick clay, as illustrated in Figure 5.2. In Figure 5.8, a picture of the layering can be seen from when the first temperature test was finished and the isolation box was opened.

The reason for the binder choice, both type and amount, is based on a wish for easy handling and a lot of heat development. As the material from Tiller-Flotten has a relatively high water content, there is a considerable amount of hydration taking place rapidly. This results in the clay becoming dry, lumpy and difficult to work with. Hence, a quite low binder content is chosen to make the handling as easy as possible. Lime as the only binder, was chosen due to

---

the fact that lime generates the most heat. As it was desirable to have a large heat development to properly test the monitoring system based on the DFOS-technology, the choice fell on lime solely as the binder for this experiment.

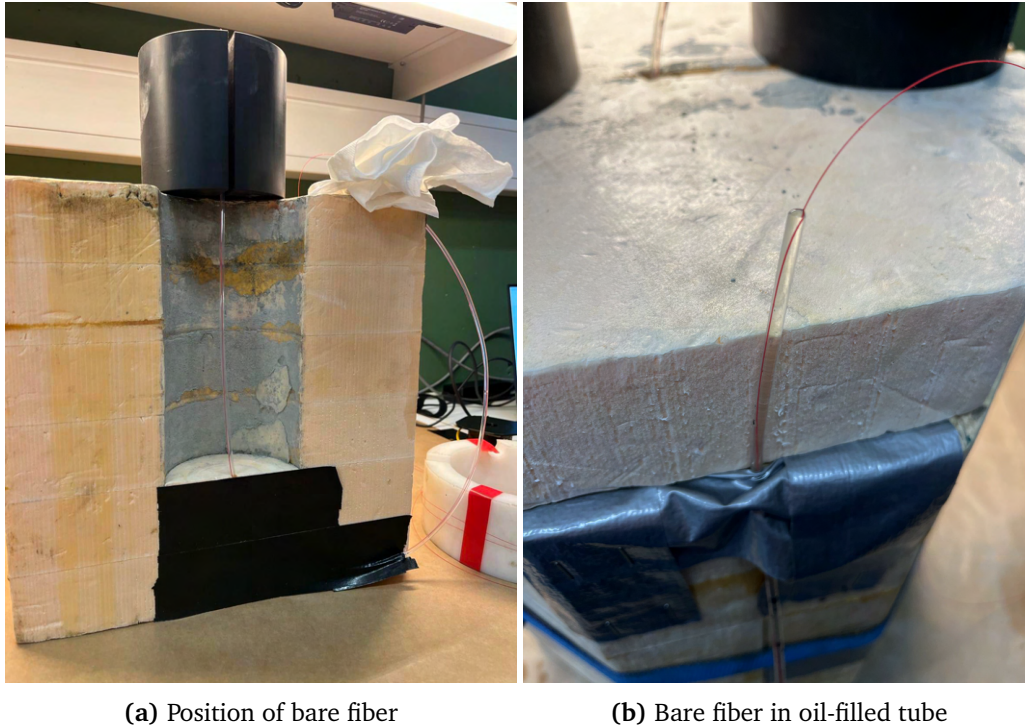


**Figure 5.2:** A schematic drawing illustrating the layering and setup of the temperature tests.

As a bare fiber was used, in other words, there was no protective jacket/cladding of the fiber optic core, it was put inside a thin plastic tube. To avoid heat transfer in the air inside the tube, the tube was filled with hydraulic oil. The idea was that the reduced thermal conductivity of the oil would ensure that the situation of air inside the tube is heated, and thus also rising upwards, did not occur. As the aim of the experiment was to observe how the temperature developed along the height of the layered soil sample, any heating of internal air would prevent the possibility of examining the correct heat transfer. The significant thermal conductivity of air would see the stabilized quick clay heat the air in the bottom of the tube, followed by the heated air rising quickly upwards.

The positioning of the bare fiber, and the setup of it being protected inside an oil-filled plastic

tube, are shown in Figure 5.3.



**Figure 5.3:** Position of bare fiber inside isolation box and close-up of the protecting plastic tube filled with hydraulic oil.

The reduced thermal conductivity of the oil was supposed to make sure that all positions along the length of the fiber core inside the soil sample were heated due to the soil being in the immediate vicinity. It was not supposed to be heated by rising air warmed up by the stabilized soil at the bottom of the sample.

One other area of use of hydraulic oil, which was of high importance, was the fact that it ensured that the bare fiber was allowed to expand freely, in other words without friction, inside the plastic tube. The technology used measures strains along the length of the fiber core. Hence, to accurately measure temperature change in the soil sample, it is of high importance to decouple the mechanical strains from the thermal strains of the fiber core. As shown in Equation 5.1, the strain of the fiber cable is equal to the sum of mechanical strain and thermal strain. As this test aims at measuring solely temperature, no mechanical strains can be allowed in the fiber core.

$$\varepsilon^{tot} = \varepsilon^M + \varepsilon^T \quad (5.1)$$

After the stabilized quick clay was tamped and the remoulded quick clay had been filled, with the bare fiber placed centrally, the isolation box was closed. Weight was put on top of the lid,

to ensure a sufficiently airtight curing condition. The weight which was put on top of the lid is a cylinder made of a rigid polymer material. This cylinder is designed with a slot to guide the fiber core safely out of the box, without the fiber braking. This feature of the cylinder is very important, as the bare fiber core is extremely fragile and easy to break.

The final setup of the first temperature test is shown in Figure 5.4.



Figure 5.4: Setup of the the first temperature test.

In the middle of the picture, the closed isolation box with the rigid polymer cylinder can be seen. The soil sample is, as described, stored inside this box. Also, the measurement setup of the test is clearly shown in Figure 5.4. To the left are the measurements from the integrated thermocouples. The thin wires connect the two thermocouples to a switch, which is further connected to a laboratory computer. As can be seen from the picture, there were four thermocouples integrated into the isolation box. However, two of them were defective, hence only number 1 and 3 from the bottom gave valuable measurements. More precisely, thermocouple measurements were conducted about 1 cm above the bottom of the stabilized clay and about 1 cm above the transition from stabilized to unstabilized clay. The positions of the two functional thermocouples are shown in Figure 5.2.

On the right-hand side of Figure 5.4, the measurement setup based on the DFOS-technology is

---

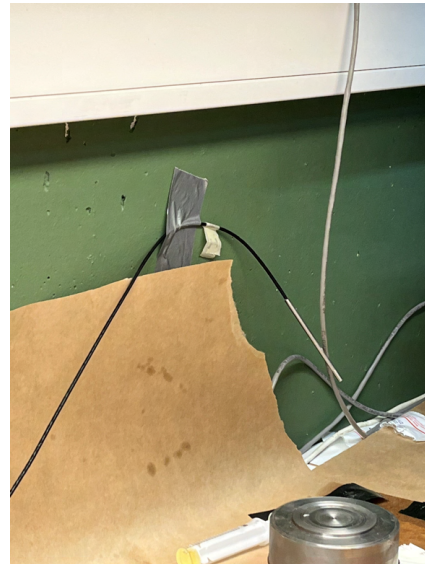


shown. The fiber core was connected to a few different connecting cables, which are the yellow cables that were lying on the table. These cables were further connected to the interrogator. The second laboratory computer was used to control the interrogator and to perform the measurements and calculations by use of a desktop program created for that specific machine. A python-script is utilized to make the measurement process automatic.

Straight after mixing the remoulded quick clay with lime, a reference sample of  $D = 50$  mm and  $H = 100$  mm was tamped. After tamping, a PT100 thermo element was embedded into the sample, and it was wrapped with bubble wrap to ensure insulation for the curing process. The reference sample was made to control the temperature development from the hydration of lime and to be able to compare it to the temperature measured with the thermocouples integrated into the isolation box. The isolated reference sample can be seen in Figure 5.5a. Also, the room temperature was recorded by PT100 elements. Figure 5.5 is showing the setup of these two reference measurements.



(a) Reference sample with PT100



(b) PT100 for room temperature measurement

Figure 5.5: Setup of reference measurements performed simultaneously as temperature tests.

## 5.4 Procedure

In the following section, the procedure is described step by step.

### 5.4.1 Preparations

Quick clay from Tiller-Flotten was pushed out of the sampling cylinder, put in a large bucket, and remoulded by hand. This can be seen in Figure 5.6a. Further on, approximately 1.75 kg

---

was weighed up and put in the steel bowl which belongs to the Kenwood stand mixer that was later on used for the mixing procedure. The bowl was covered with plastic wrap to avoid drying the remoulded quick clay. Also, lime corresponding to  $50 \text{ kg/m}^3$  was weighed up and put in a small plastic box.

The bare fiber was threaded through the plastic tube, and it was led out of the isolation box through a slot. Outside of the box, the tube with the bare fiber inside was taped to the wall of the box. Then, hydraulic oil was filled into the plastic tube. This prepared setup of the fiber core inside the oil-filled plastic tube is clearly shown in Figure 5.3.

Before starting the mixing, the isolation box, which was made up of two parts, was closed with the use of a strap. The OBR interrogator, which is produced by an American company called Luna Innovations, was mechanically aligned and calibrated prior to the mixing and tamping process. This is essential to do before using an interrogator to perform DFOS-measurements. Also, both computers were prepared with their corresponding laboratory programs, so that measurements could be performed immediately after the mixing process was initiated. The plastic cylinder for the reference sample, with its belonging isolation material, was also arranged in advance, and the PT100 elements were mounted in positions free from interference.

#### 5.4.2 Mixing of quick clay

As described in Section 5.4.1, the quick clay was pushed out of the sampling cylinders and remoulded by hand in a large plastic bucket. Further on, enough material to fill one half of the isolation box was weighed up, with some extra margin. The necessary mass of burnt lime corresponding to a binder amount of  $50 \text{ kg/m}^3$  was also weighed up, and then put in an airtight plastic box to avoid some hydration being initiated due to the humidity in the air.

When the mixing process started, efficiency was of the highest importance, as we know that hydration is initiated immediately when the lime reacts with the natural water in the clay. As discussed in Section 2.5.2, the heat generation from the hydration of lime is extremely rapid. Hence, in order to be able to monitor as much heat development as possible in these temperature tests, efficiency is the clue. Thus, all preparations discussed above are crucial.

Before adding lime, the quick clay was remoulded a little further by the Kenwood stand mixer. Then, lime was added, and that was the point where the efficiency had to start. The two components were roughly mixed together by hand using a spatula, to avoid the rotational energy blowing the binder powder up in the air and away from the clay. All of the binder has to be mixed with the clay, and this is especially important for being completely sure about which binder content the final stabilized clay has. After mixing with the spatula, the Kenwood mixer was started again. It was working for 1-2 minutes, with some stops in between to move material that had stuck to the side of the bowl and the mixing tool back to the rest of the material. The total time of the mixing procedure was about 5 minutes.

Two pictures showing some of the important steps of the mixing process described above are shown in Figure 5.6.

---



(a) Bucket of quick clay remoulded by hand



(b) Mixing of quick clay and lime

**Figure 5.6:** Two important steps in the process of performing temperature tests on the Tiller-Flotten clay. Firstly, quick clay remoulded by hand in a bucket, followed by the weighed-up clay and lime which are mixed together.

### 5.4.3 Tamping of stabilized clay and filling of remoulded clay

The samples were built directly in the isolation box. The steps of creating the samples are shown in Figure 5.7.

Firstly, the freshly mixed clay was squeezed by hand to ensure that there were as few air bubbles as possible in the sample. As it is desirable to recreate the real world as much as possible in the laboratory, it is always important to avoid air bubbles when performing laboratory stabilization of soil. There is no air in the soil in situ, as most of the areas that are stabilized are below the groundwater level. In other words, the soil is assumed to be completely saturated ( $S_w = 100\%$ ), and the voids are thus entirely consisting of pore water.

After having squeezed a few small lumps of lime-stabilized quick clay, they were put into the isolation box and tamped by using a tamping stick made of metal. This was done repeatedly until half the height of the box was tamped with stabilized clay. A squeezed lump can be seen in Figure 5.7a and the tamped bottom part of lime-stabilized clay is shown in Figure 5.7b. The tamping stick can be seen in Figure 7.3c. Whilst tamping, one additional person was needed to hold the oil-filled plastic tube with the bare fiber inside. It was important to ensure no damage to the fiber, that it was centrally placed and that clay was packed tightly around it.



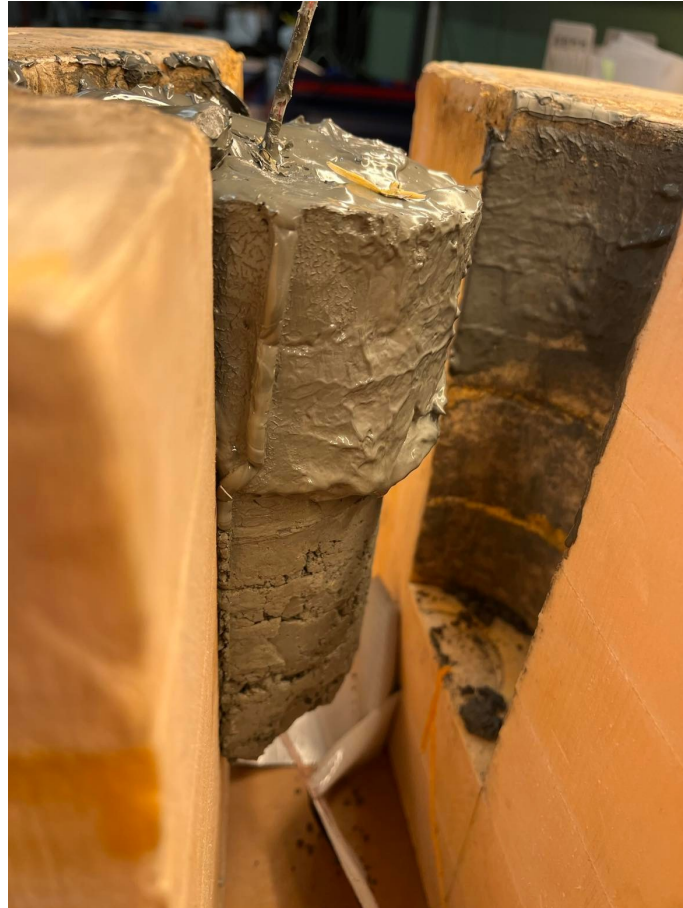
(a) Lumps of stabilized clay      (b) Tamped stabilized clay      (c) Remoulded quick clay

**Figure 5.7:** The process of tamping lime-stabilized clay in the lower half of the isolation box and filling of remoulded quick clay in the upper half.

After the tamping was over, remoulded quick clay was poured by the use of a spoon directly from the bucket in Figure 5.6a. This was a quick process, and following it the lid was put on top of the box, the tube was led out through a slot and weight was put on top. The isolation box topped up with remoulded quick clay, right before it was closed, can be seen in Figure 5.7c.

A very good visualization, by the form of a picture and not a sketch, of the layered sample

is given in Figure 5.8. There, the sample from when the first temperature test was opened is shown.



**Figure 5.8:** The layered soil sample with lime-stabilized quick clay in the bottom and remoulded, unstabilized quick clay in the top.

#### 5.4.4 Reference measurement for DFOS

The fiber optic measurements are relative. This means that a measurement performed by the DFOS-technology is giving a change of the studied parameter relative to a given situation. This given situation has to be defined in a way. Hence, reference measurements are made. These measurements are normal measurements performed with the interrogator and the fiber core, but they act as a starting point or a zero reading. All the following measurements that are performed, are giving results that can be calculated relative to the reference measurements.

For the described temperature experiments, two reference measurements were performed, one before the tamping and one straight after the sample was created and the isolation box was closed. This enabled us to calculate how the temperature changed relative to either the

---

situation before tamping or the situation immediately after tamping.

#### 5.4.5 Measurements

Both the thermocouples and the PT100 elements can be considered as standard temperature sensors in this context. They were connected to a switch, which was further connected to a laboratory computer. These temperature measurements were logged by the use of respectively customized laboratory programs. It was the absolute temperature of the embedded sensors which was logged, and the recording was saved as a text file. Logging with the customized laboratory program is shown on the left computer in Figure 5.4.

The measurements performed by the interrogator and the fiber core are based on light scattering, as described in Section 3.3. See Section 3.3 for a thorough description of the methodology of DFOS-measurements. In short, a light pulse is sent through the fiber core, and the backscattered light is changed due to the outer effect of the temperature change. The backscattered light is analyzed by the interrogator and its corresponding desktop program, and the temperature change along the cable can be determined. As it was temperature change that was measured, it was Distributed Temperature Sensing (DTS) that was applied as the DFOS-measurement technique. The technique was based on Optical Frequency Domain Reflectometry (OFDR) with Rayleigh scattering, and a spatial resolution of 1 cm was utilized.

The physical consequence of the outer effect which is temperature change, is that the fiber core is strained due to the temperature change it is exposed to, and it is actually the strain that is measured. As described above, when referring to Equation 5.1, it is crucial to decouple the mechanical strains from the thermal strains in order to be able to measure purely temperature change.

The strain type caused by temperature change is called thermal strain, and the formula for thermal strain is shown in Equation 5.2.  $\alpha$  is the coefficient of thermal expansion and is a material parameter that is known for the specific fiber core which has been used in this work. As the thermal strain,  $\varepsilon^T$ , is measured and the coefficient of thermal expansion,  $\alpha$ , is known, the temperature change along the length of the fiber core can easily be calculated by using Equation 5.2. Measurements by the OBR were taken every 5 minutes for a few days. However, it is the first hours of the tests which are of interest, as most of the temperature development from lime occurs within hours.

$$\varepsilon^T = \alpha \cdot \Delta T \quad (5.2)$$


---

## Chapter 6

# Cross-sectional temperature test

The cross-sectional temperature test which was mentioned in Chapter 5 will in the following chapter be described.

### 6.1 Purpose

After performing the first test of the temperature experiments that are described thoroughly in Chapter 5, some differences were found between the temperature measurements from the fiber core and the thermocouples. A few degrees difference in the temperature development with time was observed. In addition to the numerical difference, also the shape of the graphs was a little bit different. It seemed as though the temperature development measured by the thermocouples was slightly delayed compared to the measurements conducted with the fiber core.

The two functional thermocouples were compared to the two points along the fiber core that were closest with regard to height in the sample. In other words, the thermocouples and their corresponding points on the bare fiber should have been exposed to the same clay condition. The only difference between the two different measurements when it comes to positioning is the fact that whilst the bare fiber was placed in the middle, with clay at all sides, the thermocouples were placed at the edge of the sample, and integrated into the isolation box.

To summarize, both measurements were taken at the same height of the sample, in the same clay conditions. However, they were not similarly placed in the radial direction. Whilst the bare fiber was placed in the center of the sample, the thermocouples sat at the edge of the sample. Hence, the possibility of differences along the cross-section with regard to heat development had to be studied. Thus, the cross-sectional temperature test that is described in the following was performed to investigate this possibility.

## 6.2 Equipment

For the cross-sectional temperature test, the same equipment as for the temperature tests in Chapter 5 was used. See Section 5.2 for a detailed description of the area of usage for the different equipment. One difference from the other temperature experiment was that the three PT100 thermo elements were not used for measuring room temperature and a reference sample. In this cross-sectional temperature test, the PT100s were placed directly in the sample inside the isolation box. They were placed equally spaced from the middle of the sample and out to the edge at one side.

In addition to the equipment mentioned in Section 5.2, small pellets of isolation styrofoam were used as isolation material. As will be discussed in later sections, the sample in this test was only approximately 70 mm in height. Hence, the rest of the hole in the box had to be filled with isolation to ensure an ideal curing condition. Also, a thin metal pin was used to attach the PT100s in a stable position. The isolation styrofoam pellets used as isolation fill is pictured in Figure 6.1d and the thin metal pin can be seen in the top of the box in Figure 6.1a.

## 6.3 Test setup

The setup of the cross-sectional temperature test is well documented in Figure 6.1.

The sample was, similarly as for the experiment described in Chapter 5, of cylindrical shape and tamped directly in the XPS-box. The dimension and structure of the sample were not exactly the same, though. This sample also had a diameter of  $D = 100$  mm, but the height was only about 70 mm. Also, this sample was made purely of stabilized quick clay, it was not layered as for the other temperature tests. A binder content of  $50 \text{ kg/m}^3$  with lime as the binder was used also for this test. Figure 6.1c is showing the cylinder of stabilized clay, with both PT100s and the fiber core embedded inside it.

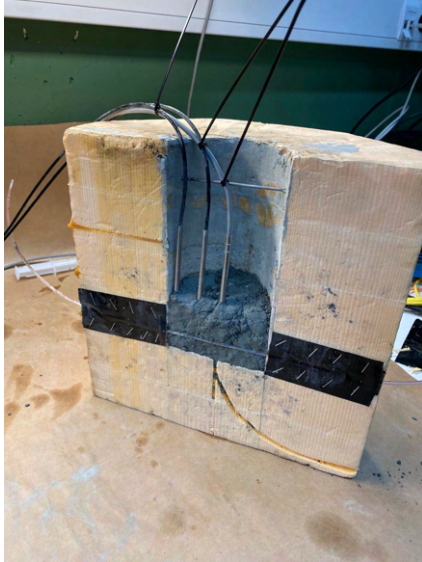
As the aim of this experiment was to examine the temperature development along the cross-section of the sample, there was no need to have a layer of unstabilized clay. It was sufficient to have the heat-generating, stabilized soil to study this phenomenon. The reason for the sample being only 70 mm in height was that this was all the remaining material available, without pushing out a whole new sampling cylinder. The only thing that was important for the height of the sample, was that there was enough clay for embedding the PT100s and the bare fiber, without the two different sensor types interfering with each other.  $H = 70$  mm was enough to ensure this.

To be able to measure the cross-sectional temperature development, the fiber core in this test setup was passed across the sample. In other words, the fiber core was lying horizontally, not vertically, when the isolation box was upright. It was positioned about 1 cm above the bottom of the box. Equally, as for the other temperature experiment, the bare fiber was protected inside an oil-filled plastic tube. The tube with the fiber inside was led out of the box at each

---



side through thin slots and fixed to the corresponding outside walls.



(a) Setup of half of the box



(b) Close-up of sensor positions



(c) Whole sample after opening of box



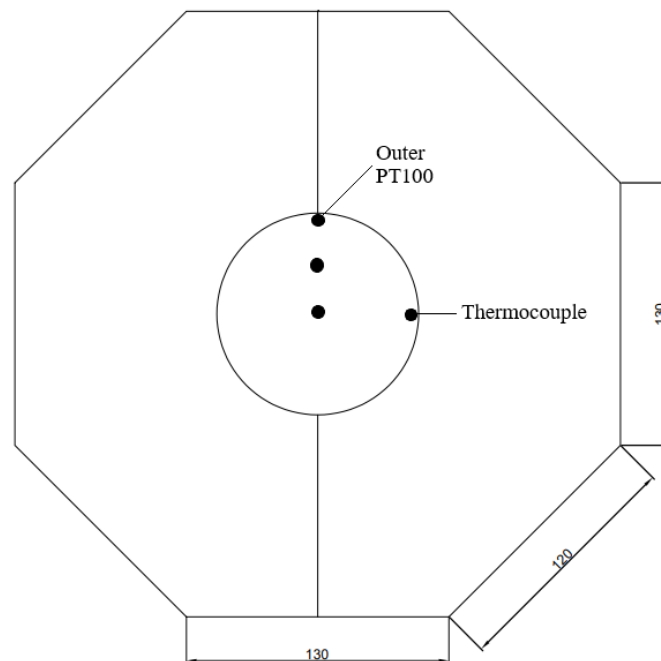
(d) Closed box filled with styrofoam pellets

**Figure 6.1:** The setup of the cross-sectional temperature test, including the position of the PT100s, the position of the fiber core and the closed box filled with isolation styrofoam pellets.

As described briefly earlier, the PT100 thermo elements were positioned from the middle to the edge of the sample, with equal spacing. It was only the tip of the elements that was buried in the lime-stabilized clay, and the tips were located slightly above the horizontal fiber core. The different sensor types were not in contact with each other, to avoid any temperature meas-

urements being affected by interference with other materials than the studied lime-stabilized clay. To ensure that the three PT100s maintained a stable position throughout the test, they were attached to the metal pin that had been inserted across the box for this purpose. This attachment solution can be seen in Figure 6.1a.

A point that is important to make, is that the PT100 element located at the edge of the sample is not at the same position as the thermocouples. The PT100s are distributed radially from the center of the sample, in the direction of  $90^\circ$  to the line from the center to the position of the thermocouples. More precisely, the outer PT100 thermo element in this cross-sectional temperature test is located right next to the contact surface between the two parts of the box. Whilst on the other hand, the position of the thermocouples lies halfway along the semicircle of one part of the box. In section 1-1, which is shown in drawing no. 2 in Appendix A, the cross-section of the two box parts put together can be seen. This drawing is a good starting point for visualizing the position of the two different sensor types. A cutout of the drawing, together with markers indicating the positions of the sensors, is shown in Figure 6.2.



**Figure 6.2:** A schematic drawing illustrating the position of the PT100 thermo elements and the thermocouple in the cross-section of the box.

The actual execution of the temperature measurements was done in the exact same way as for the experiment described in Chapter 5, with switches, connecting cables, laboratory computers and desktop programs.

---

## 6.4 Procedure

In the following, the procedure is described step by step. A lot is similar to what is done in the experiment from Chapter 5, but any differences will be highlighted below.

### 6.4.1 Preparations

The preparations for this cross-sectional temperature test were much the same as the ones presented in Section 5.4.1. However, some preparations were unique for the test described in this chapter, and they will be discussed now.

The plastic tube with the bare fiber inside was threaded horizontally through the box, opposite from the other temperature experiment where it was led vertically through the box. It was put in thin slots, and fastened using tape that was stapled to the box. At the outside of the box, the plastic tube was mounted to the walls of the box and filled with hydraulic oil.

Unlike the other temperature experiment, the box was not closed before tamping in this test. The box was split in two, and at the same half as the fiber core was connected to, a metal pin was inserted in the top as a support for the PT100 elements. The cables of the three PT100s were fixed with strips to the metal pin. This was done, as mentioned above, to ensure stable positioning of the thermo elements.

### 6.4.2 Mixing of quick clay

The amount of material, both clay and lime, was not the same as for the other temperature tests. However, the mixing procedure was exactly the same as described in Section 5.4.2.

### 6.4.3 Tamping of stabilized clay

As explained in Section 6.4.1, the isolation box was open during tamping. The process of tamping was a little different in the cross-sectional test compared to the other temperature tests. As a sensitive fiber core, inside a plastic tube, was lying across the box, it was essential to be careful not to damage it. Hence, most of the tamping in the box half in question was performed by hand. The use of hands for tamping was also important to ensure the satisfactory embedment of the three PT100 elements. The tamped clay half-cylinder, with the different temperature sensors, can be seen clearly in Figure 6.1a and 6.1b. The other half of the box was tamped in the same dimensions, and lastly, the two box halves with lime-stabilized clay were put together, and the box was locked. The strap surrounding the box was tightened, styrofoam pellets were filled into the box, the lid was put on and weight was placed on top.

---

#### **6.4.4 Reference measurement**

Reference measurement by the use of the OBR-interrogator and the bare fiber core was performed in the same way as discussed in Section 5.4.4.

#### **6.4.5 Measurements**

The measurements with both the thermocouple, the PT100s and the bare fiber were carried out in the exact same manner as described in Section 5.4.5. DTS, using DFOS and Rayleigh scattering, with a spatial resolution of 1 cm was utilized also here.

---

# Chapter 7

## Strain tests

Also three strain tests have been carried out during the work with this M.Sc. Thesis. Unconfined compression tests of samples with a centrally embedded fiber cable were conducted. These tests were performed to examine whether it is possible to reliably monitor strains in lime/cement-stabilized quick clay by the use of Distributed Fiber Optic Sensing. All three tests were carried out during the spring of 2023. The first test was performed in week 12, whilst the last two were carried out in week 16.

### 7.1 Purpose

As already explained in Chapter 5, the aim of using DFOS for stabilized soil is to monitor the achieved integrity. Strength and stiffness are key parameters when talking about the integrity of stabilized soil. To be able to know about these two parameters of LC-columns, it is essential to manage to follow the strain development. By following the strain that develops in LC-columns it is possible to calculate settlements with high precision, but also early warnings of failures can be given.

Hence, the purpose of this test is to examine whether we are able to reliably monitor the strain in LC-stabilized quick clay during loading by the use of a fiber optic cable. The stabilized samples were compressed slowly but surely by the use of a uniaxial device. Later on, the strain calculated from the deformation related to the movement of the piston was compared to the strain changes along the sample measured with the fiber cable. The aim was to verify the performance of the chosen fiber optic cable with regard to strain monitoring.

### 7.2 Equipment

For the strain tests, the following equipment has been used:

- Plastic bucket
- Kenwood stand mixer
- Laboratory weights
- Spatula
- Tamping stick made of metal
- Plastic cylinders for tamping
- EpsilonSensor fiber optic cable for strain sensing produced by Nerve-Sensors
- Two rigid plastic blocks for carrying out the cable and load transfer
- Rigid plastic block for push-out of the samples
- Luna OBR interrogator
- Uniaxial testing device
- Laboratory computer for fiber optic measurements
- Laboratory computer for uniaxial measurements

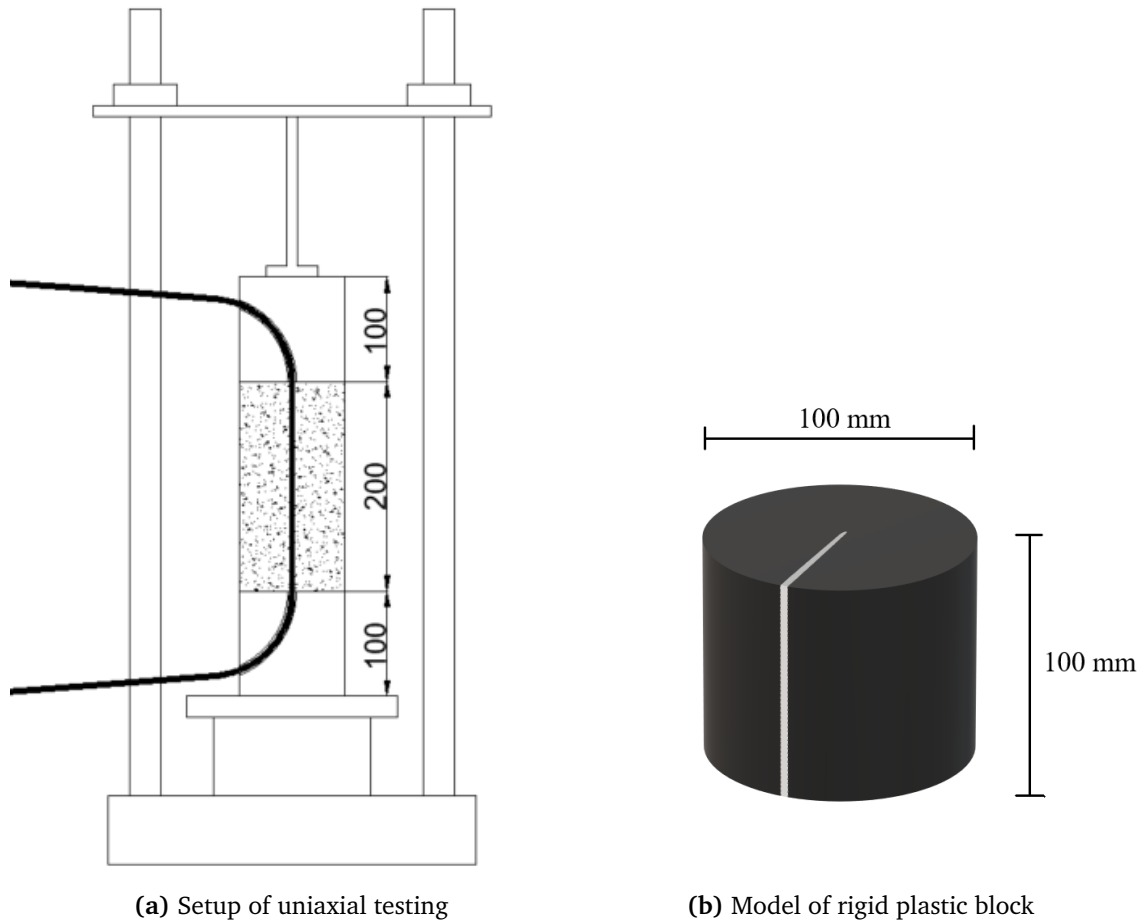
Equally as for the sample creation for the temperature tests, some standard laboratory stabilization equipment was used for the preparation of the strain samples. The use of the plastic bucket, laboratory weights, spatula, tamping stick and the Kenwood stand mixer was the same as what is described for the temperature tests in Section 5.2. However, for this test, the samples have not been tamped and cured inside the XPS-box.

The strain samples were tamped in a similar manner as what is the standard procedure for stabilized quick clay samples in Norway, i.e. in a hollow and open plastic cylinder. However, whilst a diameter of  $D = 50$  mm and a height of  $H = 100$  mm are the normal dimensions of laboratory-stabilized samples, these samples had a diameter of  $D = 100$  mm and a height of  $H = 200$  mm. In other words, the samples were made, relatively, very large. This was done to try to avoid any negative effects on the integrity of having a cable in the middle of the sample and to ensure enough bonding between the cured material and the fiber optic cable.

EpsilonSensor, from the Polish company Nerve-Sensors, was used as the fiber optic cable for strain monitoring. This cable has a monolithic section that ensures very accurate measurements, as the strain exposing the outside of the cable is directly transferred to the fiber optic core. EpsilonSensor is suitable for laboratory testing due to its easy handling, and the outer part of the cable is designed to give adhesion.

Fiber optic cables are sensitive. To avoid breakage, the cables have to be guided carefully away from the compressive pistons. The minimum bending radius is an important parameter for the health of fiber cables, and for the EpsilonSensor this parameter is approximately 50 mm. To handle this challenge, two rigid, cylindrical blocks made of polymer were produced. The blocks were approximate of diameter  $D = 100$  mm and height  $H = 100$  mm, and designed with a slot from the center and out to the edge along its whole height. A 3D model of the rigid plastic blocks is shown in Figure 7.1b where the design of the slot is visualized clearly. These rigid plastic blocks are the same as the plastic cylinder used for guiding the bare fiber core safely out of the isolation box during the temperature tests, as described in Section 5.3.

---



**Figure 7.1:** A schematic drawing illustrating the setup of the unconfined compression testing of the lime/cement-stabilized strain samples. Also, a model of the rigid plastic blocks is included.

The samples were placed on top of one block and had the other block above them during unconfined compression testing. Thus, load was transferred from the uniaxial device to the strain samples with the help of the two rigid plastic blocks, without the cable braking. A schematic drawing of the setup of the strain testing is given in Figure 7.1a, and the mentioned function of the plastic blocks can be clearly observed. The fiber cable was safely guided away from the compressive pistons, with a tolerable bending radius, through the slots in the plastic blocks. A similar, but smaller, rigid plastic block was produced and utilized to enable safe push-out of the cured sample from the plastic cylinder.

For compressing the LC-stabilized samples a large uniaxial device, with a solid load cell, was utilized. Actually, it was a rebuilt triaxial device. The size of the machine was important both because the samples together with the two plastic blocks took up a lot of space and because more force is needed to bring these large samples to failure. Despite this uniaxial device being slightly different from other types of uniaxial devices, the operation of the machine was similar to the others. After reaching full contact with the soil sample, a piston was compressing the

sample, and both deformation and force from the piston were recorded. Figure 7.1a is a simple sketch of the rebuilt triaxial device.

Also for these measurements, a laboratory computer had to be used to perform the DFOS-measurements. In addition, another laboratory computer was needed to record the uniaxial measurements.

The sketches of both the uniaxial testing setup and the rigid plastic block with a slot are shown in Appendix B as well.

### 7.3 Test setup

Much of the test setup has already been discussed in Section 7.2, however, it will still be fully presented in the following. Figure 7.2 is showing the setup of the strain testing procedure. The uniaxial device with the rigid plastic blocks, a strain sample and the embedded fiber cable which is bent out from the blocks can be seen. The upper part of the EpsilonSensor cable hangs freely, whilst the lower part is connected to the interrogator outside the right edge of the picture.

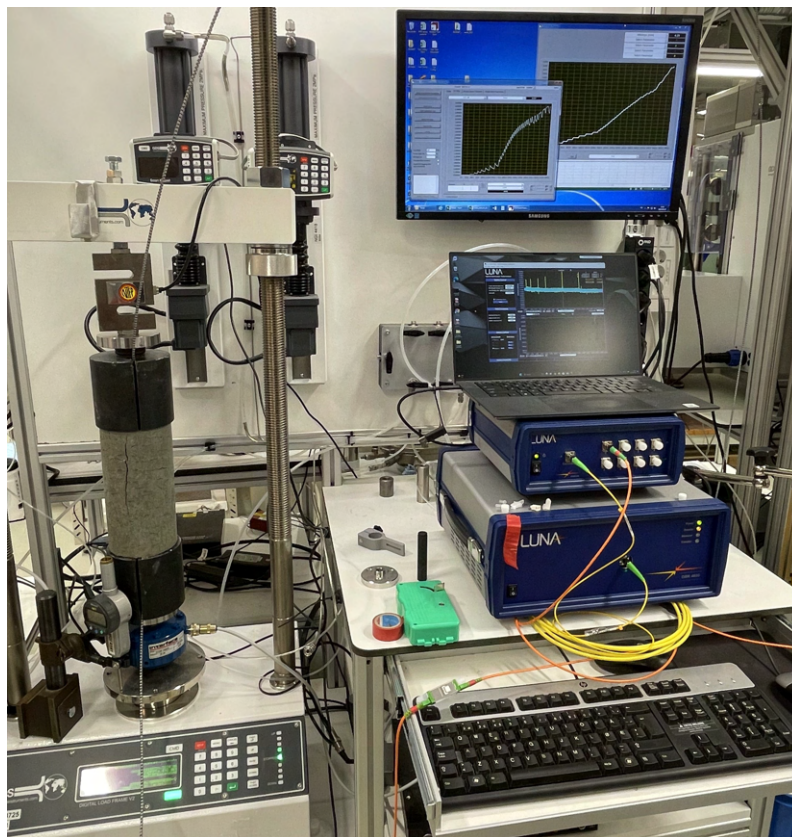


Figure 7.2: The setup of the strain testing procedure.

---



The three soil samples were, equally as for the temperature tests, of cylindrical shape with a diameter of  $D = 100$  mm and a height of  $H = 200$  mm. They were all stabilized with a binder content of  $50 \text{ kg/m}^3$ , where 50% was burnt lime whilst the other 50% was ordinary Portland cement. The choice of binder content was based on easy handling. It is known that the Tiller-Flotten quick clay becomes dry and lumpy when it is stabilized, and previous experiences at NGI have shown that the Kenwood is struggling when using higher binder contents.

The reason for choosing both lime and cement, by an equal amount, is that this is what is mostly used for soil stabilization in Scandinavia. This is also representative of the binder compositions that will be used in future field tests that will be carried out as a part of the GOAL-project. The EpsilonSensor was embedded in the center of the strain samples during tamping. Stabilized clay was tightly packed around it, and the samples were cured for 19-27 days. The samples were wrapped in plastic also during the testing, to ensure that no drying of the samples occurred.

As described in Section 7.2, and also shown in Figure 7.2, the samples were placed upon one of the rigid plastic blocks and had the other one above them during compression from the uniaxial device. This was done to transfer the load to the samples, and at the same time ensure that the cable was routed away safely. The piston of the uniaxial device was moving steadily upwards, and both deformation and force were recorded.

Instead of performing dynamic monitoring of the strain development in the samples, static measurements were conducted. The piston was moved a chosen distance with a given speed before it was stopped and DFOS-measurements were performed. This procedure was carried out until failure was reached for the LC-samples. For the first sample, the distance of movement was 0.25 mm for the two first OBR-scans, before it was ramped up to 0.4 mm. For the two last samples, the corresponding distance was 0.1 mm between all scans, before failure was initiated. Then the steps were ramped up to 0.4 mm until full failure had developed.

Measurements during this experiment are, as mentioned in Section 7.2, performed with two laboratory computers. One computer is connected to the uniaxial device through a LabVIEW desktop program and is measuring deformation and force from the compression machine. The other one is connected to the interrogator through the OBR desktop program and is calculating the DFOS-measurements.

The setup of the measurement devices can be seen on the right side of Figure 7.2. In the lower part, the OBR interrogator including its corresponding switch is shown. Upon the switch, a laboratory computer with a DFOS-scan can be seen. At the top of the picture, there is a laboratory computer with uniaxial-measurements, more precisely force vs. elapsed time to the left and deformation vs. elapsed time at the right-hand side. Also the cables connecting the fiber cable to the interrogator can be observed from the picture.

---

## 7.4 Procedure

In the following section, the procedure is described step by step.

### 7.4.1 Preparations

With regard to sample preparation, much was same as for the preparations for the temperature tests described in Section 5.4.1. However, for the strain samples about 3.5 kg of clay was used, as the amount of stabilized clay was double so high in this test, compared to the temperature tests. Also, both lime and cement were used this time. The binders were weighed and sealed in plastic boxes separately.

As the dimensions and setup of this test were not standard, some equipment had to be produced beforehand. Hollow plastic cylinders of inner diameter  $D = 100$  mm and height  $H = 200$  mm were cut from a plastic tube. Also, the solid plastic blocks were cut, and a slit was made into them. All this production of additional equipment was performed at the NGI workshop.

For the execution of the unconfined compression testing, the interrogator was mechanically aligned and calibrated. Both laboratory computers were prepared with their corresponding laboratory programs. The strain samples were pushed out of their respective plastic cylinders using a standard push-out machine. But, it was done with the help of the small plastic block to ensure no breakage of the EpsilonSensor fiber cable. Further on, the samples were positioned upon one plastic block, the other block was put on top and the piston was moved upwards until full contact was achieved in the system. Then the deformation and force of the recordings were reset, and the test setup was ready.

### 7.4.2 Mixing of quick clay

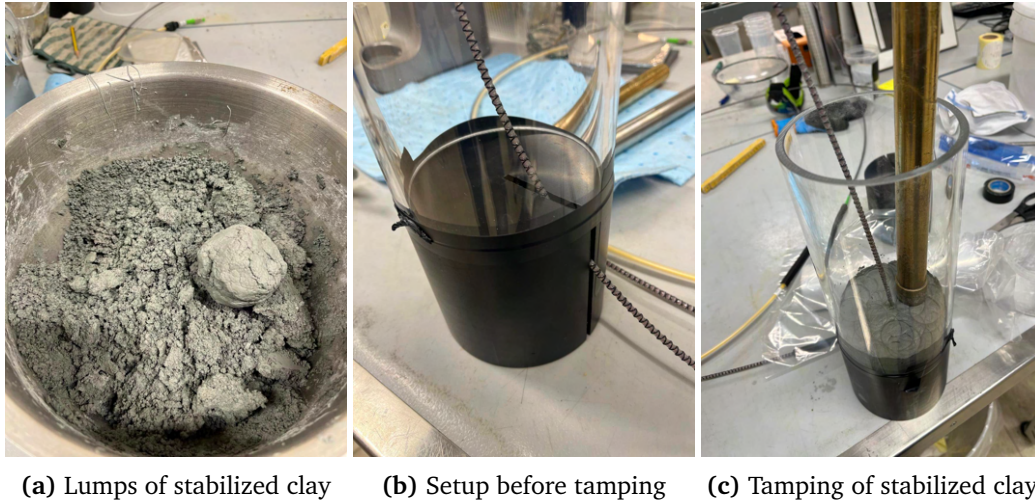
The mixing of the LC-samples was performed in the exact same manner as for the lime-stabilized samples for the temperature tests, which has been described in detail in Section 5.4.2. But, as already mentioned, the strain samples were made with a binder content of  $50 \text{ kg/m}^3$ , with an equal amount of lime and cement. Time was not wasted during the preparation of these samples, however, the need for efficiency was not as precarious during this preparation as no heat development was to be monitored.

### 7.4.3 Tamping of strain samples

The tamping procedure was of high importance for the quality of the strain tests. Unlike the temperature samples, where bond was not important as only thermal strains were to be measured, good bonding was crucial for getting any interesting results from the uniaxial testing. During the compression testing, it was the mechanical strains of the fiber optic cable that was

---

examined. In order to transfer the load, and thus also the strains, from the LC-samples to the fiber cable, the bond between the stabilized soil and the cable had to be very high. A figure illustrating the tamping process is given in Figure 7.3.



**Figure 7.3:** The process of tamping lime/cement-stabilized clay samples that is to be used for unconfined compression tests.

Before tamping, the plastic cylinder was taped to one of the solid plastic blocks, and the fiber cable was passed through the cylinder and guided out of the bottom through the slot. This prepared setup is shown in Figure 7.3b. Further on, when the quick clay had been mixed with lime and cement, the material was squeezed by hand to remove air. Squeezed lumps of lime/cement-stabilized quick clay can be seen in the steel bowl in Figure 7.3a.

A few lumps at a time were put into the taped cylinder-block setup and tamped by the use of the tamping stick shown in Figure 7.3c. The lumps were compacted into thin layers, and as far as possible, a hand was also used to press the clay tightly against the cable for each layer. This squeezing of clay lumps and compaction into thin layers was repeated until the whole cylinder was filled slightly above its top with compacted lime/cement-stabilized quick clay. A spatula was used to cut the transcending clay and to smoothen the top surface. Lastly, the samples were wrapped in plastic on both top and bottom, and further put in a safe place to cure.

The tamping of the strain samples was difficult, and it was challenging to provide enough bonding between the stabilized material and the fiber cable. As already mentioned a few times, the Tiller-Flotten quick clay gets very dry rapidly when being stabilized, and it gets difficult to work with it. The dry and lumpy material can be clearly seen in Figure 7.3a. The difficult handling resulted in a lot of small cracks in the samples. Due to the large dimensions of the samples, the need for good bond and the dry material, the tamping of a single sample took approximately one hour. However, despite a challenging procedure, adhesion between the stabilized soil and the fiber optic cable was achieved for all three strain samples.

After the samples had been tamped, plastic was wrapped around them at the top and bottom, and they were left in a quiet area to cure at room temperature ( $\sim 20^{\circ}\text{C}$ ).

#### 7.4.4 Reference measurement

Equally, as for the temperature measurements, a reference measurement had to be performed before the unconfined compression tests could be initiated. A zero reading was taken just before the deformation of the samples started. All measurements following this one were given the change of strain along the sample relative to the reference measurement scan.

#### 7.4.5 Measurements

The measurements performed by the interrogator and the fiber cable were, as discussed in the theory part, based on light scattering. For this test, the outer effect was the deformation of the surrounding lime/cement-stabilized quick clay sample. The physical consequence was that the sample was compressing (axially) the fiber cable mechanically due to the bond stress between the sample and the cable. As it was the strain that was examined for this test, the measuring technique that was utilized was Distributed Strain Sensing (DSS). A spatial resolution of 1 cm was applied for the calculations. As discussed previously, there can be two main contributors to the strain of the fiber core, more precisely a thermal contribution and a mechanical contribution. These two contributions are presented in Equation 5.1.

For the temperature measurements, the strain contributions had to be decoupled. For the strain measurements, however, this was not necessary to do because of the test setup. The tests were carried out over such a short span of time that there was no thermal strain exposing the fiber core. The strain that was measured was the real, mechanical strain that the fiber cable was experiencing. For compression tests over longer timespans, for instance, as a part of in situ testing, there has to be a temperature compensation to decouple any thermal strain from the mechanical strain.

Figure 7.4, which is a cropped version of Figure 7.2, is showing the setup of the measurement programs used for the strain testing. On the portable laboratory computer, a typical trace of a DFOS-scan can be seen. On the upper screen, the measurements given by the uniaxial device are shown. As already described above, force vs. elapsed time is shown on the left graph, while on the right-hand side deformation vs. elapsed time is plotted.

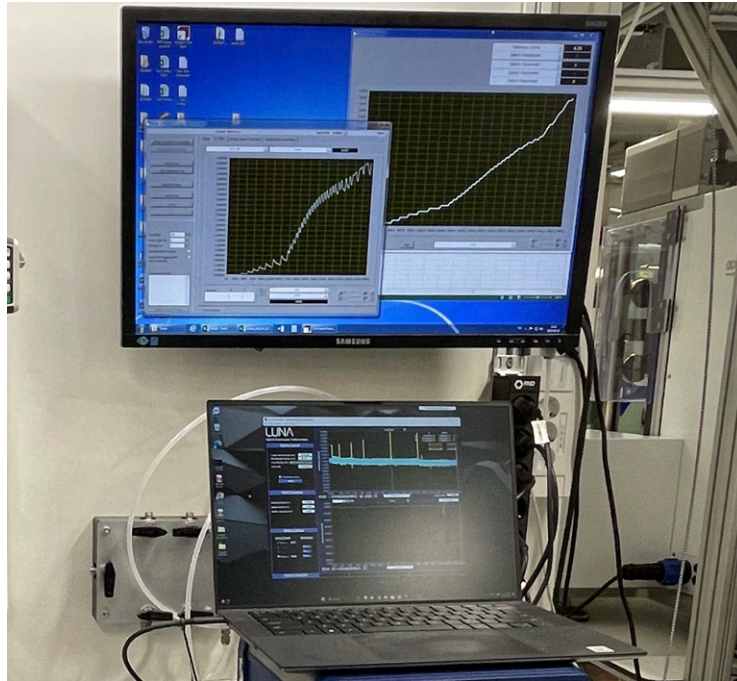
During the unconfined compression test, the loading situation was, as the name suggests, limited to axial only. A load was applied axially on the sample, and no support was given horizontally. The machine was, as explained, recording force and deformation. The axial strain of the sample was calculated by dividing the deformation from the uniaxial device by the original height. This strain can be used to calculate a corrected area for the given strain level, as shown in Equation 7.1 (NTNU 2017). The axial stress that the sample was exposed to was calculated by dividing the force by the corrected cross-sectional area. This is given in

---

Equation 7.2. The ultimate unconfined compression strength of the samples ( $q_u$ ) was given as the maximum axial stress that was calculated. The maximum shear strength ( $c_u$ ) of the samples was given as half the compression strength. As the material of the samples was clay, and the tests were conducted relatively rapidly, the maximum shear stress that was measured for the samples can be considered as an undrained shear strength.

$$A = \frac{A_0}{1 - \varepsilon_a} \quad (7.1)$$

$$\sigma_1 = \frac{F}{A_0} \quad (7.2)$$



**Figure 7.4:** The setup of the measurement devices for strain testing.

The measurements were performed statically, and not dynamically, as already mentioned. An effect of this was that while the deformation was stopped, the load decreased slightly. Hence, the load vs. time curve on the left-hand side of the upper screen has some sort of a saw pattern. By taking a close look at the upper screen in the picture in Figure 7.4 the effect of this measurement method can be observed.

Similarly as for the DTS-measurements during the temperature tests, Optical Frequency Domain Reflectometry (OFDR) with Rayleigh scattering was applied also for the DSS-measurements of strain development. The same technique is used, but the utilized coefficient is different.



## **Part 3 - Results and discussions**





## Chapter 8

# Temperature tests - results

In the following chapter, all relevant results that have been produced during the temperature testing will be presented. Firstly, a close look is taken at the DFOS-measurements along the entire height of the sample in the first few hours. Further on, temperature change with time is presented for some different OBR-points. By "OBR-point", it is referred to a measurement point along the length of the fiber cable inside the soil sample. Some of the OBR-points are lastly compared to corresponding reference measurements, conducted by both the integrated thermocouples and the PT100 thermo element embedded in a reference sample.

### 8.1 DFOS-scans along entire sample height

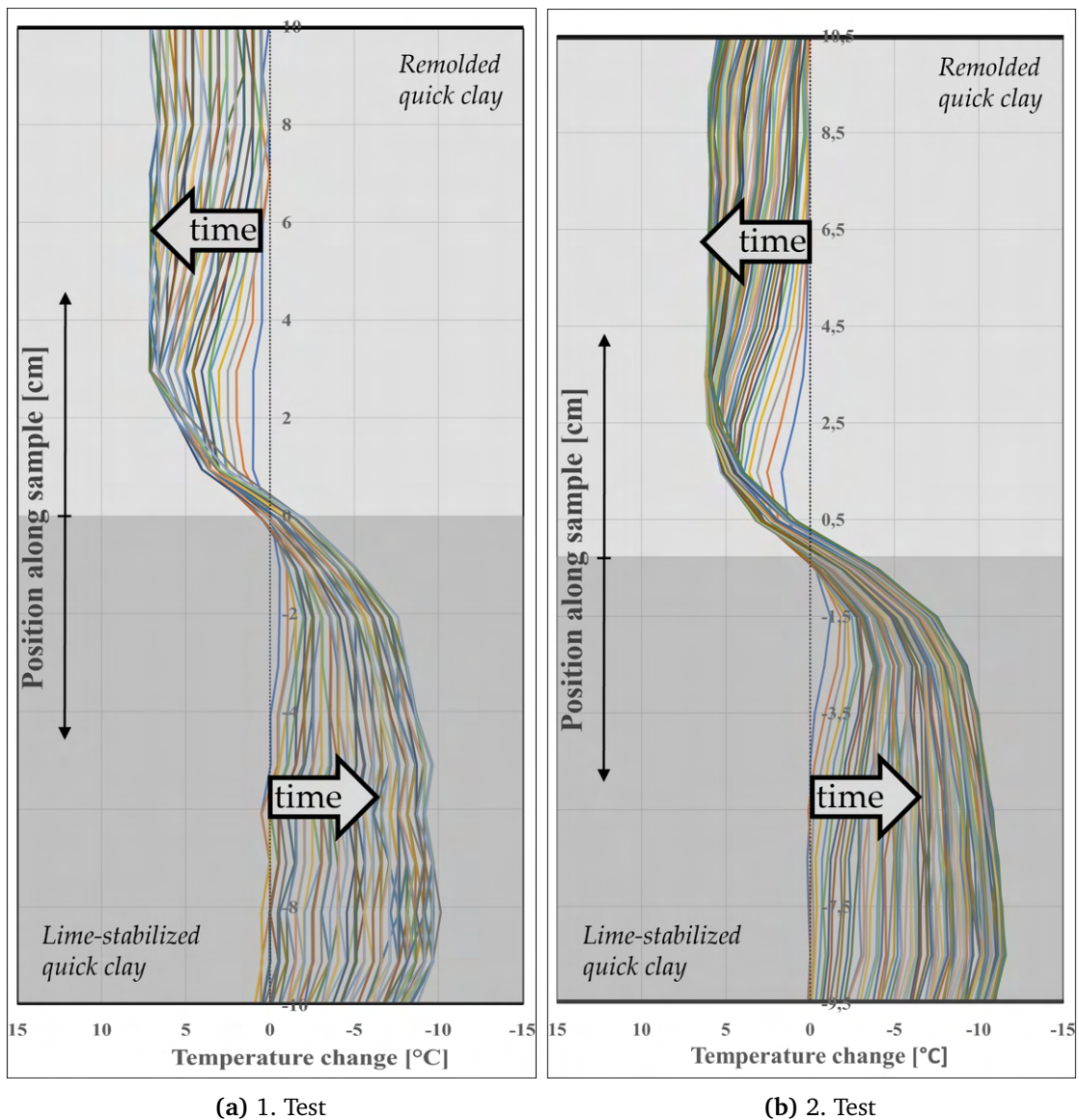
#### 8.1.1 All DFOS-scans in the first 8.5 hours

In the following, relevant plots of the temperature change at each of the mentioned OBR-points will be shown for both temperature tests. Data from several days of recording are available. However, the temperature development related to heating from the hydration of lime is happening in the first hours. Hence, only the first 8.5 hours have been included in the DFOS-scans presented below.

Plots of all DFOS-scans in the first 8.5 hours of both tests are shown in Figure 8.1. The figure is showing the temperature change along the height of the samples. For both samples, the point at which the material is changing from lime-stabilized quick clay to remoulded quick clay is defined as origo. Further on, the negative values on the y-axis is indicating the position from the transition in the stabilized part. On the contrary, the positive values are showing the position from the transition zone in the unstabilized part. The unit of the positions shown on the y-axis is cm.

From Figure 8.1, the temperature is seen to drop in the stabilized part and increase in the unstabilized part. The process of mixing clay and lime, tamping the material and pouring

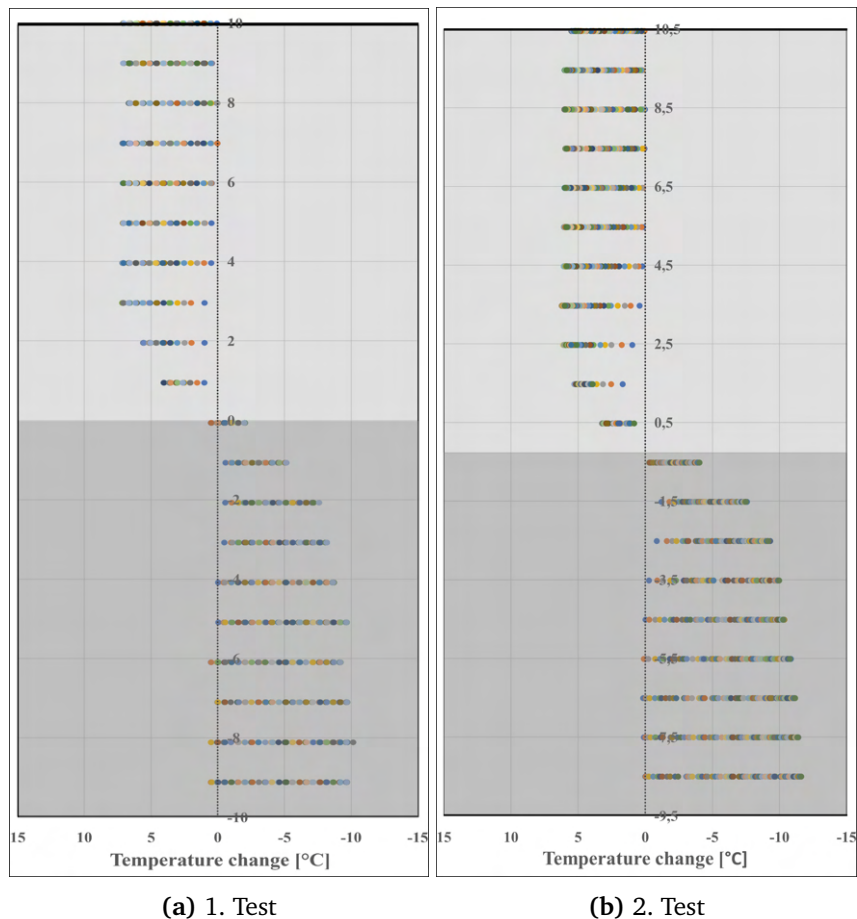
remoulded quick clay took approximately 20-30 minutes. In other words, more or less all heat generation due to the hydration of the lime was finished when the isolation box was closed and measurements could take place. Hence, when the measurements with the OBR were initiated, the temperature of the stabilized soil would drop from the reference measurement with time. Subsequently, as the heat was transferred from the stabilized to the unstabilized soil, the temperature was increasing relative to the reference measurement with time in the unstabilized part.



**Figure 8.1:** Plots of all DFOS-scans (i.e. every 5 minutes) in the first 8.5 hours of the two temperature tests. Each temperature profile shows the temperature change with respect to the reference measurement.

An important point that has to be explained, is the discrepancy between the y-values of the two plots. Whilst the plot of the first test has  $y \in [-10, 10]$ , the second test has  $y \in [-9.5, 10.5]$ . This has the simple explanation that, for the second temperature test, the tamping of lime-stabilized part was stopped 0.5 cm before half the height of the isolation box was reached. Thus, the second temperature sample consisted of 9.5 cm of stabilized clay and 10.5 cm of unstabilized clay. The first sample had the originally intended dimensions, in other words, 10 cm of both stabilized clay and unstabilized clay.

More detailed plots including legends can be found in Appendix C. It can be observed, as already indicated, that the temperature in the lime-stabilized part was dropping with time. In contrast, the temperature in the unstabilized part was increasing with time. This was a result of the heat transfer from the stabilized part to the unstabilized part. The time of reference measurement for the first temperature test was 15:16 and for the second test, the reference measurement was conducted at 18:04.



**Figure 8.2:** Scatter plots of all DFOS-scans (i.e. every 5 minutes) in the first 8.5 hours of the two temperature tests. The spatial resolution of the DFOS-measurements is clearly shown.

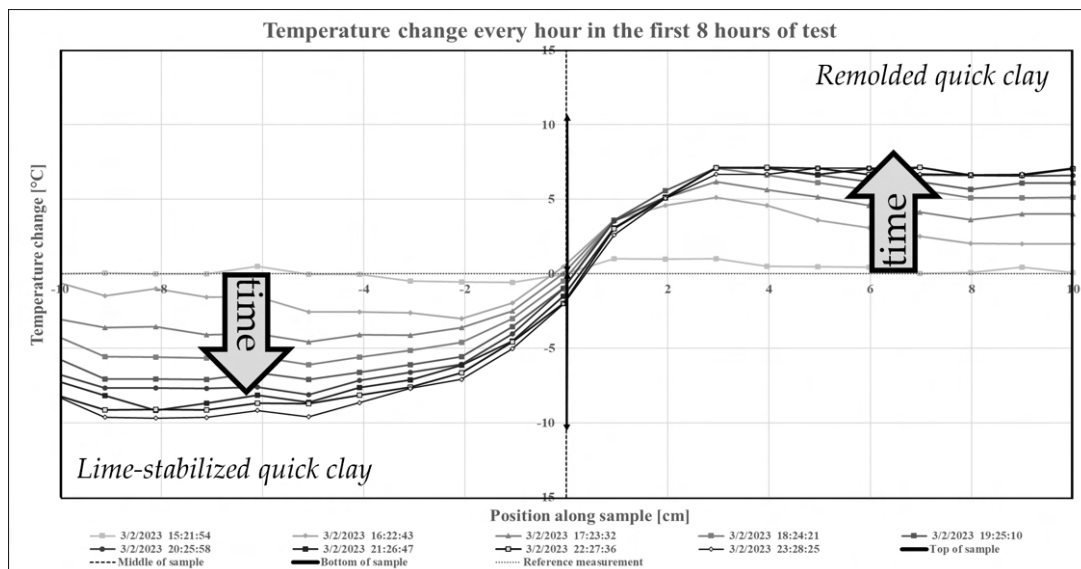
Figure 8.2 is showing the same measurements as in Figure 8.1, except in this figure the results are presented as a scatter plot. In other words, only the actual measured data points are plotted, without any linear interpolation between the points. Hence, it does not appear as a completely continuous measurement, which it is not. The essence of including Figure 8.2 is to visualize the chosen spatial resolution. It can be clearly seen from the figure that there is a datapoint for each cm, i.e. the spatial resolution of 1 cm is verified.

The results shown for the two temperature tests follow the same trends. The temperature dropped approximately 10°C in the lime-stabilized part. By contrast, the temperature increased by about 7°C in the remoulded quick clay. There are some minor differences between the two tests with regard to the temperature rise in the unstabilized parts and the temperature decrease in the unstabilized parts. However, the temperature differences between the two parts of the samples, in addition to the shapes of the plots, are very similar for the two plots. The minor differences are probably a result of reference measurements taken at different times in the hydration process.

### 8.1.2 One DFOS-scan per hour the first 8 hours

In the following, plots including one scan per hour of the first 8 hours of the temperature tests are presented. The decreased density of graphs makes it easier to see the trend with time in the first 8.5 hours of the tests. In these Figures, the labels are included.

The 9 DFOS-measurements showing the first measurement in addition to one measurement per each of the 8 subsequent hours of the first temperature test are shown in Figure 8.3.

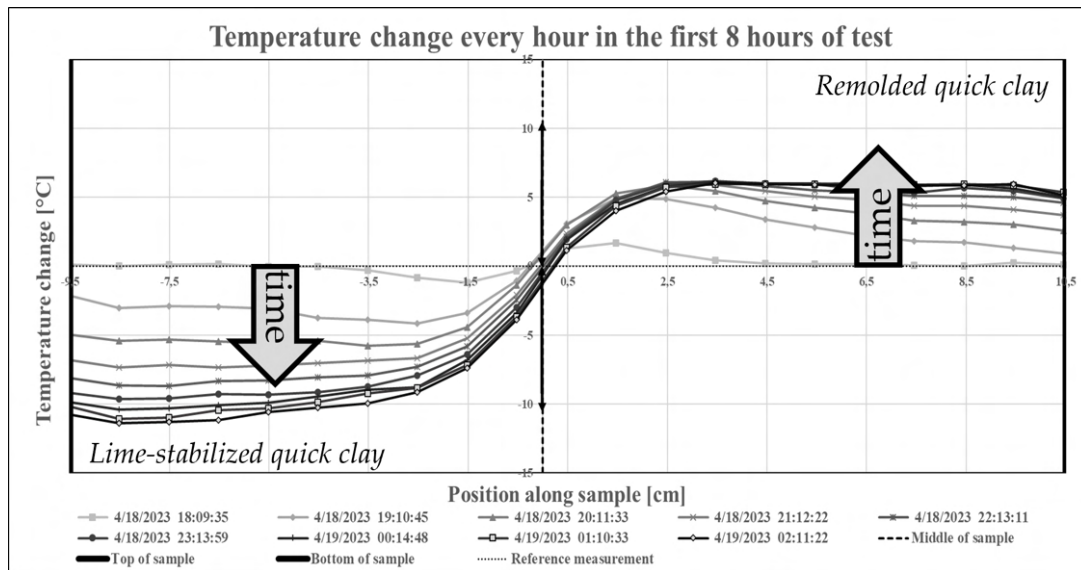


**Figure 8.3:** One scan per hour of temperature change along the height of the first temperature sample in the first 8 hours of the test. Reference measurement conducted 15:16.

The left-hand side of Figure 8.3, which shows the temperature development within the stabilized part of the specimen, indicates a notable temperature reduction (i.e.,  $\sim 10^{\circ}\text{C}$ ) within the first eight hours after the reference measurement. From this plot, it can be seen that the temperature reduction was almost constant between  $x = -10\text{ cm}$  to  $x = -5\text{ cm}$ . Between  $x = -5\text{ cm}$  to  $x = 0\text{ cm}$ , the temperature change is reduced which can be related to the heat transfer to the unstabilized part of the sample. By contrast, the opposite trend was observed in the remoulded clay part of the specimen. From  $x = 0\text{ cm}$  to  $x = 3\text{ cm}$ , the temperature change increased with distance from the interface between the stabilized and remoulded clay. For  $x > 3\text{ cm}$ , a minor decrease in the temperature change becomes evident. After 4 hours, the temperature change became almost constant between  $x = 3\text{ cm}$  to  $x = 10\text{ cm}$ .

What also can be seen from Figure 8.3, is that the temperature change rate was highest in the first hours of the test. This yielded both the stabilized part and the unstabilized part. The temperature change was biggest in the first hour before it decreased slightly from hour to hour in the first four hours of the test. This phenomenon can be observed from the fact that the plots for each hour get closer to the previous plot with time. After the first four hours as discussed above, there were minimal temperature changes with time.

Equally as for the first temperature test, the temperature changes along the height of the sample in the first 8 hours, with one scan per hour, are shown in Figure 8.4.



**Figure 8.4:** One scan per hour of temperature change along the height of the second temperature sample in the first 8 hours of the test. Reference measurement conducted 18:04.

Also from Figure 8.4, the temperature trend discussed for the first temperature test can be clearly seen. The bottom 5 cm are more or less constant with regard to temperature change, between  $x = -5\text{ cm}$  and  $x = 3\text{ cm}$  there were considerable changes to the derivative of the temperature changes. More precisely, the temperature changes decreased from  $x = -5\text{ cm}$  to-

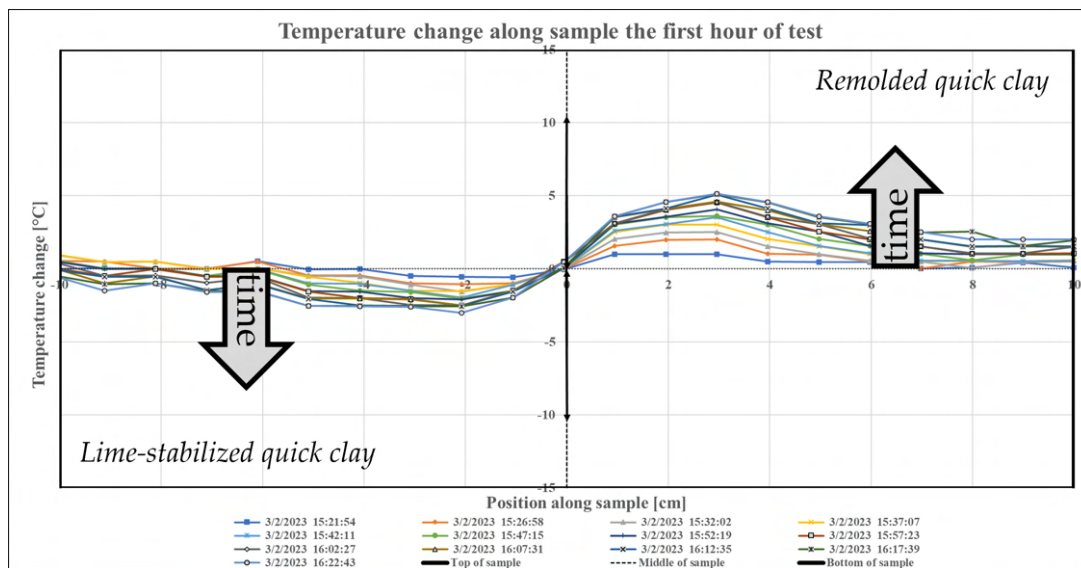
wards origo, and from origo to  $x = 3$  cm the temperature changes increased. From  $x > 3$  cm a minor decrease in temperature change is seen, but this inclination was more or less flattened out after about 4 hours. This is very similar to what was seen in Figure 8.3.

The results with regard to temperature change with time along the height of the sample are very consistent between the two tests. The maximum temperature decrease was about  $10^{\circ}\text{C}$  for both tests. Similarly, the maximum temperature increase was around  $6-7^{\circ}\text{C}$  in both tests. The temperature change rate was highest at the beginning of the tests and decreased steadily in the first four hours. After this, the temperature profiles are more or less constant in both parts of the two samples.

### 8.1.3 All DFOS-scans in the first hour

In this section, all scans taken by the OBR in the first hour of both tests will be presented. This enables the possibility to observe how the temperature spreads in the short term, immediately after the stabilized soil had reached its peak temperature. The first period of temperature development is very important, as the hydration of lime is a relatively rapid chemical reaction.

The first hour of the temperature development in the primary temperature sample is plotted in Figure 8.5.



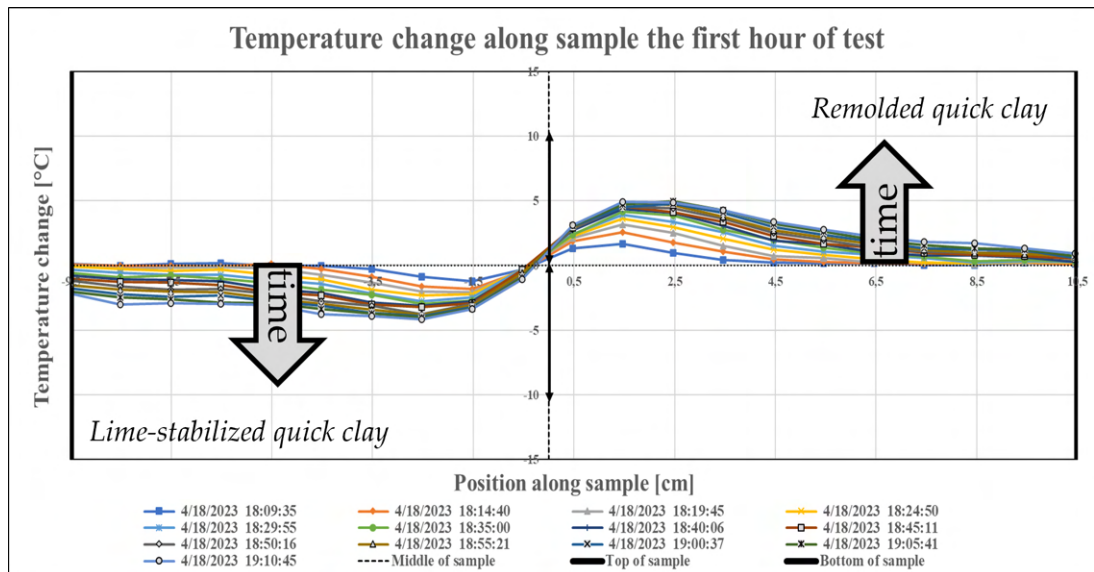
**Figure 8.5:** All scans of temperature change along the height of the first temperature sample in the first hour of the test.

Some interesting aspects can be observed from Figure 8.5. First of all, a relatively steady temperature drop can be observed for the stabilized part, in other words, at the left-hand side of the figure. Also, a distinct temperature rise in the first half of the remoulded quick clay, more precisely for  $x \in [0, 5]$ , is obvious from Figure 8.5.

There is a clear difference between the first half of the remoulded quick clay part and the second half of the same part in Figure 8.5. The changes related to temperature are clearly higher for  $x \in [0, 5]$  than for  $x \in [5, 10]$ . It is obvious that the heat from the lime-stabilized part is using more than one hour to be transferred and distributed evenly in the unstabilized part. This finding can also be observed in Figures 8.3 and 8.4. It took approximately, as mentioned above, 4 hours before the slope of the right-hand side plots had decreased more or less completely and a stable temperature situation was reached.

It is also possible to observe that, despite the temperature drop in the stabilized part being relatively uniform, the temperature drops more and more the closer the OBR-points are to the transition zone (i.e. origo). This was due to the fact that this was the part of the stabilized soil that had to transfer its heat first because of its unisolated connection to the remoulded quick clay. It loses heat when its heat is transferred to the first part of the remoulded quick clay. The bottom part of the lime-stabilized soil was protected by either isolation material or lime-stabilized material on all sides, hence this part used more time to lose its heat. It can be observed from Figure 8.5 that the derivative of the temperature change, in other words, the change of the temperature change from the reference measurement, is largest in the zone from just before to just after origo.

All of the DFOS-scans which were conducted during the first hour of the second temperature test are shown in the plot in Figure 8.6.



**Figure 8.6:** All scans of temperature change along the height of the second temperature sample in the first hour of the test.

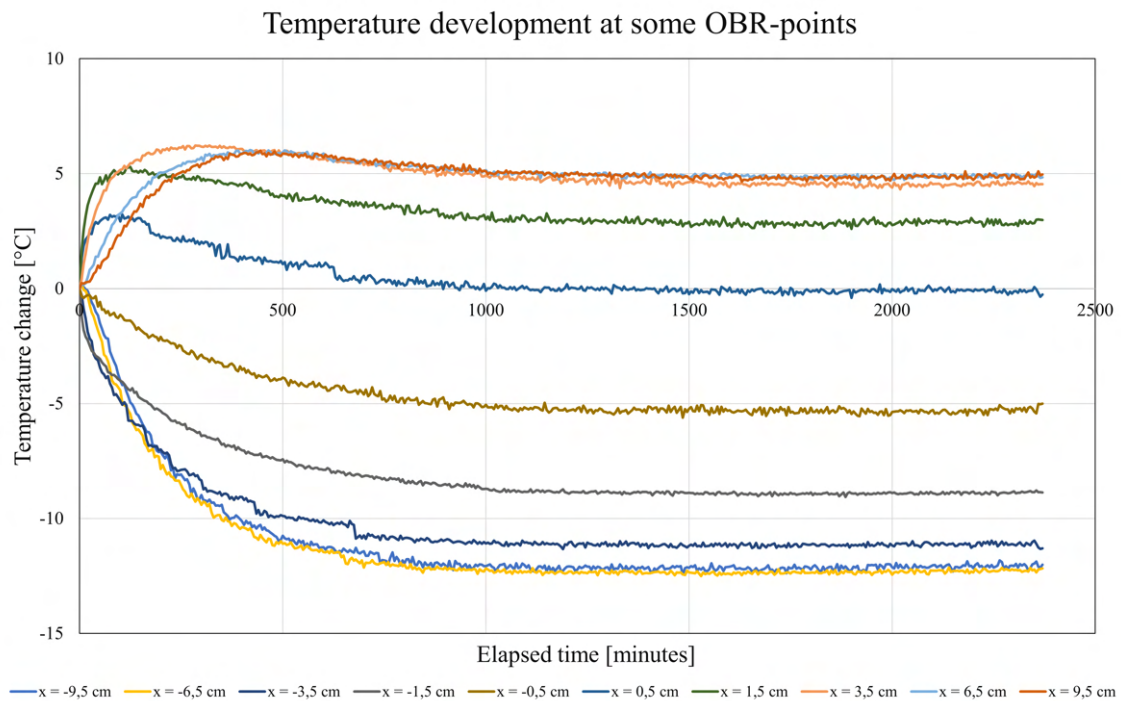
The results from the two temperature tests are very similar. This is as expected for two similar tests. However, it is still a good verification of the performance of the DFOS-system. The trends discussed for the first temperature test can also be seen in Figure 8.6.

Larger versions of Figures 8.3, 8.4, 8.5 and 8.6 are included in Appendix C.

## 8.2 Temperature change with time for 2. test

In the remaining sections of this chapter, a closer look has been taken at the second temperature test. However, very similar results can be extracted for the first temperature test.

Below, plots of the temperature change with time for a few fiber core points along the height of the second temperature sample are given in Figure 8.7. A Figure with the plots of all the DFOS measurement points can be found in Appendix C.



**Figure 8.7:** Temperature change with time for some of the DFOS measurement points along the height of the sample in the second test.

Figure 8.7 contains data of the temperature change from one day and 15.5 hours for the different DFOS points. There was a lot of development in the temperature change profiles during the first 500 minutes, in other words, the first 8 hours, before the profiles started stabilizing. Steady-state was reached within 1000 minutes, which corresponds to approximately 17 hours.

In the two lowest points, the temperature profiles are very similar. From  $x = -3.5$  cm to  $x = 3.5$  cm it is clearly seen that the temperature change with time develops steadily from temperature decrease to increase. In other words, it is verified that the temperature was rising from the

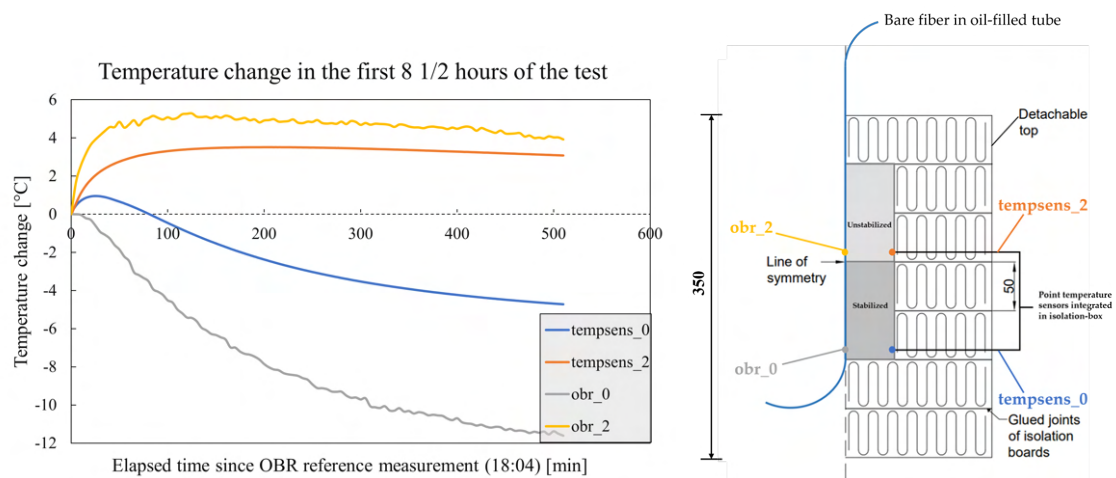


bottom to the top of the sample.  $x \in [-3.5, 3.5]$  corresponds to the zone where the derivative of the temperature change graphs changed the most in Figures 8.3 and 8.4. The two upper points show similar temperature profiles as for  $x = 3.5$  cm.

### 8.3 Comparison between thermocouples and DFOS for 2. test

As described in Chapter 5, the isolation box was instrumented with two integrated thermocouples. These were integrated into the isolation box to give reference measurements, one measurement for the lime-stabilized clay and one for the remoulded quick clay. In the post-processing, the two measurement points along the bare fiber core which were closest in position in the sample height to the thermocouples, were compared to the the integrated temperature sensors.

The comparison between the two measurement methods can be seen in Figure 8.8. Figure 8.8b shows the position of the OBR measurement points relative to the integrated thermocouples. Figure 8.8a includes the plot of the temperature change from the time of reference measurement, i.e. 18:04, for the two thermocouples and their corresponding DFOS measurement points.



(a) Temperature change since the time of reference measurement (b) Positions of the different measurement points

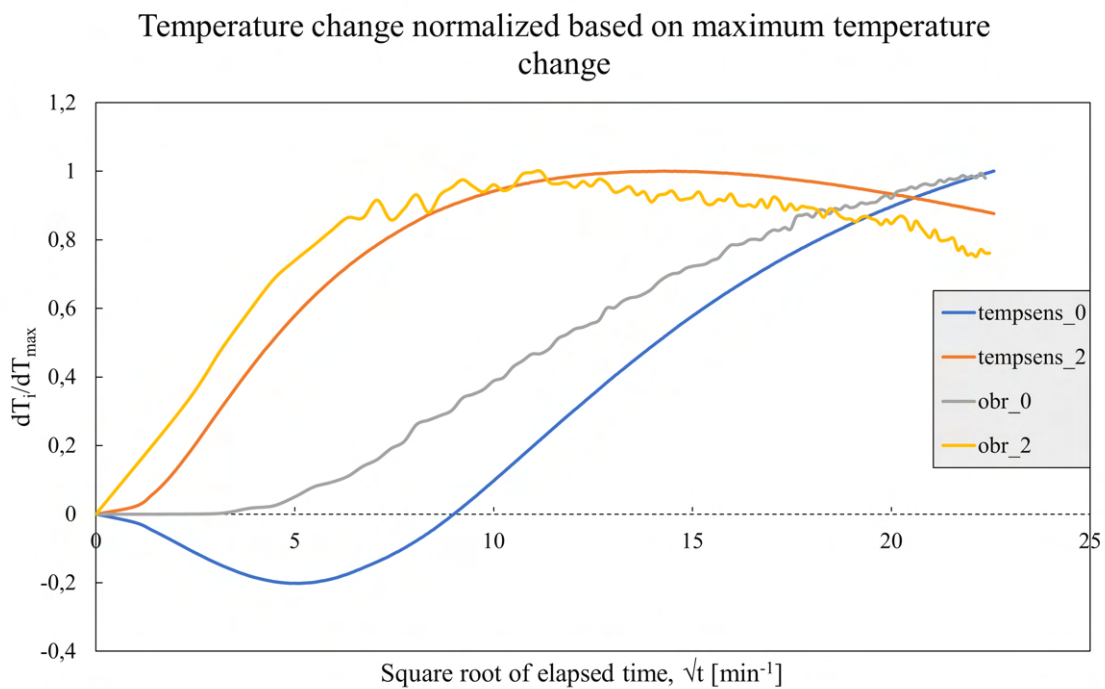
**Figure 8.8:** Comparison between DFOS-measurements and measurements performed by thermocouples for the second temperature test.

The shape is similar between the corresponding graphs in Figure 8.8a. The numerical values of the graphs, however, are different. This is probably due to the two different temperature sensors not being heated as much, as a result of their different positioning in the radial direction. The maximum difference between the temperature measurements from the unstabilized part, in other words, the two upper graphs, is about 2°C. This maximum difference was

reached close to the two graphs' peak, following the peak the temperature difference decreased with time. For the two temperature graphs in the stabilized soil, the difference increased with time, and the maximum difference in Figure 8.8a was approximately 7°C. It was the DFOS-measurements that recorded the biggest temperature changes in both parts of the sample.

Note that the positions of the DFOS measurement points and the thermocouples are similar only in the vertical direction. They are positioned differently in the cross-section, as discussed in Section 6.3. In addition to Figure 6.2, also Figure 8.8b is visualizing the difference between the DFOS points and the thermocouples with regards to positioning inside the temperature samples. In Figure 8.8 and 8.9, the thermocouples are referred to as "tempsens" and the DFOS points are referred to as "obr". The number 0 has been used for the lower points, more precisely the points in the stabilized material, while 2 has been used for the upper points, in other words, the points in the remoulded quick clay.

To be able to compare the temperature measurements, despite the numerical values being different, the four temperature graphs have been normalized based on their own maximum temperature change in the first 8.5 hours after 18:04.



**Figure 8.9:** The temperature change normalized based on each measurement's own maximum temperature change in the first 8.5 hours after reference measurement in the second temperature test.

Figure 8.9 is showing the results of the normalization. The figure is visualizing that, despite the numerical values being different, the temperature trends measured with the DFOS-technology

and the thermocouples are very similar.

Equally as for the plots presented previously in this chapter, the data presented in Figure 8.9 is from the first 8.5 hours of the second temperature test. In other words, the x-axis is showing the time which has elapsed since the reference measurement was conducted. It is important to note that this time-axis is showing the square root of the elapsed time. This is done to better visualize how the trends of temperature changes develop with time.

It can be observed from Figure 8.9 that the measurements performed with the OBR and the bare fiber core fit well with the results recorded by the thermocouples. Especially in the un-stabilized part, the two measurement methods give very similar trends. Another interesting finding from the results in Figure 8.9, which also can be observed from Figure 8.8, is the fact that the measurements performed with the integrated thermocouples are delayed compared to the DFOS-measurements. This is seen from the fact that the peak is reached slower in the thermocouple measurements than in the measurements by DFOS.

#### 8.4 Comparison between thermocouples and the reference sample for 2. test

The performance of the thermocouples was also compared to other standard temperature sensors. As described in Section 5.3, a reference sample was prepared to enable the possibility of tracking the hydration process. This reference sample was measured with a standard PT100 thermoelement which was embedded centrally into the sample. This was done for the second temperature test. The lime-stabilized clay in the reference sample is taken from the same stabilization process as the material that has been measured in the plots in Section 8.3. A comparison between the PT100 measurement and the measurement from *tempsens\_0* has been carried out. It is important to note that Figure 8.10 is showing the absolute temperature, not the temperature change. This is opposite from all of the previously presented plots in this chapter.

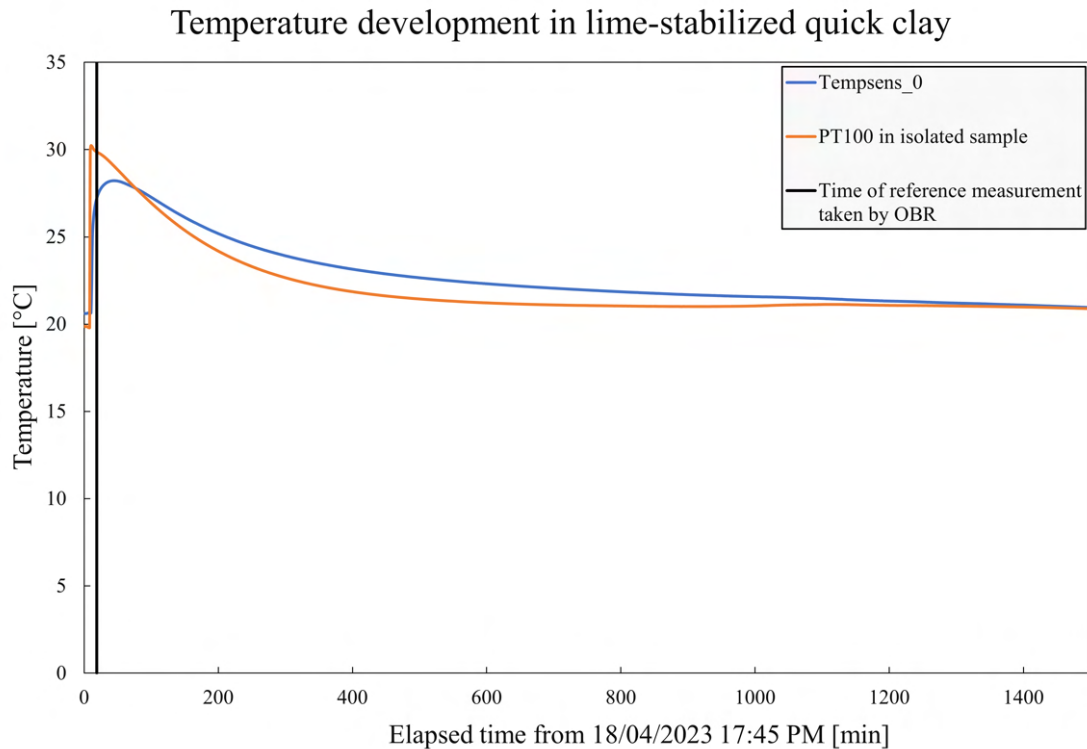
In Figure 8.10 the absolute temperature from the measurements taken by *tempsens\_0* and the PT100, from when both method's recordings were initiated, are plotted. In addition, there is a vertical black line indicating the point of time where the reference measurement for the DFOS was taken.

Figure 8.10 is verifying the assumption that the thermocouples are not heated as much as temperature sensors embedded in the center of the stabilized material. Also, it is verifying that the thermocouple measurements are delayed compared to measurements taken by other temperature sensors. The reason for the thermocouples being heated slower and to a lesser extent is probably due to the design of these temperature sensors.

The sensors were embedded in insulation material, which probably affected their heating. The steel material of the thermocouple may have carried some heat into the XPS-plates, in addition, the isolation of the sensor has probably resulted in the heating process taking more

---

time. The fact that the thermocouples were not surrounded by clay at all sides, but instead embedded in insulation with only the tip exposed to the heating material, has affected the heating with regard to both rate and extent. The temperature developments from the two different temperature sensors stabilized at the same temperature after some time.

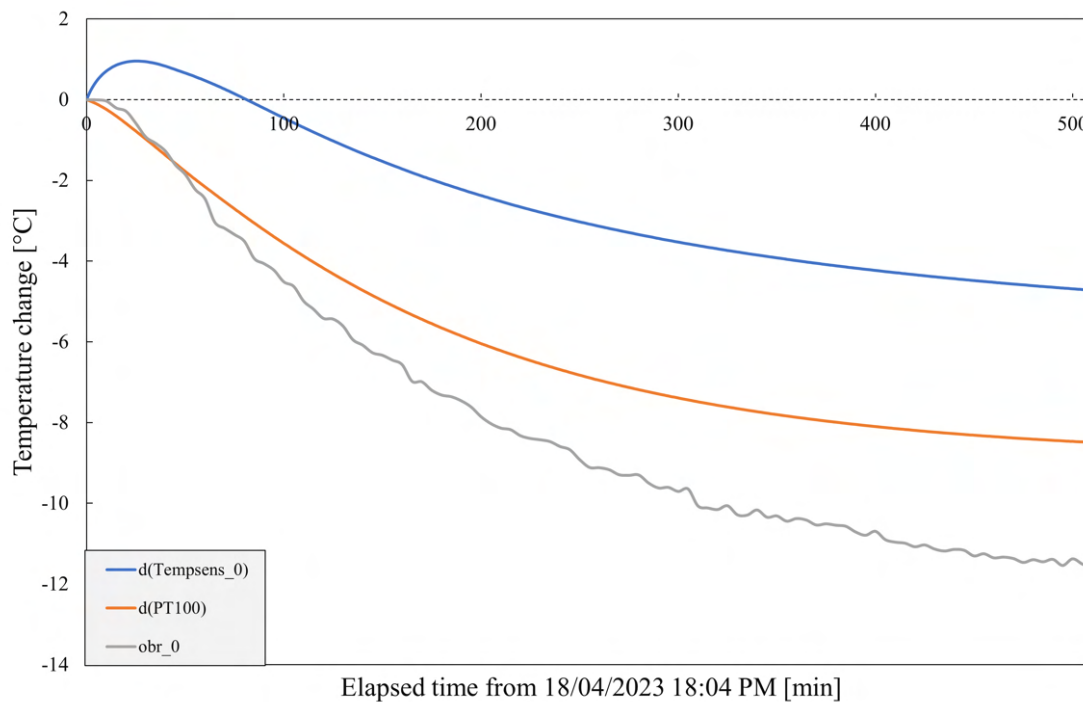


**Figure 8.10:** A comparison between the measurement taken by the thermocouple in the stabilized part of the isolation box and the measurement from a PT100 element in a reference sample of the same lime-stabilized quick clay.

Another point highlighted from Figure 8.10 is that the peak temperature rise in the lime-stabilized material due to hydration was already reached at the point of time where the DFOS reference measurement was taken by the OBR, i.e. 18:04. The PT100-measurement is showing this fact. This is despite *tempsens\_0* indicating that the peak temperature was not reached yet at 18:04. This fact, in addition to the thermocouple measurements being delayed, explains why the temperature change from the OBR was dropping while the temperature change from *tempsens\_0* was increasing in the first approximately 20 minutes in Figure 8.8a.

The fact that the temperature sensor embedded centrally in the reference sample, in other words, the PT100, is heated more implies that the temperature drop with time will be higher for this temperature measurement. This is similar to what was seen for the centrally embedded bare fiber in Figure 8.8a. A plot comparing the change in temperature after the reference measurement, measured by the PT100 and the lower thermocouple is given in Figure 8.11.

For comparison, also the measurement from DFOS measurement point *obr\_0* is included in the figure. It can be seen that the temperature development measured by the PT100 is between the measurement from *tempsens\_0* and *obr\_0*. In fact, the PT100 measurement is more similar to the DFOS measurement than the thermocouple measurement. Still, there is a difference between what was measured with the OBR and the bare fiber core and what was measured from the reference sample. Both measurements were taken from an isolated, lime-stabilized material. However, the isolation conditions were different, and this had probably an effect on the differences which were observed with regard to the respective temperature developments.



**Figure 8.11:** A comparison between the measurement taken by the thermocouple in the stabilized part of the isolation box, the OBR measuring point at the same height and the measurement from the PT100 element in the reference sample.

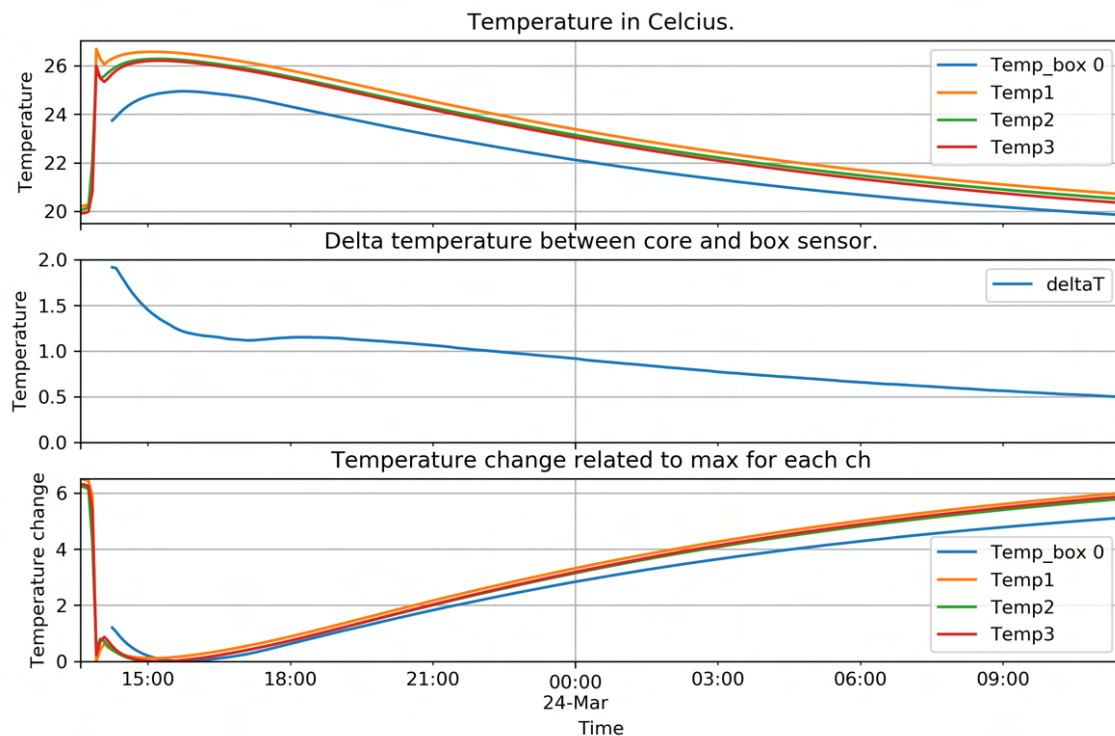
## 8.5 Cross-sectional temperature test - Results

In the following chapter, all relevant results that have been produced during the cross-sectional temperature test will be presented. This includes the evaluation of heat transfer in the radial direction based on PT100 measurements and a comparison between temperature measurements performed with a PT100 element and a thermocouple. Unfortunately, there was a problem with the interpretation of the DFOS-measurements. This will also be discussed.

---

### 8.5.1 Thermo element (PT100) measurements

The three PT100 thermo elements were placed equally spaced from the center of the lime-stabilized sample and out to the interface between the stabilized soil and the isolation box. The positions of the PT100s are shown in Figure 6.2. In the following, the PT100 thermo elements will be referred to as "Temp1", "Temp2" and "Temp3". A plot of the absolute temperature across the lime-stabilized material is shown in the upper part of Figure 8.12.



**Figure 8.12:** Three different plots comparing the measurements from the PT100s with the measurements with the lower thermocouple, i.e. tempsens\_0. Delta temperature in the middle graph is calculated as the difference between the middle PT100 and the thermocouple.

What can be observed from the figure, is very similar trends. The shapes of the three graphs are more or less exactly the same. The values of the graphs are slightly different. However, the differences are roughly constant throughout the test. It also has to be stressed that the minor differences were already apparent before the test of the lime-stabilized material was started. By looking at the first values of the upper plots in Figure 8.12 these initial differences can be confirmed. In short, Figure 8.12 is indicating that there should not be any considerable heat transfer in the radial direction, as the temperature profiles across the sample are more or less equal.

### 8.5.2 Comparison of measurement methods

A comparison between the measurements from the PT100s and from the lower thermocouple has also been carried out, and the relevant graphs are shown in Figure 8.12. Note that the thermocouple previously known as "tempsens\_0" is referred to as "Temp\_box 0" in Figure 8.12.

In the upper plot, the measurement from the thermocouple is also included. Something that has been seen previously can also be observed in this figure. Namely, the thermocouple measurements differ from other temperature sensors in the beginning, by being approximately 2°C less, before it approaches the values of the other measurement methods with time. This has also been observed in Figures 8.8a and 8.10.

In the two temperature increase graphs in Figure 8.8a, it can be seen that the temperature change measured by the thermocouple is about 2°C less than the corresponding measurement performed by the DFOS-technology. The difference decreases with time. In Figure 8.10, a difference of about 2°C in the absolute temperatures between measurements conducted by a PT100 element and the lower thermocouple can be seen. It was the PT100 measurement that showed the highest temperature in the beginning. With time, the two measurement methods gave the same temperature.

In the standard temperature tests, the thermocouple was compared to a DFOS measurement point in the center of the sample cross-section. The difference between the thermocouple and the centrally placed temperature sensor during this test has also been studied. This was done to examine whether there was a reason for a lower temperature at the edge compared to the center. The middle graph is visualizing how the difference between the thermocouple and the centrally placed PT100 was at approximately 2°C at the beginning but decreased with time. This difference is similar to what was observed between the thermocouple and the DFOS point in Figure 8.8a. The reason for this initial difference which decreases with time is probably related to the design of the thermocouples that already has been discussed. The thermocouple is not heated as much as other temperature sensors, but it is giving reliable measurements when the temperature is approaching the steady state.

The lower graph in Figure 8.12 is a normalized version of the upper graph. This normalization is similar to what was done in Figure 8.9. Here, the temperature changes which were measured with *Temp1*, *Temp2*, *Temp3* and *tempsens\_0* (**Temp\_box 0**) have been divided by their respective maximum temperature change. The temperature change values are given as absolute values, with the maximum temperature change equal to zero. These graphs show how similar the trends/shapes of the different temperature developments are. The normalized PT100 measurements are more or less exactly the same. The thermocouple measurement, in other words, *Temp\_box 0*, is also very similar to the other graphs, but like what has been seen in other results in this thesis, the thermocouple measurement is somehow delayed. This is due to its design.

---

### **8.5.3 DFOS measurements**

Unfortunately, the position of the sample is not known more precisely than that it is somewhere between 15.3 m and 16.5 m. In other words, the length of 10 cm can be anywhere in this 120 cm interval. Hence, no conclusion with regard to the heat transfer across the lime-stabilized sample in the radial direction can be drawn from the DFOS results. As a consequence, these results are not included here. However, the DFOS-scans are added to Appendix C, and can be seen in Figure C.1.

---



## Chapter 9

# Strain tests - Results

In the following, all the relevant results obtained from the unconfined compression tests will be presented.

Equally as for the temperature tests, a spatial resolution of 1 cm was used during the strain testing. This spatial resolution is, for what has been studied in this M.Sc. Thesis, sufficient with regard to both the amount of measurement points and the quality of the measurements.

### 9.1 Mechanical properties of the samples

Table 9.1 presents some general results related to the mechanical properties of the three samples. The results are based on the measurements obtained from the uniaxial device. In Table 9.1, the undrained shear strength ( $c_u$ ), failure strain ( $\varepsilon_f$ ) and Young's modulus ( $E_{50}$ ) for the three strain samples are presented. All of these properties originate from the stress-strain curves that were produced based on the uniaxial recordings. The curves, with all relevant information, are attached in Appendix D.

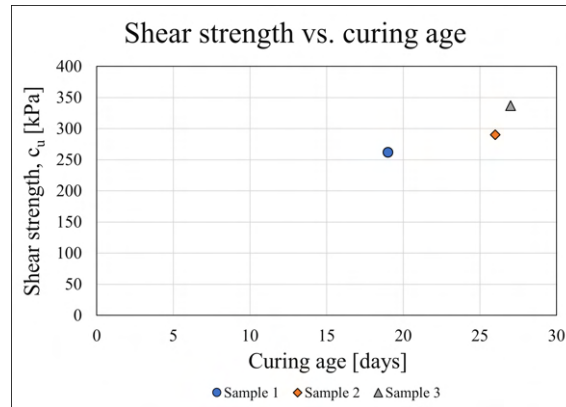
Sample nr.	Curing time [days]	$c_u$ [kPa]	$\varepsilon_f$ [%]	$E_{50}$ [kPa]	$\varepsilon_{cableslip}$ [%]
1	19	262	2.97	27 314	1.30
2	26	290	2.37	54 101	1.01
3	27	337	3.14	48 656	1.20

**Table 9.1:** A summary of some of the most important mechanical properties of the three strain samples. In addition, the strain at which slippage between the cable and the surrounding stabilized soil is included.

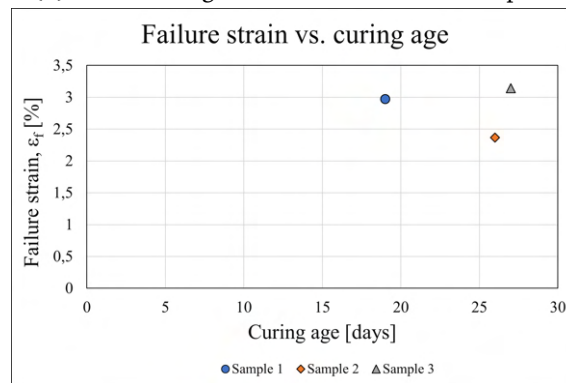
In addition, Table 9.1 presents the number of days that each sample cured before they were tested and at which strain level the fiber optic cable slipped from the surrounding stabilized soil. By slipping, it is referred to when the DFOS measurements started to show decreasing

strain although the uniaxial strain was increased. At this point, more and more bond was lost between the cable and the lime/cement-stabilized soil, and the cable followed the sample to a lesser extent.

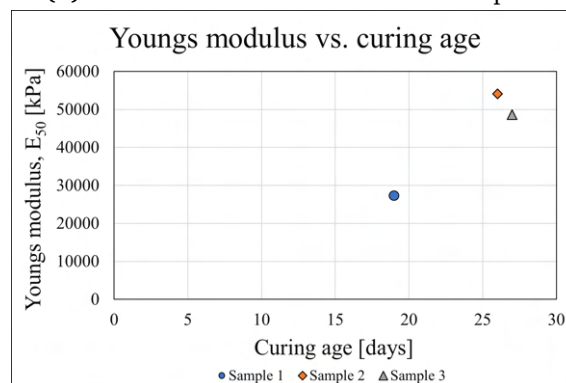
Some plots visualizing the mechanical properties of the strain samples have also been produced. The plots are presented in the following.



(a) Shear strengths of the three strain samples.



(b) Failure strain of the three strain samples.



(c) Stiffness of the three strain samples

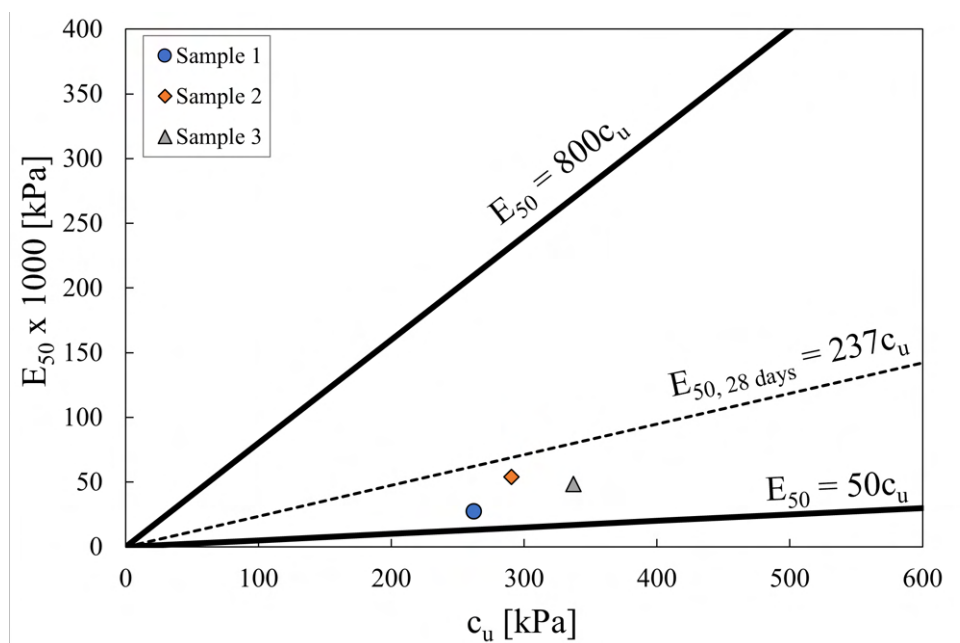
**Figure 9.1:** Three plots summarizing the integrity of the different strain samples.

Figure 9.1a is a plot of the shear strength and corresponding curing age for the three strain samples. The figure shows that the shear strength increased along with the curing age. This finding fits well with what was described in Section 2.7.2 and shown in Figure 2.8.

Figure 9.1b presents the failure strain as a function of the curing age of the samples. It can be observed that the highest failure strain occurs in Sample 3, whilst the lowest failure strain belongs to Sample 2. The values range from 2.37% to 3.14%, with Sample 1 having almost the same failure strain as Sample 3.

In Figure 9.1c, the stiffness of the strain samples is plotted against their curing age. It is seen from the figure that, equally as for strength, also the stiffness increase alongside the curing age. However, in the plot presented in Figure 9.1c the stiffness is highest for Sample 2.

To relate the results from these samples, which are larger and tested in a slightly different manner compared to what is the standard method in Norway, a comparison with previous experience has been performed. Paniagua et al. (2019) carried out a thorough evaluation of the mechanical properties of laboratory-stabilized Norwegian clays. The correlation between undrained shear strength ( $c_u$ ) and stiffness ( $E_{50}$ ) of lime/cement stabilized clay samples with a 50/50 binder ratio was one of the evaluations that were performed. Based on the results, a trendline for  $E_{50}$  as a function of  $c_u$  for samples stabilized for 28 days, in addition to upper and lower bounds were produced. In Figure 9.2, the mechanical properties of the special samples of this M.Sc. Thesis has been plotted together with the trendlines from Paniagua et al. (2019). The results show that the samples tested in this thesis fit well within the proposed range of mechanical properties for 50/50 LC-stabilized Norwegian clays based on experience values.



**Figure 9.2:** Mechanical properties of the lime/cement-stabilized clay samples plotted within experience range from Paniagua et al. (2019).

As mentioned at the beginning of this section, all these plotted properties were calculated based on the measurements from the uniaxial device. As the test that was performed for the strain samples was an unconfined compression test, the vertical compressive stress from the device was the maximum principal stress,  $\sigma_1$ . Correspondingly, the non-existent horizontal stress was the samples' minimal principal stress, in other words,  $\sigma_3 = 0$ . Hence, the maximum shear stress ( $\tau_f = c_u$ ) in the samples corresponded to the maximum compressive stress ( $q_u$ ) divided by two. Equation 9.1 is showing the calculation.

$$\tau_f = \frac{\sigma_1 - \sigma_3}{2} = \frac{q_u}{2} = c_u \quad (9.1)$$

The ultimate compressive strengths of the samples were found as the maximum compressive stress in the stress-strain curves shown in Appendix D. Also the failure strains were obtained from these curves. The failure strain corresponds to the strain level at which the maximum compressive stress was reached. The stiffness of the samples, i.e.  $E_{50}$ , are found as the inclination of the straight black lines in the curves in Appendix D (NGF 2011). These black lines are drawn from the point where full contact was achieved between the piston and the sample, and cross the stress-strain curves at the point where 50% of the ultimate compressive strength was reached.

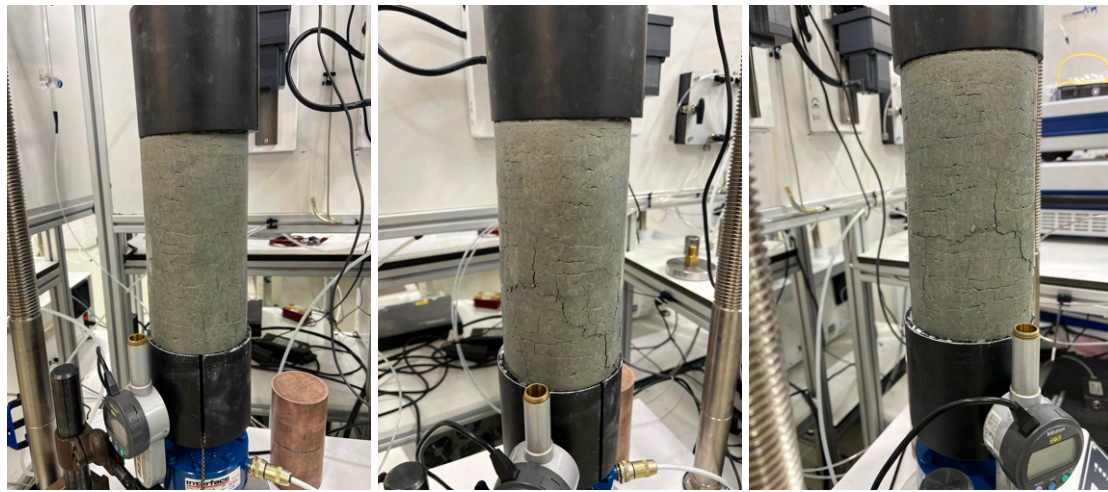
There were observed some quality differences between the samples based on the measured mechanical properties. The quality difference was best visualized based on Sample 2 and Sample 3. Sample 2 was cured for 26 days, whilst Sample 3 was cured for 27 days. Despite only one day difference in curing age, the oldest sample (Sample 3) had an undrained shear strength ( $c_u$ ) which was 16% higher than the corresponding strength of the one-day younger sample (Sample 2). This difference is probably higher than what could be expected solely due to the longer time of curing for samples of respectively 26 and 27 days of curing age. In other words, this strength difference is a sign of quality difference for the strain samples. In addition, the results show a higher stiffness ( $E_{50}$ ) for Sample 2 than for Sample 3, which does not correspond with the general trend of increasing stiffness with increasing curing age. Sample 2 had a stiffness that was 11% higher than the stiffness of Sample 3. This is another example of the quality difference between the three samples, which also is expected for laboratory samples.

## 9.2 Failure pattern of the samples

In the following, the failure patterns of the three samples are discussed.

Figure 9.3 shows how an initial, small, vertical crack at the bottom of Sample 1 was transformed into a radial crack. The initial vertical crack can be seen in Figure 9.3a and how the failure pattern further develops to a horizontal crack shown in Figure 9.3b. Lastly, the radially developed part of the failure crack can be observed from Figure 9.3c. The radial crack also has several other small vertical cracks. This multiple fracturing of Sample 1 can be seen in Figures 9.3b and 9.3c.

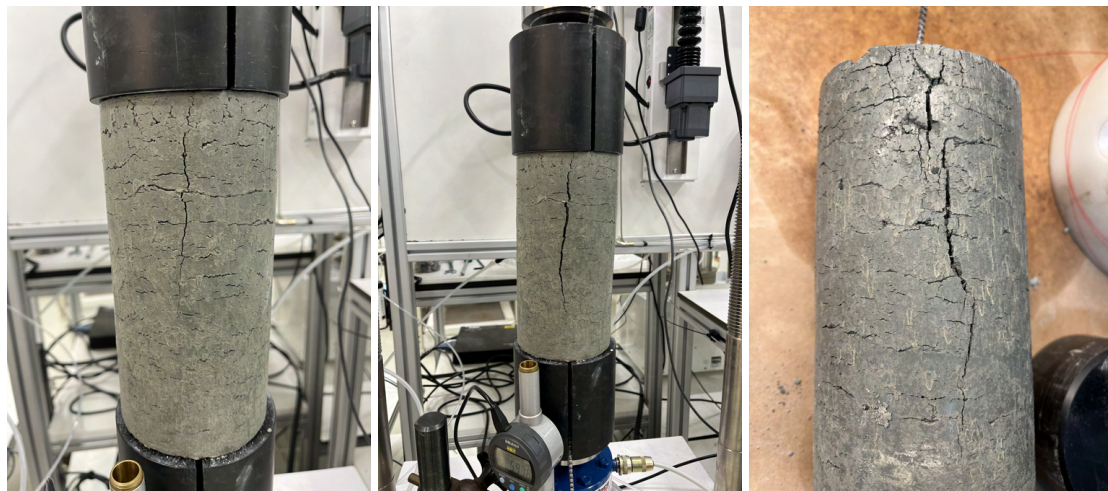
---



(a) Initial failure. (b) Fully developed failure (1). (c) Fully developed failure (2).

**Figure 9.3:** Pictures showing the failure pattern of Sample 1 from several angles.

Figure 9.4 visualizes how the failure pattern of Sample 2 developed. Equally as for the first sample, a small vertical crack initiated failure on Sample 2. However, in Sample 2 this vertical, initial failure occurred at the top, not at the bottom. The small, initial vertical crack at the top of the sample can be observed from Figure 9.4a.



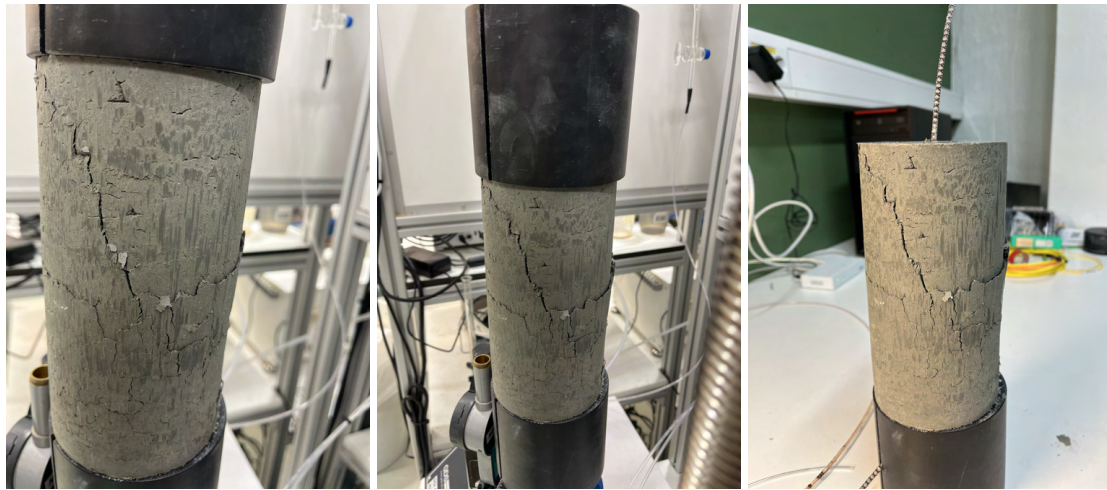
(a) Initial failure. (b) Fully developed failure (1). (c) Fully developed failure (2).

**Figure 9.4:** Pictures showing the failure pattern of Sample 2 from several angles.

Further on, a large vertical crack appeared during the compressive testing. Such a large vertical crack was developed at both the front and the back of the sample. The failure pattern at the front is shown in Figure 9.4b, whilst the failure pattern at the back can be seen in Figure 9.4c. The figures are clearly showing the axial splitting of Sample 2.

Lastly, the failure pattern of Sample 3 is shown in Figure 9.5. Equally as for Sample 2, the initial failure crack appeared at the top of Sample 3. However, for this sample the initial crack had an inclination, it was not vertical as for Samples 1 and 2. The oblique initial cracking can be seen in Figure 9.5a. Opposite from the axial splitting of Sample 2, shearing was the failure mode for Sample 3.

The initial crack of Sample 3 was significantly more developed at the time it was being photographed, compared to the initial cracks of Sample 1 and Sample 2. The fully developed failure pattern is shown in Figure 9.5b and 9.5c. A more complex failure pattern appeared for the third sample, compared to the previous two samples, and also peeling (i.e. some material falling off) occurred for Sample 3. The peeling can be seen in Figure 9.5b, but the phenomenon appears most clearly in the right-hand crack in Figure 9.5c.



(a) Initial failure. (b) Fully developed failure (1). (c) Fully developed failure (2).

**Figure 9.5:** Pictures showing the failure pattern of Sample 3 from several angles.

The failure modes that were observed for the three samples, in other words axial splitting, shearing and multiple fracturing, are very common failure mechanisms for stabilized soil. This is an indication that the embedded fiber cable has not affected the structural integrity of the stabilized soil samples. Thus, the samples tested in this research are typical and resemble stabilized soil.

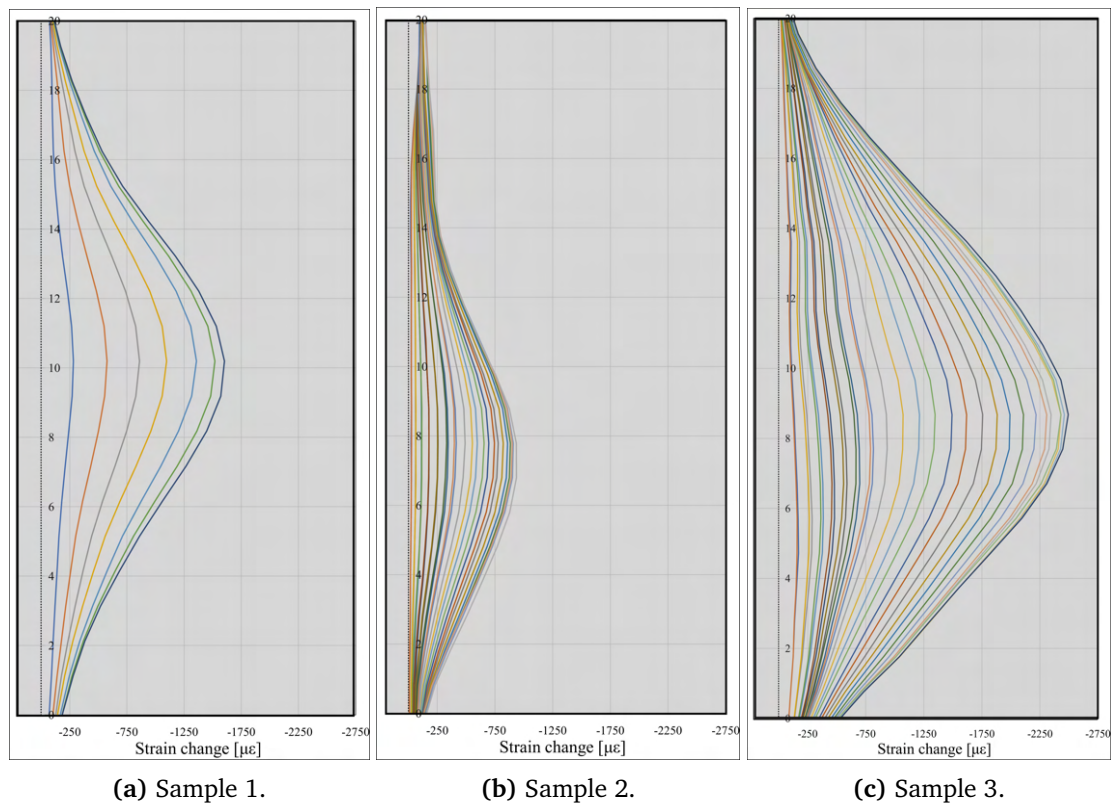
### 9.3 Strain change along sample height before cable slippage

In this section, plots of strain change in the cable during the compressive testing of all three samples will be discussed. As described in detail in previous chapters, the DFOS-technology only produces relative values. Hence, a reference measurement was conducted just before the compressive testing of the samples was started. This was when contact was achieved in the

---

system consisting of compressive piston, rigid plastic cylinders and the stabilized soil sample, and the deformation recording of the uniaxial device was set to zero. All subsequent measurement scans performed by the OBR interrogator and the EpsilonSensor fiber optic cable gave the strain change relative to the reference measurement.

In the plots in this section, only the measurements performed before the cable slipped the LC-samples are included. Thus, the strain change shows an increase with each scan in the presented plots. The y-axis is representing the position along the sample height, with the origin now placed at the bottom of the samples. Strain change relative to the reference measurement is given on the x-axis. The strain change scans before cable slippage for all three samples are given in Figure 9.6. Single plots, including labels, for the three samples, can be found in Appendix D. In addition, larger versions of the plots in Figure 9.6 are also added to Appendix D.



**Figure 9.6:** Strain change along the height of all three strain samples.

In Figure 9.6a, the strain change of the fiber optic cable along the height of Sample 1 during the unconfined compression testing is plotted. Sample 1 was deformed 0.25 mm before the first scan and additionally 0.25 mm before the second scan. After the two first scans, the sample was deformed 0.4 mm between each DFOS-scan. The strain rate was 0.4 mm/min.

Figure 9.6a shows an increase of strain towards the middle of the sample and with time. The

largest strain measured with the fiber optic cable was  $1603 \mu\epsilon$ . The strain profiles are similar to a sinusoidal shape, with maximum strain change in the middle of the sample. The shape is different from the theoretical shape of a sample being compressed, which should be equal along the height of the sample. This theoretical example would have more of a square response, with the same strain change along the whole sample. The strain profiles measured by the fiber optic cable should build up to a given strain value from both ends and then the profiles should have been constant at this plateau. However, this was not the case for any of the three strain samples, and it is an indication that the DFOS-measurements were not perfect. It is probably a result of not sufficient bonding to transfer the complete load into the fiber optic cable.

The strain profiles from the second test, in other words for Sample 2, are shown in Figure 9.6b. The concept of the three strain tests was the same, however, one difference between the first test and the two following tests, was the number of measurement scans. Figure 9.6b contains a lot more plots than 9.6a. The reason for this choice was to try to catch more of the strain development at the lower strain levels.

In addition, tests of the effect of relaxation were performed for the first 7 measurements. More precisely, DFOS-scans were taken at different points of time after the deformation was stopped to study whether there was some difference in the strain measurements after some time. It was approximately one minute between the two DFOS-scans corresponding to the same deformation level. Hence, 14 DFOS-scans were conducted for the first 0.7 mm of deformation of Sample 2 and Sample 3.

A strain rate of 0.2 mm/min and strain steps of 0.1 mm was used for this test. Before the very last scans, the strain steps were increased. This was at the point in time when the failure of the sample had begun, and the reason for deforming the sample even more, was to get a fully developed failure of the sample. The strain step was set to 0.4 mm. Quickly after the step size was ramped up, no more DFOS-scans were taken, due to the fact that the cable had slipped so much that virtually no strain change was measured anymore. The maximum strain change that was measured with the fiber optic sensing for Sample 2 was  $936 \mu\epsilon$ .

Another interesting thing that can be observed in Figure 9.6b, is that the maximum points of the strain profile did not occur in the middle of the sample. This is unlike what was seen for Sample 1. The maximum strain in Sample 2 was measured at approximately 8 cm above the sample's bottom. A visible physical crater giving no bond between the fiber optic cable and the lime/cement-stabilized material at the top of the sample is probably the reason for this shifted maximum point. This crater can be seen in Figure 10.3.

Equally as for Sample 1 and Sample 2, the strain change of Sample 3 during the unconfined compressive testing has been plotted against the position along the sample height. The horizontal plot of the strain development in Sample 3 is given in Figure 9.6c. Sample 3 was deformed equally to Sample 2. In other words, the sample was firstly deformed with a strain rate of 0.2 mm/min and a strain step of 0.1 mm. When failure started to initiate, the strain step was ramped up to 0.4 mm and the sample was deformed until failure had been fully developed. A considerable number of scans were conducted for Sample 3 compared to the two other samples.

---



Equally as for Sample 2, the effect of relaxation was tested also for this sample. By taking a close look at Figure 9.6c, it can be seen that two and two scans are very similar in the first 14 plots. The maximum strain of the fiber cable that was measured for Sample 3 was  $2493 \mu\epsilon$ . The maximum point for Sample 3 was about 9 cm from the bottom of the sample. Although great care was taken during the sample preparation, there was also a crater at the top of Sample 3.

It is worth noting that the scale of the three different subplots of Figure 9.6 is the same. Hence, the figure gives a good comparison between the performance of the three strain tests. It can be clearly seen from the figure above that Sample 3 recorded the highest strain change by the DFOS-scans. Sample 2 had the poorest performance of the DFOS-measurements with regard to strain recording, with a considerably lower value for maximum measured strain change compared to the two other samples.

It can also be observed from Figure 9.6 that the strain profiles for Sample 1 have their maximum point in the middle of the sample height. Oppositely, Sample 2 and 3 have this point at approximately 8 cm and 9 cm, respectively, from the bottom of the sample. This shift of the maximum point is probably due to a lack of bonding between the fiber cable and the lime/cement-stabilized material at the top of the samples.

## 9.4 Strain magnitude

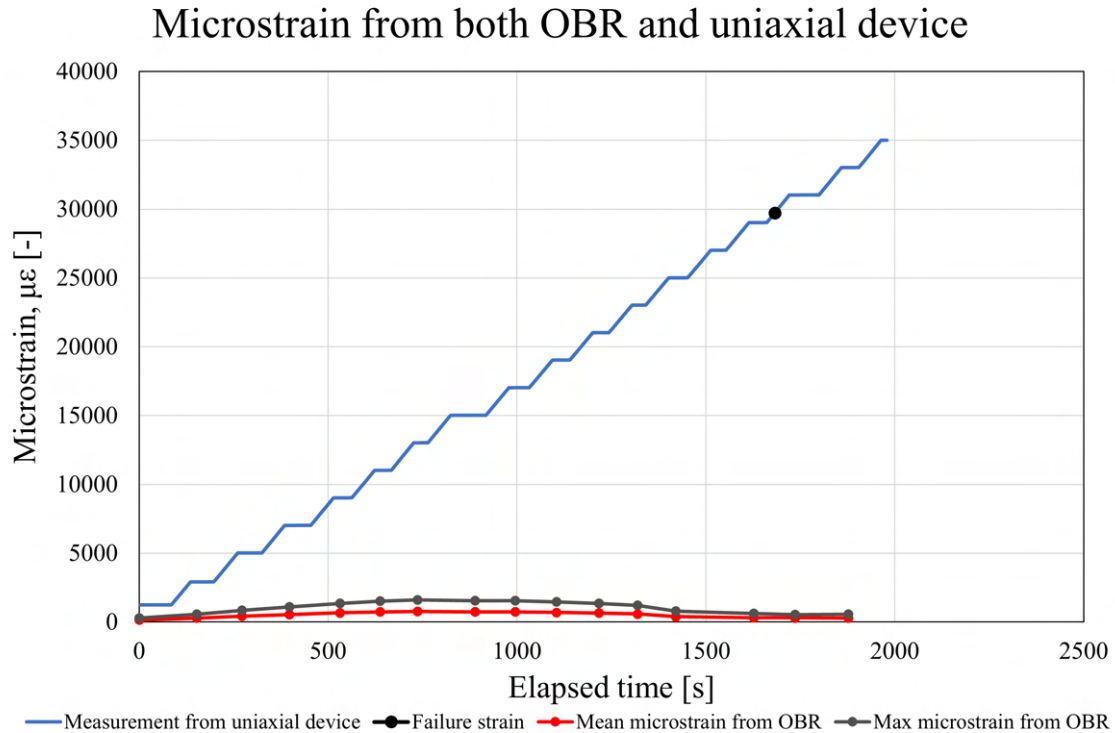
Comparisons between the results from the DFOS-technology and the uniaxial device have been carried out to examine the quality of the DFOS-measurements. Both mean and maximum strain of the DFOS-points at each measurement time are compared to the corresponding strain calculated based on the deformation recording from the compressive apparatus. The measured strain has been plotted against elapsed time since the testing was started. Hence, the uniaxial graphs have many horizontal plateaus as a result of the fact that the deformation was stopped for each scan with the OBR interrogator.

Plots of solely the mean and maximum strain measurements from the DFOS-system can be found in Appendix D.

### 9.4.1 Strain magnitude of Sample 1

The comparison of the results from the DFOS-technology with the results from the uniaxial device for Sample 1 is presented in Figure 9.7. It can be observed from the figure that the strain that is measured by the OBR interrogator and the EpsilonSensor are considerably lower than the strain calculated based on the deformation recording from the uniaxial device. Also, the point of cable slippage can be seen. At this point, the DFOS-measurements, both mean and maximum, started to decrease. When the cable slipped, it measured a maximum strain of  $1603 \mu\epsilon$  while the uniaxial results gave  $13020 \mu\epsilon$  at the same time.

---

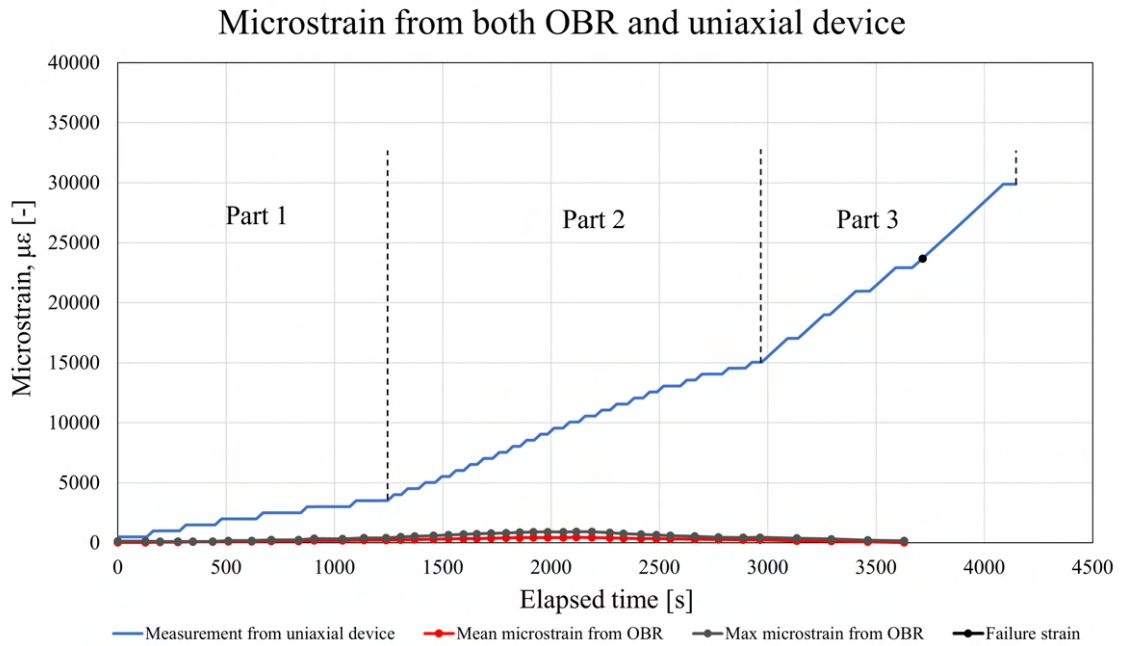


**Figure 9.7:** Strain, measured with both the DFOS-technology and the uniaxial device, plotted against the time which has elapsed since the compression of Sample 1 was initiated.

#### 9.4.2 Strain magnitude of Sample 2

Equally as for Sample 1, a comparison of the results from the DFOS-technology with the results from the uniaxial device was carried out also for Sample 2. The result of this comparison can be seen in Figure 9.8. The strain measured by the DFOS-system was even lower relative to the uniaxial measurements for Sample 2 compared to Sample 1. When the cable slipped Sample 2, it measured a maximum strain of  $936 \mu\epsilon$ . For comparison, the strain from the uniaxial measurements was  $10060 \mu\epsilon$ .

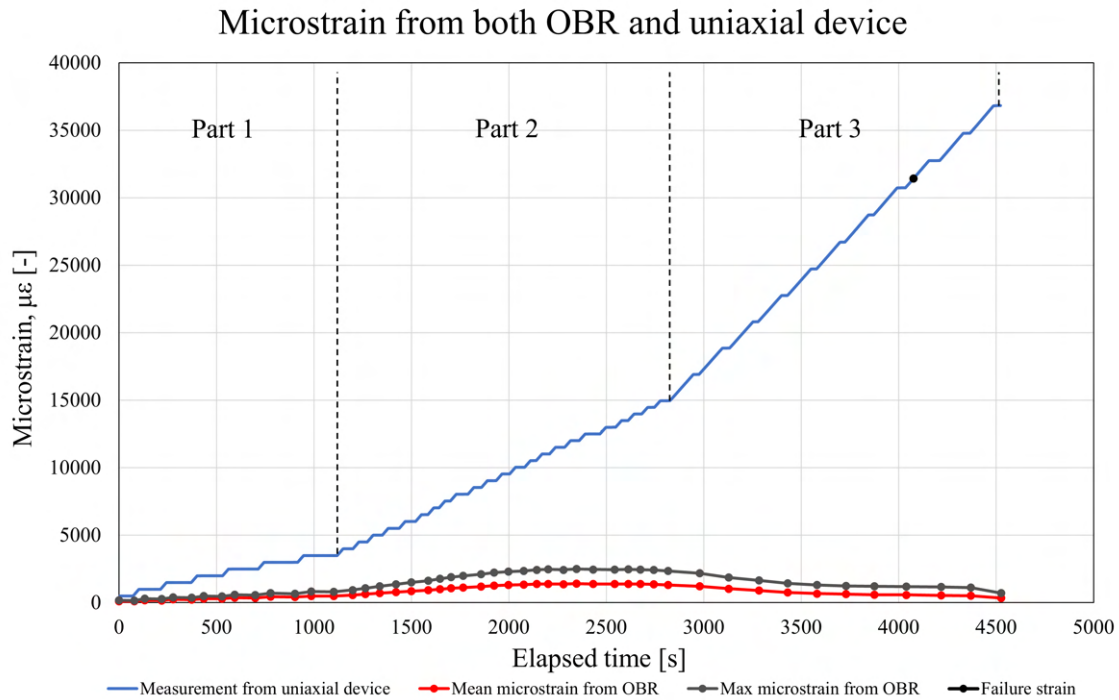
The uniaxial graph in Figure 9.8 has a slightly different shape than the similar graph in Figure 9.7. While the trend of the uniaxial graph for Sample 1 is relatively linear throughout the whole test, the graph for Sample 2 is tripartite. This is because the second strain test consisted of three parts of different procedures, whilst in the first test the procedure was more or less the same throughout the test. The three parts of the graph come from relaxation testing (part 1), normal testing (part 2) and ramp-up of both step and rate of the deformation (step 3).



**Figure 9.8:** Strain, measured with both the DFOS-technology and the uniaxial device, plotted against the time which has elapsed since the compression of Sample 2 was initiated.

### 9.4.3 Strain magnitude of Sample 3

Lastly, the comparison of the results from the DFOS-technology with the results from the uniaxial device for Sample 3 is shown in Figure 9.9. The testing procedure in strain test number three was the same as the one which was used for Sample 2. Hence, the shape of the uniaxial graph in Figure 9.9 is similar to the corresponding graph in Figure 9.8. Equally as for both of the previous strain tests, the measurements conducted by the DFOS-technology for Sample 3 are considerably lower than the values that are calculated from the uniaxial recording. However, this was the sample that performed best of the three with regards to the DFOS-measurements. When the cable slipped in Sample 3, it measured a maximum strain of 2493  $\mu\epsilon$ . At the same time, the uniaxial device showed a deformation that corresponded to a strain of 12000  $\mu\epsilon$ .



**Figure 9.9:** Strain, measured with both the DFOS-technology and the uniaxial device, plotted against the time which has elapsed since the compression of Sample 3 was initiated.

## 9.5 Shape of the strain profiles

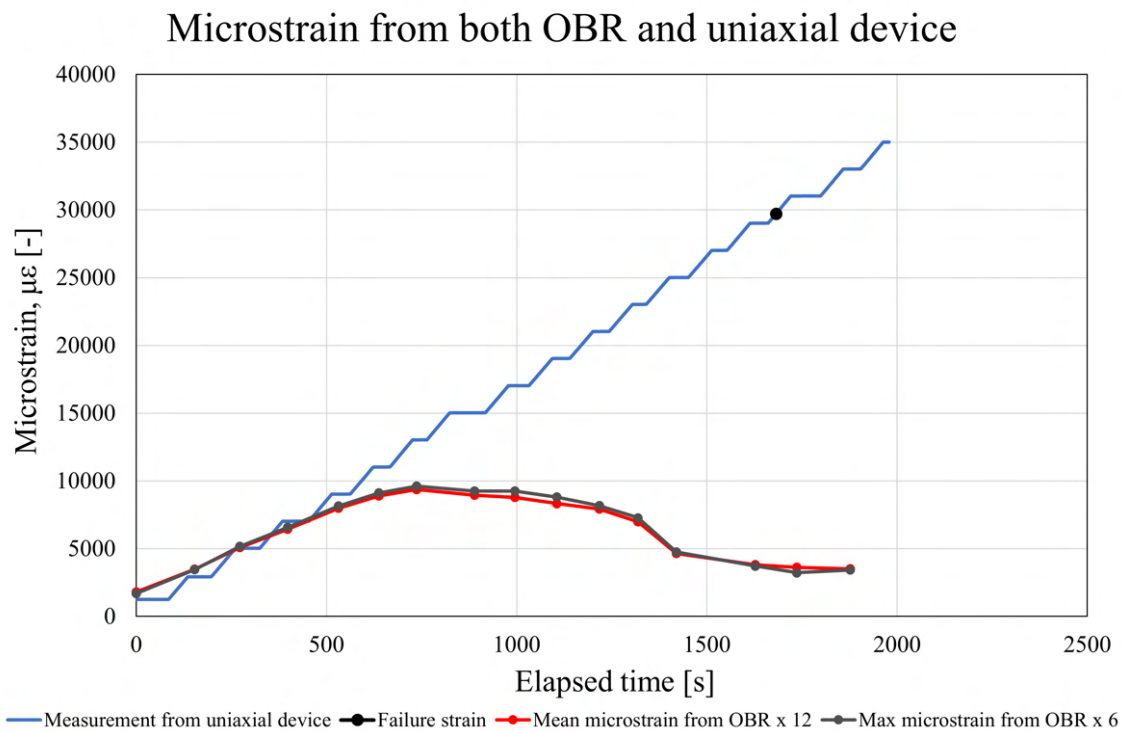
The much lower strain measurements performed by the DFOS-system compared to the calculated strain based on the deformation recordings, as seen in the plots above, indicated that there were problems with transferring the complete load into the cable due to insufficient bonding. However, it appeared like the cable had good adhesion with the samples. The assumption of good adhesion between the fiber optic cable and the stabilized soil was based on visual inspection and pulling of the cable. After the samples had failed, tests of pulling the cable out of the samples were performed by hand. The samples were also opened, to investigate the bonding between the cable and the samples. By pulling, and visual inspection, it seemed like the cable stuck relatively well to the samples, despite the problems that had been seen related to bonding. Hence, comparisons between the shapes of the uniaxial curves and the DFOS curves have been carried out for all three samples.

Figures 9.10, 9.11 and 9.12 shows the DFOS data for the three tests, separately. The DFOS data was multiplied by factors that allowed a more direct comparison between the shape of the obtained DFOS and uniaxial data. It has to be stressed that this multiplication of the graphs with some factor is done solely to compare the shapes. The chosen approach provides further insight to the performance of the DFOS-measurements with regard to shape of the graphs.

In the three plots, the strain development calculated based on the deformation recordings is referred to as "Measurement from uniaxial device". Further, "Max" refers to the maximum strain of the DFOS measurement points along the stabilized soil sample and "Mean" refers to the mean value of the DFOS measurement points. The factors that the DFOS measurements were multiplied with are shown in the corresponding labels.

### 9.5.1 Shape of strain profiles for Sample 1

The plot comparing the trend of the DFOS-measurements with the uniaxial calculations for Sample 1 is shown in Figure 9.10. The DFOS graph with the mean strain values has been multiplied by 12, while the graph with the maximum strain values was multiplied by 6. It can be observed from Figure 9.10 that the DFOS graphs are following the uniaxial graph to a certain extent for the first 5-6 measurements, however, the inclination of the graphs are smaller than for the uniaxial graph. It is also worth noting that the shapes of the multiplied mean and maximum graphs from the OBR are very similar. This means that the maximum strain values were roughly twice as high as the mean strain values measured with the DFOS-technology for the first test.



**Figure 9.10:** A comparison of the shape of the graph from the uniaxial calculation with the shapes of the DFOS curves for Sample 1.

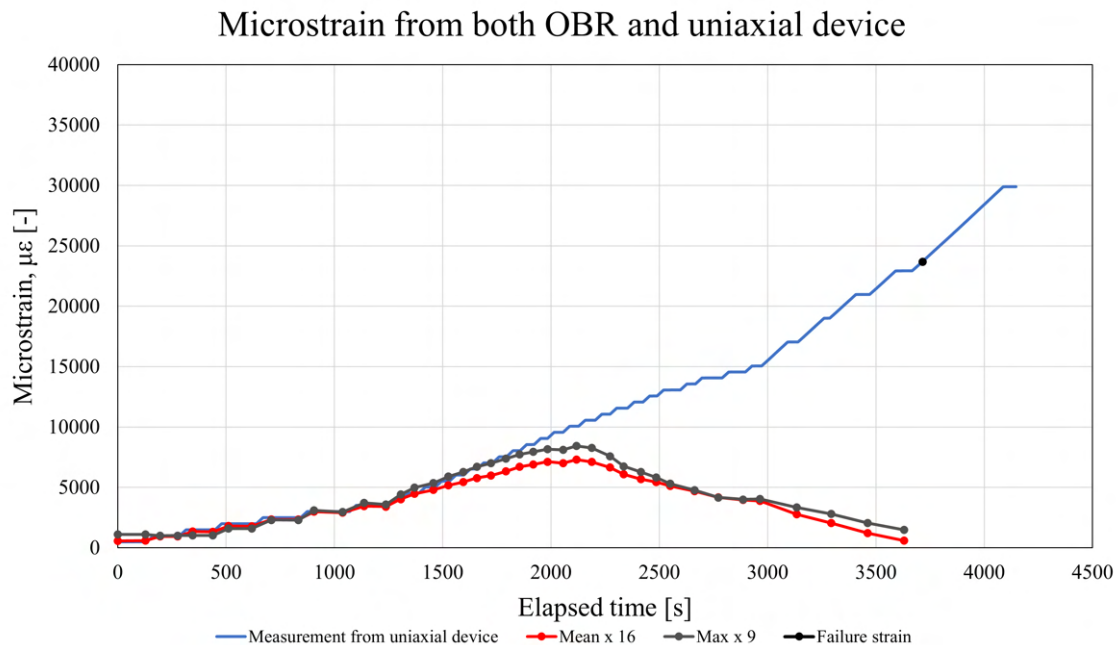
To summarize, some observations were made before the decoupling between the fiber optic

cable and the stabilized soil occurred. The maximum strain values from the DFOS measurements were about 6 times lower than the uniaxial measurements, and the mean strain values were 12 times lower. Hence, the average strain values derived from the DFOS data were approximately 50% lower than the maximum values.

### 9.5.2 Shape of strain profiles for Sample 2

The shape comparison for Sample 2 is shown in Figure 9.11. The mean graph obtained from the measurements performed by the OBR has here been multiplied by 16, whilst the corresponding maximum graph has been multiplied by 9. In other words, the average strain values from the DFOS were about 16 times lower than the calculations based on the uniaxial deformation recordings. The maximum values were approximately 9 times lower than the uniaxial calculations, which means that the mean strain measurements from the DFOS were about 43% lower than the corresponding maximum values.

These graphs followed the uniaxial graph to a higher degree than what was the case for the first strain test. It can also be observed from Figure 9.11 that the mean graph has the best fit at the beginning of the test, whilst it is the maximum graph that has the best fit in the later stages of the test. The change from the mean graph having the best fit to the maximum graph having the best fit occurs after the first 14 measurements, in other words, after the relaxation tests were finished. The shape of the maximum graph starts to deviate from the shape of the uniaxial graph after measurement numbers 24-25.

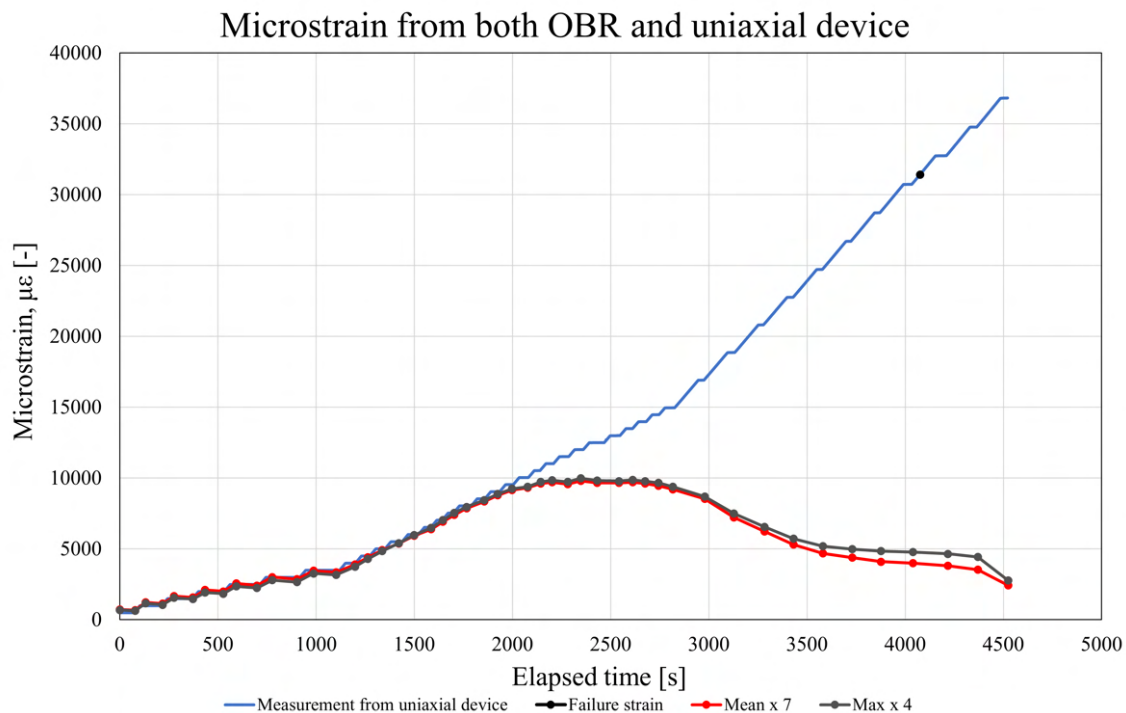


**Figure 9.11:** A comparison of the shape of the graph from the uniaxial calculation with the shapes of the DFOS curves for Sample 2.

### 9.5.3 Shape of strain profiles for Sample 3

Figure 9.12 presents the comparison between the shape of the DFOS graphs and the uniaxial graph for the third strain testing. The mean graph from the OBR is here multiplied by 7, while the corresponding maximum graph is multiplied by 4. This means that the mean strain values from the DFOS measurements are 7 times lower than the uniaxial calculations, while the maximum strain values from DFOS are 4 times lower than the calculations. The results showed that the average strain values were approximately 43% lower than the maximum strain values from the DFOS measurements.

Both of the DFOS graphs follow the shape of the uniaxial device curve very closely. Once again, the third strain testing proves to be the best of the three tests with regard to the performance of the DFOS-system. The shapes of both graphs are extremely similar to the shape of the uniaxial graph. In addition, this is the test where the graphs had the lowest multipliers. In other words, this was the numerically most similar test as well, and this has already been discussed in the previous sections.



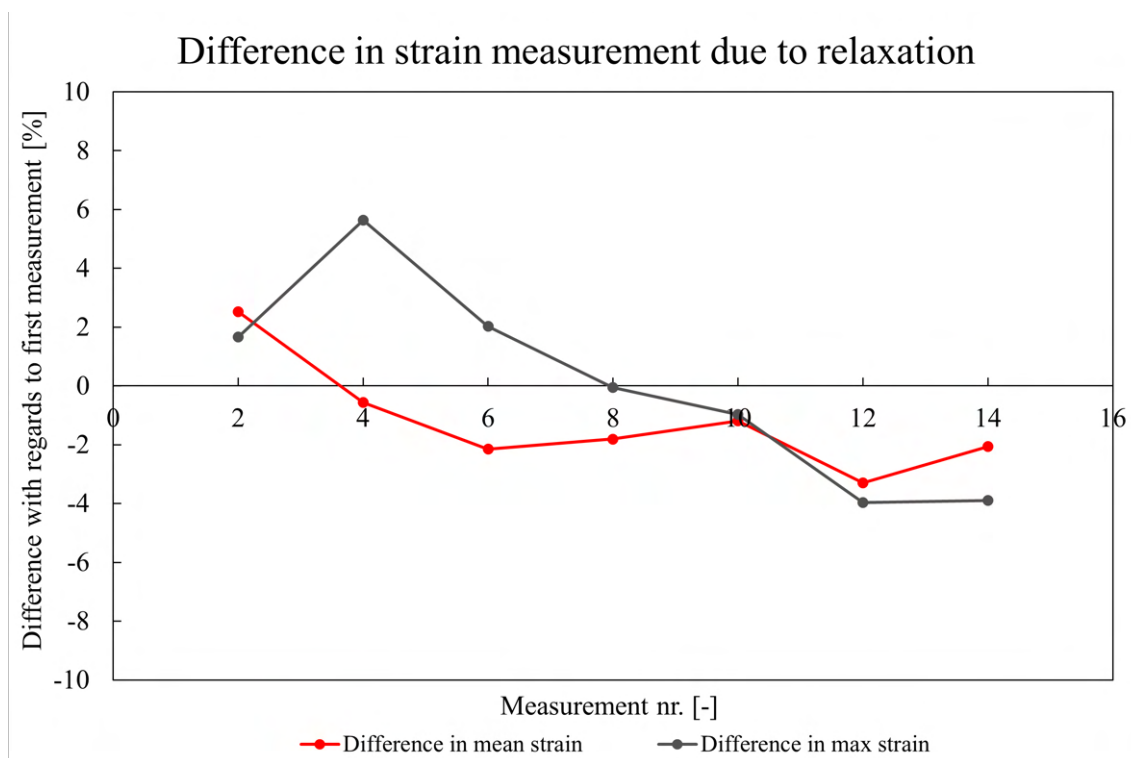
**Figure 9.12:** A comparison of the shape of the graph from the uniaxial calculation with the shapes of the DFOS curves for Sample 3.

## 9.6 The effect of relaxation for the two last tests

For the two last strain tests, evaluations of the effect of relaxation on the strain measurements from the DFOS-system were carried out. For visualizing this effect, plots of the difference in the DFOS-scan conducted approximately 1 minute after the deformations were stopped relative to the DFOS-scan performed immediately after the deformations were stopped have been made. This difference is given in percentage relative to the scan performed immediately after the deformations were stopped. Positive difference means that the strain measurement after 1 minute gave higher strain values than the first measurement. Oppositely, a negative difference means that the strain measurement after 1 minute gave lower strain values than the first measurement.

### 9.6.1 The effect of relaxation for Sample 2

Figure 9.13 is showing the evaluation of the effect of relaxation during the second strain test.



**Figure 9.13:** The percentage differences in the second measurements compared to the first measurements, with positive difference indicating that the measurements after 1 minute was the highest. An evaluation of the effect of relaxation for Sample 2.

It has to be stressed that for the first measurements, the maximum strain was measured at



the upper point of the sample. In this zone it was observed a crater, leaving a situation of no bonding between the cable and the LC-sample. In addition, the plastic block used to transfer the load from the piston to the sample had a slightly too thin slot. In the beginning of the second strain test, the cylinder hung on the cable, and it is reasonable to assume that it was this confounding effect from the hanging cylinder that was measured as the maximum strain on the lower strain levels. Hence, the results on the lower strain levels from the second strain test shown in Figure 9.13, and especially the maximum values, should be interpreted cautiously.

The data in Figure 9.13 shows that the maximum strain is higher in the measurement after 1 minute compared to the first measurement in the three first tests. The maximum strain is equal in the fourth test, and becomes negative for the remaining tests. The fact that the strain is higher after 1 minute of relaxing can seem counterintuitive, as there is no more deformation applied to the sample compared to the first measurement. The reason for this positive difference in maximum strain for the first few tests is most likely the plastic cylinder that hung on the top part of the cable. This phenomenon gave high strain values that did not represent the strain in the stabilized soil sample. The mean graph became negative already from the second test, this is due to the remaining DFOS measurement points giving strain in the sample and did not have any confounding effect. These measurements smoothed out the issue related to the maximum value measurement.

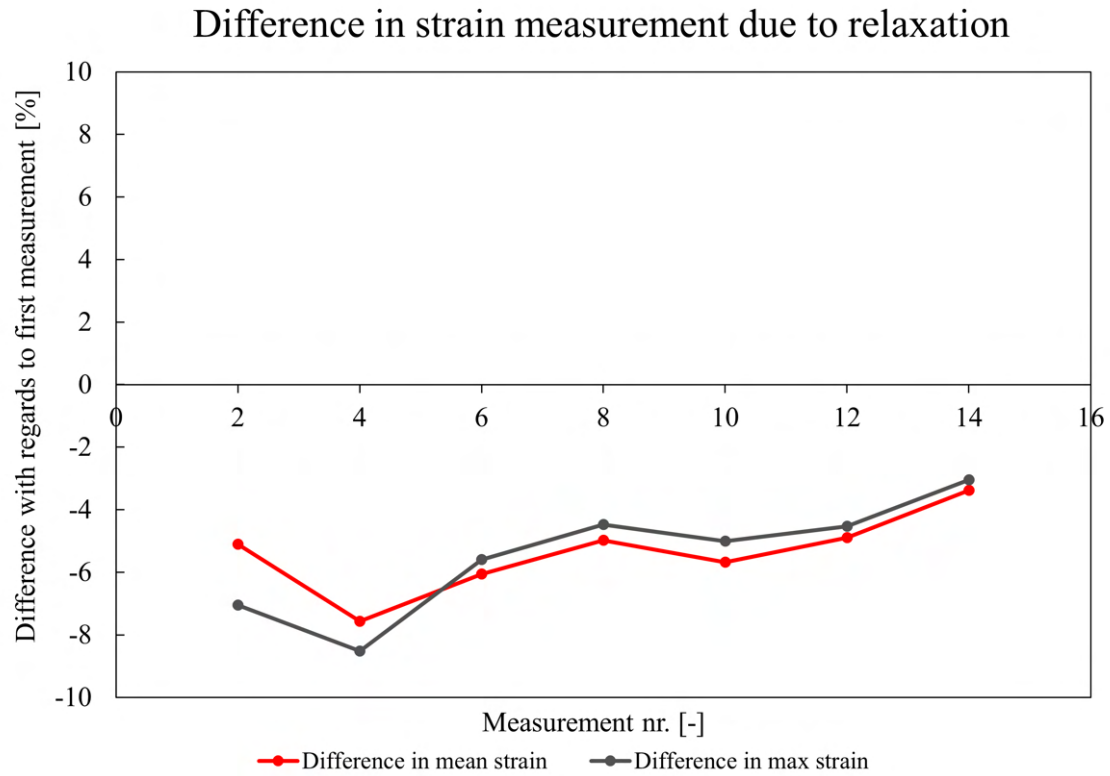
### 9.6.2 The effect of relaxation for Sample 3

Equally as for Sample 2, the effect of relaxation has been visualized by plotting the percentage differences in the second measurements compared to the first measurements. The result is shown in Figure 9.14. The rigid plastic block was not observed hanging on the fiber cable, and the maximum strains did not occur in the top zone of the cable. Hence, the situation of Sample 3 was probably more representative with regards to enabling evaluation of the relaxation effect.

What can be observed from Figure 9.14 is that the strain measured after some while is lower than the strain measured immediately after the deformation was stopped. Actually, for the low strain levels, this difference was not negligible. The largest difference measured was above 8%. In other words, an effect of relaxation on the strain measurements for Sample 3 was observed. It can also be seen from Figure 9.14 that the effect of the relaxation decreased with increasing deformation level.

These relaxation data showed that the time of measurement after loading could play a role in the measured strain. It also showed, for Sample 3, that the difference in strain measurement conducted at different times decreased with higher strain levels. The results indicate that there might be some uncertainties related to how exactly the strain is measured.

---



**Figure 9.14:** The percentage differences in the second measurements compared to the first measurements, with negative difference indicating that the measurements after 1 minute was the lowest. An evaluation of the effect of relaxation for Sample 3.

# Chapter 10

## Discussion

In the following sections, the results of both the temperature tests and strain tests are discussed.

### 10.1 Discussion of the temperature tests

In this section, the results from both the standard temperature tests and the cross-sectional temperature test are discussed. The aim of the standard temperature tests was to examine whether layers of unstabilized clay within stabilized soil columns could be detected. The cross-sectional temperature test was carried out to investigate if there was any radial heat transfer in the test setup.

#### 10.1.1 DFOS to measure temperature during curing

The results have shown that DFOS can be used to measure the temperature change during curing. Temperature development with time was produced for several points along the height of both parts of the layered samples. Additionally, the DFOS system verified how the heat from the stabilized soil was transferred to the unstabilized soil layer. It clearly showed how the temperature was transferred both spatially and temporally. Despite some differences relatively to other temperature measurement methods, which were applied as reference measurements, the system based on the DFOS-technology was able to record the trend of the temperature changes in the soil sample.

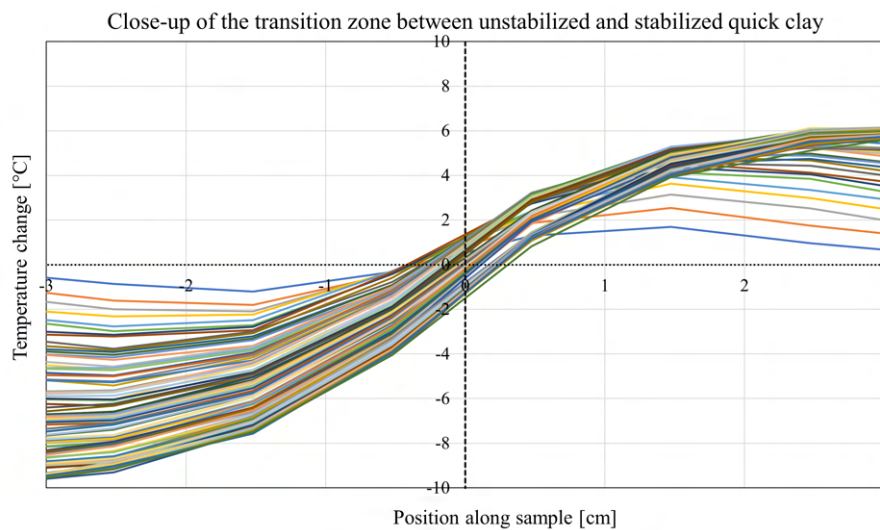
However, it can not be reliably stated that the exact temperature in a stabilized soil column can be measured based on the performed temperature tests. This is because the reference measurements that have been performed are not satisfactory to verify that the DFOS-measurements have given the exact temperature development. In addition, the DFOS-technology gives relative values, in other words, it does not give the absolute temperature in the soil columns. Hence, some additional temperature sensors are needed to measure the starting temperature of the

soil in order to know the absolute temperature. Bache et al. (2022) and Helle et al. (2022) are examples of researchers that have used some standard temperature sensors for monitoring the curing of in situ stabilized soil columns.

New possibilities would be created if, in further work, such a mentioned DFOS measurement system combined with some standard temperature sensors is implemented and investigated to give reliable results of absolute temperature curing. This would enable the possibility to reliably estimate the strength and stiffness of an entire column of stabilized soil based on the maturity concept.

### 10.1.2 DFOS to detect weakness zones

The aim of the temperature tests in this M.Sc. Thesis was not limited to accurately measuring the absolute temperature in stabilized soil. The aim was also to detect thin layers of unstabilized soil within stabilized soil columns, and that was successfully achieved. A signature profile was observed around the transition zone from the stabilized quick clay to the unstabilized, remolded quick clay. Figure 10.1 shows a close-up of the exhibited signature temperature profile from the second temperature test.



**Figure 10.1:** A close-up of the temperature change signature in the transition zone of the second temperature test.

By looking at Figure 10.1 a distinct transition from stabilized soil to unstabilized soil can be seen. As thoroughly described in previous chapters, the measurements were performed after the heat generation in the stabilized soil due to the hydration process had reached its peak. Figure 10.1 clearly visualizes that while the temperature was dropping in the stabilized soil, the unstabilized layer experienced a heat rise. This resulted in a clear signature of the plots close to the material change zone.

---

In the field, it would probably never be totally unstabilized layers within stabilized soil columns despite any possible imperfections in the creation of the columns. The imperfections could be layers that are not 100% stabilized, where the binders have not been perfectly distributed in those layers. In other words, a situation with LC-columns containing some thin layers of less stabilized soil can occur. Heat transfer between layers will happen also in these situations, and a temperature signature similar to what is shown in Figure 10.1 will occur.

In these situations with layers of less stabilized soil, the irregularities will also generate heat as they are mixed with binders, however, the heat generation will be lower than for the layers of perfectly distributed binders. Hence, the temperature signature will for these situations be similar to the trace shown in Figure 10.1, but now both zones will experience a temperature decrease after the peak heat from the hydration process has been reached. In other words, the temperature signature will be similar, but all values will be negative, which means that the whole trace is below the origo in the y-direction. Additionally, the temperature signature will not be as distinct when the difference in temperature generation is not as big as it is between a stabilized layer and a completely unstabilized layer.

Based on the findings from the plots in Chapter 8, the use of DFOS for detecting imperfections in stabilized soil columns seems to be possible. The findings suggest that layers of unstabilized clay of thickness less than 5 cm may be effectively identified. From the results of the performed laboratory tests of heat transfer, it was observed that changes occurred continuously during the first hours after mixing before steady-state was reached after approximately 16 hours. However, the biggest changes took place in the first approximately 5 hours. Hence, if a DFOS-system is installed within at least the first 5 hours after construction of the stabilized soil columns, it should probably be possible to detect any weakness zones.

It also has to be stressed that the tests performed in this M.Sc. Thesis are limited to the laboratory scale, and the situation will be slightly different in situ. Thus, field tests should be carried out to verify the performance of a DFOS-system for monitoring the temperature development during curing of stabilized soil. The LC-columns are not isolated in the same manner as what was the case in these laboratory tests. Heat transfer will also occur radially to the surrounding, unstabilized soil. It is also worth mentioning that temperature development may take some more time in the field, as this situation is not a perfectly controlled and isolated environment in the same way as the temperature tests performed in this M.Sc. Thesis. It may also be that the assumption of a more time-consuming heat development in the field not is true. Regardless, it is reasonable to assume that installation of a DFOS-system within 5 hours after mixing of LC-columns would be sufficient to detect possible weakness zones. The detection system would be investigating the heat transfer in the stabilized soil column for possible temperature signatures similar to the one shown in Figure 10.1 to detect possible weakness zones.

### 10.1.3 Uncertainties related to the temperature tests

Heat transfer in the radial direction was investigated in this M.Sc. Thesis because some degrees Celsius difference between the DFOS measurements and the measurements from the thermo-

---

couples was observed. The temperature measurements performed by the DFOS-technology was giving higher temperature changes than the measurements from the thermocouple. The study of radial heat transfer was carried out in order to find out whether there actually was a temperature difference for the two different positions of the soil sample or if the temperature sensors were providing different results for equal temperature exposure. The results conducted by the standard PT100 thermoelements in the cross-sectional temperature test indicated that no heat transfer of interest appeared along the cross-section. In other words, the cross-sectional temperature test uncovered performance differences between the two different sensor types.

The fact that the thermocouples gave lower temperature changes than the DFOS system was probably a result of their design. The design of the thermocouples that were integrated into the isolation box can be seen in Figure 5.1b. The setup of the thermocouples was made of a steel material that was embedded into the XPS-plates of the isolation box.

By comparing with both the centrally placed fiber core and measurements conducted by a PT100 thermoelement in a reference sample it seemed as though the thermocouples were not heated as much as they should. It might be that the steel material thermocouple led some of the heat away from the sensor. Also, the fact that the sensor was surrounded by isolation material, and not fully embedded into the clay, had without doubt an effect on the temperature that was measured by the thermocouple at each point in time. The thermocouple was heated in another manner than the other temperature sensors. As the thermocouple was not heated as much as the other temperature sensors, the temperature changes from the thermocouple were naturally not as significant as for the other measurement methods.

The thermocouple was the main reference for the DFOS-measurements. As there were a few uncertainties related to this temperature sensor, the DFOS-system's ability to measure exact temperature changes can not be sufficiently verified by the research performed in this M.Sc. Thesis. Better reference measurements should indeed be utilized in future work.

## 10.2 Discussion of the strain tests

In this section, results from the three unconfined compression tests, where the aim was to measure the strain development of the samples when being compressed, are discussed.

### 10.2.1 Strain profiles

For the strain tests, one of the plots that was made was a plot of measured strain against elapsed time since the first DFOS-measurement was conducted. The plot consisted of one graph of strain calculated from recordings of the uniaxial device, one graph of the mean strain along the fiber cable inside the samples and one graph of the maximum strain along the fiber cable inside the samples. As described in Chapter 8, all of the different DFOS-graphs were multiplied with some scaling factor in one of the plots, and this was solely done to compare

---

the shapes of the graphs. First of all, the shapes of the mean and maximum graphs were very similar within each sample.

However, an even more interesting finding was the fact that the trends of the DFOS-graphs were comparable to the uniaxial-graph for all three samples until the cable slipped. For Sample 1, the shapes were comparable, but the DFOS-graphs did not have as high an inclination as the uniaxial graph. Hence, the trend looked relatively similar, but the differences increased with time. However, the DFOS-graphs for both Sample 2 and Sample 3 followed the uniaxial graphs extremely precisely. The fact that the shapes of the graphs are so similar, tells that the cable must have followed the deformation of the samples. The deformations were transferred from the stabilized soil to the fiber but to a much lower degree. There must have been relatively good adhesion between the fiber optic cable and the surrounding stabilized soil. The shapes of the curves are compared in Figures 9.10, 9.11 and 9.12.

### 10.2.2 Strain magnitude

Despite the shapes of the curves from the two different measurement methods being similar, the numerical values were very different between the methods. In Sample 2, where the values were farthest apart, the mean and maximum graphs were multiplied by 16 and 9 respectively in order to be able to compare the graphs. For the best-performing sample, the corresponding graphs were multiplied by 7 and 4 respectively. In other words, the strain values measured by the DFOS-technology was far away from the exact strains in the samples. The fact that the graphs of Sample 2 had to be multiplied by 16 and 9 indicates measurements that are extremely far from what is correct. However, multiplication by 7 and 4 is still too far off for the results of the measurements with this new method to be acceptable.

To summarize, the strain values that were measured by the DFOS-technology in relation to this M.Sc. Thesis are considerably lower than the theoretical axial strain in a uniaxially loaded stabilized soil sample. The interaction between a stiff cable and a less stiff stabilized soil sample causes the fiber optic cable to measure different strains than what is calculated based on the deformation recordings. For the given stiffness difference between the cable and the stabilized soil, the dimensions of the samples are too small for the entire load to be transferred from the stabilized soil to the cable.

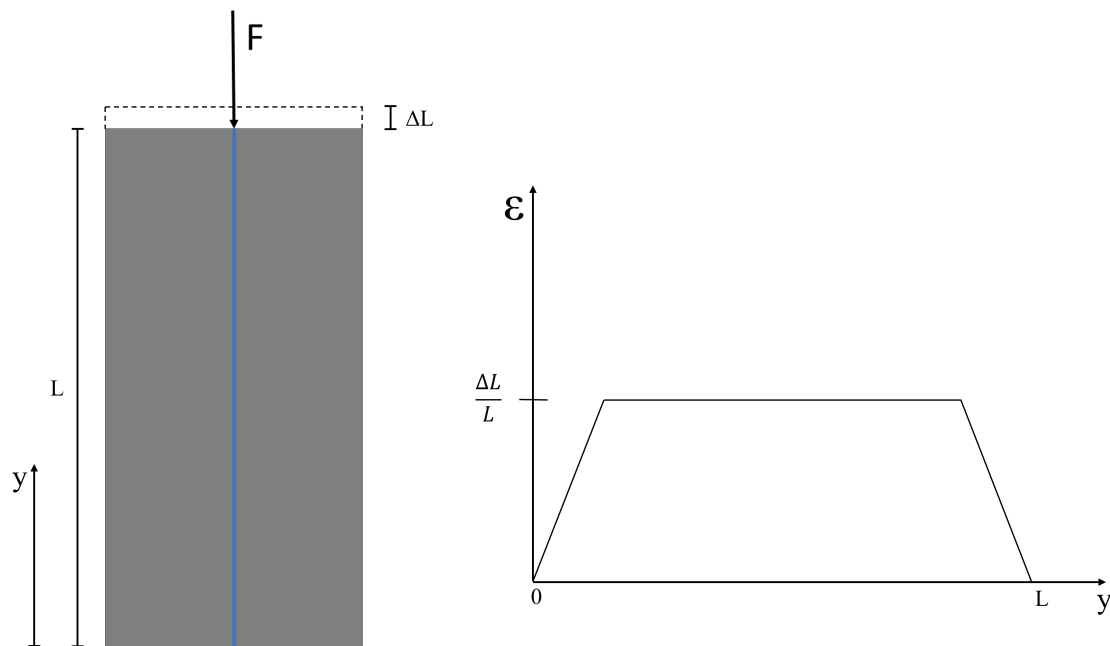
### 10.2.3 The role of interface bonding

Bond has been a big challenge for strain monitoring with Distributed Fiber Optic Sensing (DFOS) in the discussed laboratory tests. This is despite the good adhesion that was observed between the fiber optic cable and the lime/cement-stabilized material, as described above and seen in Figure 10.6a.

The shapes of the DFOS-scans are not similar to what is theoretically expected, as mentioned in Section 9.3. For a sample being uniformly compressed, a constant strain level is expected

---

throughout the height of the sample. However, when the strain is to be measured by an embedded fiber optic cable some length is needed at both ends to reach the given strain level. Hence, a roughly linear development of the strains is expected from both ends, before the correct strain level is reached and a plateau is formed for the remaining part of the strain curve. Chapeleau and Bassil (2021) has studied the strain profiles of fiber optic cables, and even though the strain build-up to the correct strain plateau is not perfectly linear, this assumption has been used in the following. This simplification is also used in the concrete industry. A schematic drawing of the theoretical simplified strain profile is shown in Figure 10.2.



**Figure 10.2:** The theoretical strain profile from a fiber optic cable that is embedded in a compressed sample.

In Chapter 9, a more sinusoidal-like shape was observed for the plots of strain along the height of the samples. The graphs had a distinct maximum point more or less in the middle of the height, and strain was building up to this strain level from both sides. In other words, there were no plateaus developed for the strain profiles. This is related to the mentioned lack of bonding between the fiber optic cable and the surrounding material. With the setup that has been used for these tests, it was not been possible to transfer the full load into the fiber optic cable. This is clearly observed from the deviating shapes of the curves.

The EpsilonSensor fiber optic cable had a stiffness of 3 GPa. In other words, the stiffness of the fiber cable was a lot higher than the stiffness of the LC-samples. In fact, the stiffness was approximately 60 times higher than Sample 2 and Sample 3, and the cable was more than 100 times stiffer than Sample 1. A plot of the stiffness ratio between the stiffness of the fiber cable and the LC-sample for all three samples is included in Appendix E. This situation was somehow similar to what is the case for reinforcement bars in concrete. Also reinforcement



bars need some length to accommodate the load from the concrete, and it exists formulas to calculate this length. In the following, a calculation of the required bonding length for being able to transfer the load from the LC-sample into the cable based on formulas from the concrete industry is carried out. It has to be stressed that concrete and lime/cement-stabilized quick clay is not entirely the same material, this calculation is performed solely to visualize the problem related to the bonding of the cable.

First of all, a fundamental assumption for the following calculation is the assumption of a full bond between the fiber cable and the surrounding material. We know that this was most likely not the case. By assuming a full bond, the lime/cement-stabilized clay and the fiber optic cable has to be compressed equally. In other words, the strain in the fiber cable should be equal to the strain in the LC-clay when there is a full bond, and it is this assumption that provides the first line in Equation 10.3. This condition, together with Hooke's law (see Equation 10.1), has been used to derive a formula for the force in the fiber cable as a function of the force in the surrounding LC-clay.

The force applied from the uniaxial device on the system has to be taken up by the LC-material and the fiber cable. Hence, the sum of the force in the fiber cable and the force in the LC-material has to be equal to the applied force. The derivations of both the expression of the distribution of the total force and the expression of the force in the fiber cable as a function of the force in the LC-sample are shown below. The expression for the total force is shown in Equation 10.2, while the expression for the force in the fiber cable is derived in Equation 10.3.

$$\sigma = E \cdot \varepsilon \quad (10.1)$$

$$F = F_{FC} + F_{LC} \quad (10.2)$$

$$\begin{aligned} &\text{Assuming full bond} \rightarrow \varepsilon_{FC} = \varepsilon_{LC} \\ \rightarrow \frac{\sigma_{FC}}{E_{FC}} = \frac{\sigma_{LC}}{E_{LC}} &\rightarrow \frac{F_{FC}}{\frac{\pi}{4} \cdot \varphi_{FC}^2 \cdot E_{FC}} = \frac{F_{LC}}{\frac{\pi}{4} \cdot \varphi_{LC}^2 \cdot E_{LC}} \rightarrow F_{FC} = \frac{\varphi_{FC}^2 \cdot E_{FC}}{\varphi_{LC}^2 \cdot E_{LC}} \cdot F_{LC} \end{aligned} \quad (10.3)$$

In these equations  $F$  means force,  $\sigma$  means stress,  $E$  means stiffness (Young's modulus),  $\varphi$  means diameter and  $\varepsilon$  means strain. "FC" is short for Fiber Cable and "LC" is short for Lime/Cement. It is important to not confuse  $\varphi$  with the geotechnical parameter which is friction angle.  $\varphi$  was chosen because this is what is used in the concrete industry in the formulas that will be presented below. The diameter of the EpsilonSensor was  $\varphi = 3$  mm.

To be able to continue the calculations and perform comparisons, a loading situation for the LC-samples need to be known. The force that was applied from the uniaxial device is needed to calculate the needed bonding length, and both the calculated and the measured strain was needed to carry out any comparison. Hence, the loading situation for Sample 3 (the best-performing sample) at 1% strain according to the deformation recordings of the uniaxial device

---

was adopted. In this situation the force that was applied was  $F = 3.166$  kN, the calculated strain was  $\varepsilon = 1\%$  and the maximum measured strain from the DFOS-scans was 0.23%.

By putting in  $F = 3.66$  kN, in addition to the values related to stiffness and diameters, it could be found that the force that theoretically should be taken by the fiber cable at the given loading situation was  $F_{FC} = 0.17$  kN. All calculations related to the required bonding length are attached in Appendix E.

When the force that was supposed to be transferred into the fiber optic cable was known, the concrete formulas could be utilized to calculate the required bonding length for the given situation. The formulas were taken from Eurocode 2 (Standard Norge 2021). The bond strength,  $f_{b,d}$ , of the composite structure of the fiber cable and the LC-stabilized quick clay was calculated from Eq. (8.2) in EC2, 8.4.2(2) (Standard Norge 2021). This is, normally, a measure of the quality of the bond between concrete and its reinforcement. Eq. (8.2) in EC2 corresponds to Equation 10.4 in this M.Sc. Thesis. The required bond length,  $L_{b,rqd}$ , for the fiber cable under the given loading situation was calculated by the use of Eq. (8.3) in EC2, 8.4.3(2) (Standard Norge 2021). This corresponds to Equation 10.5 presented below.

$$f_{bd} = 2.25 \cdot \eta_1 \cdot \eta_2 \cdot f_{ctd} \quad (10.4)$$

$$L_{b,rqd} = 0.25 \cdot \varphi_{FC} \cdot \frac{\sigma_{FC}}{f_{bd}} \quad (10.5)$$

$\eta_1$  and  $\eta_2$  in Equation 10.4 are parameters developed for concrete, where the first one is dependent on bond conditions and placement of the rebar while the last one is dependent on the bar diameter.  $\eta_1$  is equal to 1 for "good" bond conditions and  $\eta_2$  is set to 1 for bar diameters smaller than 32 mm. In the calculations on required bond length performed here both  $\eta_1$  and  $\eta_2$  were assumed to be equal to 1.  $f_{ctd}$  in Equation 10.4 refers to the tensile strength of the concrete. In these calculations, the tensile strength of the LC-stabilized material was assumed to be 10% of the ultimate compressive strength ( $q_u$ ) that was presented in Table 9.1.

The required bond length, in other words, the length that is needed to transfer the full load from the LC-sample to the fiber cable, is calculated to be  $L_{b,rqd} = 116.5$  mm. This length was needed from both ends in order to fully transfer the load to the cable. In other words, the samples should have been longer than  $L = 2 \cdot L_{b,rqd} = 233$  mm. The samples were only 200 mm in height, in other words, they were not long enough to transfer the full load into the fiber cable, and the plateau described in 10.2 was never reached. The claim that perhaps the full force had not been implemented to the cable based on the strain profiles from the DFOS-measurements is now further supported.

By assuming a linear build-up of strain in the fiber optic cable as shown in Figure 10.2, it was possible to calculate what the real strain in the cable actually was. Because, when the required bond length is longer than half the height of the sample, and full bond is hence not achieved, the force in the fiber optic cable was not the calculated  $F_{FC} = 0.17$  kN. By assuming the linear

---

relation and using a simple geometric relationship, the real stress and strain in the cable were calculated. These calculations are shown in Appendix E. The real strain in the fiber optic cable based on these relations, and the presented formulas for bond in concrete, was calculated to be  $\varepsilon_{FC,real} = 0.674\%$ .

This strain was still not the same as the strain measured by the DFOS-scans, however, 0.674% was much closer to 0.23% than 1%. It also has to be stressed that the tested stabilized soil and fiber optic cable was not reinforced concrete, and hence the formulas and parameters are not developed for the tested material. It is likely that the empirically derived parameters  $\eta_1$  and  $\eta_2$  should be lower for lime/cement-stabilized quick clay. In addition, the estimation of  $f_{ctd} = 10\% \cdot q_u$  is quite rough an approximation. In other words, it is quite likely that the bond strength of the interface between the fiber optic cable and the stabilized clay should not be as high as what was calculated based on the bonding situation between concrete and a reinforcement bar. A lower bond strength would result in a longer required bond length, and thus also a lower real strain in the fiber cable.

There are several other uncertainties and assumptions related to the calculations that have just been presented. For example, the use of Hooke's law, which requires a linearly elastic material, was a simplification. In addition, it has to be mentioned that the bond between the fiber cable and the stabilized soil at the two ends of the samples did not exist. Small craters were formed at both ends of the samples. These craters were several millimeters ( $\sim 10$  mm) in height, leading to the effective bonding length of the cable being shorter than the height of the sample ( $H = 200$  mm). This loss of effective length further reduced the achieved bond length compared to the required bond length, which again influenced the DFOS-measurements. A picture of the imperfections from Sample 2 is included in Figure 10.3.



**Figure 10.3:** A crater at the top of Sample 2 causing no bonding in this upper area. The same situation was observed at the bottom.

---

However, the calculations that were performed on the topic of bonding are not supposed to be exact calculations of the real strain in the cable or the bond strength. The calculations were carried out to visualize the problem with the bonding that arose for the chosen laboratory setup. The samples were too short for the fiber cable to fully take up the load, and hence also too short for the DFOS-technology to measure the correct strain. For future testing, to avoid problems related to bonding, either the dimensions have to be changed or the stiffnesses have to be changed. Decreasing the diameter of the fiber optic cable, increasing the diameter of the LC-sample or decreasing the stiffness ratio are possible measures that can be taken without changing the length of the samples, to effectively avoid bond problems. These measures would, according to Equation 10.3, decrease the force that should be transferred from the sample to the cable, and hence also decrease the required length to transfer this load ( $L_{b,rqd}$ ). Else, the sample length can be increased, so that it gets longer than two times the calculated required bond length. In Appendix E, a parametric study on how the required bond length is changed by changing some of the mentioned parameters is included.

The lack of sufficient bonding length between the fiber optic cable and the stabilized soil is most likely the biggest reason why reliable strain values have not been achieved from the strain monitoring based on the DFOS-technology.

#### 10.2.4 Bond loss at cable slippage

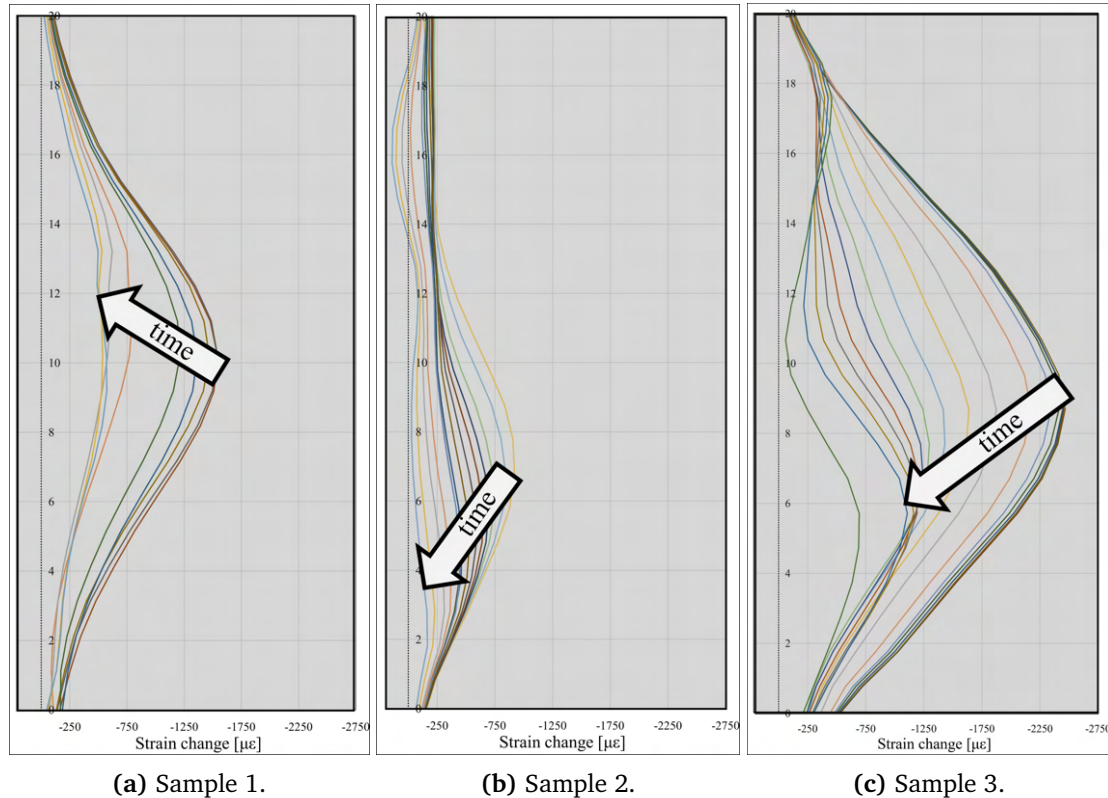
As already discussed extensively, bonding between the fiber optic cable and the lime/cement-stabilized material is essential for good quality measurements from the DFOS-technology. Cable slippage is evidently proof of this. At some point, the bond between the fiber cable and the stabilized clay started to be lost. This could be due to initial cracks having developed so much that the adhesion was lost.

An interesting, yet completely natural, finding from the DFOS-scans is the fact that bond is lost firstly in the areas where the first small failures initiated in the samples. The initial failures of the three samples are discussed and shown in Chapter 9. Sample 1 had an initial failure developing at the bottom, whilst the two others had their initial failures developing at the top. The fact that the bond is firstly lost at the zones of initial failure can be seen by the maximum point of the strain profiles after slippage moving towards the opposite edge of the samples. This is due to no bonding at the zone of initial failure will cause the strain to start developing in a later zone of the sample. Hence, the maximum points will have to move farther away from the zones of initial failure. The effective bond length will be shorter as well, hence also the maximum strain values will be lower.

A figure illustrating this movement of the maximum points after cable slippage is presented in Figure 10.4. Arrows are included to clearly visualize the movement of the maximum points with time. Figure 10.4a is showing how the maximum strain in Sample 1 is moving higher and higher upwards for each DFOS-scan after the cable had started to slip. This happened due to an initial failure crack developing in the bottom of Sample 1, resulting in a loss of bond at the bottom. Oppositely, the maximum strain is moving downwards for each DFOS-scan for Sample

---

2 and Sample 3. This happened due to these samples developed initial cracks in their top part, which caused bond to be lost in these zones. This can be seen from Figures 10.4b and 10.4c. What can also be seen, from all three arrows, is the fact that the maximum strain is decreasing in all Samples for each DFOS-scan. This is due to that the failures developed more and more, leading to more and more bond being lost, which again led to a shorter effective bond length. And this also happened for a continuously increasing force in the samples, which required an increasing bonding length in order to transfer the increasing load.



**Figure 10.4:** Strain measurements after the fiber optic cable has started to slip for all three strain samples.

### 10.2.5 Limitations

The quality differed between the three strain samples. With regard to mechanical properties, it was natural that the sample that was cured for only 19 days did not have the same strength and stiffness as the longer-curing samples. However, there were still some differences between the two last samples which highlighted the quality difference between the samples. Sample 1 and Sample 3 had similar failure strains, while the failure strain of Sample 2 was slightly lower compared to the two other samples. The three strain samples also showed significant differences with regard to the performance of the DFOS-system used for the samples. There were considerable differences with regard to numerical values, the capability of following the

trend of the strain developments from the uniaxial device and at which deformation level the cable slipped the samples.

The quality differences can probably be related to the preparation of the samples with an embedded fiber optic cable because the tamping procedure of the strain samples was difficult. The difficulties related to a dry and lumpy material, little accessibility in the hollow plastic cylinder and the need for good adhesion between the cable and the stabilized material. The large dimensions of the samples resulted in a more time-consuming preparation procedure, in addition to the imperfections of the samples being quite large. This time-consuming procedure resulted in the stabilized material drying more than usual, which further resulted in an even more difficult material to work with. Figure 10.5 shows how the difficult tamping procedure resulted in a lot of imperfections and cracks on the strain samples.



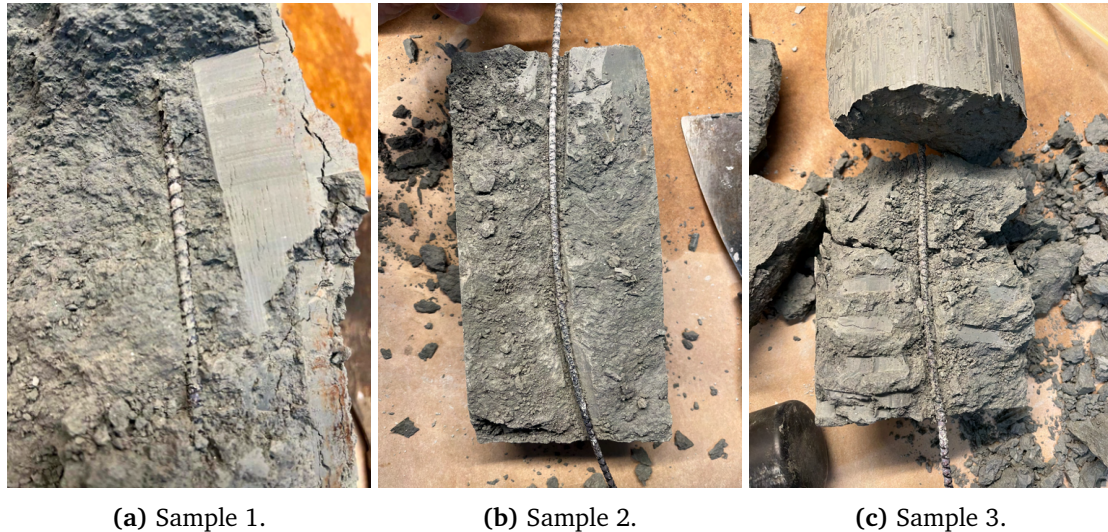
**Figure 10.5:** Sample 2 straight after it had been pushed out of the plastic cylinder it was cured inside. A lot of small cracks and imperfections can be seen.

The challenging tamping procedure made it difficult to ensure a completely vertical and centrally placed fiber optic cable throughout the whole sample height, in addition to ensuring good adhesion along the entire interface. A perfectly vertical cable is fundamental to accurately measure the axial strains of a sample. To be able to estimate how much the stabilized soil has been compressed based on the compression of the fiber optic cable, it is important that the cable is perfectly vertical. If the cable is slightly bent in a part of the sample, it is not possible to know how much the cable has been compressed axially as the cable is not compressed purely vertically. However, it is worth mentioning that a completely vertical cable is probably not achieved in the field either.

After the samples had been tested until failure, they were opened and the positioning of the cable was investigated. The positions for all three samples are shown in Figure 10.6. The

---

opening of the samples was difficult.



**Figure 10.6:** Position of the fiber optic cable in all three strain samples.

Figure 10.6 indicates that the cable in Sample 2 deviated from the ideal position (Figure 10.6b). A large bend of the cable can be seen in the bottom part of Figure 10.6b, and it must have affected the strain measurements from Sample 2. When this part was compressed, the fiber optic cable failed to adequately capture it due to the bottom part of the cable not being compressed purely vertically, despite the cable being mostly vertical. This is an interesting finding as it has been already discussed that Sample 2 was the sample that performed the poorest with regard to the numerical measurements performed by the DFOS-technology. The deviant positioning has undoubtedly influenced the results for Sample 2.

Despite the cable not being exactly vertical, Figures 10.6a and 10.6b are still showing that the fiber optic cable had been relatively well placed into the core of both Sample 1 and Sample 2. In addition, it was observed good adhesion between the fiber optic cable and the stabilized material for all three samples when they were opened. The cable was tried to be pulled out of the samples, and a large resistance was encountered. The good adhesion was also observed visually and is shown especially well for Sample 1 in Figure 10.6a.

Bulging is another challenge related to the chosen laboratory setup. When compressing a sample, Poisson's effect will occur. That is, when the sample is loaded, and then also deformed, axially there will be some deformation in the transverse direction. In the case of an unconfined compression test, the sample will expand in the horizontal direction when it is compressed in the axial direction. The samples are bulging. This bulging phenomenon will cause a loss of bond between the fiber optic cable and the surrounding clay. As the samples are not supported radially they are completely free to move, and this movement leads to loss of adhesion and the fact that the cable will slip more and more with increasing bulging. In situ, the lime/cement-stabilized columns are supported on all sides by the surrounding clay. This can maybe reduce

the challenges related to bulging.

It was seen in Chapter 9 that relaxation had some effect on the strain measurements. It is not completely clear whether it is the fiber optic cable or the LC-sample itself that is relaxing, or if it is a combination of both. From Figure 9.14 it was observed that the differences between the first measurements and the relaxation measurements decreased for increasing deformation. The differences were seen to be biggest at the very low strain levels. At higher strain levels the stabilized soil will probably become more compact, making relaxation less possible. The challenge related to relaxation in the field, where the soil is supported on all sides, is possibly limited to such an extent that the possibility of catching the main strain developments in situ exists.

There have, naturally, been several possible sources of error related to the work in this M.Sc. Thesis that has to be mentioned. The measurement methods that have been used are quite sensitive methods, and the measurements have examined intricate phenomena. Hence, there can be some sources of errors related to the setup and use of the measurement systems that can have played a role. There was some trouble related to the calibration of the OBR interrogator which can have affected the results slightly. For the last temperature test dust was encountered in the system, and it was very problematic to calibrate the interrogator. In addition, the OBR interrogator needs to be mechanically aligned. This very delicate instrument can have been affected by some movements of the table it was sitting on during both the tamping and curing processes which could have affected the calculations.

The temperature measurements can have been affected by the setup of the fiber core inside an oil-filled plastic tube. For instance, there was probably an inertia in the measurement system related to the heat transfer through the plastic material of the tube and through the hydraulic oil. In addition, there are uncertainties related to the heat transfer in the oil, it is not known if it transferred heat only horizontally or if it also led some heat upwards inside the plastic tube.

Lastly, there are also some uncertainties related to the exact positioning of the fiber optic cables inside the stabilized soil samples. The positional calibrations were performed by squeezing the cable together with two fingers at the top and bottom of the samples. Hence, the fingers induced heating of the cable so that it was possible to see the range along the cable where the samples had to be in between. As fingers usually are of 1-2 cm thickness, there is a chance that the positions of the samples have been misinterpreted by a few centimeters. This positional uncertainty yields for both the temperature samples and the strain samples.

---







## **Part 4 - Conclusion**



# Chapter 11

## Conclusion

### 11.1 Conclusions

The aim of this research was to examine the possibility of using Distributed Fiber Optic Sensing (DFOS) for monitoring stabilized clay. More precisely, the research objectives were the following:

- Is DFOS able to measure the temperature development in stabilized soil?
- Can DFOS be used to reliably detect zones of unstabilized quick clay within a stabilized soil column?
- Can DFOS reproduce the strain development of stabilized soil subjected to loading?

The results from the laboratory tests performed for this M.Sc. Thesis shows that it is possible to detect layers of unstabilized quick clay in stabilized soil columns by the use of Distributed Fiber Optic Sensing. A clear distinction was seen between the different soil layers, and a temperature signature showing the transition from one layer to the other was uncovered. Based on the laboratory results, it is reasonable to believe that unstabilized layers of thickness less than 5 cm ( $t < 5$  cm) can be reliably detected. Most of the heat development is evolving in the first hours after mixing. Hence, installation of the DFOS-system should be carried out as swiftly as possible. However, if the installation is performed within the first 5 hours, it should probably be sufficient to clearly detect any possible transition signature and then also any possible weakness zones.

The DFOS-technology is not capable of measuring absolute temperature on its own. However, despite not providing the absolute temperature of the curing process, the DFOS-system is still giving a very accurate recording of the temperature development with time. The fiber optic cable is very sensitive and capable of measuring even the slightest temperature change. If some additional standard temperature sensors are installed at a few different depths, it will be possible to produce a high-quality plot of the absolute temperature more or less continuously along the height of the LC-columns. This will enable the possibility of estimating the strength

and stiffness of the cured columns based on some maturity relations.

The DFOS-system was able to follow the trend of the strain developments of the samples during the unconfined compression test quite well in the first part of the test. However, numerically the strain measurements from the DFOS-system were considerably lower than the strains calculated based on the deformation recordings. The main reason for this was the problem related to bond that has been extensively discussed in Chapter 10. Despite an observed good adhesion between the fiber optic cable and the lime/cement-stabilized soil, a full bond was never achieved. The samples were too short to transfer the full load from the stabilized soil into the fiber optic cable. This was a result of the stiffness differences between the cable and the samples in addition to the dimensions of the samples. Thus, the fiber optic cable followed the movement of the samples, but not to the same extent as the samples. In other words, the cable was strained similarly to the samples but at a considerably lower scale.

The cable slipped the samples at a certain strain level. By slipping, it is referred to the point where the fiber optic scans go from showing increasing strain to decreasing strain under progressively increasing load. After the point of cable slippage, no reliable measurements could be taken. The reasons for cable slippage are probably several phenomena, such as initial failure cracks developing and bulging of the samples.

## 11.2 Limitations

There are several limitations associated with this study. Firstly, the investigations conducted in this study have been confined to laboratory-scale experiments. This restricts the generalizability of the findings to real-world scenarios. Furthermore, the number of soil samples examined in the laboratory was limited, which may affect the statistical robustness of the results. Additionally, the study focused on a single binder content and composition for the two main tests, namely the analysis of heat transfer in layered soil samples and the measurement of strain development in an LC-sample under loading conditions. Similarly, only one type of cable was tested for each evaluation. The absence of multiple binder compositions and cable types may limit the comprehensiveness and applicability of the study's conclusions. Moreover, the findings have not been complemented through numerical modeling, which could provide theoretical support and enhance the reliability of the results. Lastly, only one layering scenario was used for the temperature tests in this M.Sc. Thesis and further scenarios should be examined in the future.

## 11.3 Further work

The presented experimental data has provided new insights and these data have formed the basis for the discussed conclusions. However, there is still a need for more research to widen and further generalize the findings in this thesis. Hence, more tests of both the heat transfer in a layered soil sample and the strain development in a stabilized soil sample should be conducted.

---

Also field tests of both temperature and strain monitoring should be carried out. In addition, several different types of fiber optic cables should be tested in both the temperature tests and the strain tests.

### 11.3.1 Temperature tests - Further work

Tests of an unstabilized layer in between two layers of stabilized clay should be performed. It would be valuable to observe how the temperature transfer signature and the rest of the temperature profiles are affected by the situation of heating from both sides. Else, tests of the heat transfer between layers of different binder content should be carried out. Despite the possibility of some imperfections along the height of LC-columns, it is not very probable that a completely unstabilized layer is found. It is more probable that some layers where the binders have not been perfectly distributed, and hence have a lower binder content than the rest of the column, can be found. Thus, tests of heat transfer between layers of different binder content would be interesting to conduct, to examine how clearly the mentioned temperature signature would be in such a situation.

For any future testing of a similar setup as the one used for the temperature tests in this work, a better reference measurement method should be applied. The method with the thermocouples integrated into the isolation box was not satisfactory. Numerical modeling should also be carried out in the future, in order to support the laboratory findings with some theoretical relations. The laboratory setup should be carefully replicated, both in order to verify the already obtained results and to easily test a lot of different scenarios related to heat transfer through imperfections. Both laboratory and field scales can and should be modeled numerically.

### 11.3.2 Strain tests - Further work

Equally as for the temperature tests, numerical modeling should be used also for the strain tests. It should be used to replicate the results from the laboratory, but in addition, it can be used to investigate the problem related to bonding. The situation of the fiber optic cable with a given stiffness inside the LC-sample with another stiffness which together is exposed to a loading should be modeled numerically. Such a numerical model would enable the possibility to calculate the required bond length, and then also give what dimensions should be used for future samples to avoid the same challenges related to bonding. A replication, by the use of numerical modeling, of the already achieved results from the laboratory would also make it possible to find out what stress and strain the fiber optic cable actually was exposed to during the testing.

The most important thing for future testing of monitoring strain development in LC-stabilized quick clay samples is to avoid the challenge related to bonding. There are several ways of doing this. First of all, the samples can be made larger. Another point that should be assessed, is the application of a simpler preparation method. This can for instance be the wet mixing method, as this method gives a slurry that can be easily poured into the formwork and conform tightly

---

to the fiber optic cable. Lastly, it can be an idea to test a slightly stronger material, for instance, weak concrete. The use of a stronger material will decrease the challenge related to bonding, but in addition, it would give a much simpler preparation method. The preparation method would be simpler because also the concrete mix would be in the form of a slurry. The simpler preparation methods that follow the use of both wet mixing and the use of weak concrete could ensure a more consistent quality of all the prepared samples.

In any further work on the same principles, it might also be an idea to perform some tests with support around the sample. This can limit the challenges related to slippage, especially the challenges around bulging, and it is also closer to the situation that will be in situ.

---



# Bibliography

- Åhnberg, Helen and Göran Holm (1987). *Om inverkan av härdningstemperaturen på skjuvhållfastheten hos kalk- och cementstabiliserad jord*. Swedish. SGI Rapport 30. Linköping: Swedish Geotechnical Institute, p. 144.
- Åhnberg, Helen, Sven-Erik Johansson et al. (1995). *Cement och kalk för djupstabilisering av jord*. Swedish. SGI Rapport 48. Linköping: Swedish Geotechnical Institute, p. 222.
- Bache, Bjørn Kristian et al. (Mar. 2022). 'Effect of Temperature on the Strength of Lime–Cement Stabilized Norwegian Clays'. In: *Journal of Geotechnical and Geoenvironmental Engineering* 148. DOI: 10.1061/(ASCE)GT.1943-5606.0002699.
- Barnes, Graham (2022). *SOIL MECHANICS Principles and practice*. English. 4th ed. Vol. 560 p. London: Bloomsbury Academic.
- Boynton, Robert S (1980). *Chemistry and Technology of Lime and Limestone*. 2nd ed. JOHN WILEY & SONS, INC.
- Chapeleau, Xavier and Antoine Bassil (Aug. 2021). 'A General Solution to Determine Strain Profile in the Core of Distributed Fiber Optic Sensors under Any Arbitrary Strain Fields'. en. In: *Sensors* 21.16, p. 5423. ISSN: 1424-8220. DOI: 10.3390/s21165423. URL: <https://www.mdpi.com/1424-8220/21/16/5423>.
- Christensen, Stein et al. (June 1998). *GRUNNFORSTERKNING MED KALKSEMENTPÆLER*. Norwegian. URL: <https://www.sgi.se/globalassets/publikationer/svensk-djupstabilisering/sdar9.pdf>.
- Giles, David (2023). *GeoEngineering Blog*. en-US. URL: <https://www.cgl-uk.com/geoengineering-blog/> (visited on 26th Mar. 2023).
- Helle, Tonje et al. (Nov. 2022). 'KLIMAGRUNNS ARBEIDSMETODIKK FOR DOKUMENTASJON OG PREDIKSJON AV SKJAERFASTHET OG STIVHET I BINDEMIDDEL- STABILISERTE PELER Documenting strength and stiffness of ground-improved soils applying KlimaGrunns methodology'. Norwegian. In: Norway. URL: [https://www.researchgate.net/publication/366007469\\_KLIMAGRUNNS\\_ARBEIDSMETODIKK\\_FOR\\_DOKUMENTASJON\\_OG\\_PREDIKSJON\\_AV\\_SKJAERFASTHET\\_OG\\_STIVHET\\_I\\_BINDEMIDDEL-STABILISERTE\\_PELER\\_Documenting\\_strength\\_and\\_stiffness\\_of\\_ground-improved\\_soils\\_applying\\_KlimaGrunn](https://www.researchgate.net/publication/366007469_KLIMAGRUNNS_ARBEIDSMETODIKK_FOR_DOKUMENTASJON_OG_PREDIKSJON_AV_SKJAERFASTHET_OG_STIVHET_I_BINDEMIDDEL-STABILISERTE_PELER_Documenting_strength_and_stiffness_of_ground-improved_soils_applying_KlimaGrunn).
- Hjelstuen, Magnus (Oct. 2020). *Distributed fiber optic sensing*. English. Oslo, Norway. URL: <https://www.tekna.no/en/professional-areas/it-and-telecommunications/it-blog/distributed-fibre-optic-sensing/>.

- Hov, Sølve et al. (2022). 'Lime-cement stabilisation of Trondheim clays and its impact on carbon dioxide emissions'. In: *Soils and Foundations* 62.3, p. 101162. ISSN: 0038-0806. DOI: <https://doi.org/10.1016/j.sandf.2022.101162>. URL: <https://www.sciencedirect.com/science/article/pii/S0038080622000701>.
- Jacobsen, Stefan et al. (Dec. 2021). *Concrete Technology*. English. 2022nd ed. Trondheim, Norway: NTNU Department of Structural Engineering.
- Jafarbiglookarami, Ali (June 2021). *Alternative binders for improvement of soft soils – A geoenvironmental approach*. English. URL: <https://ntnuopen.ntnu.no/ntnu-xmlui/handle/11250/2976436>.
- Janz, Mårten and Sven-Erik Johansson (July 2002). 'The Function of Different Binding Agents in Deep Stabilization'. English. In: p. 47. URL: <https://www.sgi.se/globalassets/publikationer/svensk-djupstabilisering/sd-r9e.pdf>.
- Kartverket (Apr. 2023). *Høydedata*. Norwegian. Lidar map. Hønefoss, Norway. URL: <https://hoydedata.no/LaserInnsyn2/>.
- L'Heureux, Jean-Sébastien et al. (2019). 'The Tiller-Flotten research site: Geotechnical characterization of a very sensitive clay deposit'. en. In: *AIMS Geosciences* 5.4, pp. 831–867. ISSN: 2471-2132. DOI: 10.3934/geosci.2019.4.831. URL: <http://www.aimspress.com/article/10.3934/geosci.2019.4.831>.
- Larsson, Stefan (2005). *State of Practice Report - Execution, monitoring and quality control*. English.
- NGF (2011). *Veiledning for symboler og definisjoner i geoteknikk - Identifisering og klassifisering av jord*. Norwegian.
- (2012). *VEILEDNING FOR GRUNNFORSTERKNING MED KALKSEMENTPELER*. Norsk. Oslo: Norges Geotekniske Forening.
- NGI (2023). *NGTS - Nasjonale Geoforsøksfelt*. no. URL: <https://www.ngi.no/Prosjekter/NGTS-Nasjonale-Geoforsoksfelt> (visited on 26th Mar. 2023).
- NGU (Apr. 2023). *Løsmasser - Nasjonal løsmassedatabase*. Norwegian. Quarternary geology map. Trondheim, Norway. URL: [https://geo.ngu.no/kart/losmasse\\_mobil/](https://geo.ngu.no/kart/losmasse_mobil/).
- Norcem (Nov. 2022). *Environmental product declaration CEM I*. Oslo, Norway. (Visited on 24th May 2023).
- NTNU (Oct. 2017). *Geotechnics Field and Laboratory Investigations*. English. Compendium for TBA4110 Geotechnics, Field and Laboratory Investigations.
- (2020). *Introduksjon til GEOTEKNIKK*. Norwegian. Compendium for TBA4100 Geoteknikk og geologi at NTNU.
- NVE (2020). *Sikkerhet mot kvikkleireskred - Vurdering av områdestabilitet ved arealplanlegging og utbygging i områder med kvikkleire og andre jordarter med sprøbruddegenskaper*. Norwegian. Veileder I/2019. Oslo, Norway: Norges vassdrags- og energidirektorat, p. 86. URL: [https://publikasjoner.nve.no/veileder/2019/veileder2019\\_01.pdf](https://publikasjoner.nve.no/veileder/2019/veileder2019_01.pdf).
- Paniagua, Priscilla et al. (Oct. 2019). 'Strength and stiffness of laboratory-mixed specimens of stabilised Norwegian clays'. English. In: *Ground Improvement* 175.2, p. 14. DOI: 10.1680/jgrim.19.00051. URL: <https://www.icevirtuallibrary.com/doi/epdf/10.1680/jgrim.19.00051>.
-

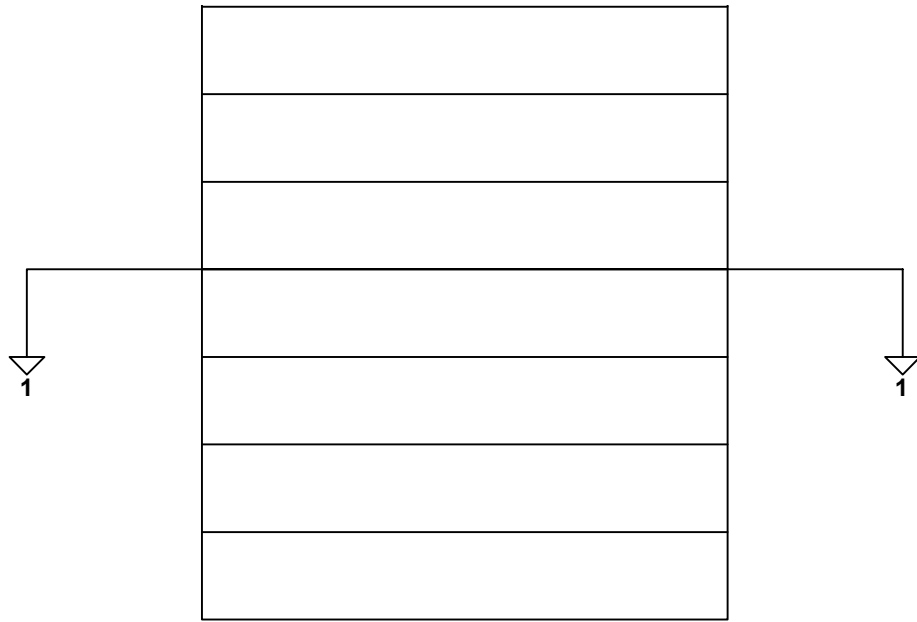
- Patel, Anjan (Jan. 2019). '3 - Soil stabilization'. en. In: *Geotechnical Investigations and Improvement of Ground Conditions*. Ed. by Anjan Patel. Woodhead Publishing Series in Civil and Structural Engineering. Woodhead Publishing, pp. 19–27. ISBN: 978-0-12-817048-9. DOI: 10.1016/B978-0-12-817048-9.00003-2. URL: <https://www.sciencedirect.com/science/article/pii/B9780128170489000032>.
- Reite, Arne J., Harald Sveian and Eyolf Erichsen (1999). 'Trondheim fra istid til nåtid - landskaphistorie og løsmasser'. Norwegian. In: *Gråsteinen 5 5*, p. 39. URL: [https://www.ngu.no/upload/Publikasjoner/Grasteinen/Graasteinen05\\_Trondheim.pdf](https://www.ngu.no/upload/Publikasjoner/Grasteinen/Graasteinen05_Trondheim.pdf).
- Rui, Yi et al. (Dec. 2017). 'Integrity Testing of Pile Cover Using Distributed Fibre Optic Sensing'. In: *Sensors* 17, p. 2949. DOI: 10.3390/s17122949.
- Shi, Bin et al. (Feb. 2021). *DFOS Applications to Geo-Engineering Monitoring*. English. URL: <https://link.springer.com/content/pdf/10.1007/s13320-021-0620-y.pdf>.
- Soga, Kenichi and Linqing Luo (Jan. 2018). 'Distributed fiber optics sensors for civil engineering infrastructure sensing'. In: *Journal of Structural Integrity and Maintenance* 3, pp. 1–21. DOI: 10.1080/24705314.2018.1426138.
- Standard Norge (Jan. 2017). *Geotechnical investigation and testing - Laboratory testing of soil - Part 4: Determination of particle size distribution (ISO 17892-4:2016)*. English.
- (June 2021). *Eurocode 2 - Design of concrete structures - Part 1-1: General rules and rules for buildings*. English.
- Taylor, H.F.W. (1990). *Cement chemistry*. 2nd ed. ICE Virtual Library. URL: <https://www.icevirtuallibrary.com/doi/book/10.1680/cc.25929>.
- Timoney, Martin, Bryan McCabe and Alan Bell (Feb. 2012). 'Experiences of dry soil mixing in highly organic soils'. In: *Proceedings of the Institution of Civil Engineers Ground Improvement* 165, pp. 3–14. DOI: 10.1680/grim.2012.165.1.3.
- Topolnicki, Michał (Feb. 2016). *General overview and advances in Deep Soil Mixing*.
- Wiersholm, Pernille (June 2018). 'Temperatureffekter i kalksementstabilisert leire'. no. In: p. 179.
- Wu, Jun et al. (2021). 'A Generic Framework of Unifying Industrial By-products for Soil Stabilization'. In: *Journal of Cleaner Production* 321, p. 13. ISSN: 0959-6526. DOI: <https://doi.org/10.1016/j.jclepro.2021.128920>. URL: <https://www.sciencedirect.com/science/article/pii/S0959652621031140>.
- Zhang, R. et al. (Aug. 2014). 'Long-Term Effect of Curing Temperature on the Strength Behavior of Cement-Stabilized Clay'. In: *Journal of Geotechnical and Geoenvironmental Engineering* 140, p. 04014045. DOI: 10.1061/(ASCE)GT.1943-5606.0001144.
-



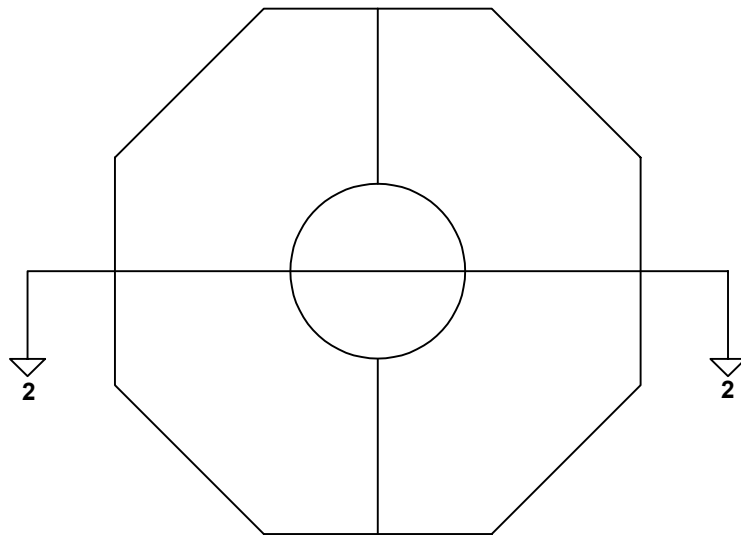
## **Appendix A**

# **Sketches of the isolation box used for temperature tests**

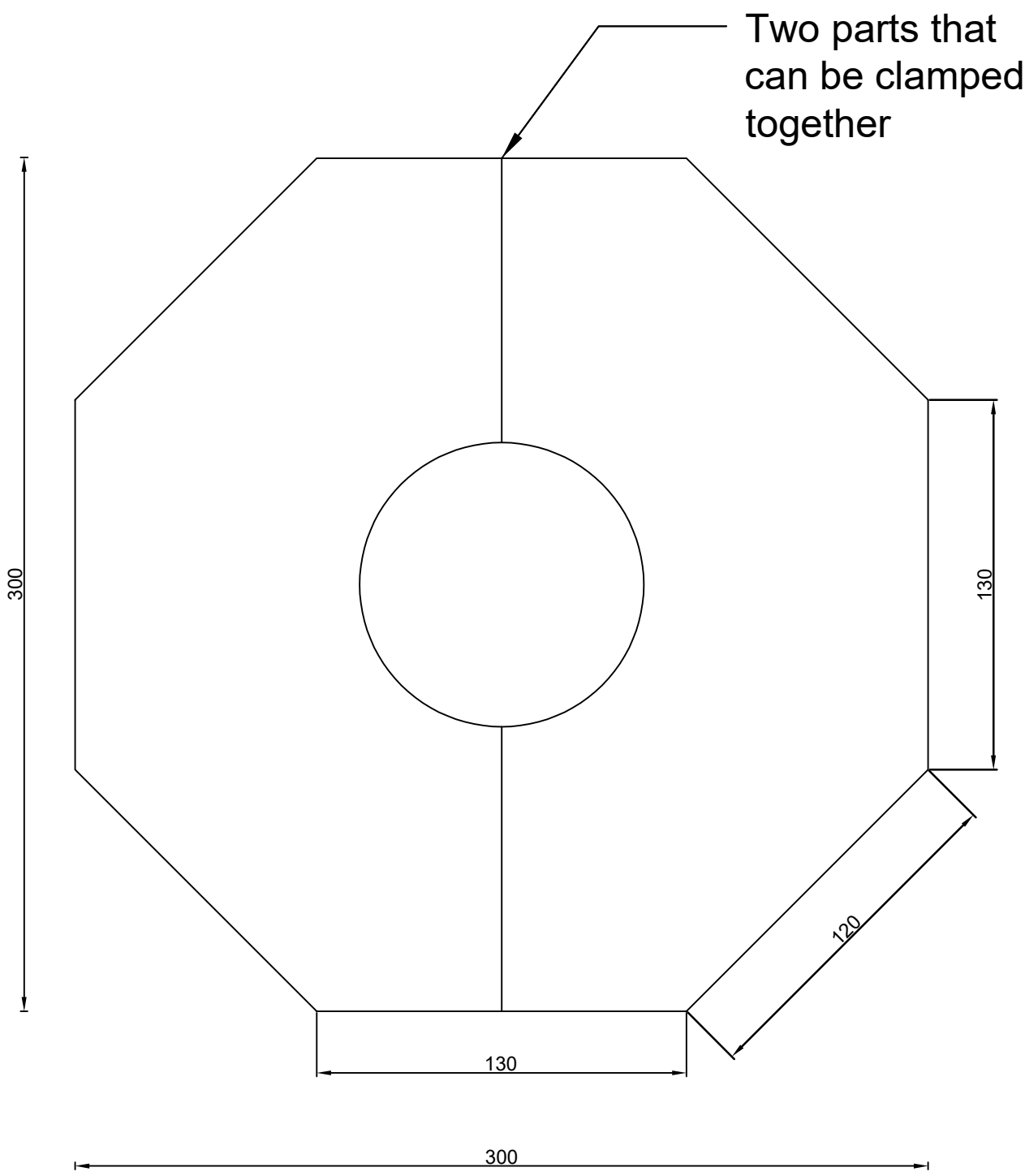
# Elevation:



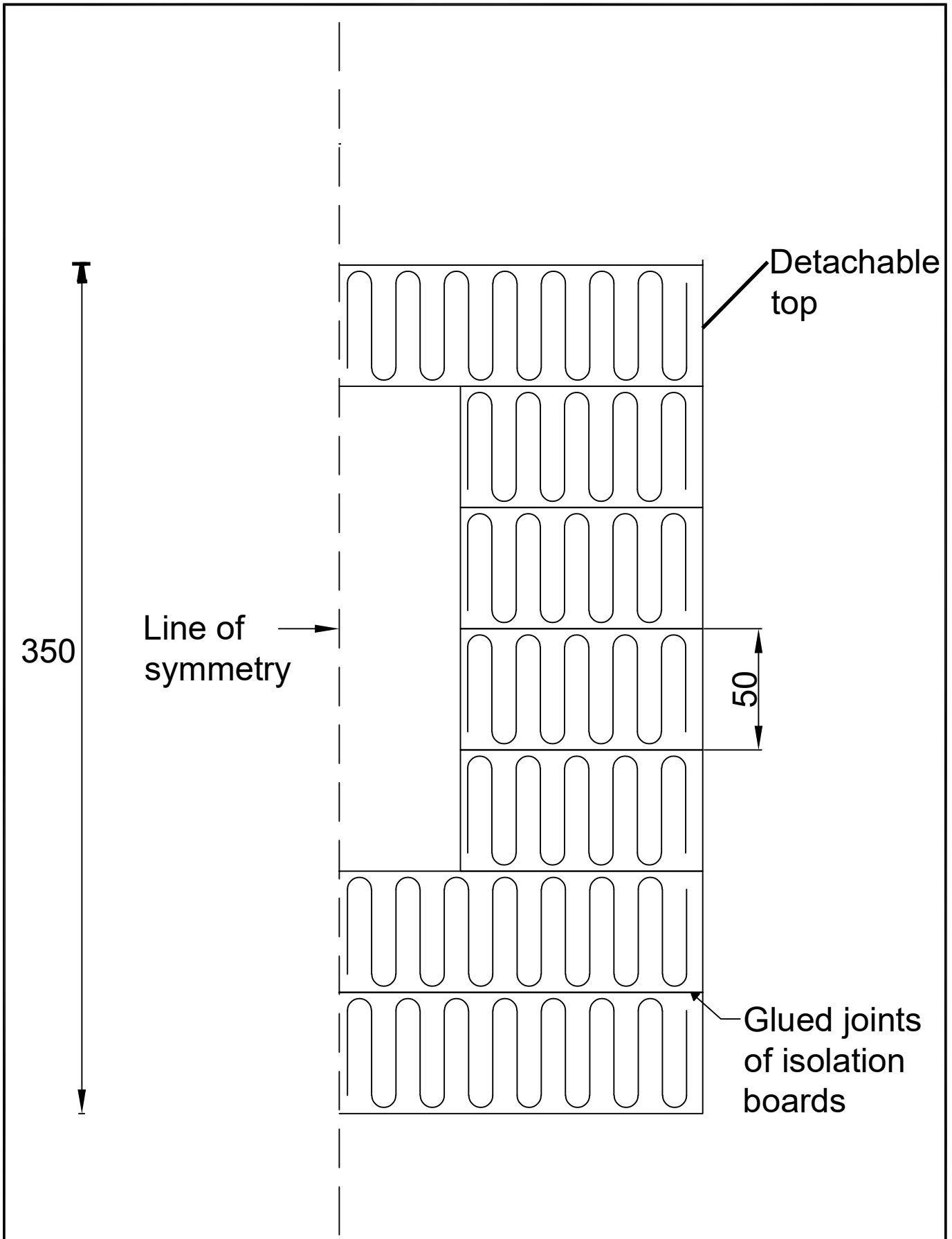
# Plan:



<b>Drawing No.</b> 1	<b>Information</b> Overview of drawn cross-sections of the insulation box	<b>Drawn by</b> Eivind Rørvik Solum	<b>Material</b> Sundolitt XPS (50 mm thickness)		
<b>Title</b> Cross-sections		<b>Date</b> 07.02.2023	<b>Scale</b> 1:100	<b>Language</b> English	<b>Sheet</b> 1/3



<b>Drawing No.</b> <p style="text-align: center; font-size: 24pt;">2</p>	<b>Information</b> Plane section of the center of the box. Dimensions in mm.	<b>Drawn by</b> Eivind Rørvik Solum	<b>Material</b> Sundolitt XPS (50 mm thickness)		
<b>Title</b> Section 1-1		<b>Date</b> 07.02.2023	<b>Scale</b> 1:50	<b>Language</b> English	<b>Sheet</b> 2/3

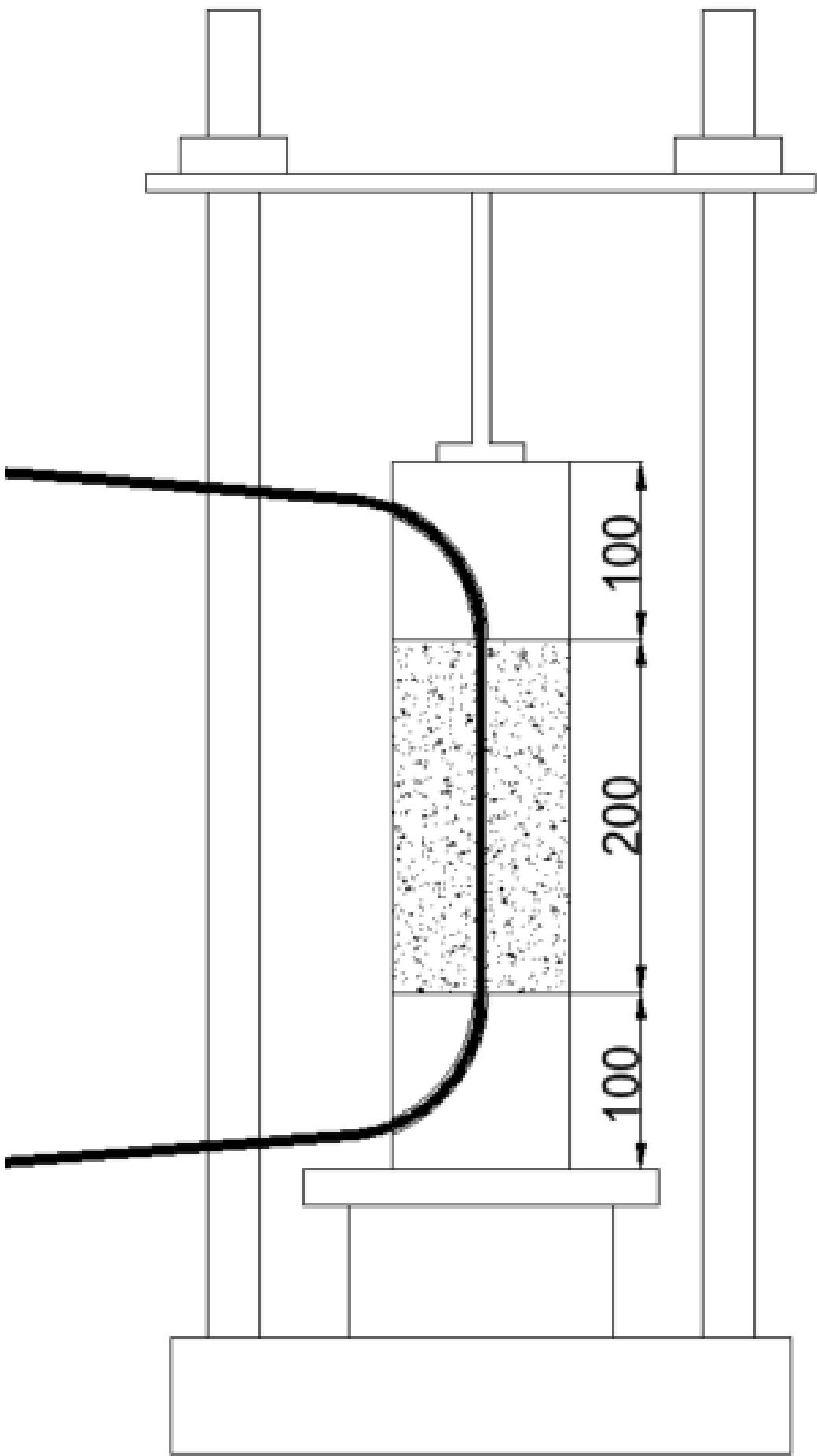


<b>Drawing No.</b> 3	<b>Information</b> Elevation section of 1 of the 2 parts of the box. Dimensions in mm.	<b>Drawn by</b> Eivind Rørvik Solum	<b>Material</b> Sundolitt XPS (50 mm thickness)		
<b>Title</b> Section 2-2		<b>Date</b> 07.02.2023	<b>Scale</b> 1:50	<b>Language</b> English	<b>Sheet</b> 3/3

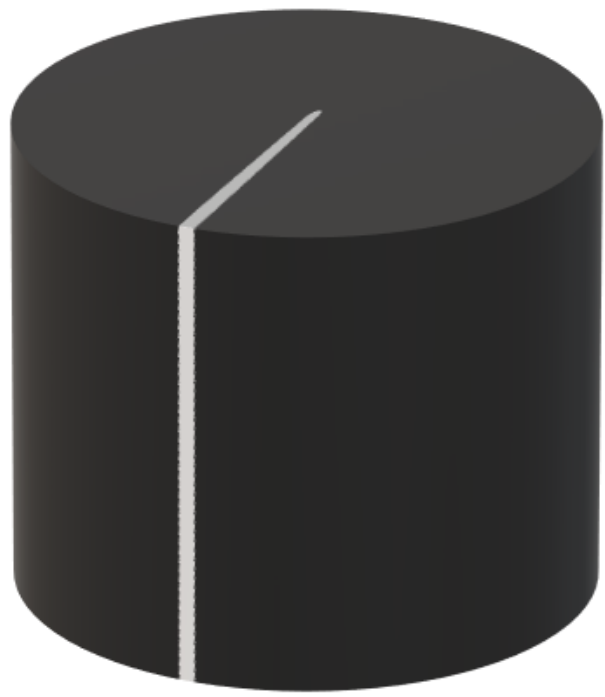


## **Appendix B**

# **Sketches of the uniaxial device and plastic blocks used for strain tests**



100 mm



100 mm

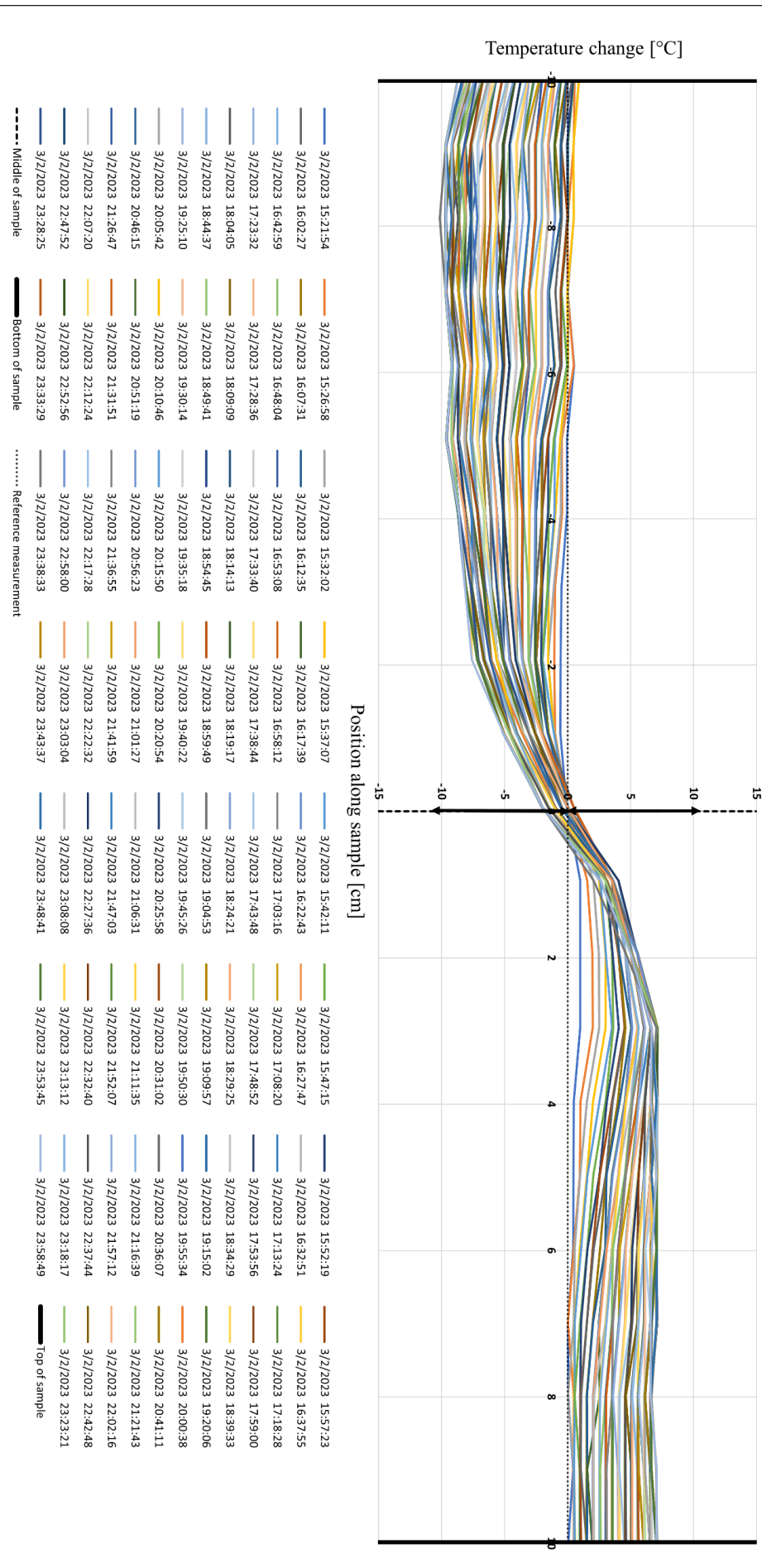


## Appendix C

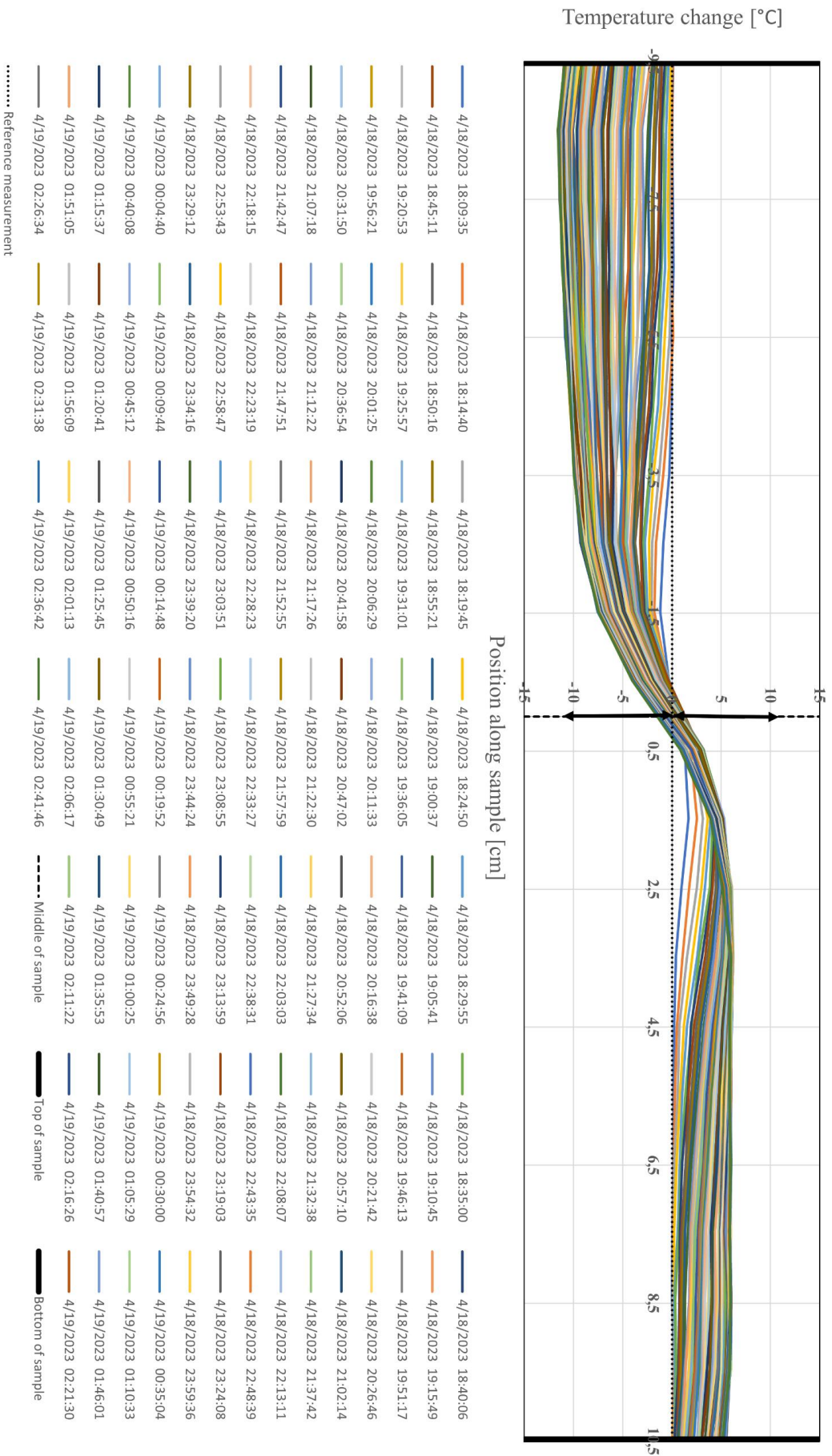
# Results from the temperature tests

All DFOS-scans from the first 8.5 hours of the tests, including labels, are shown in the two plots below. The first plot is from the first test and the second plot is from the second test.

Temperature change along sample the first 8 1/2 hours of test



## Temperature change along sample the first 8 1/2 hours of test



In the six plots below, the following are presented:

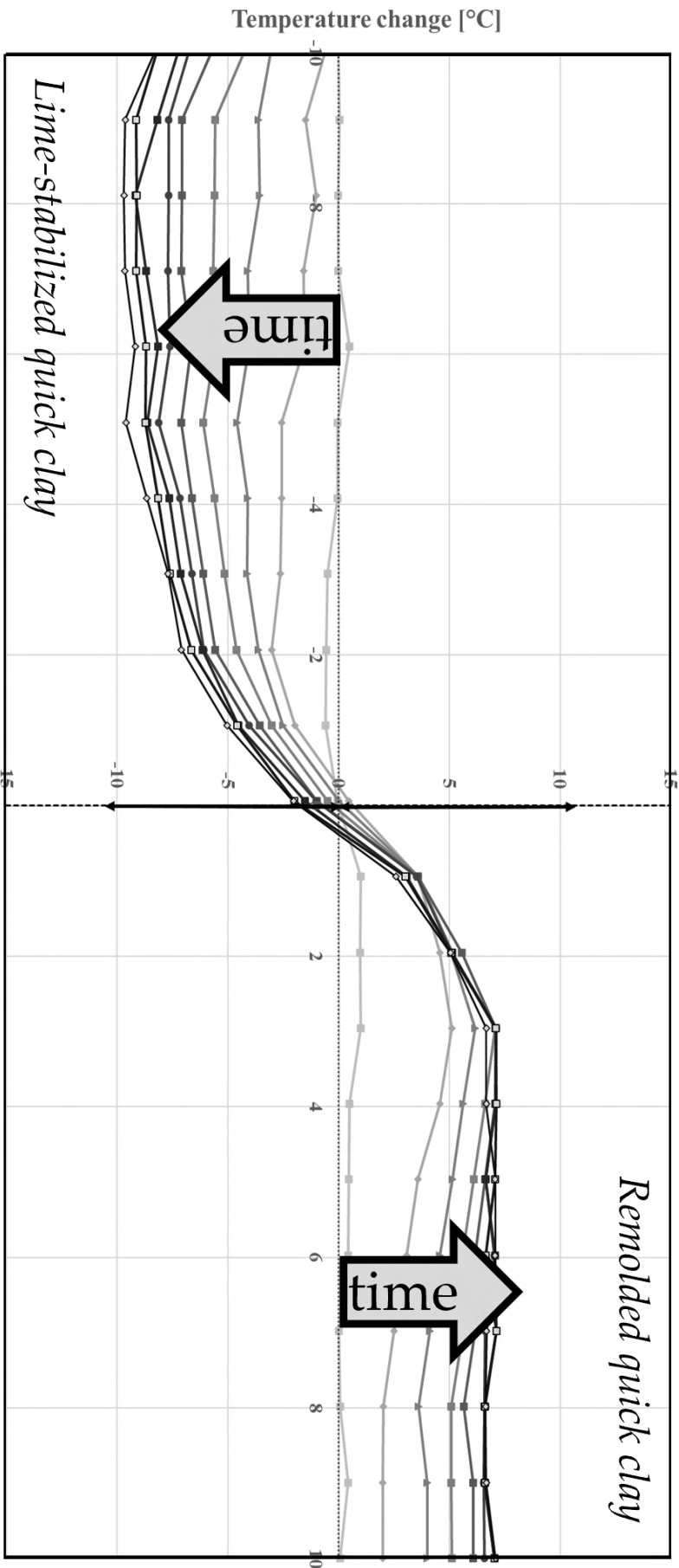
- One plot pr. hour from the first 8 hours of the first temperature test
- One plot pr. hour from the first 8 hours of the second temperature test
- All plots from the first hour of the first temperature test
- All plots from the first hour of the second temperature test
- Temperature development with time for each DFOS-point for the second temperature test
- DFOS-scans from the cross-sectional temperature test

The plots are presented in the same order as above.

---



Temperature change every hour in the first 8 hours of test



3/2/2023 15:21:54  
3/2/2023 20:25:58  
Middle of sample

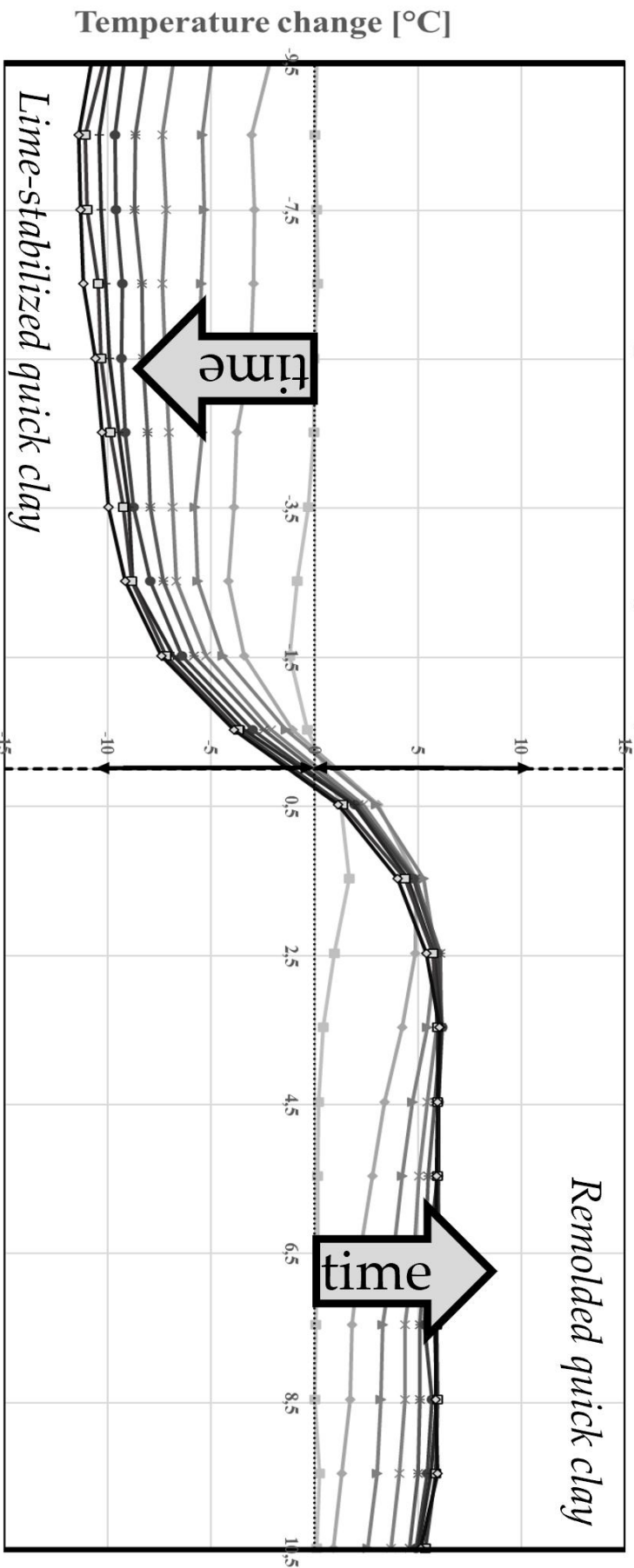
3/2/2023 16:22:43  
3/2/2023 21:26:47  
Bottom of sample

3/2/2023 17:23:32  
3/2/2023 22:27:36  
Reference measurement

3/2/2023 18:24:21  
3/2/2023 23:28:25

3/2/2023 19:25:10  
Top of sample

# Temperature change every hour in the first 8 hours of test



4/18/2023 18:09:35  
4/18/2023 23:13:59

4/18/2023 19:10:45  
4/19/2023 00:14:48

Position along sample [cm]  
4/18/2023 20:11:33  
4/19/2023 01:10:33

4/18/2023 21:12:22  
4/19/2023 02:11:22

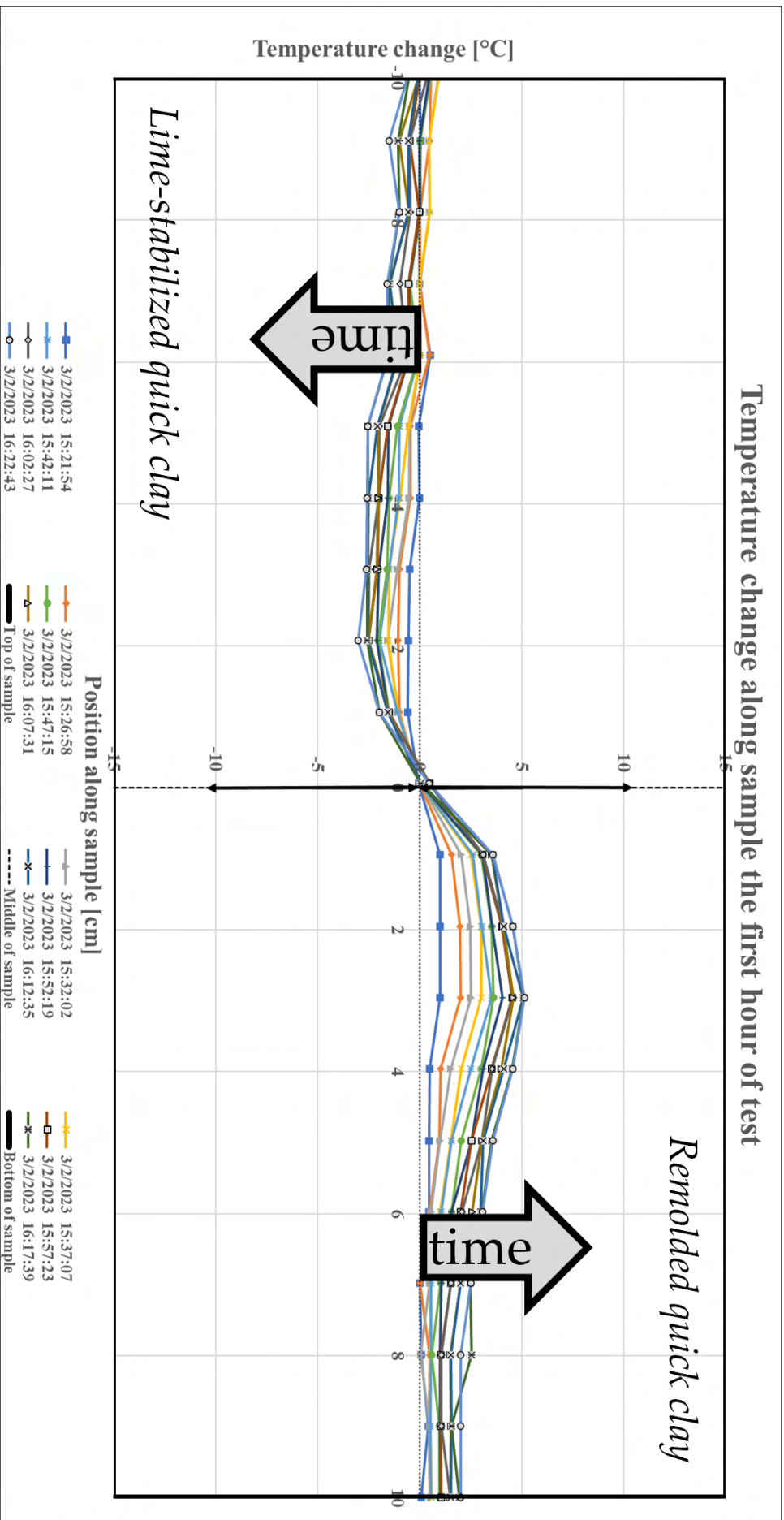
4/18/2023 22:13:11  
Middle of sample

Top of sample

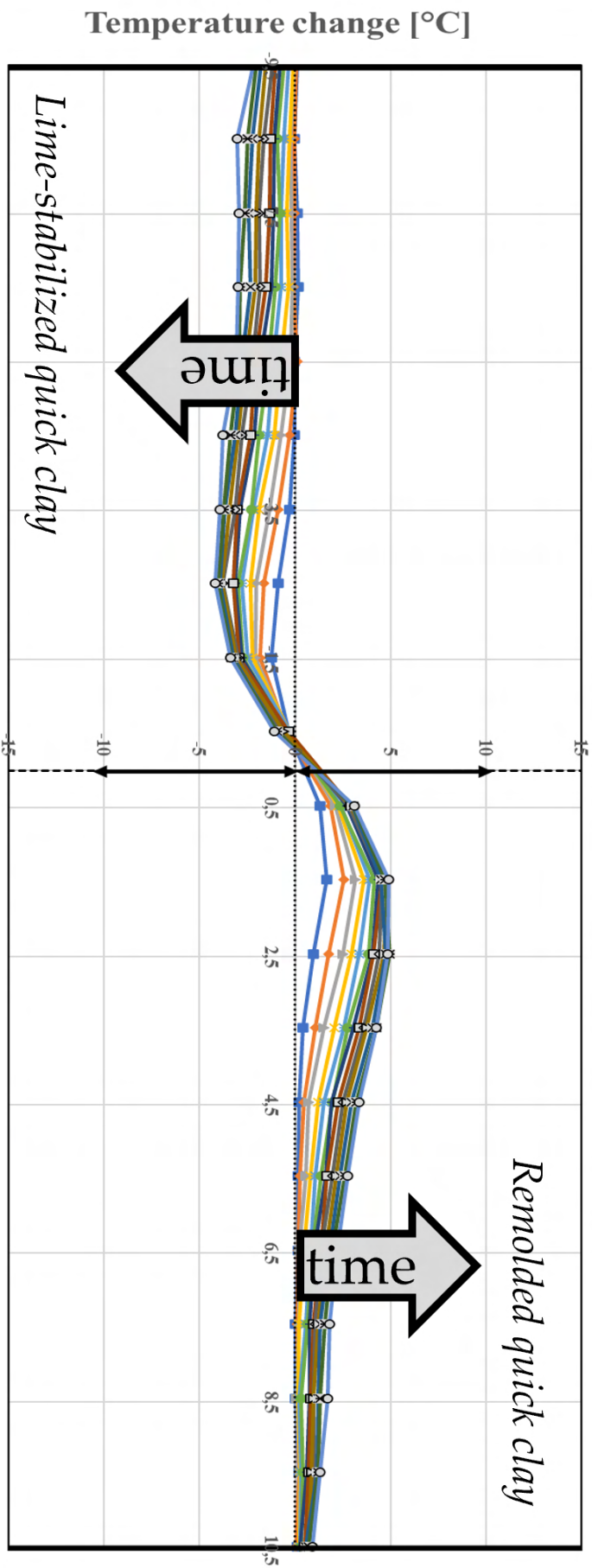
Bottom of sample

Reference measurement

## Temperature change along sample the first hour of test

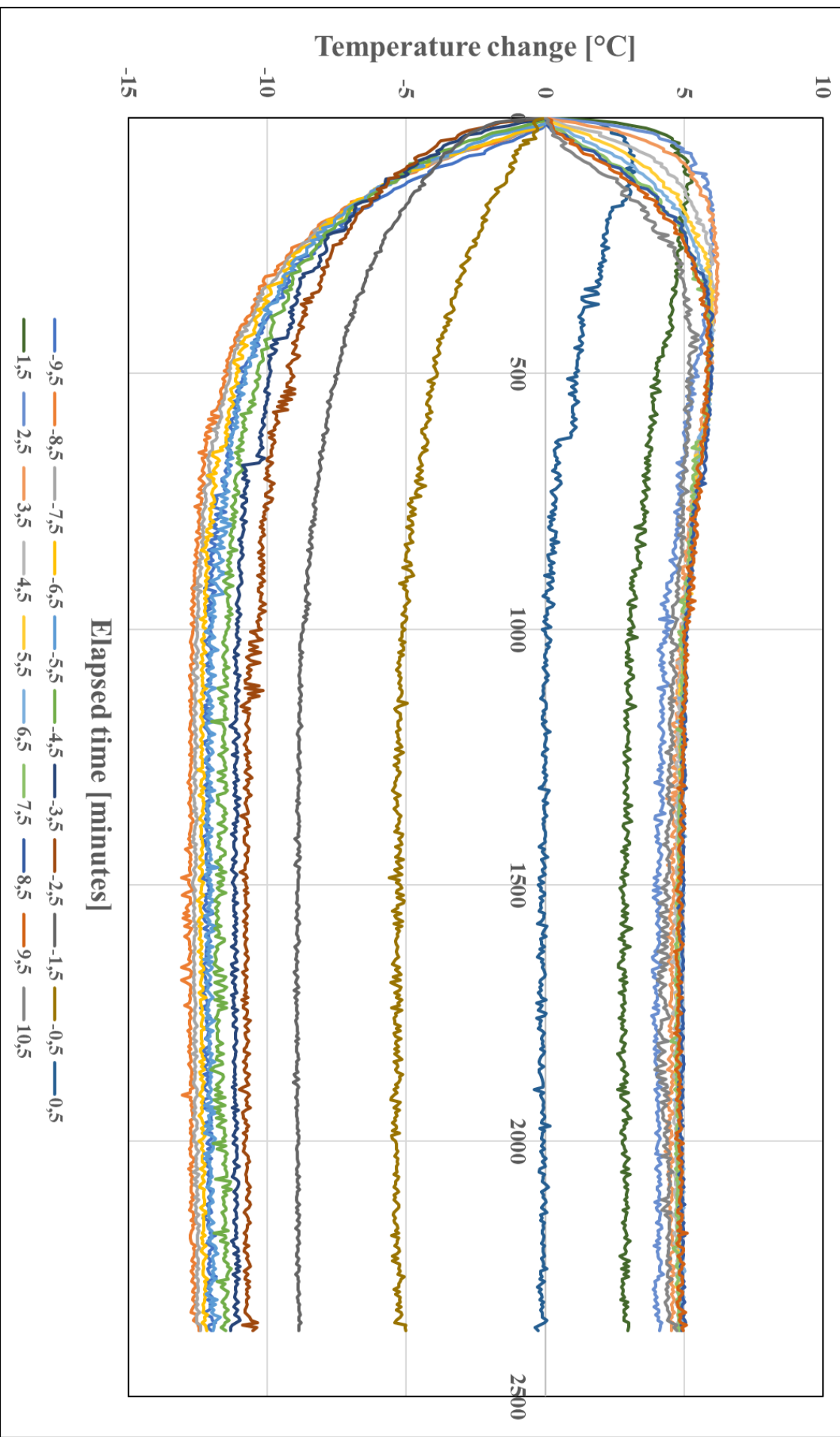


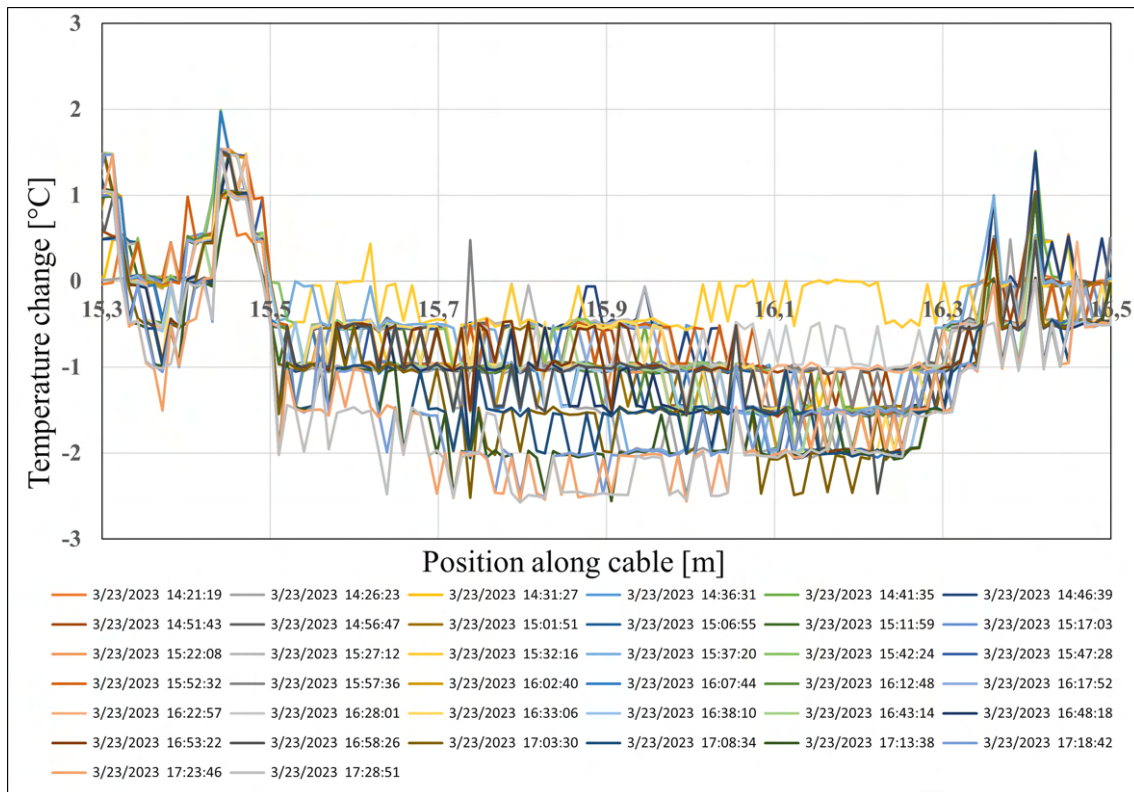
# Temperature change along sample the first hour of test



- Position along sample [cm]**
- 4/18/2023 18:09:35
  - 4/18/2023 18:29:55
  - 4/18/2023 18:50:16
  - 4/18/2023 19:10:45
  - 4/18/2023 18:14:40
  - 4/18/2023 18:35:00
  - 4/18/2023 18:55:21
  - Middle of sample
  - 4/18/2023 18:19:45
  - 4/18/2023 18:40:06
  - 4/18/2023 19:00:37
  - 4/18/2023 18:24:50
  - 4/18/2023 18:45:11
  - 4/18/2023 19:05:41
- Top of sample
- Bottom of sample

## Temperature development at each OBR-point



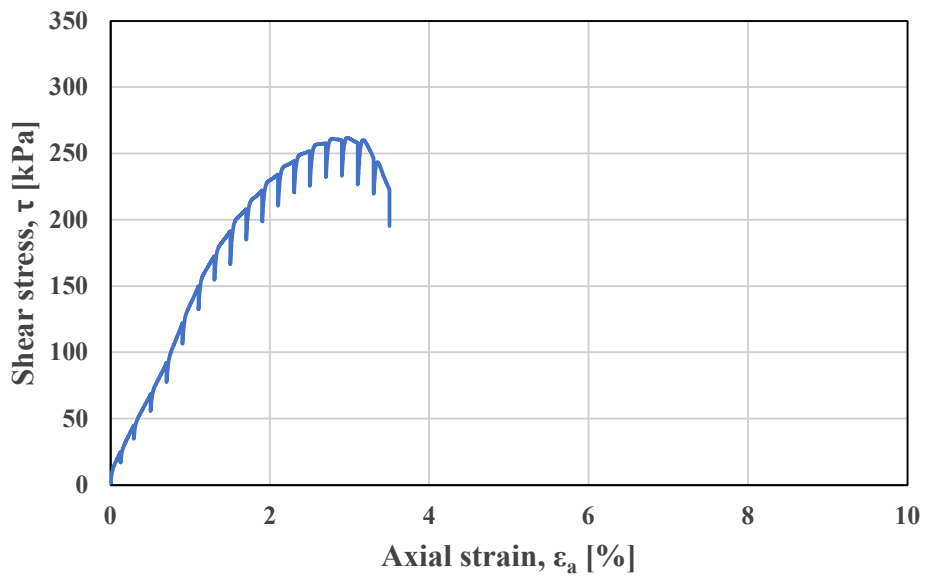
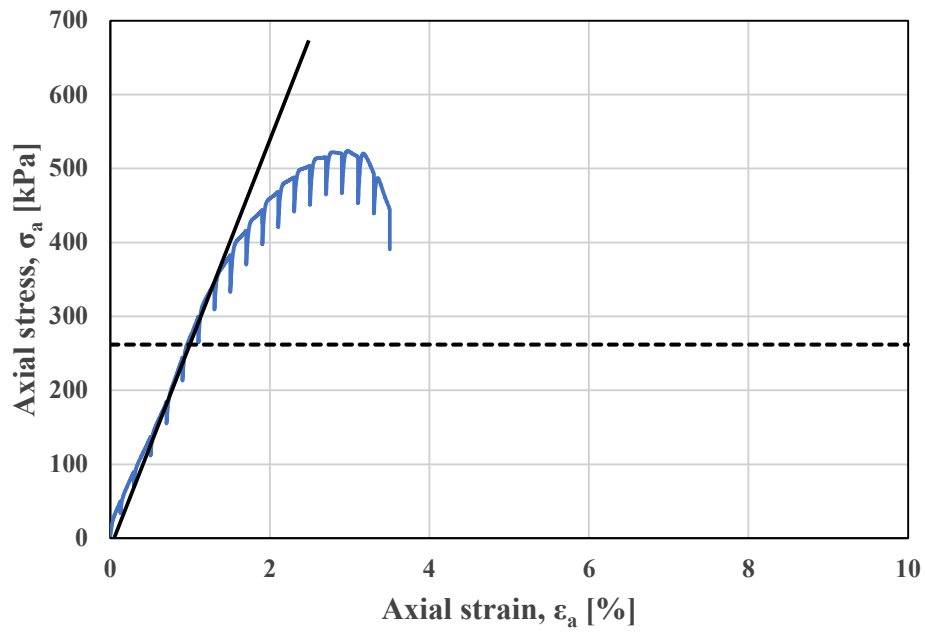


**Figure C.1:** Temperature development measured with the bare fiber positioned along the cross-section of the lime-stabilized quick clay sample.

## Appendix D

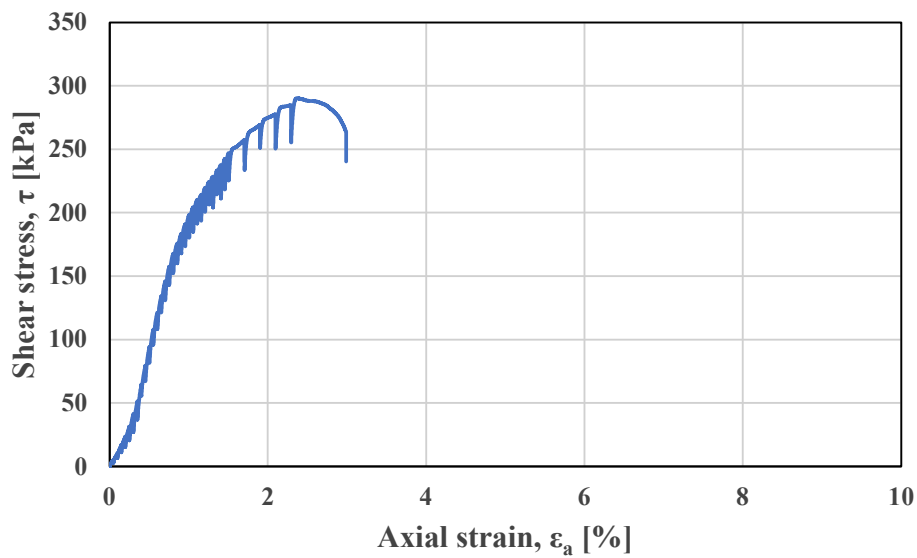
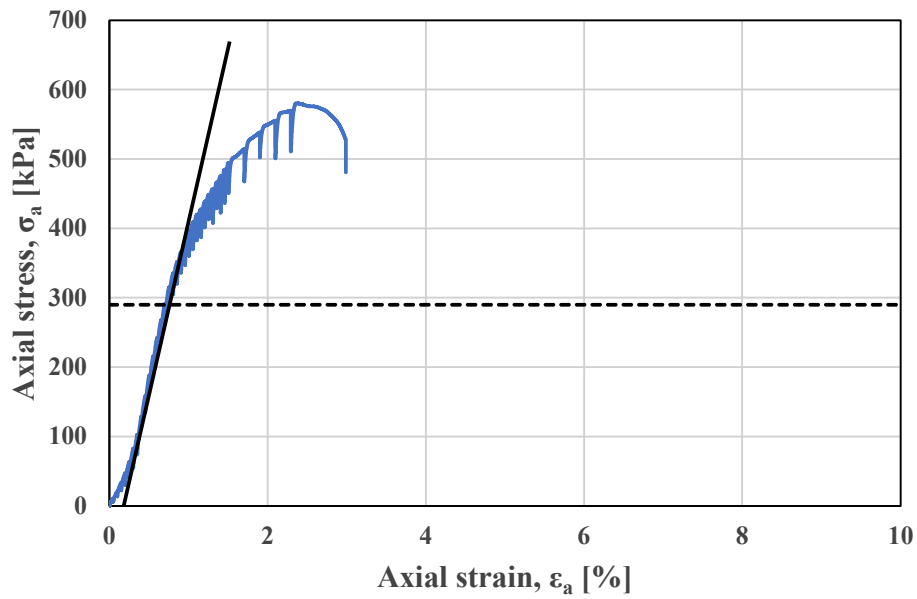
### Results from the strain tests

In the following, a few different plots containing important results for all three strain samples are included. For each plot type, the order of the different plots is chronological. I.e., for the different plot types it is the plot belonging to Sample 1 that comes first, further on comes the plot of the results for Sample 2 and lastly comes Sample 3's plot.

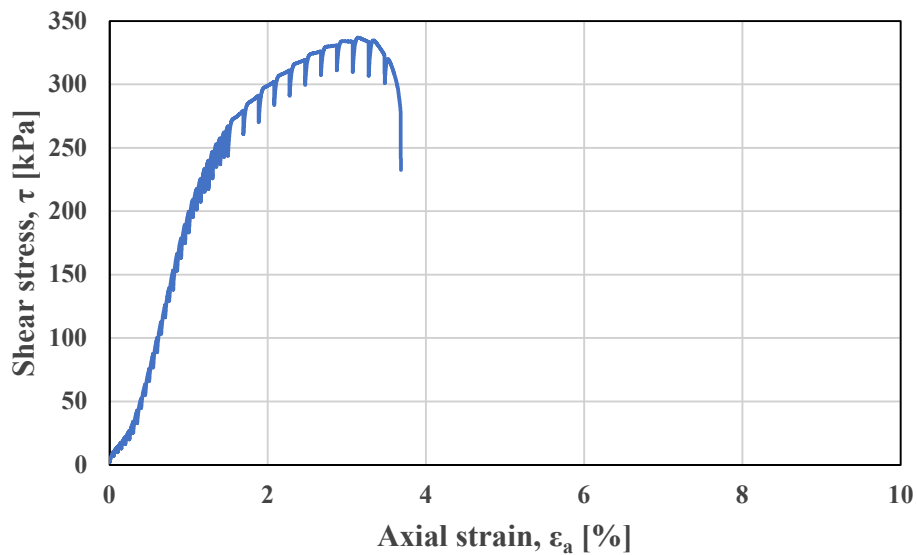
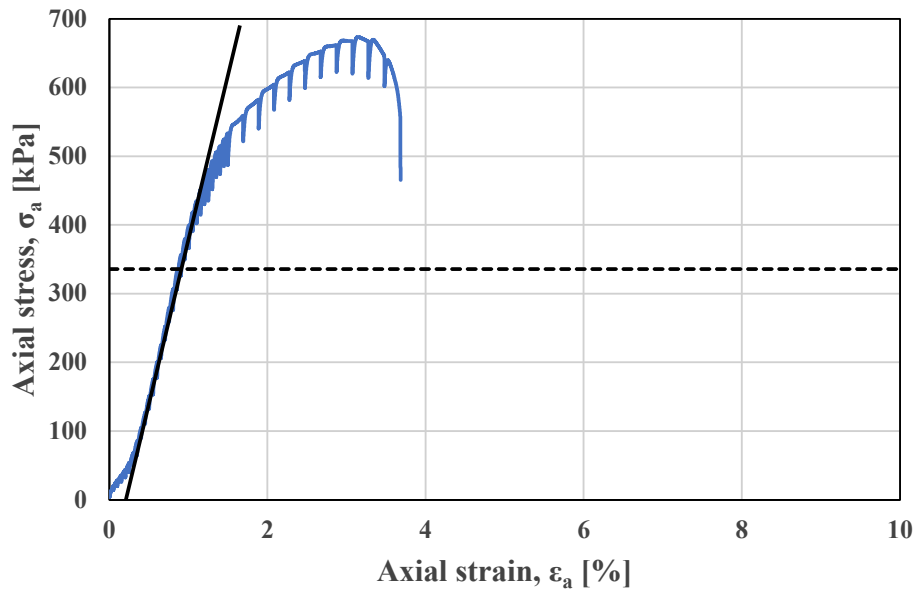


Sample nr.	Curing age	Test date
1	19	21.03.2023
Sample height, H	200	[mm]
Sample diameter, D	100	[mm]
Cross-sectional area, $A_0$	7853,982	[mm <sup>2</sup> ]
Ultimate compressive strength, $q_u$	523,97	[kPa]
Undrained shear strength, $c_u$	261,985	[kPa]
Failure strain, $\epsilon_f$	2,972	[%]
Estimated stiffness, $E_{50}$	27313,576	[kPa]

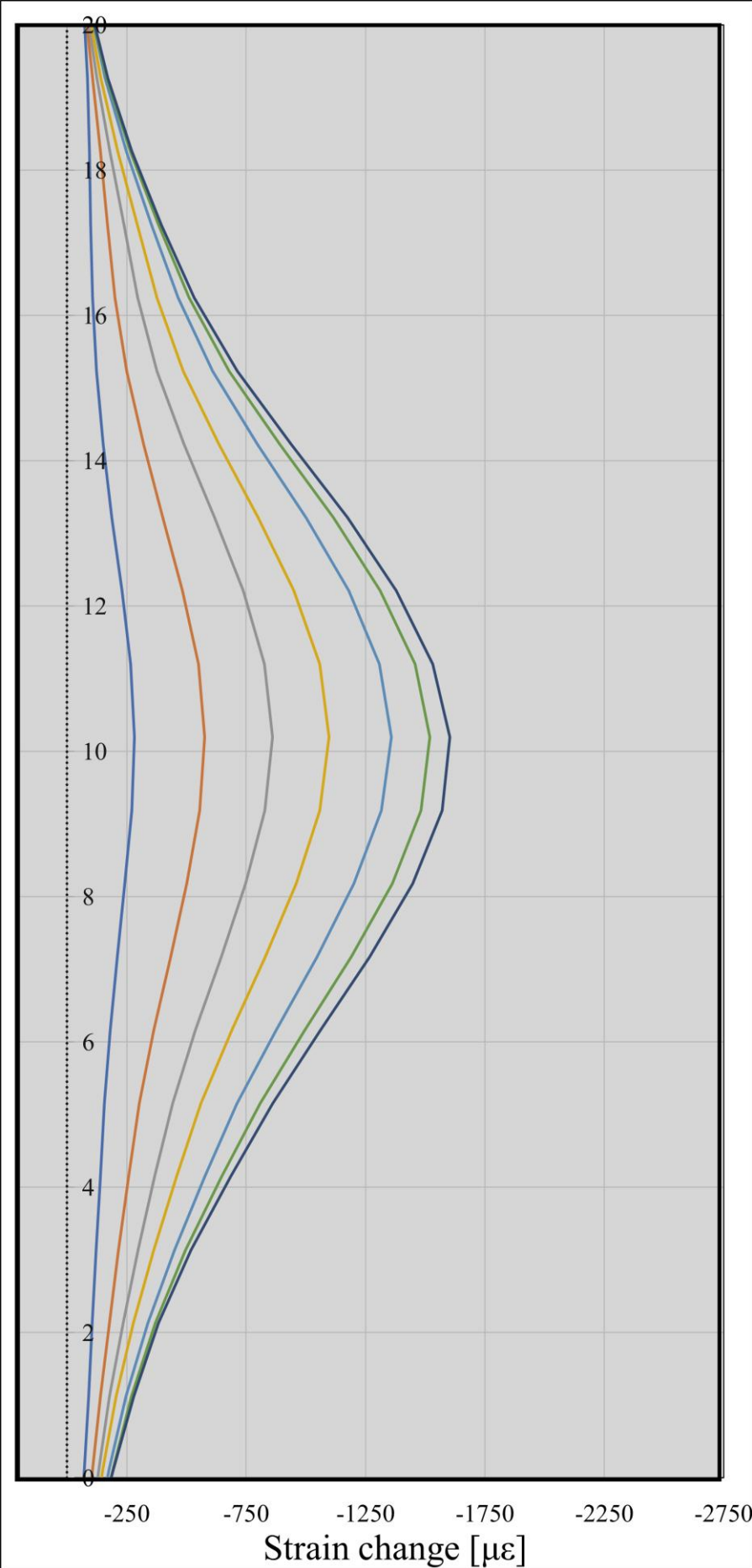




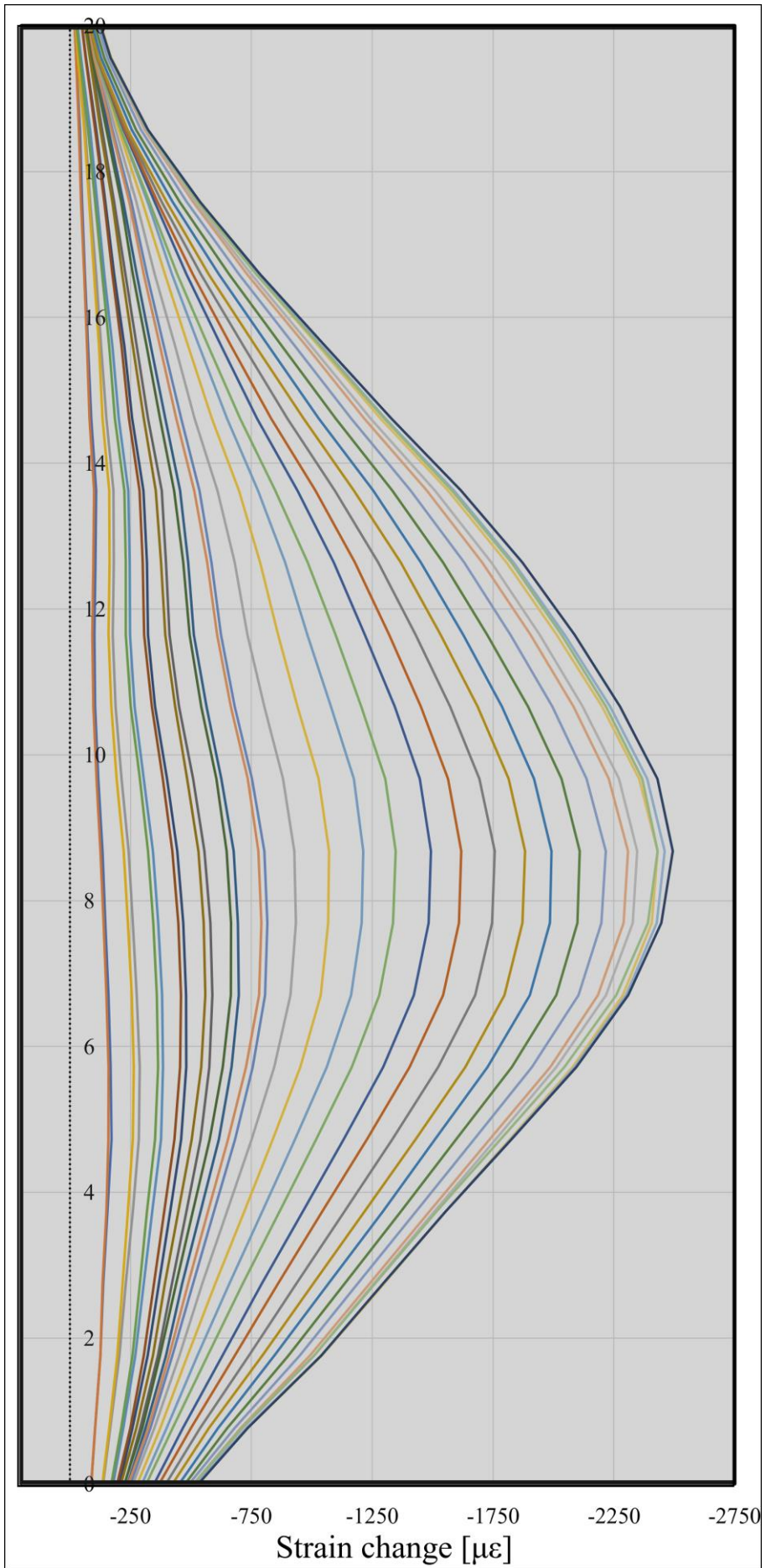
	<b>Sample nr.</b>	<b>Curing age</b>	<b>Test date</b>
	2	26	17.04.2023
	Sample height, H	200	[mm]
	Sample diameter, D	100	[mm]
	Cross-sectional area, $A_0$	7853,982	[mm <sup>2</sup> ]
	Ultimate compressive strength, $q_u$	580,678	[kPa]
	Undrained shear strength, $c_u$	290,339	[kPa]
	Failure strain, $\epsilon_f$	2,369	[%]
	Estimated stiffness, $E_{50}$	54100,923	[kPa]



	<b>Sample nr.</b>	<b>Curing age</b>	<b>Test date</b>
	3	27	18.04.2023
	Sample height, H	200	[mm]
	Sample diameter, D	100	[mm]
	Cross-sectional area, $A_0$	7853,982	[mm <sup>2</sup> ]
	Ultimate compressive strength, $q_u$	673,958	[kPa]
	Undrained shear strength, $c_u$	336,979	[kPa]
	Failure strain, $\epsilon_f$	3,142	[%]
	Estimated stiffness, $E_{50}$	48656,141	[kPa]







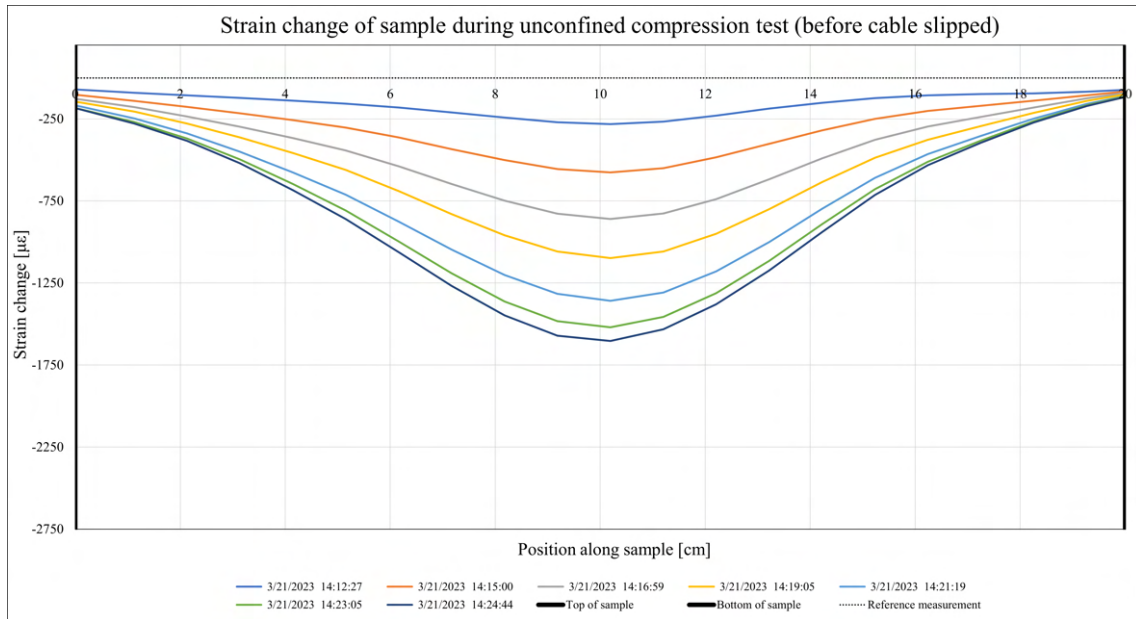


Figure D.1: Strain change for each measurement before the cable slipped for Sample 1.

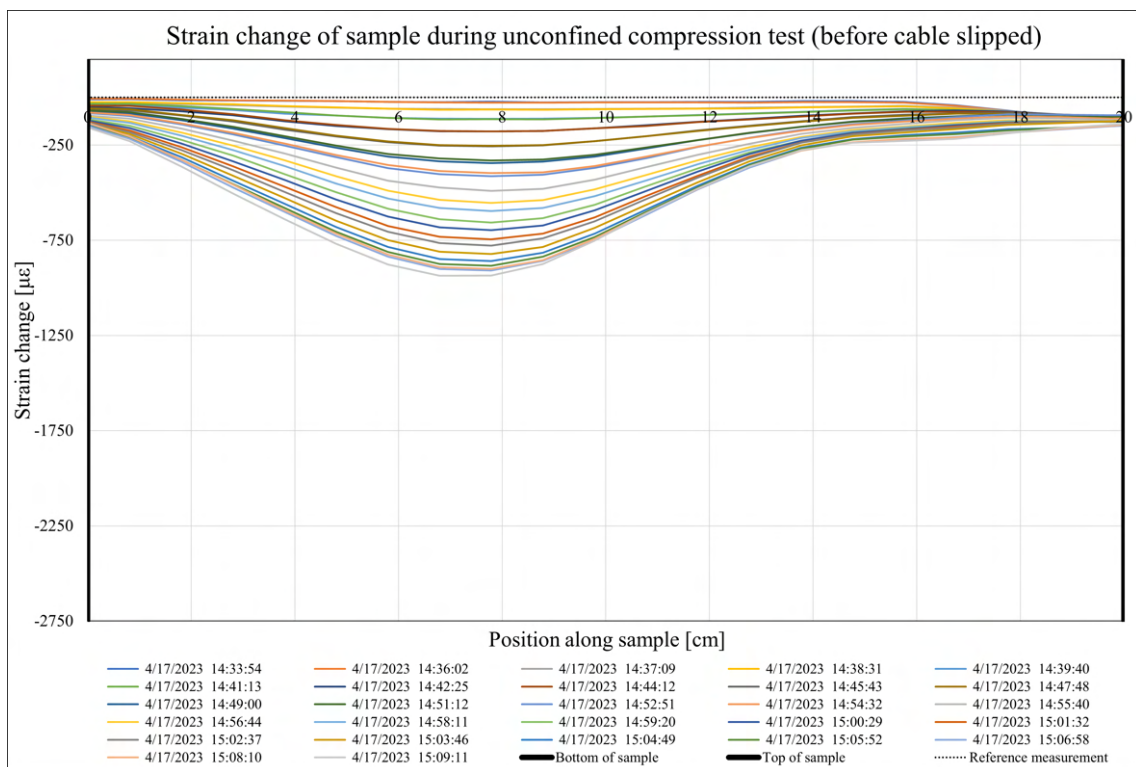
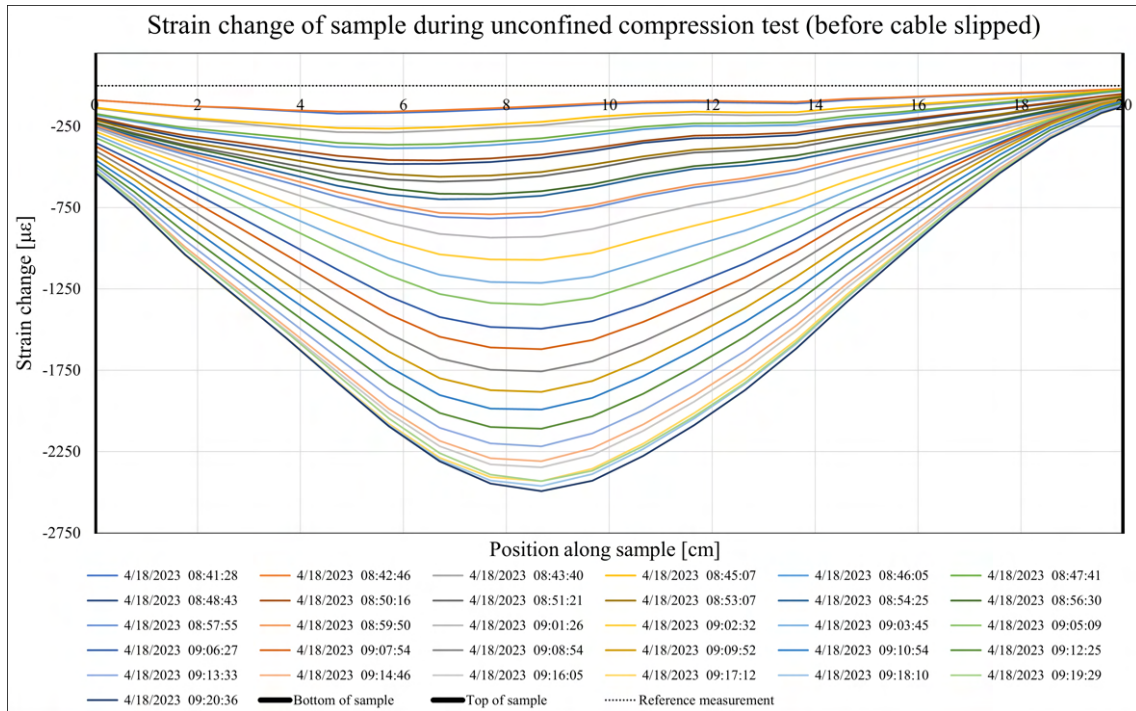
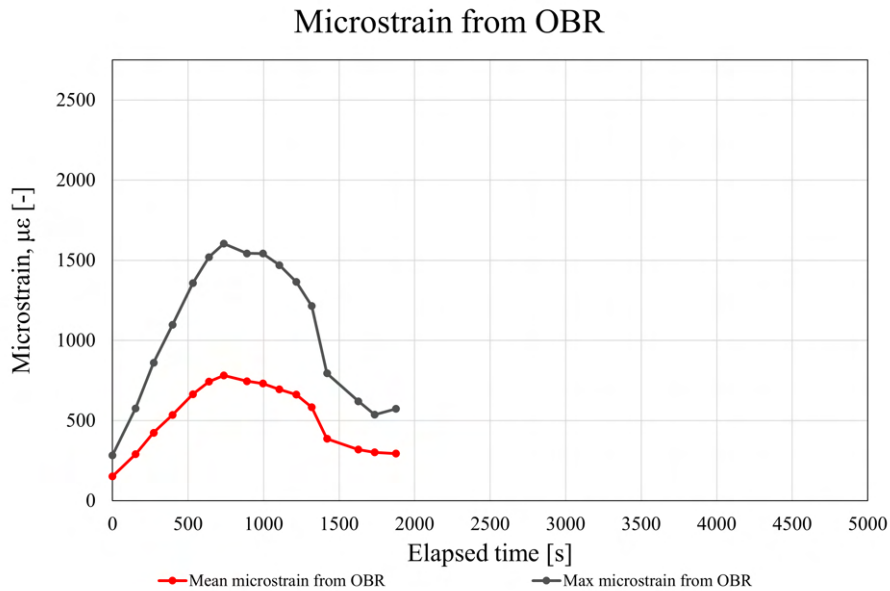


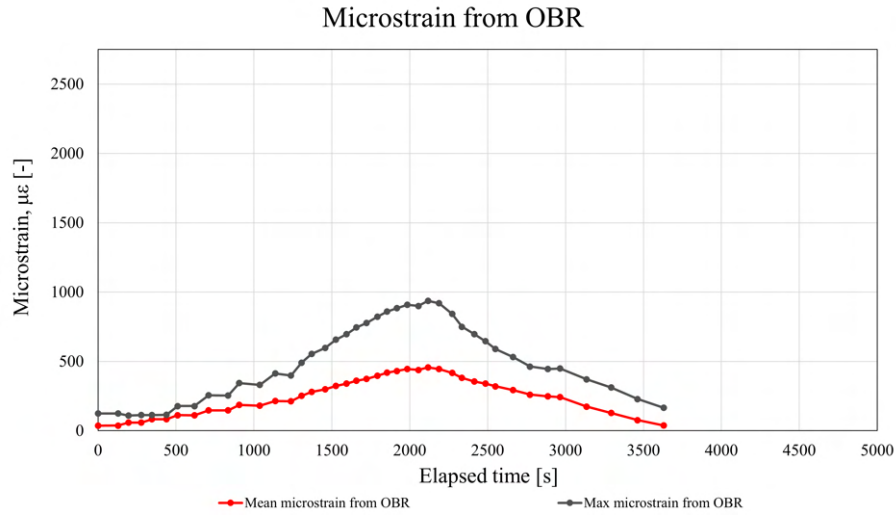
Figure D.2: Strain change for each measurement before the cable slipped for Sample 2.



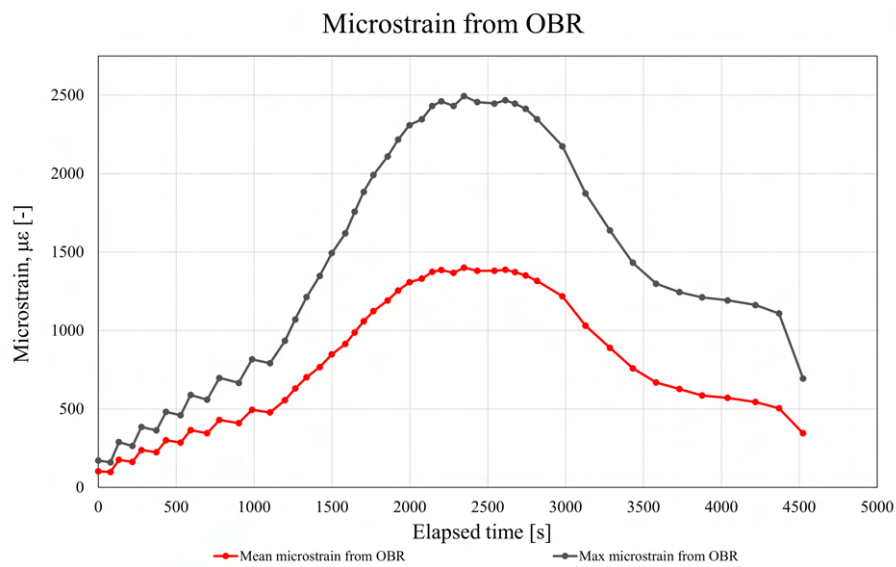
**Figure D.3:** Strain change for each measurement before the cable slipped for Sample 3.



**Figure D.4:** Mean and maximum strain measured with the DFOS-technology plotted against the time which has elapsed since the compression of Sample 1 was initiated.



**Figure D.5:** Mean and maximum strain measured with the DFOS-technology plotted against the time which has elapsed since the compression of Sample 2 was initiated.



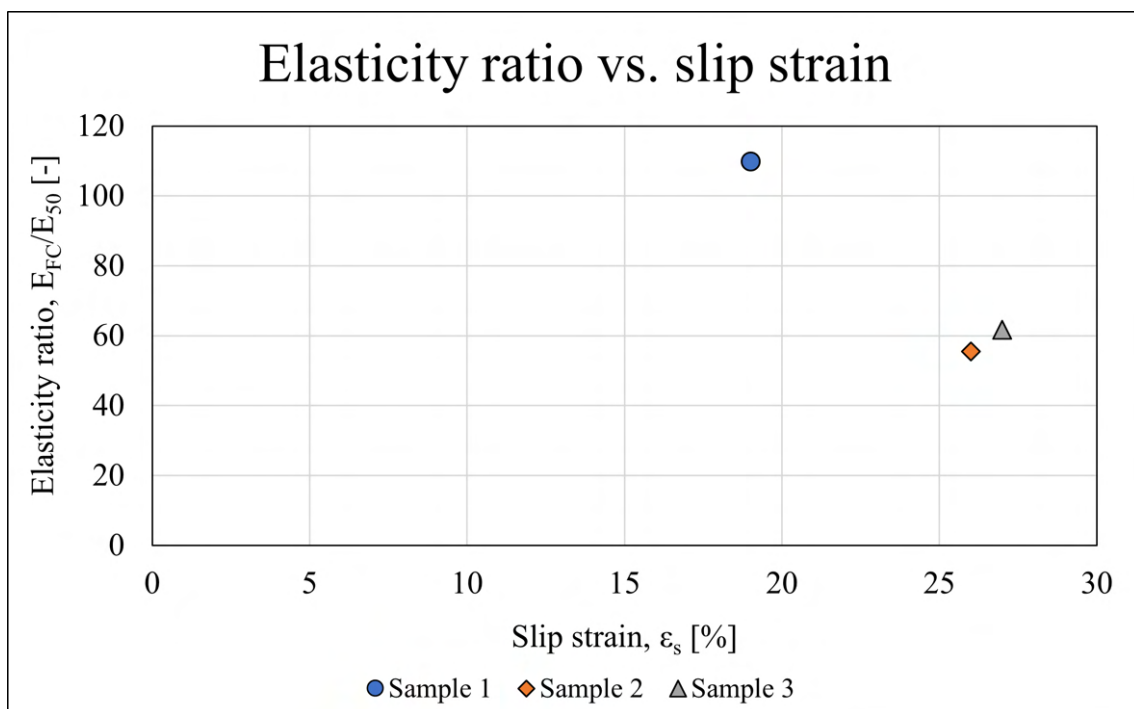
**Figure D.6:** Mean and maximum strain measured with the DFOS-technology plotted against the time which has elapsed since the compression of Sample 3 was initiated.



## Appendix E

# Calculations of required bond length for Sample 3

Below is a plot of the elasticity ratio for the three strain samples.



**Figure E.1:** The ratio of the stiffness of the fiber cable and the LC-samples plotted against the samples' curing age.

On the next page, the Excel-calculations of the required bond length and real strain in the fiber cable are included.

$$F = F_{FC} + F_{LC}$$

Assuming full bond  $\rightarrow \varepsilon_{FC} = \varepsilon_{LC}$

$$\rightarrow \frac{\sigma_{FC}}{E_{FC}} = \frac{\sigma_{LC}}{E_{LC}} \rightarrow \frac{F_{FC}}{\frac{\pi}{4} * \varphi_{FC}^2 * E_{FC}} = \frac{F_{LC}}{\frac{\pi}{4} * \varphi_{LC}^2 * E_{LC}} \rightarrow F_{FC} = \frac{\varphi_{FC}^2 * E_{FC}}{\varphi_{LC}^2 * E_{LC}} * F_{LC}$$

$$f_{bd} = 2,25 * \eta_1 * \eta_2 * f_{cta} \quad (\eta_2 = 1,0 \text{ for } \varphi \leq 32 \text{ mm})$$

$$L_{b,rqd} = 0,25 * \varphi * \frac{\sigma_{FC}}{f_{bd}}$$

Examining force and strain in the cable at 1% (from uniaxial device) strain of the sample. The force that is transferred at this point of time is 3,166 kN.

$\varphi_{FC}$ [mm]	3
$\varphi_{LC}$ [mm]	100
$E_{FC}$ [kPa]	3000000
$E_{LC}$ [kPa]	48656
$q_{LC}$ [kPa]	674
$\eta_1$ [-]	1
$\eta_2$ [-]	1

$$F_{FC}/F_{LC} [-] \quad 0,05549161$$

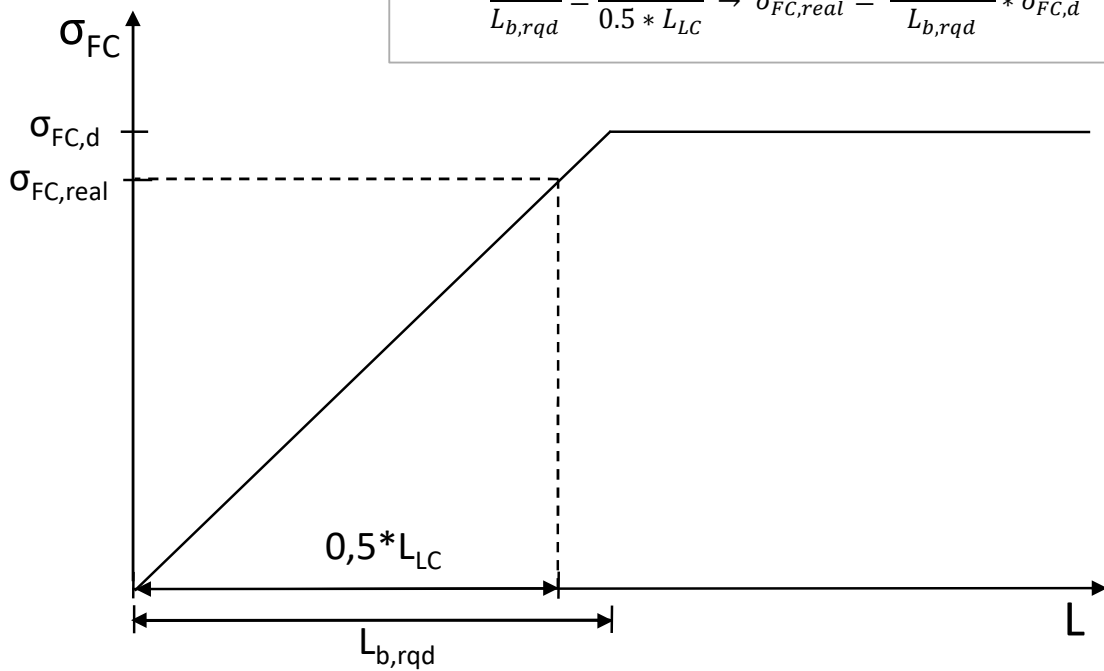
$$F = F_{FC} + \frac{1}{0,05549161} * F_{FC} = 3,166 \text{ kN}$$

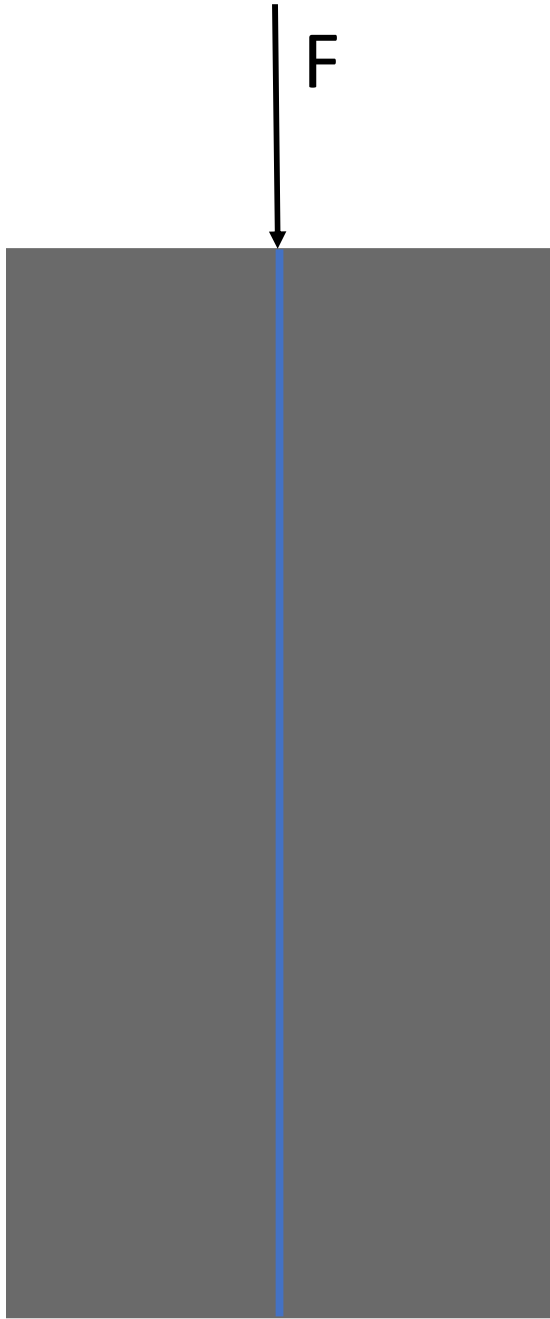
$F_{FC}$ [kN]	0,16644988
$\sigma_{FC}$ [kPa]	23547,8409
$f_{bd}$ [kPa]	151,65
$L_{b,rqd}$ [mm]	116,458165

Real stress and strain in fiber cable:

$\sigma_{FC, real}$ [kPa]	20220
$\varepsilon_{FC, real}$ [%]	0,674

$$\frac{\sigma_{FC,d}}{L_{b,rqd}} = \frac{\sigma_{FC,real}}{0,5 * L_{LC}} \rightarrow \sigma_{FC,real} = \frac{0,5 * L_{LC}}{L_{b,rqd}} * \sigma_{FC,d}$$

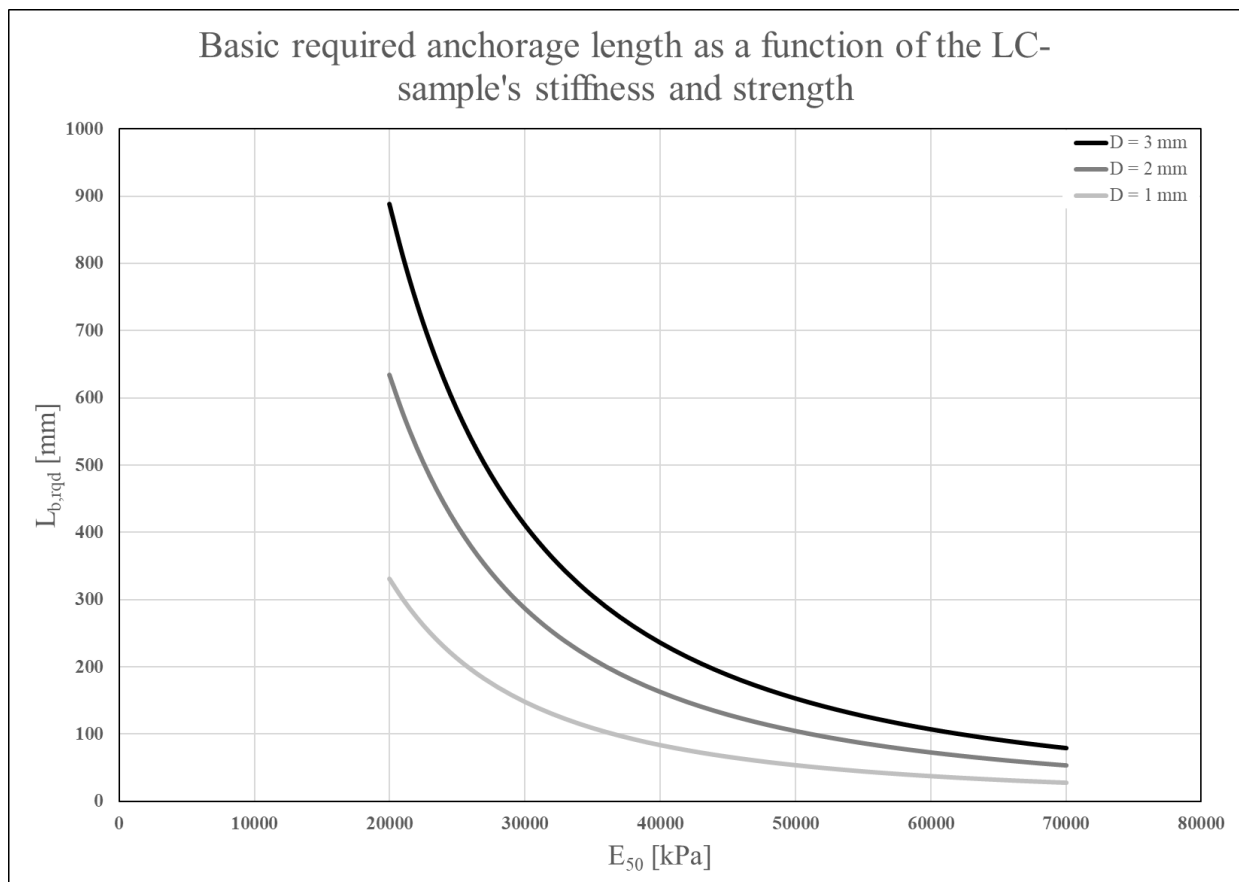




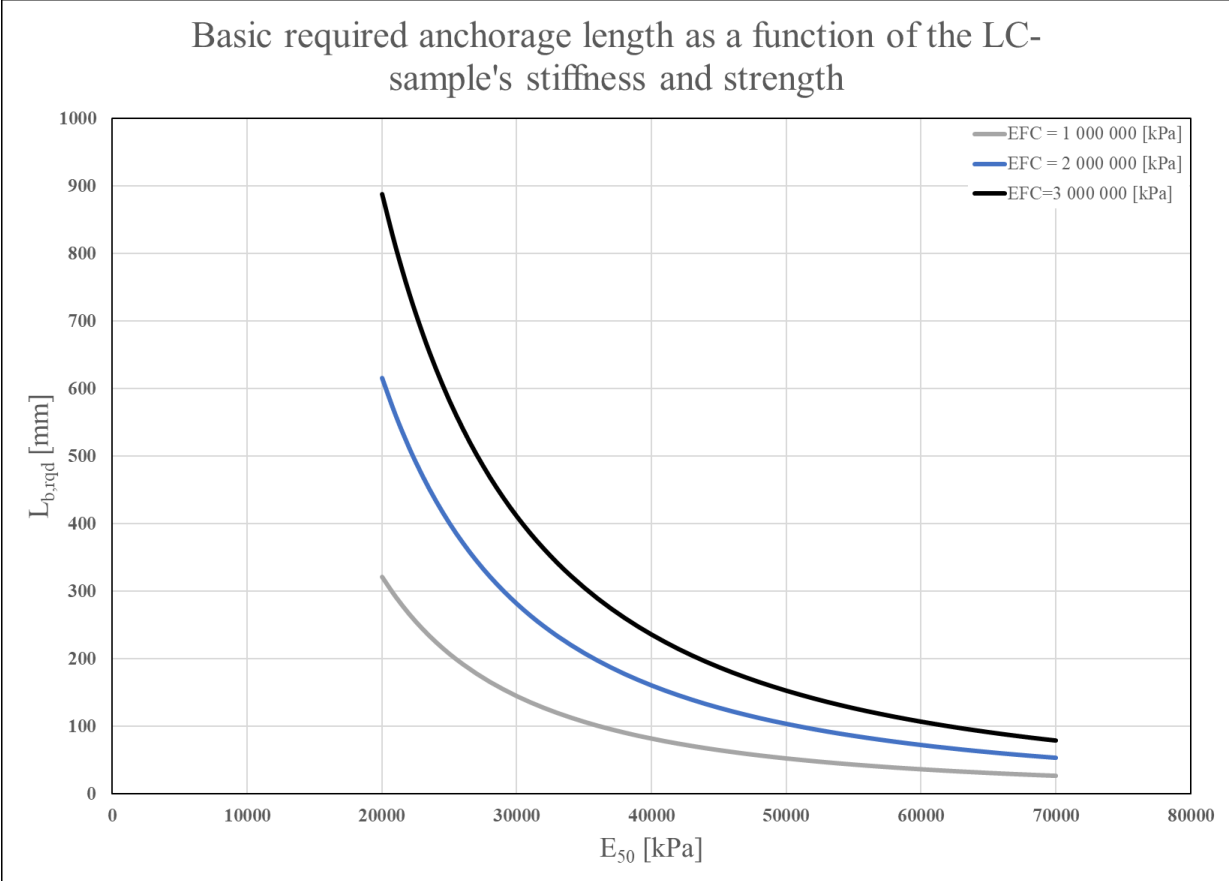
## Development of required bond length – A parametric study

It is essential to mention that the following parametric studies are based on the loading situation described in the discussion chapter. I.e., a force of  $F = 3.166$  kN from the uniaxial device is assumed for all the plots. In addition, the simplified relation that the stiffness of the LC-samples is 100 times bigger than the ultimate compressive strength has been used. The formulas from the discussion chapter forms the basis for the calculations that have been performed.

The first plot, shown below, is a parametric study on the effect of changing the diameter of the fiber optic cable on the required bond length. Three different diameters have been studied, more precisely  $D = 1$  mm,  $D = 2$  mm and  $D = 3$  mm. The EpsilonSensor from Nerve-Sensors can be produced in all these diameters. A distinct decrease in required bond length is observed for decreasing cable diameters.

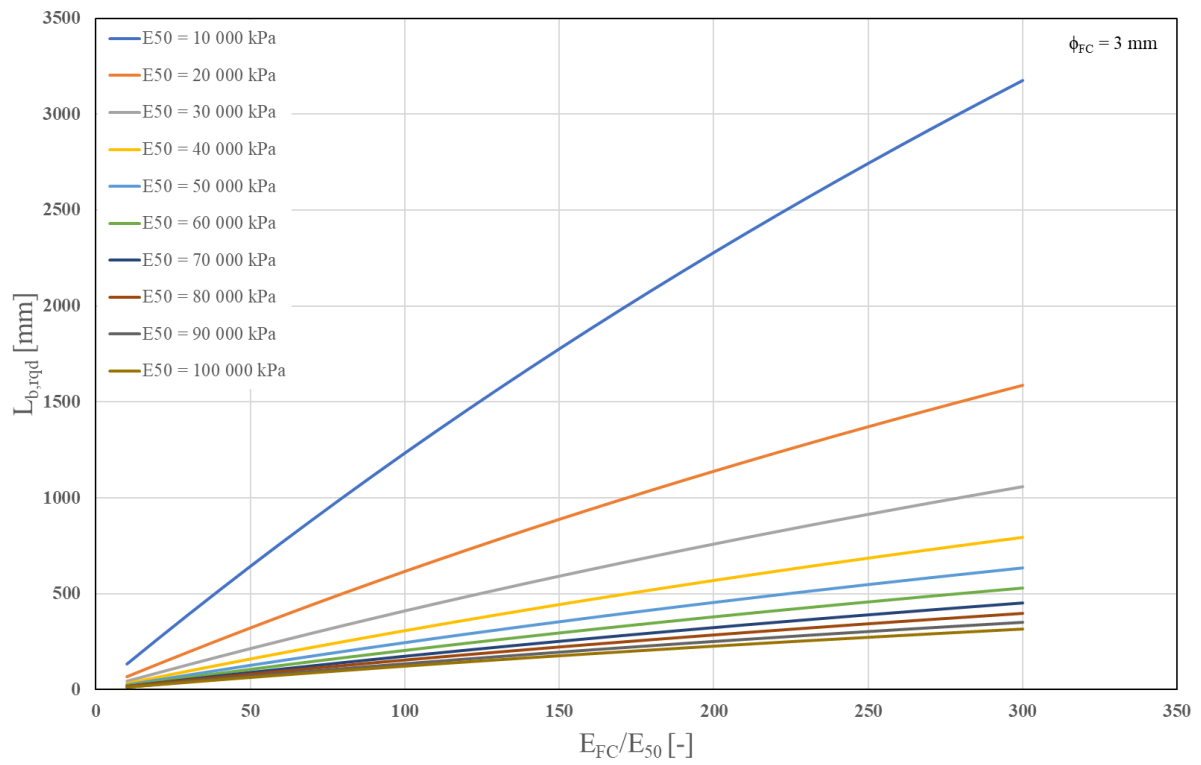


The second plot is a parametric study on the effect of changing the stiffness of the fiber optic cable. A diameter of 3 mm is presumed for the cable. Three different stiffnesses have been studied, more precisely  $E = 1 \text{ GPa}$ ,  $E = 2 \text{ GPa}$  and  $E = 3 \text{ GPa}$ . Also here a noticeable decrease in the required bond length is observed for a change in the given parameter. More precisely, a lower stiffness of the fiber cable gives a significantly shorter required bond length.



Lastly, a more general study has examined how the required bond length is affected by changes in the elasticity ratio between the fiber optic cable and LC-stabilized quick clay from Tiller-Flotten. A graph is made for LC-stiffnesses from  $E_{50} = 10\,000 \text{ kPa}$  to  $E_{50} = 100\,000 \text{ kPa}$ . Shorter bond lengths are observed for higher stiffnesses. What is also observed from the plot, is the fact that for higher stiffnesses of the LC-sample, the effect of changing the elasticity ratio becomes less significant. The plot is shown on the next page.

### Basic required anchorage length as a function of the stiffness ratio between cable and LC-sample

















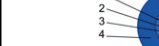

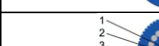



## **Appendix F**

### **Table of cable comparison**





DFOS-Sensors

Acronym	Picture	Manufacture	Color	Diameter	Jacket material	Standard
OFS_Y_02	 polyimide	OFS Optics	Yellow	0.155 mm	Polyimide	G.657.A1
NZ_W_09	 polyamide	NanZee	White	0.9 mm	Polyamide/polyimide	G.652.D
TLC_W_09	 PVC	The Light Connection	White	0.9 mm	PVC	G.657
OFS_K_09	 PFA silicone	OFS Optics	Black	0.9 mm	Central silicone, PFA outer sheath	G.657.A1
NZ_K_20 NZS-DSS-C07	 polyurethane polyamide	NanZee	Black	2.0 mm	Central polyamide/polyimide and (thermo-plastic) Polyurethane outer sheath	G.652.D
SLF_B_32	 PA metal tube	Brugg Kabel	Blue	3.2 mm	Central metal tube, Structured PA outer sheath. (BRUsens Strain V9 metallic)	—
NZ_K_50 (NZS-DSS-C02)	 stranded steel Optical fiber Metal reinforcement Silicone	NanZee	Black	5.0 mm	Stranded steel armored, polyethylene (PE) outer jacket	G.652.D
NS_R_50 (Epsilon rebar)		Nerve-sensors	Red	5.0 mm (5-20, but 5 is standard)	Monolithic cable - made of GFRP (glass fiber + epoxide)	—
NS_W_30 (EpsilonSensor)		Nerve-sensors	White	3.0 mm	Monolithic cable - made of PLFRP (polyester fiber + epoxide)	—
SF_B_32 (BRUsens DSS 3.2mm V9 grip)		Solifos	Blue	3.2 mm	Central metal tube, Structured PA outer sheath. (BRUsens Strain V9 metallic)	—
SF_R_DTS_34 (BRUsens DTS STL PA)		Solifos	Red	3.4 - 4.8 mm	Stainless steel loose tube, stainless steel strength members, PA outer sheath	—
B_K_78 (Central loose tube cable)		Belden	Black	7.8 mm	Polyethylene (PE)	G.657.A1 & G.652.D
SF_B_59 (BRUsens DSTAS V13)		Solifos	Blue	5.9 mm	PA outer sheath (option: smooth or structured)	—
SF_B_28 (BRUsens DSS 2.8mm V1 non-metallic)		Solifos	Blue	2.8 mm	EPR outer sheath	—
SF_B_35 (BRUsens DSS 3.5mm V0 alarm)		Solifos	Blue	3.5 mm	Metallic armoring wires and HDPE outer sheath	—
SF_B_72 (BRUsens DSS 7.2mm V3 grip)		Solifos	Blue	7.2 mm	Metallic armoring wires and structured PA outer sheath	—
FBGS_W_5/10 (SMW-01)		FBGS	White	0.5 mm and 1 mm	Glass Fiber Reinforced Plastic wire, optionally additional High-Density Polyethylene (HDPE)	—
FBGS_G_10_T (TC-X01)		FBGS	Grey	1 mm	The fibers are contained in a stainless steel tube	—
T_K_30/40/50 (T110)		Technica	Black	3 mm, 4 mm, 5 mm, other	Mid-layer coat of PE, PU or Teflon. Outer layer is armored with some relevant material	—
T_G_21 (T140)		Technica	Grey	2.1 mm	Mid-layer coat of Glass Fiber Reinforced Polymer (GFRP). Outer layer is very armoured	—
ATG_K_30/40/50		ATGRATING	Black	3 mm, 4 mm, 5 mm, other	Mid-layer coat of PE, PU or Teflon. Outer layer is armored with some relevant material	—

FBG-Sensors

<https://www.essentracomponents.com/en-us/news/solutions/wire-cable/>

Dependent on interrogator

General rule:  $r_{min} = 10 \times OD$  (however, very often observed  $20 \times OD$ )

Type of measurement	Spatial resolution	Sensitivites	Minimum bending radius	Links
Strain				
Strain	100 mm (from a laboratory test)	490 MHz/% (strain sensitivity)	18 mm (20 x OD) with tensile load, 13.5 mm (15 x OD) without tensile load (assumption)	<a href="https://www.etsc-tech.be/upload/file/Strain%20sensing%20cable.pdf">https://www.etsc-tech.be/upload/file/Strain%20sensing%20cable.pdf</a>
Strain			9 mm	
Strain				
Strain	100 mm (from a laboratory test)	485.5 MHz/% (strain sensitivity)	40 mm (20 x OD) with tensile load, 30 mm (15 x OD) without tensile load (assumption)	<a href="https://www.etsc-tech.be/upload/file/Strain%20sensing%20cable.pdf">https://www.etsc-tech.be/upload/file/Strain%20sensing%20cable.pdf</a>
Strain	10 mm	450 MHz/% (strain sensitivity)	64 mm (20 x OD) with tensile load, 48 mm (15 x OD) without tensile load	<a href="https://solifos.com/app/uploads/2020/01/Solifos_3-50-2-005_en.pdf">https://solifos.com/app/uploads/2020/01/Solifos_3-50-2-005_en.pdf</a>
Strain	1000 mm (from a field test)	$\pm 50 \mu\epsilon$ (Strain accuracy)	100 mm (20 x OD) with tensile load, 75 mm (15 x OD) without tensile load (assumption)	<a href="https://www.etsc-tech.be/upload/file/Strain%20sensing%20cable.pdf">https://www.etsc-tech.be/upload/file/Strain%20sensing%20cable.pdf</a>
Strain and cracking (concrete), temperature is optional	1-5 mm	$\pm 1.0 \mu\epsilon$ (Strain accuracy)	(50 mm) (probably too stiff for such low bending radius)	<a href="https://nerve-sensors.com/wp-content/uploads/2021/04/EpsilonRebar-1.pdf">https://nerve-sensors.com/wp-content/uploads/2021/04/EpsilonRebar-1.pdf</a>
Strain and cracking (concrete), temperature is optional	1-5 mm	$\pm 1.0 \mu\epsilon$ (Strain accuracy)	30 mm	<a href="https://nerve-sensors.com/wp-content/uploads/2021/04/EpsilonSensor-1.pdf">https://nerve-sensors.com/wp-content/uploads/2021/04/EpsilonSensor-1.pdf</a>
Strain	10 mm	450 MHz/% (strain sensitivity)	64 mm (20 x OD) with tensile load, 48 mm (15 x OD) without tensile load	<a href="https://solifos.com/app/uploads/2020/01/Solifos_3-50-2-005_en.pdf">https://solifos.com/app/uploads/2020/01/Solifos_3-50-2-005_en.pdf</a>
Temperature			20 x OD with tensile load, 15 x D without tensile load	<a href="https://solifos.com/app/uploads/2020/01/Solifos_3-50-1-001_en.pdf">https://solifos.com/app/uploads/2020/01/Solifos_3-50-1-001_en.pdf</a>
Temperature (+ strain)			117 mm (short term)	<a href="https://info.belden.com/hubfs/ESD-Assets/Product-Pages/Fiber/Part-Numbers/cable_loose-tube.pdf">https://info.belden.com/hubfs/ESD-Assets/Product-Pages/Fiber/Part-Numbers/cable_loose-tube.pdf</a>
Temperature + strain		See data sheet. Dependent on scattering	118 mm (20 x OD) with tensile load, 88.5 mm (15 x OD) without tensile load	<a href="https://solifos.com/app/uploads/2022/05/Datasheet-BSSH-V13.pdf">https://solifos.com/app/uploads/2022/05/Datasheet-BSSH-V13.pdf</a>
Strain		450 MHz/% (strain sensitivity)	56 mm (20 x OD) with tensile load, 42 mm (15 x OD) without tensile load	<a href="https://solifos.com/app/uploads/2020/01/Solifos_3-50-2-004_en.pdf">https://solifos.com/app/uploads/2020/01/Solifos_3-50-2-004_en.pdf</a>
Strain		450 MHz/% (strain sensitivity)	70 mm (20 x OD) with tensile load, 53 mm (15 x OD) without tensile load	<a href="https://solifos.com/app/uploads/2020/01/Solifos_3-50-2-006_en.pdf">https://solifos.com/app/uploads/2020/01/Solifos_3-50-2-006_en.pdf</a>
Strain		450 MHz/% (strain sensitivity)	144 mm (20 x OD) with tensile load, 108 mm (15 x OD) without tensile load	<a href="https://solifos.com/app/uploads/2020/01/Solifos_3-50-2-002_en.pdf">https://solifos.com/app/uploads/2020/01/Solifos_3-50-2-002_en.pdf</a>
Strain	$\geq 10$ mm distance between FBGs	$\pm 0.3 \text{ nm}$ (relative) $\pm 1 \text{ nm}$ (absolute) Wavelength accuracy	60 mm for OD = 0.5 mm    100 mm for OD = 1.0 mm	<a href="https://fbgs.com/components/strain-sensor-smw-01/#sf_form_salesforce_w2l_lead_3">https://fbgs.com/components/strain-sensor-smw-01/#sf_form_salesforce_w2l_lead_3</a>
Temperature	Number of sensors and their internal distance may be requested	0.1°C Temperature resolution, 3°C precision	Not defined, probably not very high. Described as "insensitive to bending"	<a href="https://fbgs.com/components/temperature-sensor-tc-x01/#sf_form_salesforce_w2l_lead_3">https://fbgs.com/components/temperature-sensor-tc-x01/#sf_form_salesforce_w2l_lead_3</a>
Strain	FBG length of 5 to 10 mm with customer defined spac- ing between FBG-points	$\approx 8 \text{ pm/g}$ (Strain sensing sensitivity)	Not defined, but designed to make handling easy. Probaly not very high bending radius	<a href="https://technicasa.com/wp-content/uploads/2017/01/T110-Armored-Cable-FBG-Array-Sensor.pdf">https://technicasa.com/wp-content/uploads/2017/01/T110-Armored-Cable-FBG-Array-Sensor.pdf</a>
Temperature	FBG length of 5 to 10 mm with customer defined spac- ing between FBG-points	0.059 C/pm (Temperature sensing sensitivity)	Not defined. Quite stiff, but at the same time designed to make handling easy.	<a href="https://www.technicasa.com/wp-content/uploads/2017/01/T140-High-Tensile-Strength-Temperature-Cable-Sensor.pdf">https://www.technicasa.com/wp-content/uploads/2017/01/T140-High-Tensile-Strength-Temperature-Cable-Sensor.pdf</a>
Strain	FBG length of 5 to 10 mm with customer defined spac- ing between FBG-points	8 pm/g (Strain sensing sensitivity)	Not defined, but designed to make handling easy. Probaly not very high bending radius	<a href="https://www.atgrating.com/products/armored-fbg-sensing-cable.html">https://www.atgrating.com/products/armored-fbg-sensing-cable.html</a>

[fiber-optics-fags-the-advantages-bend-radius-explained-and-more](#)

with tensile load and 15 x OD without tensile load)

Additional information	Wavelength [Tolerance]
Easily integrated into loose media, can be directly buried in soil to monitor deformation, low Young's modulus of $E \approx 1$ Gpa and should not be overly stretched, tensile strength of 20-25 Mpa, <a href="#">suitable for laboratory physical modeling</a> , is matched well with Brillouin DFOS-technology (BOTDR/A), 1 core, $\pm 7.5 \mu\epsilon$ strain accuracy	
Easily integrated into loose media, can be directly buried in soil to monitor deformation, low Young's modulus of $E \approx 1$ Gpa and should not be overly stretched, tensile strength of 20-25 Mpa, <a href="#">suitable for laboratory physical modeling</a> , is matched well with Brillouin DFOS-technology (BOTDR/A), 1 core, $\pm 7.5 \mu\epsilon$ strain accuracy	
Tensile strength of 260 N during installation, crush resistance of 250 N/cm, high chemical and abrasion resistance, robust, high strain sensitivity, compact design, good flexibility, strain range up to 1 %, structured for better strain transfer, used with Brillouin and FBG, made for direct burial in harsh environment, laterally watertight.	
Young's modulus of $E \approx 8$ Gpa, tensile strength of up to 120 Mpa, i.e. high mechanical performance, can survive harsh environments, easy to install due to high strength, suitable for direct embedment in soil, is matched well with Brillouin DFOS-technology (BOTDR/A), single mode, 1 core, <a href="#">suitable for field application</a>	
Young's modulus of $E \approx 50$ Gpa, can have a reinforcement-effect due to its very high stiffness, high mechanical resistance to loads and environmental conditions, made for direct embedding, monolithic section giving accurate measurements, heavyweight, used with Rayleigh, Brillouin or Raman scattering, <a href="#">suitable for field application</a>	
Young's modulus of $E \approx 3$ Gpa, easily installed due to extremely low stiffness and low bending radius, ensures very good bond, <a href="#">very suitable for laboratory applications</a> , monolithic section giving very accurate measurements, lightweight, used with Rayleigh, Brillouin or Raman scattering	
Tensile strength of 260 N during installation, crush resistance of 250 N/cm, high chemical and abrasion resistance, robust, high strain sensitivity, compact design, good flexibility, strain range up to 1 %, structured for better strain transfer, used with Brillouin and FBG, made for direct burial in harsh environment, laterally watertight.	
Depending on diameter it has tensile strength of 800-3000 N during installation and 600-2000 N during operation, lightweight, high flexibility, robust and abrasion resistant outer sheath, high crush resistance, high chemical resistance, fast temperature response, easy deployment, can be used with Raman, Brillouin, FBG etc.	
Tensile strength of 2700 N during installation and 890 N during operation, economical option for low fiber counts, quick and easy end preparation, crush, impact and abrasion resistant.	
Tensile strength of 400 N during installation, crush resistance of 300 N/cm, robust outer sheath, either smooth or structured outer sheath for enhanced grip, hermetically sealed tubes, two strain-sensing optical fibers in metal tubes and gel-filled 316L stainless steel Fiber In Metal Tube (FIMT) for temperature and/or acoustic sensing.	
Tensile strength of 5 N during installation, max crush resistance of 150 N/cm, lightweight, good chemical resistance, compact design, good flexibility, non-metallic i.e. not armored, sensitive, strain range up to 1 %, used with Brillouin and FBG, made for direct burial in harsh environment, laterally watertight.	
Tensile strength of 700 N during installation, max crush resistance of 800 N/cm, high chemical resistance, compact design, good flexibility, armored with central metal tube and metallic armoring wires, good strain sensitivity, strain range up to 1 %, used with Brillouin and FBG, made for direct burial in harsh environment, robust outer sheath	
Tensile strength of 600 N during installation, max crush resistance of 500 N/cm, high chemical resistance, compact design, good flexibility, armored with central metal tube and metallic armoring wires, good strain sensitivity, strain range up to 1 %, used with Brillouin and FBG, made for direct burial in harsh environment, robust outer sheath	
The cable can optionally be protected by an additional HDPE outer jacket, $E \geq 31$ Gpa for OD = 0.5 mm, $E \geq 48$ Gpa for OD = 1.0 mm, maximum tensile strain 20 000 $\mu\epsilon$ , maximum tensile loads are 125 N (OD = 0.5 mm) & 760 N (OD = 1.0 mm), lightweight, suitable for harsh environments, good adhesion between buffer material and sensing fiber	
Offering absolute measurement of temperature, can be read out over very large distances, good corrosion resistance, no significant influence on the distortion of the thermal distribution profile to be measured, can be configured according to customer needs, offering distributed temperature sensing, single ended configuration	
More than 689 MPa pull strength, fast and easy strain monitoring, made for fast, easy and intuitive handling and deployment, many of the advantages to all FBG based sensors while elevating the degree of ruggedness, the manufacturing process allows for significant variations in cable construction, i.e. room for much customer impact	1460 to 1620 nm [+/- 0.5] (other options available)
More than 1100 MPa tensile strength, more than 50 Gpa tensile Young's modulus, designed for harsh environments, made for fast, easy and intuitive handling and installation, many of the advantages to all FBG based sensors while elevating the degree of ruggedness, room for much customer impact on cable construction	1460 to 1620 nm [+/- 0.5]
More than 689 MPa pull strength, fast and easy strain monitoring, made for fast, easy and intuitive handling and deployment, many of the advantages to all FBG based sensors while elevating the degree of ruggedness, the manufacturing process allows for significant variations in cable construction, i.e. room for much customer impact	1460 to 1610 nm [+/- 0.5]



 **NTNU**

Norwegian University of  
Science and Technology